Structural, Magnetic and Magnetocaloric Properties of $RE_{0.55}(Ca_xSr_{1-x})_{0.45}MnO_3$ (RE= Sm, Pr, La) Perovskite

by

Most. Asma Akter Bally

Department of Physics
BANGLADESH UNIVERSITY OF ENGINEERING AND TECHNOLOGY
September 2021

Structural, Magnetic and Magnetocaloric Properties of $RE_{0.55}(Ca_xSr_{1-x})_{0.45}MnO_3$ (RE= Sm, Pr, La) Perovskite

by

Most. Asma Akter Bally

DOCTOR OF PHILOSOPHY

Department of Physics
BANGLADESH UNIVERSITY OF ENGINEERING AND TECHNOLOGY
September 2021

The thesis titled "Structural, Magnetic and Magnetocaloric Properties of $RE_{0.55}(Ca_xSr_{1-x})_{0.45}MnO_3$ (RE= Sm, Pr, La) Perovskite" submitted by Most. Asma Akter Bally, Roll No.: 1015144007 F, Session: October 2015, has been accepted as satisfactory in partial fulfillment of the requirement for the degree of DOCTOR OF PHILOSOPHY on 18 September, 2021.

BOARD OF EXAMINERS

1. (_____)
Dr. Md. Feroz Alam Khan (Supervisor) — Chairman
Professor, Department of Physics, BUET, Dhaka.

2. (_____)
Dr. Md. Rafi Uddin — Member
Professor and Head, Department of Physics, BUET, Dhaka. — (Ex-officio)

3. (_____)
Dr. Jiban Podder — Member
Professor, Department of Physics, BUET, Dhaka.

4. (_____)
Dr. A.K.M. Akther Hossain — Member
Professor, Department of Physics, BUET, Dhaka.

5. (_____)
Dr. Engr. Sheikh Manjura Hoque — Member
Chief Scientific Officer and Head,
Materials Science Division, AEC, Dhaka

6. (_____)
Dr. Md. Fakhrul Islam — Member
Professor, Department of GCE, BUET, Dhaka.

7. (_____)
Dr. M. Khalilur Rahman Khan — Member
Professor, — (External)
Department of Physics, Rajshahi University, Rajshahi.

CANDIDATE'S DECLARATION

It is hereby declared that this thesis or any part of it has not been submitted elsewhere for the award of any degree or diploma.

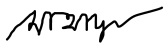

Most. Asma Akter Bally

Dedicated

to

My Beloved Family Members

Acknowledgments

At first I praise to Almighty Allah for giving me the opportunity, strength, courage and patience to complete my research work.

Then I would like to express my sincere thanks to my supervisor Dr. Md. Feroz Alam Khan, Professor, Department of Physics, Bangladesh University of Engineering and Technology (BUET), Dhaka, Bangladesh, for giving his valuable time in guiding me through the process of the study, for his continuous encouragement, close supervision and fruitful discussion during my research work. I am also grateful to all the members of the doctoral committee for their kind encouragement and valuable suggestions.

I am thankful to CASR, BUET, Dhaka, Bangladesh for financial and technical supports in completing my research work. I would like to thank Prof. Dr. Md. Rafi Uddin, Head of the Department of Physics, BUET, Dhaka for his kind cooperation. I am thankful to all the teachers, staff and assistants who helped me in their capacity.

I acknowledge the International Science Programs, Uppsala University, Sweden, for providing me three months scholarship for conducting research work at Uppsala University and financial support for conference registration fees and part of PPMS measurement's fees. Experimental supports from the Department of Glass and Ceramics Engineering, BUET, Dhaka is also thankfully acknowledged. I am thankful to the staff of the Materials Science Division of AEC, Dhaka for their assistance during PPMS measurements. I am thankful to Dr. A. K. M. Akther Hossain, Professor, Department of Physics, BUET, Dhaka for permitting me to work in his laboratory for sample sintering.

Also thanks go to all of my lab mates specially M. A. Islam, Dr. M. Z. Ahasan, Md. Masum Billah, and Md. Tofayel Hossain. My special thank goes to my husband Md. Abdur Razzak Sarker, my parents, sisters and brothers for their support during the course of my research work.

Finally, I would like to convey my sincere gratitude to the Ministry of Education, Dhaka, Bangladesh for granting me the opportunity of deputation to carry out my Ph. D. research work. I would also thankfully acknowledge the University Grants Commission, Dhaka, Bangladesh for awarding me with a Ph. D. fellowship.

Most. Asma Akter Bally

September 2021

Abstract

The structural, magnetic and magnetocaloric properties of three series of compositions $La_{0.55}Ca_xSr_{0.45-x}MnO_3$, $Pr_{0.55}Ca_xSr_{0.45-x}MnO_3$ and $Sm_{0.55}Ca_xSr_{0.45-x}MnO_3$ (x = 0.00, 0.05, 0.1, 0.2 and 0.25) synthesized by solid state reaction technique have been investigated. Room temperature XRD measurements reveal rhombohedral structure for all the compounds of $La_{0.55}Ca_xSr_{0.45-x}MnO_3$ and orthorhombic structure for all the compounds of $Pr_{0.55}Ca_xSr_{0.45-x}MnO_3$ and $Sm_{0.55}Ca_xSr_{0.45-x}MnO_3$. With increase in Ca content, lattice parameters and Mn-O-Mn bond angles are found to decrease. These structural changes control ferromagnetism in the materials via double-exchange mechanism. The calculated values of chemical composition using the EDX data were in well agreement with the nominal one. Arrott plots confirm that all the samples undergo second-order ferromagnetic (FM) to paramagnetic (PM) phase transition for $La_{0.55}Ca_xSr_{0.45-x}MnO_3$ and $Pr_{0.55}Ca_xSr_{0.45-x}MnO_3$ series and first-order FM to PM phase transition for $Sm_{0.55}Ca_xSr_{0.45-x}MnO_3$ series. Curie temperature (T_C) decreases with increase in Ca content for all three series but saturation magnetization decreases with increase in Ca content in $La_{0.55}Ca_xSr_{0.45-x}MnO_3$, and $Sm_{0.55}Ca_xSr_{0.45-x}MnO_3$ while increases for $Pr_{0.55}Ca_xSr_{0.45-x}MnO_3$. Critical exponent values calculated from modified Arrott plots, Kouvel–Fisher method and critical isotherm analysis disclose the presence of long range ferromagnetic interaction in $Pr_{0.55}Ca_xSr_{0.45-x}MnO_3$ and $La_{0.55}Ca_xSr_{0.45-x}MnO_3$ with x=0.00, 0.05, 0.1 and short-range ferromagnetic interactions in samples with x=0.2 and 0.25. The magnetocaloric effect was calculated in terms of entropy change ($-\Delta S_M$) and relative cooling power (RCP). The T_C values of $Pr_{0.55}Ca_xSr_{0.45-x}MnO_3$ series are found to decrease from 290 to 230 K while both maximum entropy change ($(-\Delta S_M)_{max}$) and RCP increase with the increase of Ca content. For $La_{0.55}Ca_xSr_{0.45-x}MnO_3$ series values of $(-\Delta S_M)_{max}$ and RCP are found to decrease with the increase in Ca content while increase in Ca content tunes the T_C near room temperature. The T_C values of the samples of series $Sm_{0.55}Ca_xSr_{0.45-x}MnO_3$ are found to decrease from 116 to 75 K and both $(-\Delta S_M)_{max}$ and RCP values also decrease with increase in Ca content. These properties make $Pr_{0.55}Ca_xSr_{0.45-x}MnO_3$, $La_{0.55}Ca_xSr_{0.45-x}MnO_3$ and $Sm_{0.55}Ca_xSr_{0.45-x}MnO_3$ as potential materials for magnetic cooling technology at below room temperature, above room temperature and low temperature applications, respectively.

Contents

Contents (cont…)

CHAPTER 3: SAMPLE PREPARATION AND CHARACTERIZATION TECHNIQUES

CHAPTER 4: RESULTS AND DISCUSSION

Contents (cont…)

List of figures

List of Tables

List of Abbreviations and symbols

MCE	Magnetocaloric Effect
ΔS_M	Magnetic Entropy Change
$(-\Delta S_M)_{max}$	Maximum Magnetic Entropy Change
ΔT_{ad}	Adiabatic Temperature Change
$< r_A >$	A-site Average Ionic Radius
T_C	Curie Temperature
RCP	Relative Cooling Power
FWHM	Full Width at Half Maximum
AFM	Anti-ferromagnetic
FM	Ferromagnetic
DE	Double-Exchange
SE	Super-Exchange
K	Kelvin
M	Magnetization
T	Temperature
H	Applied Magnetic Field
ZFC	Zero Field Cooled
FC	Field Cooled
T_R	Irreversibility Temperature
θ	Paramagnetic Curie Temperature
χ	Magnetic Susceptibility
t	Tolerance Factor
D	Grain Size
MAP	Modified Arrott Plot
KF	Kouvel-Fisher
CIA	Critical Isotherm Analysis
β, γ and δ	A Set of Critical Exponents
μ_B	Bohr Magnetron
M_S	Spontaneous Magnetization
ΔH	Applied Magnetic Field Change

CHAPTER 1
INTRODUCTION

1.1 Theoretical Background of the Problem

The magnetocaloric effect (MCE) occurs as the heating or cooling of a magnetic material due to the rearrangement of the magnetic moments in response to the application or withdrawal of a magnetic field. When magnetic field is applied on a ferromagnetic material under adiabatic condition, the moments of the material are aligned in the direction of applied field. As a result, magnetic entropy of the material decreases. Therefore, temperature of the system rises. Conversely, when magnetic field is removed from a magnetic material under adiabatic condition, temperature of the material decreases [1]. This effect is also known as adiabatic demagnetization. In 1881, the MCE was first discovered by Warburg in iron [1]. After that, Debye and Giaque explained the origin of this effect in 1926 independently [2, 3] and suggested the first practical application of the MCE to attain temperatures lower than 4 K by using paramagnetic salts. Giaque and Mac Dougall have applied this idea for practical application in 1933 and experimentally shown the use of MCE to reach temperatures below 1 K [4]. It was an emerging challenge to use MCE for application in room temperature magnetic refrigeration. Brown proposed a prototype of room temperature magnetic refrigerator creating possibility of magnetic household refrigeration in 1976 [5]. Now a day, the MCE is used as environment friendly technology for magnetic refrigeration from the room temperature to that of the liquid hydrogen or helium (<2 K).

The magnetic refrigeration as a cooling technology based on MCE has attracted much attention because of its higher energy efficiency and environment friendly technology over the conventional gas-compression refrigeration [6]. Compared to conventional gas-compression refrigeration, solid state magnetic refrigeration has benefits, such as, it is safer, quieter, and more energy efficient, and is more environment friendly as it does not use coolant gases harmful for ozone-layer [5]. All the magnetic materials show MCE. But the strength of the effect depends on the material's properties. The MCE is described quantitatively in terms of magnetic entropy change, adiabatic temperature change, and relative cooling power. The MCE reaches its maximum value when the magnetic material is near its magnetic phase transition temperature. All the magnetic

materials undergo a magnetic phase transition. But the values of the magnetic entropy change and the adiabatic temperature changes are larger in case of ferromagnetic materials.

1.2 Motivation of this Research Work

Till now extensive research works have been done to identify refrigerant materials to be used in magnetic refrigerator. Rare-earth metal gadolinium is considered as the most promising solid state refrigerant due to its large value of magnetic entropy change and Curie temperature (T_C) around room temperature [7]. However, its actual application is hindered due to its expensive price. Therefore, the search for new working substance with low price and large MCE near room temperature becomes a main research topic in this field. After that, some other candidates, Heusler alloys such as $LaFe_{13-x}Si_x$, $MnFeP_{1-x}As_x$, and Ni_2MnX (X = Ga, Co, In, Al, Sb) [8-10] possess high value of magnetic entropy change around room temperature but those have limitations for using in air atmosphere. Over the past few years, the hole-doped manganites with the general formula $RE_{1-x}M_xMnO_3$ (RE = rare earth ion, M= divalent alkaline-earth metal ion) [11–15] have been considered as potential refrigerant materials because its T_C and saturation magnetization greatly depends on their chemical composition and those have wide working temperature range [8]. Besides, their higher resistivity is favorable for reducing eddy current heating. For these reasons the perovskite manganites have been suggested as a strong candidate for application in magnetic refrigeration technology. In addition, manganite as magnetocaloric compounds exhibit large magnetic entropy change, simple preparation technique, tunable transition temperature, and those are also chemically stable [16]. Besides, achieving large magnetic-refrigeration properties using less expensive materials is a big challenge now. This project based on $RE_{0.55}(Ca_xSr_{1-x})_{0.45}MnO_3$ (RE= Sm, Pr, La) prepared by less expensive materials, is expected to show large magnetocaloric effect with tunable T_C.

The $La_{1-x}M_xMnO_3$ type compounds have drawn much attention in the scientific community due to their rich magnetic phase diagrams and their important properties such as colossal magneto-resistance and MCE [6-10]. Conventionally, these properties are explained with the help of the anti-ferromagnetic (AFM) super-exchange and ferromagnetic (FM) double exchange interactions, polaronic effect and phase separation

[11]. In recent days, determination of critical point exponents around second order FM to PM transition temperature is considering as important way for theoretical and experimental description of magnetic materials. The critical behavior around T_C in double exchange model is conventionally interpreted by long range interactions belonging to mean field theory [12]. However some reports suggest that critical point behavior can also be clarified by short range interactions belonging to 3-D Heisenberg model [12], or 3-D Ising model [13]. Rear-earth lanthanum manganite $LaMnO_3$ is AFM insulator due to the super-exchange AFM interaction between Mn^{3+}-O- Mn^{3+} ions or Mn^{4+}-O- Mn^{4+} ions. The substitution of rare earth La^{3+} ion by divalent alkaline-earth metal M^{2+} ion in $LaMnO_3$ creates a conversion of Mn^{3+} to Mn^{4+} ion which is proportional to doping amount. This mixed valence state of Mn^{3+} and Mn^{4+} ions is responsible for double exchange mechanism in $La_xM_{1-x}MnO_3$ [17, 18]. This double exchange mechanism is the source of FM behavior in these doped manganites and affect significantly on magnetism and conductivity of the manganite. This system exhibits many interesting properties such as colossal magneto-resistance, charge and orbital ordering, metal-insulator transition etc. Recent researches on manganites have also shown magnetocaloric effect and thus have made them promising candidates for magnetic refrigeration. Till now significant research work is going on to achieve that goal. In $La_{1-x}Sr_xMnO_3$ compounds partial substitution of La^{3+} ion by Sr^{2+} ion introduces ferromagnetism and metallic behavior for certain doping level. This system exhibits a rich phase diagram depending on temperature, applied magnetic field, doping content, A-site average ionic radius and A-site size-disorder. According to phase diagram, for $0.175 \leq x \leq 0.5$ the above mentioned system behaves as ferromagnetic material and for $x > 0.5$ this compound shows AFM insulating properties [19]. Within the FM region, for $0.175 \leq x \leq 0.3$ and $0.4 \leq x \leq 0.5$, T_C remains in between 250 and 365 K but for $0.3 \leq x \leq 0.4$ region, T_C remains almost constant at 365 K. $La_{0.7}Sr_{0.3}MnO_3$ and $La_{0.6}Sr_{0.4}MnO_3$ are large band-with ferromagnetic material having T_C values around 365 K, possess high value of MCE [19, 20]. Many studies have been reported during the last decade on these compounds and on partial substitution of Sr^{2+} ion by other divalent or monovalent element to tune the T_C and magnetization. However, compounds with T_C values at room temperature are till now interest of researchers for using the compound in room temperature applications as both colossal magneto-resistance and MCE are maximized around T_C values of the materials. The T_C values depend on chemical composition of the compounds. According to phase diagram, $La_{0.55}Sr_{0.45}MnO_3$ has comparatively low T_C

value (around 350 K) which also stays above room temperature [19]. On the other hand, Ca doped manganites $La_{1-x}Ca_xMnO_3$ [21] show T_C values around 250 K which are below room temperature. These materials are not suitable for room temperature applications [21, 22]. Thus partial substitution of Sr by Ca in A-site of $La_{0.55}Sr_{0.45}MnO_3$ manganite may tune the T_C toward room temperature. From this line of view, Sr have been substituted by Ca in $La_{0.55}Ca_xSr_{0.45-x}MnO_3$ (x=0.00, 0.05, 0.1, 0.2 and 0.25) compounds. In this research work, the influence of Ca doping on structural, magnetic and magneto-caloric properties of $La_{0.55}Ca_xSr_{0.45-x}MnO_3$ manganites have been investigated. The critical exponents around T_C were also investigated to elucidate the critical behaviors that occur around the PM to FM phase transition. It is noted that no such research work has been reported till now. Here the magnetic and magneto-caloric properties of different $La_{0.55}Ca_xSr_{0.45-x}MnO_3$ compounds as a function of temperature and applied magnetic field have also been demonstrated.

The alkaline doped rare-earth samarium manganites, $Sm_{1-x}M_xMnO_3$ (M =alkaline-earth element) have also attracted considerable attention since they possess interesting properties like metal insulator transition, colossal magneto-resistance effect and MCE [18, 23–25]. These compounds also exhibit higher resistivity, which reduces eddy current heating [26]. In these manganites, a decrease in the average ionic radius of the A-site cations, generally causes an increase in tilting of MnO_6 octahedral resulting decrease in the Mn-O-Mn bond angle [27, 28]. As a result, the FM state is relatively destabilized in this distorted perovskite manganite. In such a case, a FM state is frequently replaced by an AFM insulator with Charge/orbital ordering [29, 30]. $Sm_{0.55}Sr_{0.45}MnO_3$ possesses ferromagnetic metallic behaviors and $Sm_{0.55}Ca_{0.45}MnO_3$ shows antiferromagnetic charge/orbital ordered insulator like behaviors. Thus, the competing features between FM and charge/orbital ordered insulating properties with Ca content in $Sm_{0.55}Ca_xSr_{0.45-x}MnO_3$ and its influence on structural, magnetic and magnetocaloric properties of the studied samples have been investigated.

The perovskite $Pr_{1-x}Sr_xMnO_3$ is another potential member in manganite system having intermediate one electron band width [31, 32]. The Pr-based manganites show many interesting properties like charge/orbital ordering, coexistence of FM and AFM phases, and metamagnetic transition due to quenched disorder etc. [33–35]. Magnetic phase diagram of $Pr_{1-x}Sr_xMnO_3$ possesses two FM regions [19]. One is ferromagnetic insulator

region which remains in $0.1<x<0.25$ and second one is ferromagnetic metallic region with $0.25<x<0.5$. On the other hand for $x\geq0.5$, this system shows a charge ordered antiferromagnetic state. The composition of $Pr_{0.55}Sr_{0.45}MnO_3$ just lies near the boundary of FM and charge ordered antiferromagnetic phase [19], and investigation of MCE on it may possess a potential work applicable in magnetic refrigeration technology. In this research work, the influence of Ca doping on structural, magnetic and magneto-caloric properties of $Pr_{0.55}Ca_xSr_{0.45-x}MnO_3$ manganites have been investigated. After elucidating the critical exponents near the PM to FM phase transition, relation between the critical behaviors that occur around T_C and the observed magnetocaloric behavior was also investigated.

1.3 Objectives with Specific Aims

$RE_{0.55}(Ca_xSr_{1-x})_{0.45}MnO_3$, (RE= Sm, Pr, La) is expected to exhibit large MCE with a high refrigeration capacity for application in solid state magnetic refrigerator as an environment friendly and low cost new material.

The main objectives of this research work are given below:

- Three series of samples $Pr_{0.55}Ca_xSr_{0.45-x}MnO_3$, $La_{0.55}Ca_xSr_{0.45-x}MnO_3$ and $Sm_{0.55}Ca_xSr_{0.45-x}MnO_3$ have been synthesized by solid state reaction method.

- Then crystallographic structure, lattice parameters, phase purity, surface morphology have been analyzed and also chemical compositions of the samples have been calculated.

- The field cooled and zero field cooled magnetization as a function of temperature and isothermal magnetization as a function of applied magnetic field around the T_C have been measured to determine magnetic properties and magnetocaloric effect.

- The critical exponents have been calculated to find the origin of magnetic and magnetocaloric properties of the studied samples.

- The magnetocaloric properties have been calculated in terms of magnetic entropy change and relative cooling power.

- ❖ The relation between the critical behaviors around T_C and the observed magnetocaloric behavior has been also investigated in terms of scaling exponent.
- ❖ The experimental magnetic entropy change has been compared with the theoretical magnetic entropy change.
- ❖ Finally influence of Ca doping on structural, magnetic and magnetocaloric properties has been investigated.

1.4 Outline of this Thesis

In this thesis, the procedures of synthesizing of the investigated samples and experimentation with their findings and discussion are presented in the following sequences:

i. Chapter 1 deals with background, motivation and objectives of present investigation.
ii. Chapter 2 describes review of earlier works and theoretical aspects.
iii. Chapter 3 deals with sample preparation technique and experimental procedures.
iv. Chapter 4 explains the results and discussion.
v. Chapter 5 describes the conclusions and recommendations for future work.

CHAPTER 2
LITERATURE REVIEW AND THEORETIAL ASPECTS

2.1 Review of Earlier Research

Literature survey is the most important step for finding research objective to the discovery and continuous development of new materials suitable for diversified applications. A lot of researchers are working on magnetocaloric materials all over the world. In this chapter some results of recent researches on MCE have been discussed.

2.1.1 Intermetallic compounds

Gd and its alloys are considered as most promising refrigerant for magnetic refrigeration. Dankov et al. [7] investigated magnetic phase transitions and the magnetic and thermal properties of Gd and found that gadolinium undergoes second order FM to PM phase transition, possesses high value of magnetic entropy change (ΔS_M), T_C around room temperature and do not show magnetic or thermal hysteresis. After that intermetallic compounds [36-39], Heusler alloys such as Ni_2MnX (X = Ga, Co, In, Al, Sb) [8-10] and some double perovskite [40] are also potential materials for magnetic cooling applications because they have T_C near room temperature and they also possess high value of ΔS_M. Hu et al. discovered the giant MCE in the $NaZn_{13}$-type $La(Fe_{1-x}Si_x)_{13}$ compounds. Wada et al. found a large ΔS_M in $MnAs_{1-x}Sb_x$ compounds and reduced its thermal hysteresis by doping Sb [41]. Tagus et al. discovered the giant MCE in $MnFeP_{1-x}As_x$ compounds that possess first-order FM to PM phase transition and they also found that the T_C values of the compounds are tunable around room temperature by changing Arsenic content [42]. But above mentioned compounds are expensive or they have limitations for using in air atmosphere or those are not easy to synthesis.

2.1.2 $La_{1-x}M_xMnO_3$ (M= divalent alkaline-earth metal ion like Ca, Sr) system

A lot of research works have been conducted on this series of samples over the last few decades. Morelli et al. [43] reported on the MCE of $La_{1-x}M_xMnO_3$ (M = Ca, Sr, Ba) magnetic films. But they obtained small value of $-\Delta S_M$ though the temperature of maximum entropy change ($(-\Delta S_M)_{max}$) was tuned in the temperature in between 250 to 350 K due to changes in doping concentration. Guo et al. [44] reported the entropy

change in $La_{1-x}Ca_xMnO_3$ manganite with $0.2 \leq x \leq 0.33$. They have shown that, for a field change of 1.5 T, the $-\Delta S_M$ reaches a highest value 5.5 $JKg^{-1}K^{-1}$ at 230 K, 4.7 $JKg^{-1}K^{-1}$ at 224 K and 4.3 $JKg^{-1}K^{-1}$ at 260 K for x = 0.2, 0.25, and 0.33 samples, respectively. These values were greater than that of gadolinium with maximum entropy change of 4.2 $JKg^{-1}K^{-1}$, for ΔH= 1.5 T [7]. In these samples, the large value of $(-\Delta S_M)_{max}$ was produced due to the sudden reduction of magnetization which is associated to the anomalous thermal expansion near the phase transition temperature. However, very narrow full width at half maximum (FWHM) of the $-\Delta S_M$ vs T curve for $La_{1-x}Ca_xMnO_3$ samples was obtained. On the other hand, Zhang et al. [45] found smaller value of $-\Delta S_M$ of 0.6 $JKg^{-1}K^{-1}$ for ΔH=1 T and a broad δT_{FWHM} = 62 K, in $La_{0.67}Ca_{0.33}MnO_3$ (x = 0.33) than that Guo et al. [44] reported. This inconsistency may be arisen from the variation of the sample preparation method or from the variation of chemical composition. $La_{0.67}Ca_{0.33}MnO_3$ was found to exhibit the largest MCE among the manganite reported in [46-48]. Lin et al. [48] studied the MCE of $La_{0.67}Ca_{0.33}MnO_3$ and obtained adiabatic temperature change (ΔT_{ad}) of 2.4 K for ΔH= 2.02 T. This value of T_{ad} is not as large as that of gadolinium. Large magnetic entropy change was obtained due to the sharp jump in magnetization which is attributed to first order FM to PM transition. It is notable that, the MCE decreases significantly, but the FWHM becomes broader when the material undergoes from a first order magnetic phase transition to a second order phase transition.

The MCE was also reported in some deficient manganites. Szymczak et al. [49] studied MCE in $La_{1-x}Ca_xMnO_3$ and found that the oxygen deficient $La_{0.54}Ca_{0.32}MnO_{3-\delta}$ manganite exhibit large $-\Delta S_M$ = 2.9 $JKg^{-1}K^{-1}$ for ΔH = 0.9 T at T_C = 272 K which is about 10 K higher than that of the $La_{0.67}Ca_{0.33}MnO_3$ manganite for which $La_{0.54}Ca_{0.32}MnO_{3-\delta}$ might be used as promising magnetic refrigerants in near room temperature magnetic refrigeration. Phan et al. [50, 51] also reported the magnetic and magnetocaloric properties of various $(La_{1-x})_{0.8}Ca_{0.2}MnO_3$ which was La-deficient. Very interesting result was found that with increase in La-deficiency the MCE increases and T_C was tuned toward higher temperature. This author also investigated dependence of the magnetocaloric properties on oxygen content in polycrystalline $La_{2/3}Ba_{1/3}MnO_{3-\delta}$ and found tunable MCE with change in oxygen deficiency.

To tune MCE in the room temperature range, many efforts have been done such as the MCE of $La_{1-x}Sr_xMnO_3$ perovskite [52-54]. Xu et al. [55] first investigated the MCE of $La_{0.845}Sr_{0.155}MnO_3$ perovskite, which underwent a magnetic phase transition from PM to FM phase at 234 K. The $(-\Delta S_M)_{max}$ and T_{ad} were found, 6.6 $JKg^{-1}K^{-1}$ and 3.3 K respectively for ΔH= 7 T.

Hanh et al. [56] synthesized $La_{0.7}Ca_{0.3-x}Pb_xMnO_3$ (x = 0.05, 0.10, 0.15, and 0.20) using solid-state reaction method and expected that these materials could exhibit large MCE at room temperature region. The prepared samples were in single phase and crystallized in orthorhombic structure. T_C increases from 270 to 338 K with increase in x content from 0.05 to 0.20. All the samples exhibited large value of MCE and $(-\Delta S_M)_{max}$ reached the maximum value of 3.72 $JKg^{-1}K^{-1}$ with magnetic field change ΔH = 1.35 T for the sample x = 0.05. The magnetoresistance of the samples also exhibited colossal value. At low temperature, the FC and ZFC magnetization curves deviate from each other for which the samples can be regarded as spin-glass like manganite.

Islam et al. [57] prepared $La_{0.7}(Ca_{1-x}Sr_x)_{0.3}MnO_3$ (x =0, 0.05, 0.10, 0.15, 0.20, 0.25) using solid state reaction method and expected that these materials would exhibit large value of MCE at room temperature region. The materials were in single phase crystallized in orthorhombic structure with space group pnma. The lattice parameters as well as the volume and Mn-O-Mn bond angles were continuously increased with the increase of x content resulting an increase in T_C from 258 to 293 K for x =0.0 to 0.25. A large value of MCE of 5 $JKg^{-1}K^{-1}$ has been observed around its phase transition temperature of 293 K at ΔH =1.35 T for the sample x =0.25. The FC and ZFC thermo-magnetic measurements at low field and low temperature also reveal spin-glass like state in the samples.

Raoufi et al. [58] studied magnetocaloric properties of $La_{0.6}Sr_{0.4}MnO_3$ prepared by solid state reaction technique. X-ray diffraction measurement confirmed rhombohedral structure with R-3c space group as shown in Fig. 2.1. The scanning electron microscopy image identified the perovskite structure of the sample. The M-H measurements at different constant temperatures around T_C revealed the second order phase transition from PM to FM state at around 361 K as shown in Fig. 2.2. The laegest entropy change was observed near the PM to FM transition of 361 K which is equal to 2.47 $JKg^{-1}K^{-1}$ (as

shown in Fig. 2.2) making this material a good candidate for above room temperature magnetic refrigeration.

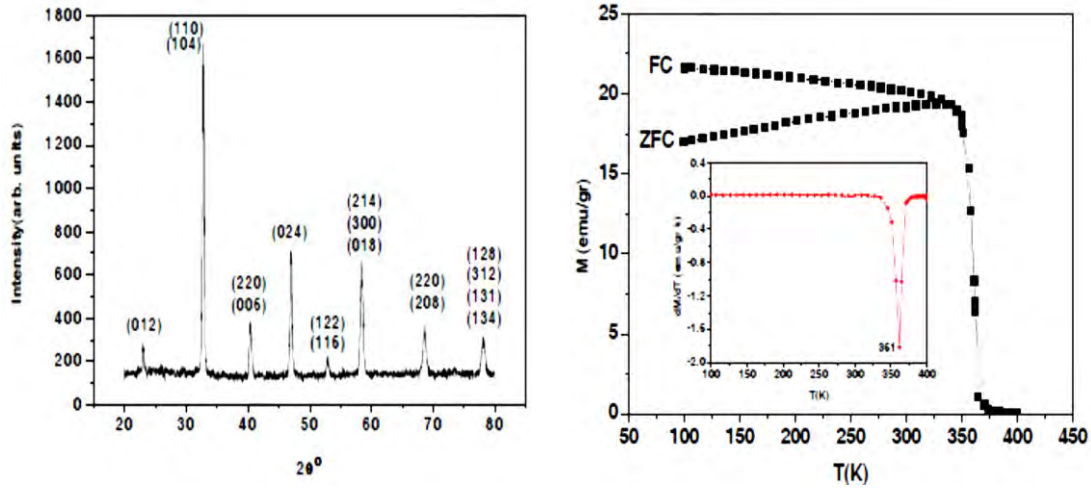

Fig. 2.1 XRD pattern and FC-ZFC magnetization of $La_{0.6}Sr_{0.4}MnO_3$ [58].

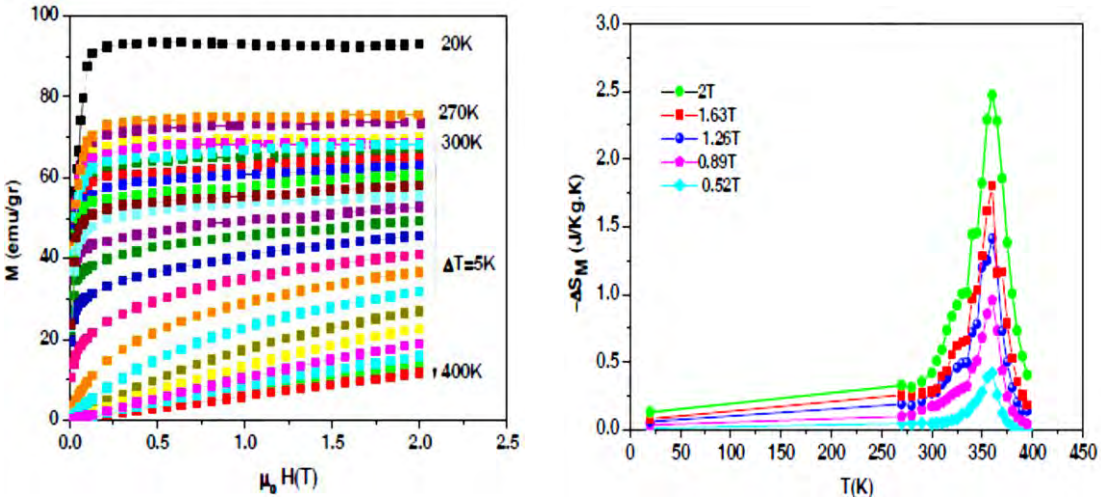

Fig. 2.2 Isothermal M-H curves and entropy change vs T of $La_{0.6}Sr_{0.4}MnO_3$ [58].

Nasri et al. [59] reported critical behavior of $La_{0.6}Ca_{0.4-x}Sr_xMnO_3$ (x=0.0, 0.2, 0.4) synthesized by solid state reaction method. The critical exponent of $La_{0.6}Ca_{0.4-x}Sr_xMnO_3$ has been studied based on the isothermal M-H measurements around its T_C using three different techniques. Those are modified Arrott plot, Kouvel–Fisher method and critical isotherm analysis. The calculated critical point exponents are found to be close to tri-critical mean field, mean field and 3D-Heisenberg model values, for x=0.0, 0.2 and 0.4,

respectively as shown in Fig. 2.3 and Fig. 2.4. The consistency of the calculated critical exponents was proved by Widom scaling relation and the universal scaling hypothesis which has been shown in Fig. 2.5. Besides these, the scaling exponent was also calculated in terms of the field dependence of the maximum magnetic entropy change.

A few research works have been published on magnetic and magnetocaloric properties of lanthanum manganite near half doping like $La_{0.55}Sr_{0.45}MnO_3$ and its co-related compounds. A-site disorder effect on colossal magnetoresistance was investigated on $La_{0.55}Sr_{0.45}MnO_3$ [60]. Effect of A-site cation disordering on the transport property of $La_{0.5}Ca_{0.5}MnO_3$ and particle size effect on magnetocaloric properties of $La_{0.5}Ca_{0.5}MnO_3$ have been reported [61].

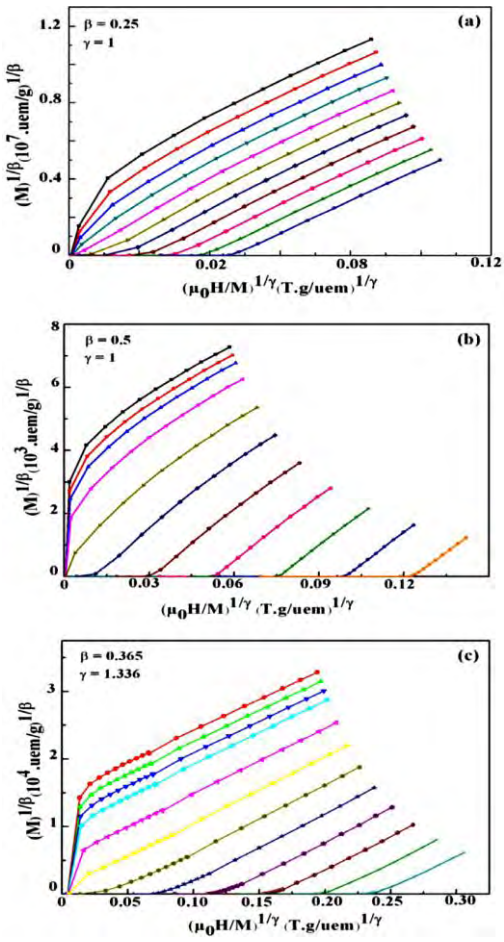

Fig. 2.3 MAP for (a) $La_{0.6}Ca_{0.4}MnO_3$, (b) $La_{0.6}Ca_{0.2}Sr_{0.2}MnO_3$ and (c) $La_{0.6}Sr_{0.4}MnO_3$ [59].

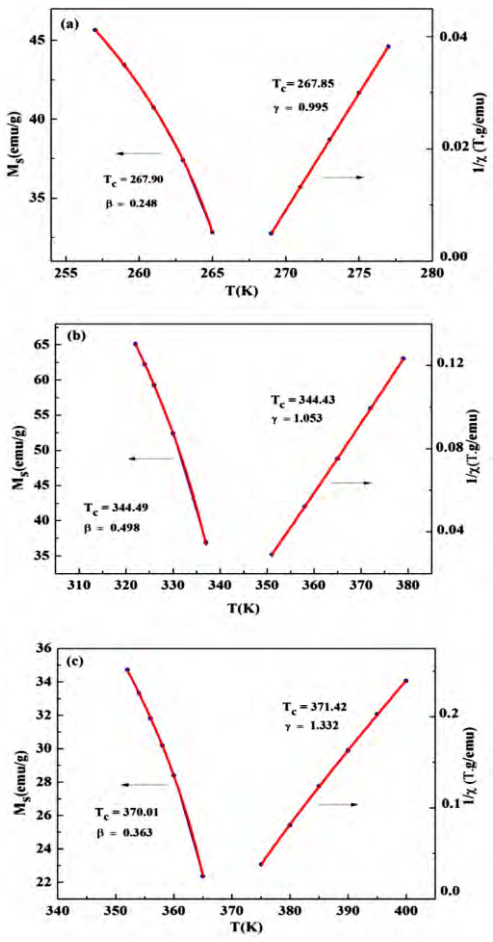

Fig. 2.4 M_S vs T and $1/\chi$ vs T for (a) $La_{0.6}Ca_{0.4}MnO_3$, (b) $La_{0.6}Ca_{0.2}Sr_{0.2}MnO_3$ and (c) $La_{0.6}Sr_{0.4}MnO_3$ [59].

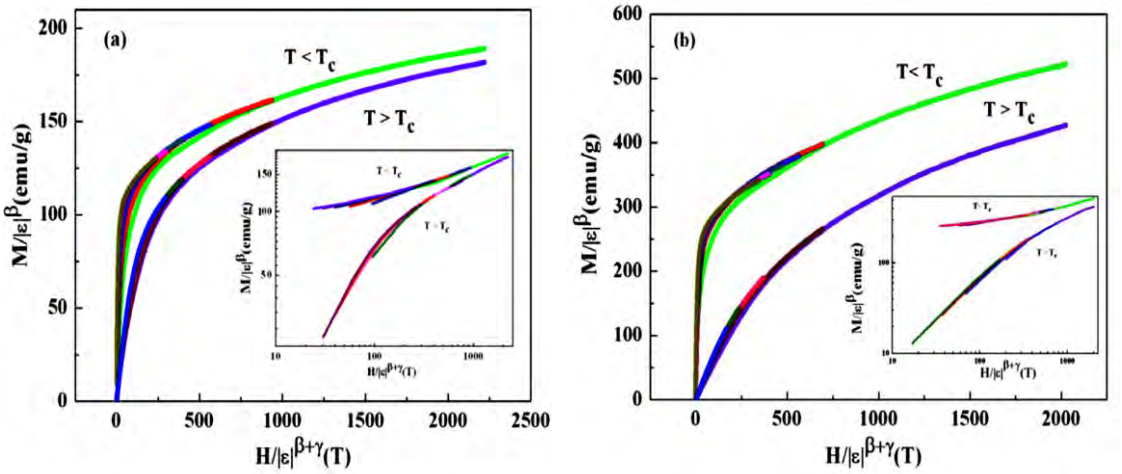

Fig. 2.5 Scaling plots for (a) $La_{0.6}Ca_{0.4}MnO_3$, (b) $La_{0.6}Ca_{0.2}Sr_{0.2}MnO_3$. Inset: corresponding plots on a log–log scale [59].

2.1.3 $Pr_{1-x}M_xMnO_3$ (M= divalent alkaline-earth metal ion like Ca, Sr) system

The perovskite $Pr_{1-x}Sr_xMnO_3$ having intermediate one electron band width [28] shows moderate value of ΔS_M and large value of colossal magneto-resistance which make this system suitable for magnetic cooling technology, spintronics, sensors etc. [5, 28].

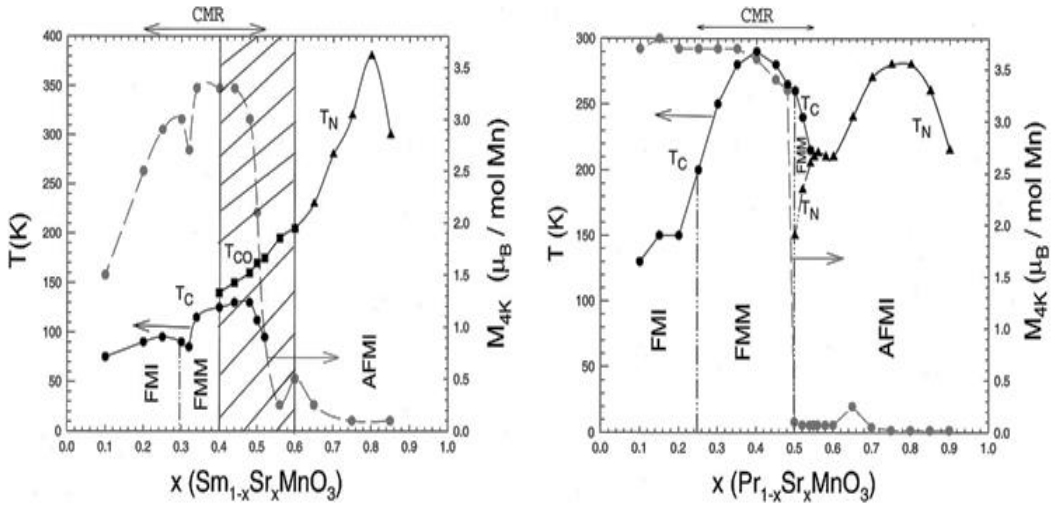

Fig. 2.6 Magnetic phase diagrams of $Pr_{1-x}Sr_xMnO_3$ and $Sm_{1-x}Sr_xMnO_3$ [62].

Martin et al. [62] studied the magnetic phase diagram of $Pr_{1-x}Sr_xMnO_3$ and observed that it possesses two FM region, one is FM insulator region belonging to $0.1<x<0.25$

and another is FM metallic region belonging to $0.25<x<0.5$, while for $x\geq0.5$, it exhibits a charged ordered AFM state as shown in Fig. 2.6. They also investigated magnetic phase diagrams of $Sm_{1-x}Sr_xMnO_3$ and found that it possesses FM metallic state for $0.3\leq x\leq0.55$ and AFM insulating state for $0.55\leq x\leq0.85$, as shown in Fig. 2.6.

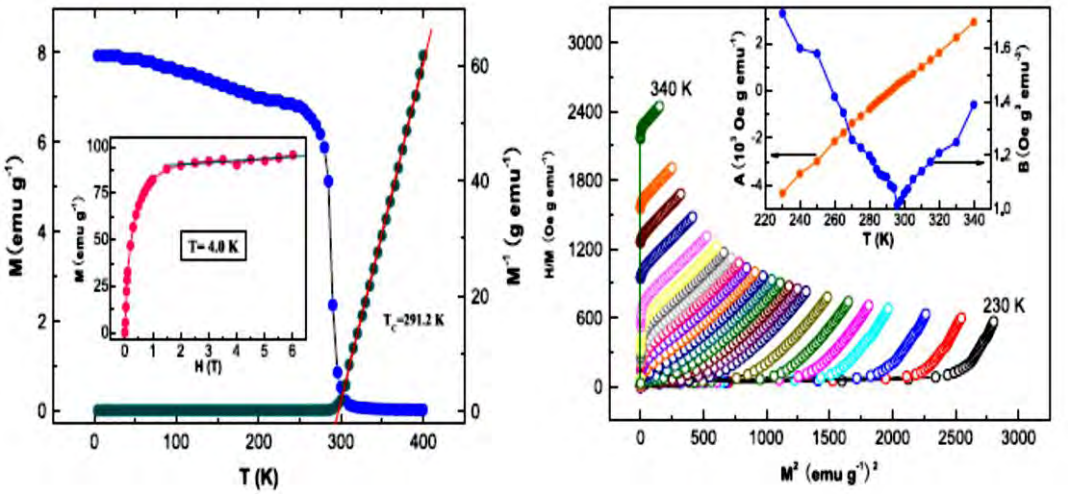

Fig. 2.7 M vs T and inverse susceptibility curve and Arrott plot of $Pr_{0.55}Sr_{0.45}MnO_3$ [63].

Fan et al. [63] investigated magnetic and magnetocaloric properties of $Pr_{0.55}Sr_{0.45}MnO_3$ prepared by solid state reaction technique and observed the PM to FM phase transition near T_C = 291 K as shown in Fig. 2.7. This PM to FM phase transition was confirmed as second order in nature by Arrott plot. The inverse susceptibility vs temperature curve obeys the Curie-Weiss law. The compound possesses moderate value of ΔS_M around T_C with large relative cooling power (RCP) of 143.64 J/Kg and a wide working temperature range (84 K). Comparing the theoretical and experimental results of entropy change as a function of temperature, they found the contribution of itinerant electrons for the large magnetic entropy change at PM region (Fig. 2.8).

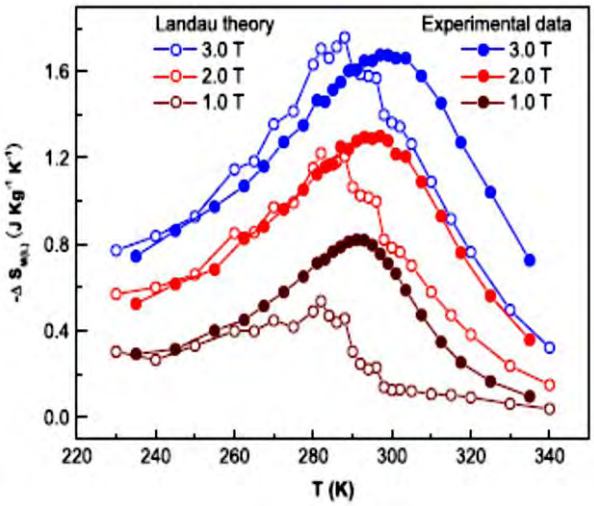

Fig. 2.8 Theoretical and experimental values of $-\Delta S_M$ vs T for the sample $Pr_{0.55}Sr_{0.45}MnO_3$ [63].

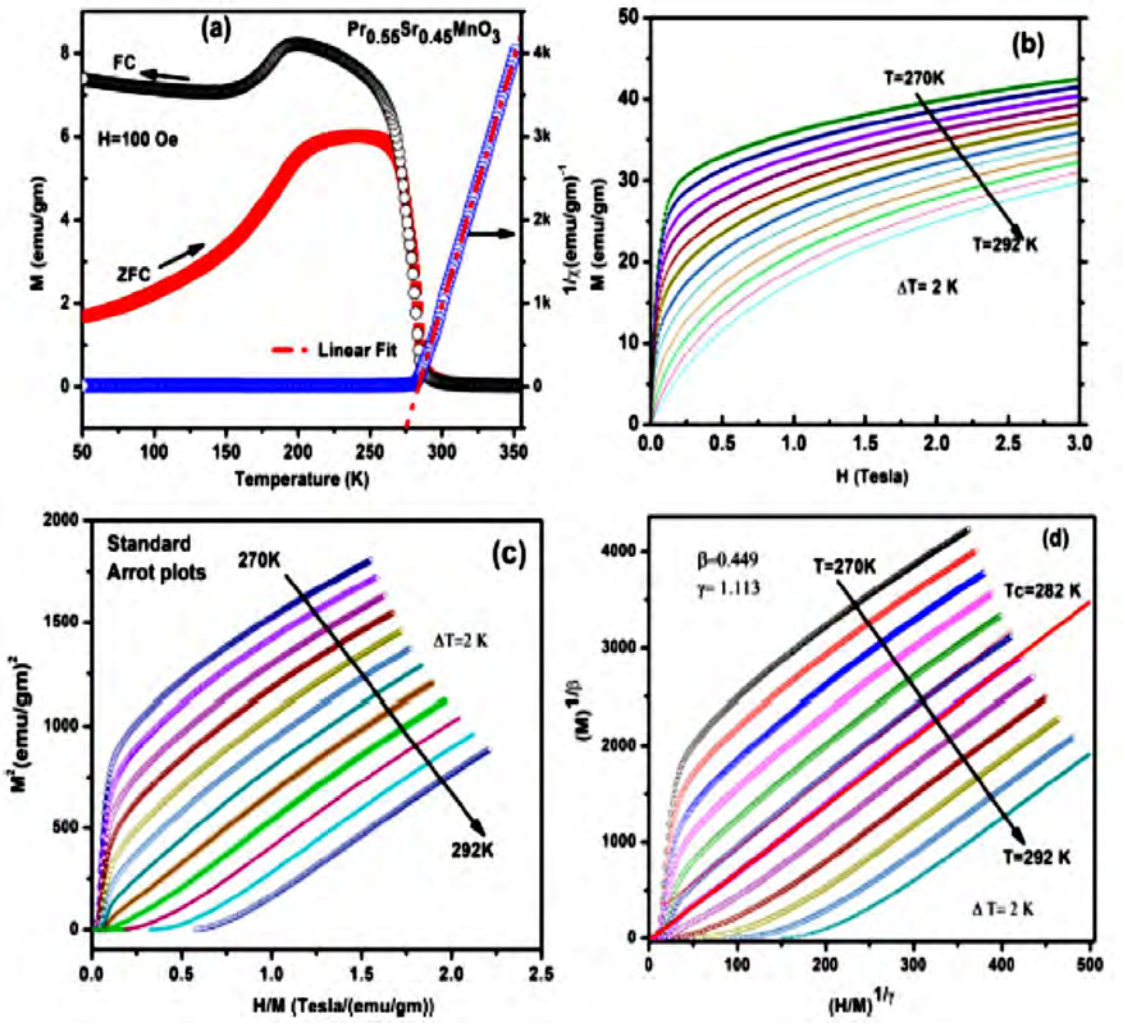

Fig. 2.9 (a) ZFC and FC curve and $1/\chi$ vs T at 0.01 T, (b) The M-H curve around T_C, (c) M^2 vs H/M around T_C and (d) modified Arrott plot of the isotherms [64].

Kumar et al. [64] studied magnetic, magnetocaloric and magneto transport properties of $Pr_{0.55}Sr_{0.45}MnO_3$ prepared by nitrate route method and found that the sample possesses FM to PM magnetic phase transition near T_C=281 K followed by another AFM transition at 182 K as shown in Fig. 2.9 (a). They have calculated the critical point exponents of the sample near phase transition temperature using the modified Arrott plot method that has been shown in Fig. 2.9 (b, c, d). The calculated critical exponents values and T_C satisfied the scaling theory. The ΔS_M was also evaluated from magnetic isotherms near T_C as shown in Fig. 2.10.

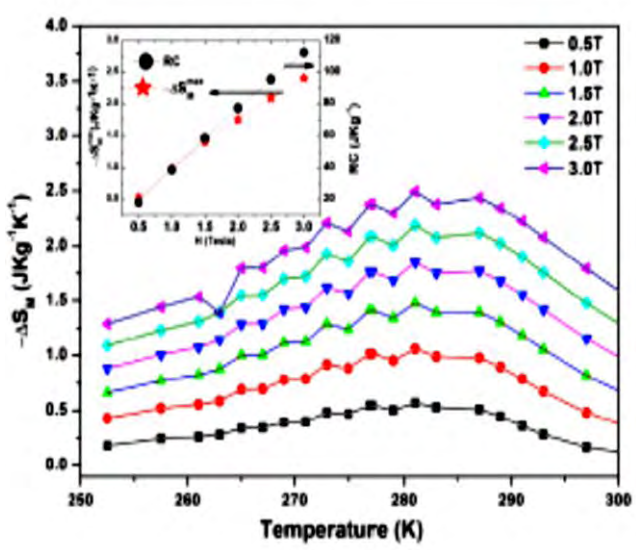

Fig. 2.10 $-\Delta S_M$ vs T for the sample $Pr_{0.55}Sr_{0.45}MnO_3$ [64].

2.1.4 $Sm_{1-x}M_xMnO_3$ (M= divalent alkaline-earth metal ion like Ca, Sr) system

Nagaraj et al. [65] studied systematically structural, electrical and magnetic properties of the family $Sm_{1-x}Sr_xMnO_3$. This system belongs to the group of low bandwidth compounds. The sample was prepared by conventional solid-state reaction method and crystalized orthorhombic crystal structure with Pbnm space group as shown in Fig. 2.11. The unit cell volume decreases with increasing Sr concentration suppressing electrical resistivity with application of magnetic field. Temperature dependent FC and ZFC magnetization measurements (as shown in Fig. 2.12) for the $Sm_{1-x}Sr_xMnO_3$ samples reveal two transitions, PM to FM state and FM to AFM state as the temperature is lowered from room temperature. However, the nature of magnetization curve depends

on doping level. Bifurcation in ZFC and FC curve was also observed at low temperature suggesting coexistence of FM and PM state.

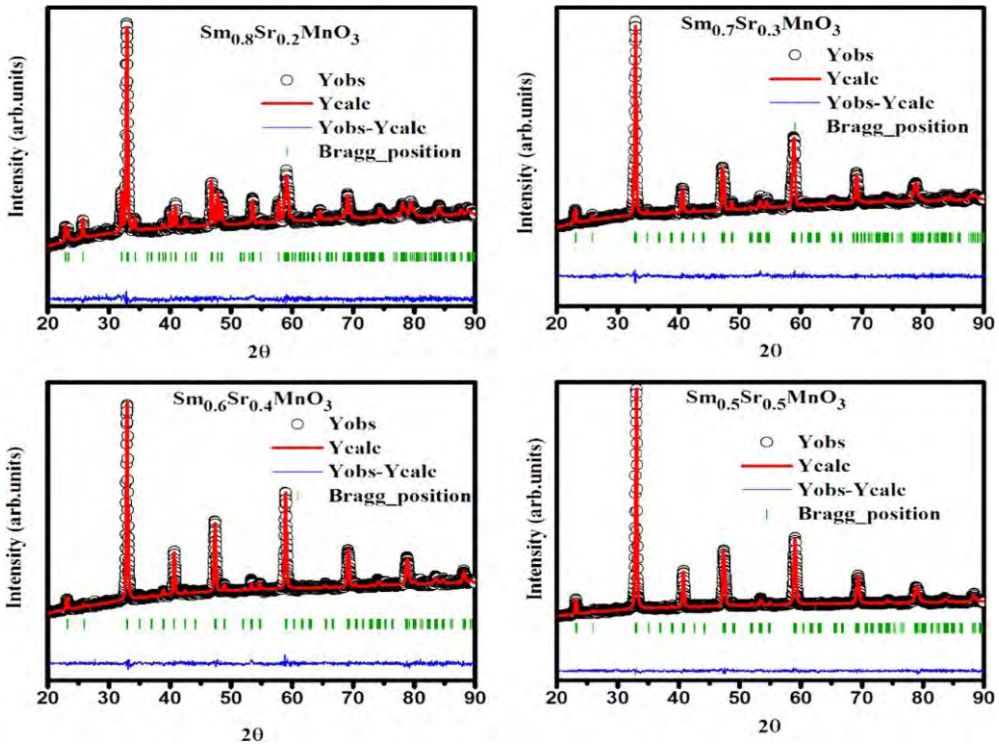

Fig. 2.11 XRD pattern of $Sm_{1-x}Sr_xMnO_3$ samples [65].

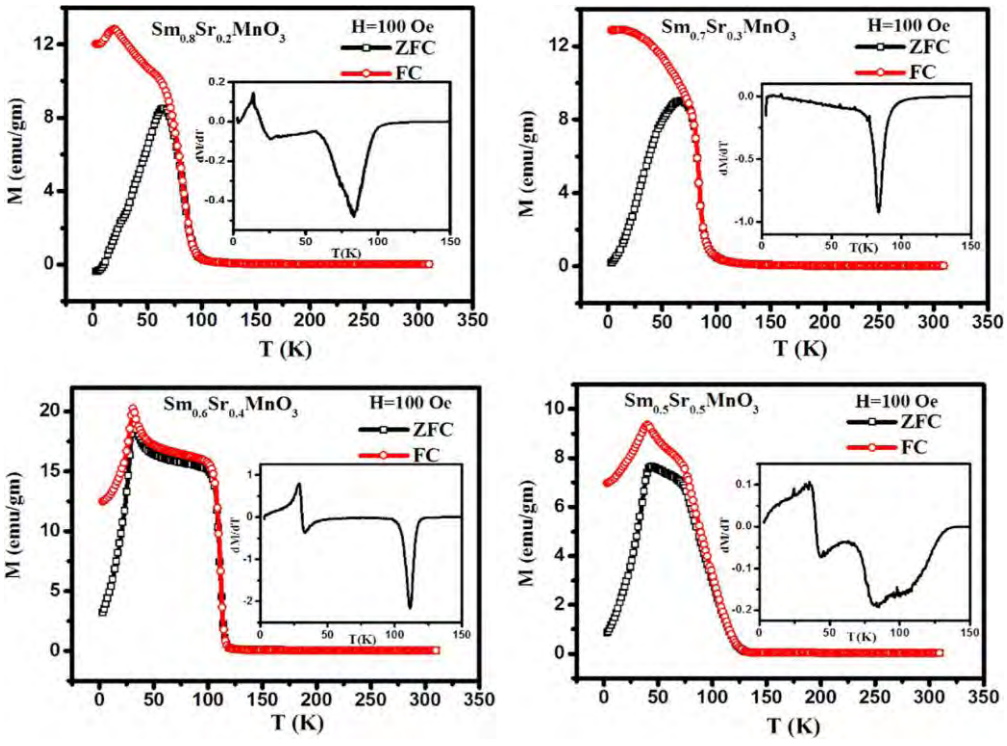

Fig. 2.12 FC-ZFC magnetization curves of $Sm_{1-x}Sr_xMnO_3$ samples [65].

Tomioka et al. [18] investigated magnetic phase diagram of perovskite manganites $RE_{0.55}(Ca_{0.45-y}\ Sr_y)_{0.45}MnO_3$ and reported that $Sm_{0.55}(Ca_{0.45-y}\ Sr_y)_{0.45}MnO_3$ possesses FM metallic state for $0.4 \leq y \leq 1$ with T_C value from 50 to 135 K as shown in Fig. 2.13.

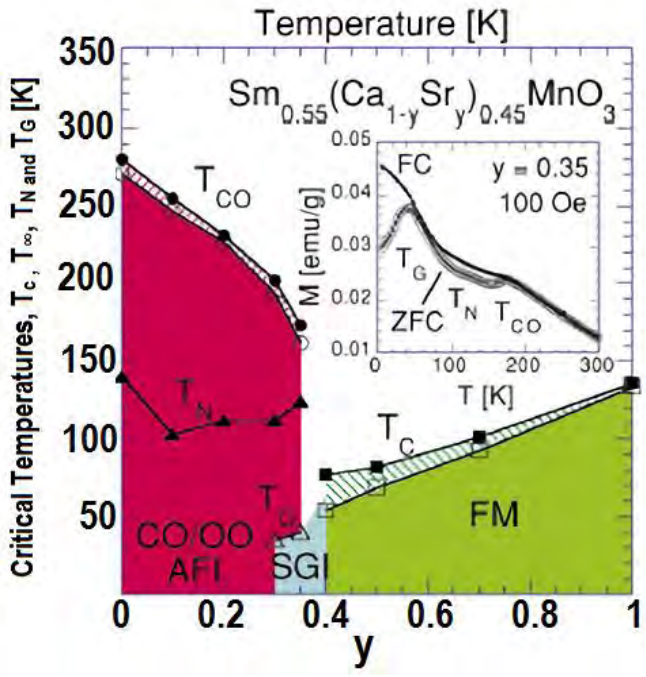

Fig. 2.13 Global phase diagram of $RE_{0.55}(Ca_{0.45-y}\ Sr_y)_{0.45}MnO_3$ [18].

Giri et al. [66] studied magnetic and magnetocaloric properties of $Sm_{0.55}Sr_{0.45}MnO_3$ applicable for magnetic refrigeration. They reported about the MCE and RCP occurred due to the first order magnetic phase transition in $Sm_{0.55}Sr_{0.45}MnO_3$ perovskite. Fig. 2.14 shows inverse susceptibility versus temperature that reveals first order FM transition for bulk (S1250) sample and second order FM transition for nano-metric manganites (S750) sample. For 6 T magnetic field change, the $-\Delta S_M$ of S1250 was found 8.48 $JKg^{-1}K^{-1}$ with a large RCP value of 574 J/Kg around its T_C = 172 K. Corresponding adiabatic temperature change is found 2.38 K for H=1 T. They also reported the magnetic field dependence of the order of FM to PM phase transition in bulk and nano-metric manganites. First order PM to FM transition is confirmed from Arrott plots using a criterion given by Banerjee. The calculated value of magnetic entropy change in bulk sample (as shown in Fig. 2.15) is greater than that of other perovskite manganites of comparable T_C. This large change has originated from the sharp change in

magnetization due to first-order meta-magnetic transition and presence of FM clusters in the PM state.

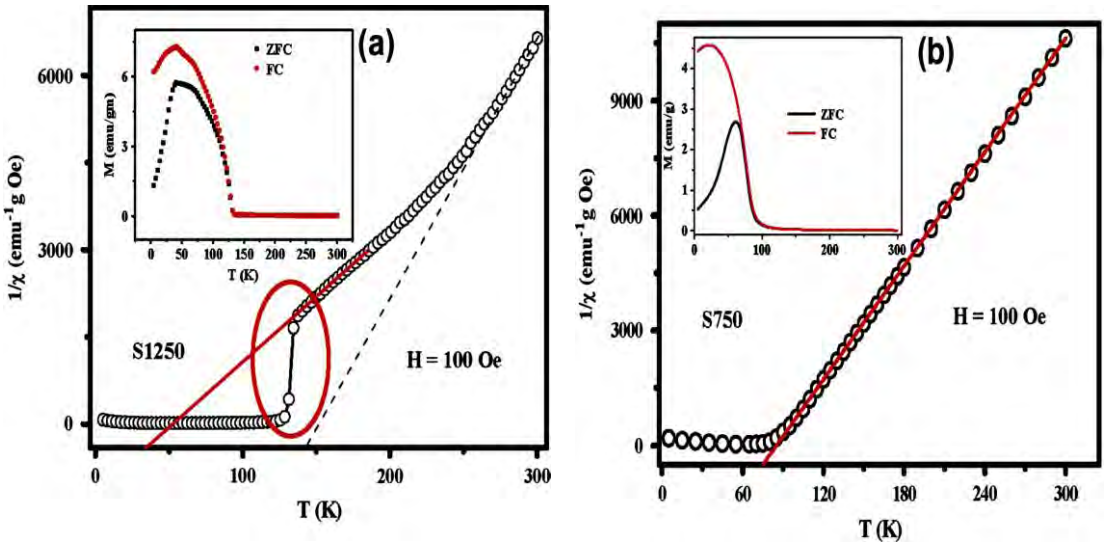

Fig. 2.14 1/χ vs T plot at H = 0.01 T. Inset: ZFC and FC magnetization vs temperature plot of the same sample (a) for S1250, (b) for S750 [66].

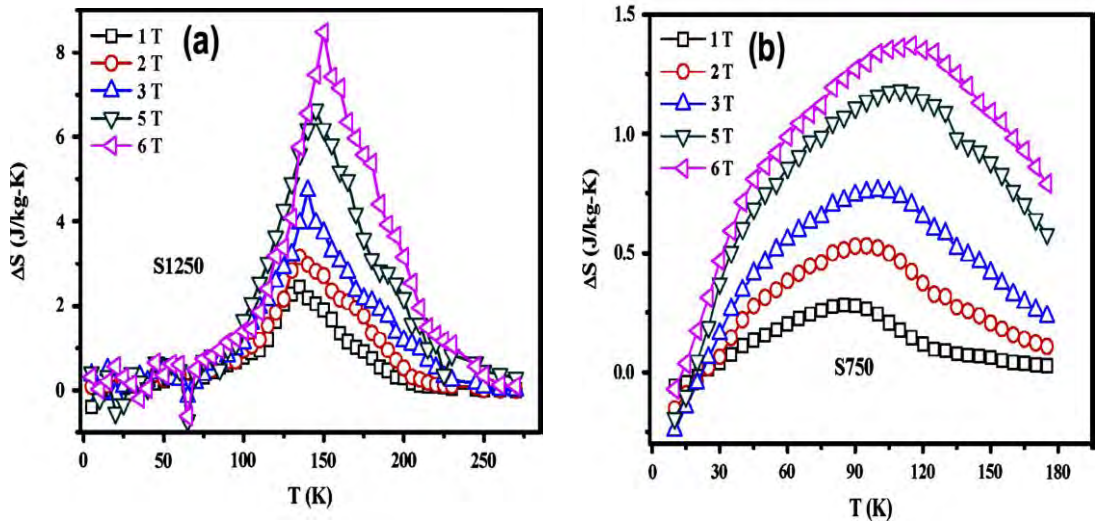

Fig. 2.15 -ΔS_M vs T at different magnetic field (a) for S1250, (b) for S750 [66].

Andrade et al. [67] synthesized $Sm_{0.6}Sr_{0.4}MnO_3$ nanoparticle by using sole gel modified method to overcome the lack of the information about nanoparticles and nanotubes of the studied manganite. The magnetic entropy change as a function of temperature of the nanoparticle was broader than that of the bulk sample. As a results temperature range of

magnetic refrigeration increases though an undesired super-paramagnetic behavior arises.

Banik et al. [68] studied polycrystalline $Sm_{0.5}(Ca_{0.5}Sr_{0.5})_{0.5}MnO_3$ to find magneto resistive properties in the studied materials. They found metamagnetic transition and extremely large value of negative magnetoresistance in $Sm_{0.5}(Ca_{0.5}Sr_{0.5})_{0.5}MnO_3$ perovskite. Mleiki et al. [27] studied the microstructure, magnetic and magnetocaloric properties in $Sm_{0.55-x}Pr_xSr_{0.45}MnO_3$ manganite synthesized by solid-state reaction technique. They also investigated the effect of praseodymium doping on those properties. XRD analysis confirms that all the samples were crystallized in orthorhombic system. With increasing Pr-content, lattice parameters and unit cell volume increases which influence magnetic properties. The T_C increases with Pr-content from 132 to 261 K for x =0.1 to 0.4. The $(-\Delta S_M)_{max}$ was calculated for magnetic field change of 5 T and is found to be 7.14, 5.23, 4.92 and 3.98 $JKg^{-1}K^{-1}$ for x = 0.1, 0.2, 0.3 and 0.4 respectively. The RCP was found 240 J/Kg for x = 0.4 with very small amount of hysteresis losses.

Anwar et al. [69] investigated $La_{0.7-x}Sm_xCa_{0.3}MnO_3$ ($0<x<0.3$) synthesized by conventional solid-state reaction technique. Crystal structure was determined by X-ray diffraction analysis. First order FM transition in un-doped sample and second order FM transition in doped sample were confirmed by temperature dependent magnetization measurements and Arrott plots. T_C was decreased with increasing Sm concentration from 182 to 109 K for x = 0.05 to x =0.30. $(-\Delta S_M)_{max}$ of 1.75 $JKg^{-1}K^{-1}$ at 0.5 T was found in $La_{0.7}Ca_{0.3}MnO_3$ sample, and the value greatly depends on disorder caused by Sm doping.

2.2 Theory of Magnetocaloric Effect

2.2.1 Base theory of MCE

The MCE is characterized in terms of ΔS_M and ΔT_{ad}. For the first case the result of ΔS_M occur due to the coupling of magnetic spins with the applied magnetic field. It has similarity with thermodynamics of a gas where isothermal compression of a gas is analogous to the isothermal magnetization of magnetic materials.

The total entropy of a magnetic material is given by the following equation:

$$S_M(T,H) = S_1(M) + S_2(E) + S_3(C) \quad (2.1)$$

Therefore entropy change is calculated using the relation [70] given in equation (2.2):

$$\Delta S_M(T,H) = \Delta S_1(M) + \Delta S_2(E) + \Delta S_3(C) \quad (2.2)$$

Here, $\Delta S_1(M)$ is associated with the net magnetic entropy change, $\Delta S_2(E)$ is the entropy change due to electron and $\Delta S_3(C)$ occurs due to the entropy change of crystal lattice. $\Delta S_3(C)$ remains constant for isothermal process. The magnetic materials which exhibit MCE, the value of ΔS_M becomes larger.

2.2.2 Principles of magnetic cooling and heating

When magnetic material is exposed to a magnetic field ranging from a initial magnetic field (H_I) to a final magnetic field (H_F) i.e. $\Delta H = (H_F - H_I)$ at constant pressure, two different type of results may occur in that material. Those are given bellow:

(a) One is the isothermal process in which the magnetic field is varied but the material remains at constant temperature. The entropy of a magnetic material is then changed by

$$\Delta S_M = S(T)_{H_F} - S(T)_{H_I} \quad (2.3)$$

Here, ΔS_M is magnetic entropy change. Then the cooling capacity (q) of the magnetic material is found from the magnetic entropy change [36] and can be expressed as

$$q = -\int_{T_1}^{T_2} \Delta S_M(T)dT \quad (2.4)$$

where 'q' indicates the amount of heat transferred from the cold end with temperature T_1 to the hot end with temperature T_2 of the refrigeration cycle.

(b) The second one named adiabatic process where the applied field is varied but the material is isolated from the surroundings so that no heat energy can enter or leave the system. Thus, the total entropy of the material remains unchanged. Then the temperature of that material is changed by

$$(\Delta T_{ad}(T))_{\Delta H} = T(S)_{H_F} - T(S)_{H_I} \quad (2.5)$$

Here, ΔT_{ad} is called adiabatic temperature change. This ΔT_{ad} represents both the cooling capacity and the temperature difference between the cold and the hot sink of the refrigeration cycle.

According to Maxwell's relation, the infinitesimal isobaric-isothermal magnetic entropy change can be related to the magnetization and the applied magnetic field [70] as given below:

$$(\frac{\partial \mathrm{S_M}}{\partial \mathrm{H}})_\mathrm{T} = (\frac{\partial \mathrm{M}}{\partial \mathrm{T}})_\mathrm{H} \tag{2.6}$$

After integrating equation (2.6), entropy change is found as

$$(\Delta S_M(T))_{\Delta H} = \int_{H_I}^{H_F} dS_M = \int_{H_I}^{H_F} (\frac{\partial M}{\partial T})_H \, dH \tag{2.7}$$

By combining equation (2.6) with equation (2.8) and (2.9) given below:

$$(\frac{\partial \mathrm{S(T,H)}}{\partial \mathrm{T}})_\mathrm{H} = (\frac{\mathrm{C(T,H)}}{\mathrm{T}})_\mathrm{H} \tag{2.8}$$

$$\mathrm{TdS} = \mathrm{T}(\frac{\partial \mathrm{S(T,H)}}{\partial \mathrm{T}})_\mathrm{H}\mathrm{dT} + \mathrm{T}(\frac{\partial \mathrm{S(T,H)}}{\partial \mathrm{H}})_\mathrm{T}\,\mathrm{dH} \tag{2.9}$$

Thus, the infinitesimal adiabatic temperature increase for the reversible adiabatic-isobaric process is expressed as

$$\mathrm{dT(T,H)} = -\left(\frac{\mathrm{T}}{\mathrm{C(T,H)}}\right)_\mathrm{H}\left(\frac{\partial \mathrm{M(T,H)}}{\partial \mathrm{T}}\right)_\mathrm{H}\mathrm{dH} \tag{2.10}$$

Here, C(T, H) is the temperature and magnetic field-dependent heat capacity at constant pressure. $\Delta T_{ad}\,(T\,)_{\Delta H}$ can be obtained by integrating equation (2.10) as give bellow:

$$(\Delta \mathrm{T_{ad}(T)})_{\Delta \mathrm{H}} = \int_{\mathrm{H_I}}^{\mathrm{H_F}} \mathrm{dT(T,H)} = -\int_{\mathrm{H_I}}^{\mathrm{H_F}} \left(\frac{\mathrm{T}}{\mathrm{C(T,H)}}\right)_\mathrm{H}\left(\frac{\partial \mathrm{M(T,H)}}{\partial \mathrm{T}}\right)_\mathrm{H}\mathrm{dH} \tag{2.11}$$

Equation (2.7) and (2.11) shows that both $(\Delta \mathrm{S_M(T)})_{\Delta \mathrm{H}}$ and $(\Delta \mathrm{T_{ad}(T)})_{\Delta \mathrm{H}}$ depend on temperature and field change. Those are usually expressed as functions of temperature for a given ΔH, or as functions of ΔH for a given temperature. Besides the characteristics of both $(\Delta \mathrm{S_M(T)})_{\Delta \mathrm{H}}$ and $(\Delta \mathrm{T_{ad}(T)})_{\Delta \mathrm{H}}$ is material dependent, cannot be easily estimated from the first principles, and hence, must be measured by experiment.

2.2.3 Perovskite structure

The general formula of perovskite compound is ABO_3, where A and B are cations and O is anions. The structure of an ideal cubic perovskite unit cell is shown in Fig. 2.16 where the A-cations are represented blue spheres occupying the corner position, yellow

spheres corresponds to the B-cation occupying the center of unit cell, and red spheres indicate oxygen anions which form an octahedra. In a perovskite structure, the tiny B-cation is placed within oxygen octahedra and larger cations forms eleven fold coordinates of oxygen. Perovskite structure was first discovered by Gustav Rose in 1839 and named after Russian mineralogist L. A. Perivski. At first the compound $CaTiO_3$ with orthorhombic structure was named as perovskite. A perovskite structure of type $A^{3+}B^{3+}O_3$ may possess rhombohedral structure, and then orthorhombic structure when a rotation of the BO_6 octahedra with respect to the cubic structure is occurred. Substitution of transition metal ion in A-site of perovskite structure introduces different type of electronics and magnetic properties. As a result, both chemical flexibility and complex character arises since transition metal ions possess certain coordination with oxygen or halides. On the other side, magnetism and electronic correlations are generally related to unfilled 3d electron shells of the transition metal ion. Where, dielectric properties are strongly related with filled 3d electron shells. Multi-ferocity is the coexistence of spontaneous ferroelectric and ferromagnetic moments, which allow a spontaneous polarization. These materials also possess the presence of competing interaction and high magneto-capacitive coupling. These properties make the materials suitable for many commercial applications such as capacitor, transducer, actuator, sensor and electro optical and switching [1, 3].

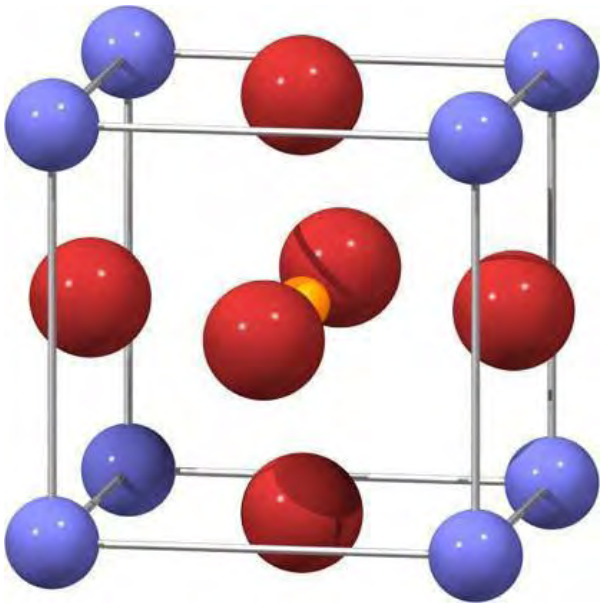

Fig. 2.16 A unit cell of cubic perovskite.

2.2.4 Double exchange and super exchange interactions

Zener [71] proposed an explanation of FM behavior in 1951 in terms of indirect magnetic exchange between 3d atoms. He proposes that the inter-atomic Hund rule exchange is strong and the carriers do not change their spin orientation when hopping from one ion to the next one. So the carrier can only hop if the spins of the two ions remain parallel. From the view point of minimum total free energy of the system, Zener found that FM interaction is favored when the magnetic atoms are well separated and conduction electrons are present. The theory is applicable for the manganite compounds [71] to explain the strong relationship between conductivity and ferromagnetism. It is also applicable for describing the value of the saturation magnetization at zero temperature, which is attributed to the sum of all the unpaired electron spins. Zener found that in insulating AFM $LaMnO_3$, electrons are localized on the atomic orbitals. Then he observed that the system should gradually become more ferromagnetic with introduction of hole doping i.e. creation of Mn^{4+} ions. He explained transfer of an electron from the Mn^{3+} to the oxygen and then from the oxygen to the next neighboring Mn^{4+}as shown in Fig. 2.17 (b). This type of transfer is called as double exchange and the interaction is known as double exchange interaction and can be given as follows:

$$Mn^{3+} - O - Mn^{4+} \leftrightarrow Mn^{4+} - O - Mn^{3+}$$

As a result, creation of sufficient proportion of Mn^{4+} in the perovskite oxides make the oxide materials ferromagnetic that exhibits metal like conductivity. The insulator metallic transition occurs around the T_C.

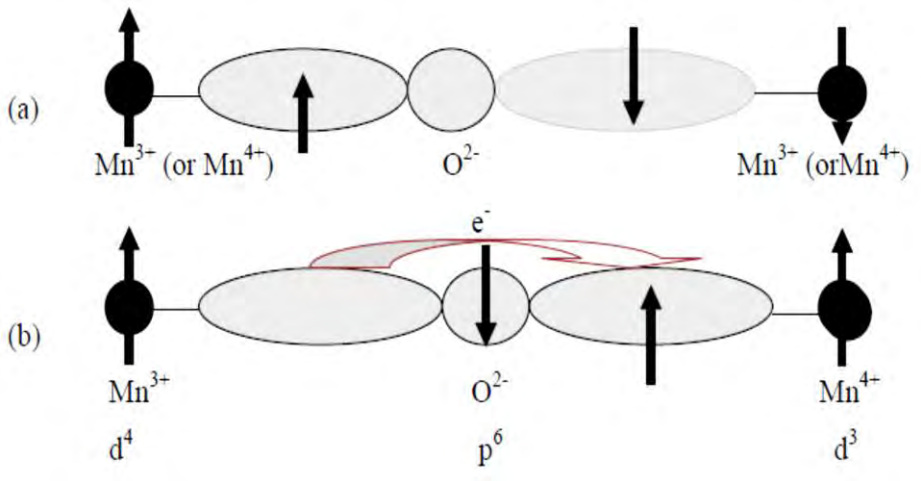

Fig. 2.17 Schematic diagram of the (a) SE and (b) DE interaction [71].

The double exchange mechanism involves with the coupling between the mobile holes and localized t_{2g}^3 electrons [14, 15], which is controlled by the transfer integral t_{ij} between Mn^{3+} and Mn^{4+} cations. It also depends on the Mn-O bond lengths and Mn-O-Mn bond angles. The Mn-O bond lengths and Mn-O-Mn bond angles (Fig. 2.18) correspond to amount of distortion in MnO_6 octahedra, and indirectly influence the magnetic and magnetocaloric properties of manganite perovskite.

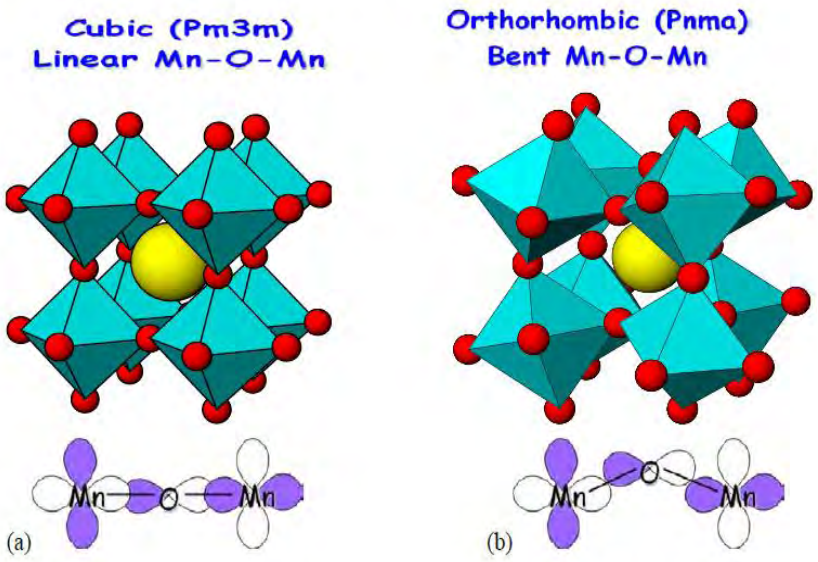

Fig. 2.18 Schematic diagrams of (a) a non-distorted perovskite and (b) a distorted perovskite structure [14].

In non-metallic compounds, an additional indirect exchange interaction may also appear between magnetic ions which is known as super-exchange interaction (shown in Fig. 2.17 (a)) and results in the AFM state. Double exchange is always ferromagnetic, while super exchange interaction which corresponds to virtual electron transfer between $Mn^{3+} - O - Mn^{3+}$ or $Mn^{4+} - O - Mn^{4+}$ and is often anti-ferromagnetic.

CHAPTER 3
SAMPLE PREPARATION AND CHARACTERIZATION TECHNIQUES

3.1 Sample Preparation Technique

3.1.1 Standard solid state reaction technique

Conventionally solid state reaction technique is used for preparing ceramic materials. It is very well-known and old technique for the preparation of the sample. This process starts with various solid compounds as raw materials. After stoichiometric calculation the raw materials are mixed properly and grinded by hand using motor and vessel. The grinding times remain around 5-6 hours. The sample wastage and contamination with organic and inorganic particles present in the atmosphere may occur during the grinding process and cautions should be taken to prevent it. After proper grinding, the sample is fired in a high temperature furnace between 1000-1500°C for initial phase formation. Then several intermediate steps are needed to get the product sample. These steps are calcination, pelletization and sintering. The performance of this technique is dependent on the kinetic and thermodynamic factor. The reaction takes place by changing the free energy according to thermodynamic factors while the rate of the reaction is determined by the kinetic factors. This technique requires more physical work and long processing time [72, 73].

3.1.1.1 Calcination

In this step initial heat treatment is carried out for the initial phase formation. The mixed and grained raw materials are heated at a temperature below its melting temperature. The heat treatment process is performed with help of a high temperature furnace. During this process, oxidation takes place removing the impurities and ingredients from the compound. At the first step of this process, the grinded powder is placed inside a high temperature furnace, and then heated it in a controlled manner for several hours. The temperature is increased in a controlled manner so that no splitting of sample is occurred inside the furnace due to direct contact with high temperature. At this stage the particles of the sample arrange themselves to give the compound homogeneity. Then the sample can be easily shaped into different form such as pellet, toroid etc. for

sintering of sample preparation [73]. In the present work, the ball-milled powders were calcined in a 'WiseTherm' furnace shown in Fig. 3.1.

Fig. 3.1 'WiseTherm' furnace.

Fig. 3.2 Hydraulic press and die set.

3.1.1.2 Pelletization

Pelletization means shaping the powder sample into the pellets or/and toroid using die set and pelletizer. The calcinated sample is put into a die set and pressure is applied to the head of the die set using a hydraulic press. The powder samples are closely packed to each other and compact strongly due to application of high pressure. Generally, the superconducting materials need high pressure for the pellet formation while some perovskite and double perovskite compound require low pressure for the shape

formation. Due to application of high or low pressure the particles are packed together with increasing the densification. Sometimes for increasing the strength of the pellet or/and toroid, binder is used [74]. Hydraulic press and die set have been shown in Fig. 3.2.

3.1.1.3 Sintering

It is final heat treatment process for final phase formation of the compound. After formation of pellet or/and toroid, those are again heated in a controlled manner keeping temperature below melting point. Then the bonding between the particles leads to coherent and predominate solid structure of the sample. Thus the strength of the pellet increases significantly due to increase in bond strength. The temperature and time ratio influences the sintering process. The temperature should be applied in controlled process with time and the temperature must remain below the melting point. If the temperature reaches above the melting point then there is a chance of phase lost and may cause destruction of the sample [74]. In the present work, the pellet/disc and toroid shaped samples were sintered in the WiseTherm furnace as shown in Fig. 3.1. In its operation, when thermal energy is applied to the sample, the compound is densified and the average grain size increases. Sintering is a heat treatment process used to produce compounds from metal or/and ceramic powders by applying thermal energy.

3.2 Short Description on Planetary Ball Milling Technique

The planetary ball milling technique is one of the versatile cost effective techniques where samples can be produced in air environment using oxides of constituent elements. It is used to produce the highest order of fineness. The ball milling process must provide the classical mixing and size reduction. Besides, it also provide all the technical requirements for colloidal grinding and energy required for mechanical alloying processes. High pulverization energy is produced due to high centrifugal forces of planetary ball mills resulting short grinding times [74]. A ball mill consists of hollow cylindrical shells which rotate about its axis. The shells are partially filled with the mixture of raw materials to be ground and the ceramic balls as grinding medium. Solid-state reactions are started due to repeated deformation, cold-welding and fracture of the raw materials during the ball milling process.

3.2.1 Working principle

The main parts of a planetary ball mill are grinding jars and the sun wheel. The grinding jars are placed on the sun wheel. When the ball mills starts working, the direction of movement of the sun wheel remains in opposite direction to that of the grinding jars by a ratio 1:-2 or 1:-2.5 or 1:-3. As a result, the grinding balls in the grinding jars possess superimposed rotational movement, which is named as Cariole's forces. Interaction between frictional and impact forces occurs from the difference in speeds between the balls and grinding jars, releasing high dynamic energies. The interaction between these forces causes very effective amount of size reduction of the sample.

Fig. 3.4 Ball mill and its cross-section picture of MSK-SFM-1benchtop planetary ball mill.

A planetary ball mill of the model MSK-SFM-1benchtopas shown in Fig. 3.4 has been used in the preparation of the investigated sample for present research work. 8 grinding balls and an amount of 10 g starting materials which were previously hand-mixed were used in ball milling for synthesizing of the investigated samples.

3.3 Sample Preparation for Present Research

All three series of samples under investigation with composition $Pr_{0.55}Ca_xSr_{0.45-x}MnO_3$, $La_{0.55}Ca_xSr_{0.45-x}MnO_3$ and $Sm_{0.55}Ca_xSr_{0.45-x}MnO_3$ (x= 0.00, 0.05, 0.1, 0.2, and 0.25)

have been prepared by the conventional solid-state reaction technique. Sample preparation process includes the following steps.

Step-1:

The raw materials with high purity $MnCO_3$ (99.9%), Pr_6O_{11} (99.9%), $SrCO_3$ (99.9%), and $CaCO_3$ (99.9%) powder were used to synthesis $Pr_{0.55}Ca_xSr_{0.45-x}MnO_3$. The raw materials of La_2O_3 (99.9%), $SrCO_3$ (99.9%), $CaCO_3$ (99.9%) and MnO_2 (99.9%) powder were used to synthesis $La_{0.55}Ca_xSr_{0.45-x}MnO_3$. Then the raw materials with high purity of $MnCO_3$ (99.9%), Sm_2O_3 (99.9%), $SrCO_3$ (99.9%), and $CaCO_3$ (99.9%) powder were used to synthesis $Sm_{0.55}Ca_xSr_{0.45-x}MnO_3$. The raw materials were stoichiometrically calculated and weighted and then thoroughly mixed by hand with help of an agate mortar and pestle in an acetone medium. The compounds were grounded in a 'Planetary Ball Mill' for 8 hours. In this step, material becomes more homogeneous, initiate solid-state reaction by diffusion of particles.

Step-2:

After ball milling, the grinded compounds were dried and again mixed by hand for 2 hours and then pre-sintered at 900 $^{\circ}$C for 12 hours to introduce the solid-state reaction. After that all the samples were grounded and heated repeatedly at 950 and 1000 $^{\circ}$C for 12 h each. In this step, both contraction of compounds and growth of particles are initiated.

Step-3:

In this step the compounds were pressed in a "Hydraulic Press" to form pellets using different size die and the polyvinyl alcohol was mixed in the powder as a binder. Then the pellets were sintered at temperatures 1050, 1100 and 1250 $^{\circ}$C for 12 hrs each with intermediate grinding and pelletizing. The samples were cooled in air and then processed for the measurements.

Step-4:

During sintering process of the samples, their density was calculated by measuring the mass and dimensions of the pellet or toroid. It was observed that the bulk density of the sample increases with increase of sintering temperatures. Thus after sintering, the sample with highest density has been selected for measurements. The final sintering

temperature were found as 1250, 1100 and 1250 °C for $Pr_{0.55}Ca_xSr_{0.45-x}MnO_3$, $La_{0.55}Ca_xSr_{0.45-x}MnO_3$ and $Sm_{0.55}Ca_xSr_{0.45-x}MnO_3$ series of samples, respectively.

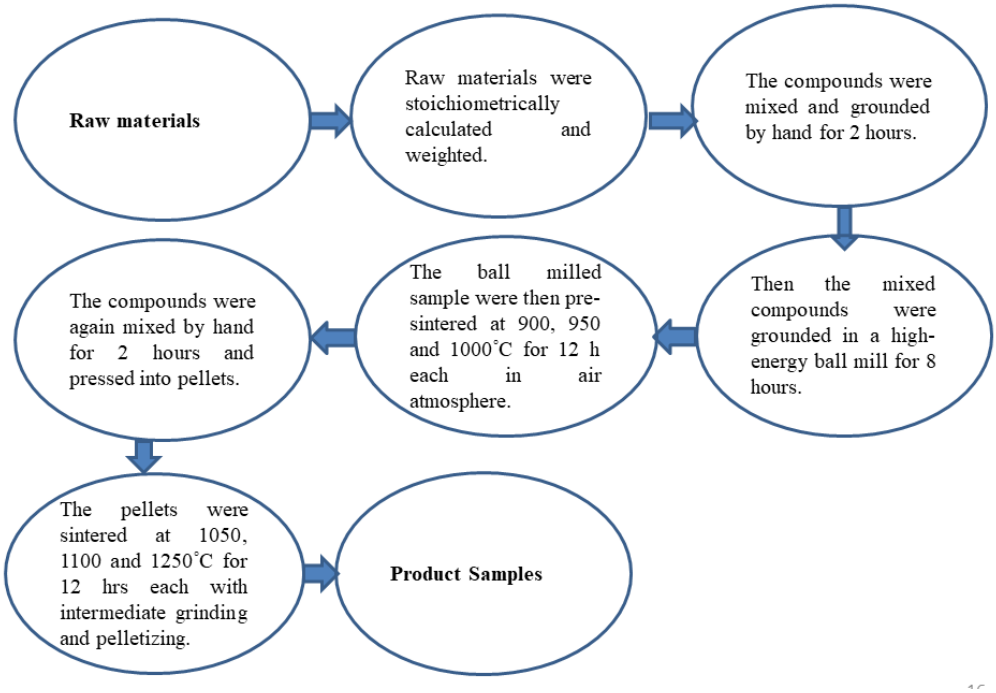

Fig. 3.3 Schematic diagram of solid state reaction technique.

3.4 Sample Characterization Techniques

3.4.1 Sample characterization

The samples were investigated in respect of structural, magnetic and magnetocaloric properties as described below:

Structural properties measurements:

i Crystal structure was analyzed using an X-ray diffractometer in the department of Glass and Ceramic Engineering, BUET, Dhaka. The intensities were measured from 2θ = 20 to 80° with a step of 0.02 degree and an acquisition time of 10 seconds in order to ensure measurements accuracy. The lattice parameters, crystallite size, and phase identification with the varying concentration of Ca content in the samples were extracted using a 'X'Pert HighSore Plus' software.

ii. Morphological and microstructural analysis was carried out in a Field Emission Scanning Electron Microscope (FESEM) in the department of Glass and Ceramics

Engineering, BUET, Dhaka. The average grain size was estimated from the FESEM images using 'ImageJ' software.

iii. Chemical composition were determined by using an energy dispersive X-ray diffractometer attached with FESEM at the department of Glass and Ceramics Engineering, BUET, for confirmation of the presence of all the constituents in the samples.

Magnetic and magnetocaloric properties measurements:

i. Magnetization as a function of temperature in FC and ZFC mode, magnetization as a function of temperature at high field and isothermal magnetization measurements as a function of applied magnetic field have been recorded using a quantum design "Physical Properties Measurement System (PPMS)" at Materials science division, AEC, Dhaka, Bangladesh.

iii. To investigate the magnetocaloric properties, magnetic entropy change as a function of temperature and applied magnetic field was calculated.

3.4.2 X-ray diffractometer

X-ray diffraction (XRD) is the most important characterization technique that provides the information regarding crystal structure, chemical composition, lattice parameter, inter planner distance etc. It consists of a filament, electrodes, cathode tube etc. The filament stays inside the cathode tube of an X-ray diffractometer. It is heated by application of alternating voltage between two electrodes. As the filament gets heated then the free electrons are produced and start travelling from cathode to anode and finally strike the anode surface resulting production of X-rays in X-ray tube. Then the generated X-ray in the tube hits on the surface of the sample. The X-rays are diffracted by the crystal plan in different direction with variation of intensity with change in incident angle. Bragg's reflection occurs when the diffracted X-ray makes the same angle as that of the incident beam with the crystal plan. Since the intensity of the X-ry beam varies with the angle between incidence and diffracted beam, fine peaks are found in the computer screen that correspond the different crystal planes known as Miller indices. The structure and elemental composition of the crystal, inter-planar distance, and lattice parameters can be calculated from those Miller indices.

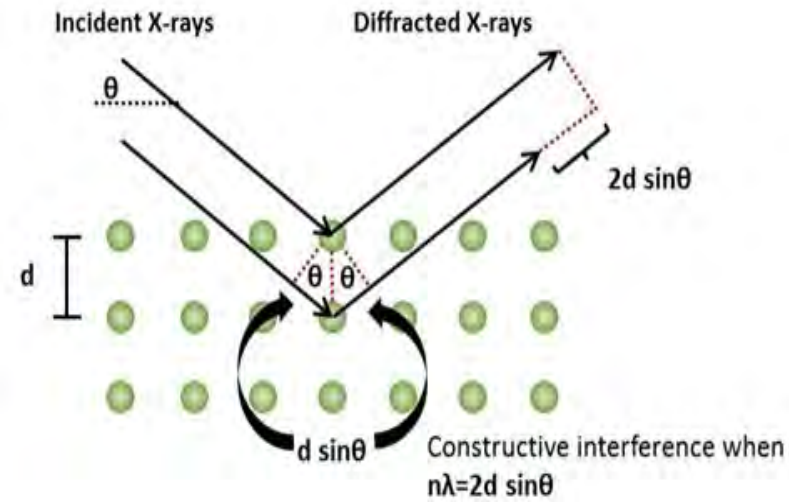

Fig. 3.5 Bragg's reflection from crystal plan.

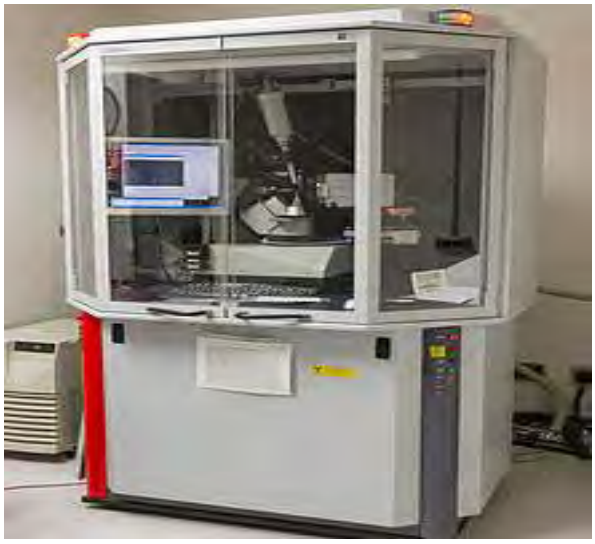

Fig. 3.6 Bruker X8 Apex diffractometer.

The working principle of XRD technique based on the principle of Bragg's law which is expressed as

$$2d \sin \theta = n\lambda$$

Where, n is related to the order of diffraction, λ represents the characteristic wavelength of the X-rays beam, d is the inter-planar distance between rows of atoms and θ is the angle of the incident beam with the rows of atoms as shown in Fig. 3.5. An X-ray diffractometer situated at the department of Glass and Ceramic Engineering, BUET has been shown in as shown in Fig. 3.6.

3.4.3 Field emission scanning electron microscope

Field Emission Scanning Electron Microscope (FESEM) was used to investigate the morphological and microstructural analysis of the investigated samples. Generally a FESEM instrument consists of electron column, sample chamber, detector, electronics console, and visual display monitors. In a FESEM, electron beam is focused over the surface of the samples to create an electronic image. Due to the interactions between electrons beam with the sample, various signals are produced that contain information about the surface morphology and chemical compositions.

A beam of electrons is produced from cathode and goes through electron lenses. This electron beam is focused on the surface of the sample. The lenses are arranged such a way that the diameter of the beam at specimen remains around the order of 100 Å. The brightness of a particular point of the image depends on the number of electrons passes through the specimen to the collector. But, the incident of electrons at the sample is a random process. Therefore, statistical fluctuation is occurred to this number resulting noise in the final image of sample. It is observed that the brightness of any point of the image is directly proportional to the secondary emission coefficient of the corresponding point of the sample when secondary electron produces the output signal. The secondary emission coefficient should be greater than one in the scanned areas. Therefore, the variation of this coefficient over the surface of the specimen creates a contrast that contain information about the surface morphology and chemical compositions. Fig. 3.7 shows both the ray diagram and a FESEM of model 'JEOL JSM 7600F' situated at the Department of Glass and Ceramic Engineering, BUET.

3.5.4 Energy dispersive X-ray spectroscopy

The Energy-dispersive X-ray spectroscopy (EDX) is the most important analytical technique which is using for the elemental analysis or chemical characterization of a sample. Its reliability depends on interaction between electromagnetic radiation and sample. Its working principle is that every element has a specific atomic structure presenting a specific set of peaks created from the interaction with electromagnetic emission spectrum. A high-energy beam of charged particles is focused into the investigated sample to create the emission of characteristic X-rays from the sample. For ground state, an atom within the sample contains electrons in different energy levels

bound to the nucleus. The incident beam may excite an electron to emit from inner shell, to the outer shell generating a hole. Then, an electron from an outer and higher-energy shell can fill the hole. As a result, energy is released in the form of an X-ray proportional to the difference in energy between the higher energy shell and the lower energy shell. An energy dispersive spectrometer can measure the energy of the X-rays emitted from the element. Since the energy of the X-rays is the difference in energy between the two shells and characteristic of the atomic structure of the emitting element, the elemental composition of the investigated sample can be measured from the EDX spectrums. The four main components of the EDX setup are the excitation source which emits X-ray beam, the X-ray detector, the pulse processor and the analyzer. Emitted X-ray energy from the elements is converted into voltage signals using detector and then this information is received by a pulse processor, which process the signals and passes them onto an analyzer for data display and analysis. In summary it is found that the EDX receive the X-rays, analyze and plots them in terms of energy, and identifies the elements responsible for the peaks in this energy distribution. In the present work, the elemental analysis was performed by using the EDX system attached to the FESEM (JEOL JSM 7600F) as shown in Fig. 3.7.

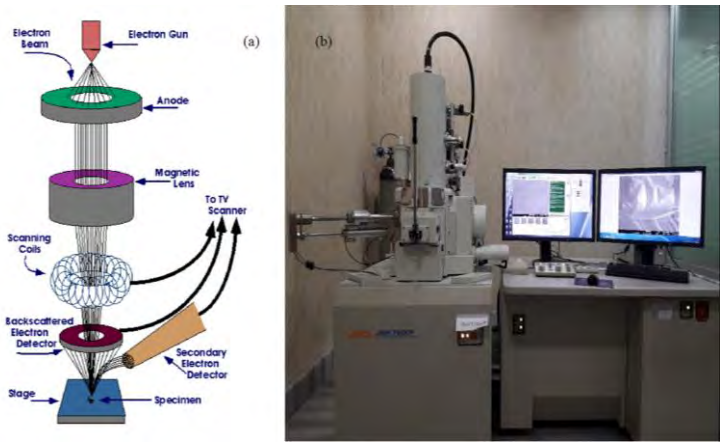

Fig. 3.7 Field Emission Scanning Electron Microscope (a) schematic diagram of FESEM, (b) FESEM of model JEOL JSM 7600F.

3.4.5 Physical Property Measurement System

The Physical Property Measurement System (PPMS) is very sensitive and suitable electromagnetic device which is used to study the magnetic and electrical transport properties of materials under well-controlled magnetic field up to ±16 T and

temperature ranging from 1.9 to 400 K. The samples used for measurements are typically in the form of a bulk, thin film, and powder if the samples are of sufficiently small to be fitted within the measurement volume of the instrument. The vibrating sample magnetometer option of the Physical Property Measurement System is a fast, sensitive, and fully automated DC magnetometer. The magnetic measurements are carried out by oscillating the investigated sample in a pickup coil and simultaneously measuring the induced voltage generated from magnetic induction due to variation of magnetic flux. The magnetometer uses a compact gradiometer pickup coil configuration to get a relatively large oscillation amplitude of 1-3 mm peak, and a frequency of 40 Hz. In this way the magnetometer can detect magnetization changes of less than 10^{-6} emu at a data rate of 1 Hz. However, samples are only limited to diameters and lengths of less than 4.5 and 5 mm, respectively because of narrow volume of the pickup coil whereas the diameter is physically limited by the bore of the pickup coil. If the lengths exceed 5 mm, it creates a reduction of magnetic moment that should be avoided. Samples are mounted to either quartz paddles or brass troughs, as required. Fig. 3.8 shows Physical Property Measurement System situated at materials science division, AEC, Dhaka, Bangladesh.

Fig. 3.8: Physical Property Measurement System.

3.4.6 The zero field cooled and field cooled magnetization measurements

Zero field cooled (ZFC) magnetization measurement: In first step of the ZFC process, sample should be cooled in absence of an applied magnetic field to the targeted temperature. Then the magnetization data should be recorded while heating under application of small applied magnetic field.

Field cooled (FC) magnetization measurement: In this process, sample must be cooled with small applied magnetic field to the lowest targeted temperature. Then the data can be collected in two ways as given below.

Two possible modes for FC measurement are:

1. Field cooled cooling (FCC): In this mode, data must be collected upon cooling
2. Field cooled warming (FCW): In this mode, data must be recorded while heating.

3.5 Determination of the magnetocaloric effect

3.5.1 Direct measurements

In direct method MCE is measured in terms of adiabatic temperature change based on measurements of initial temperature (T_0) and finale temperature (T_F) of the material due to variation of applied magnetic field from an initial value (H_0) to a final value (H_F). Then the value of adiabatic temperature change is given by the relation: $\Delta T_{ad}(T_0, H_F\text{-}H_0) = T_F - T_0$. The accuracy of this method remains in between 5-10% [32, 61].

3.5.2 Indirect measurements

In indirect method MCE is measured in terms of both $\Delta T_{ad}(T, \Delta H)$ and $\Delta S_M(T, \Delta H)$. $\Delta T_{ad}(T, \Delta H)$ is calculated from heat capacity measurements while $\Delta S_M(T, \Delta H)$ is calculated from the isothermal magnetization measurements. In this case the magnetization should be measured as a function of applied field at different constant temperature around magnetic phase transition temperature [32]. The accuracy of this method to calculate the $\Delta S_M(T, \Delta H)$ depends on the accuracy of magnetization measurements. The accuracy of this method remains in between 3-10%.

CHAPTER 4
RESULTS AND DISCUSSION

4.1 Characterization of $Pr_{0.55}Ca_xSr_{0.45-x}MnO_3$ (x=0.0, 0.05, 0.1, 0.2 and 0.25) Perovskite

4.1.1 X-ray diffraction analysis

The room temperature powder XRD patterns as well as Miller indices of various $Pr_{0.55}Ca_xSr_{0.45-x}MnO_3$ compounds have been shown in Fig. 4.1 (a). All the patterns show similar characteristic peaks and there are no trace of extra peaks due to the precursors. The XRD patterns were recorded in the 2θ range of 10-80°. The crystallite size (d) has been calculated from Debye-Scherer equation [75] given as $d = \frac{K\lambda}{\beta\cos\theta}$, where, d = crystallite size in nm, K = 0.9 (Scherer constant), λ = 0.15406 nm (wavelength of the X-ray), β = FWHM in radians and θ = peak position in radians. Fig. 4.1 (b) represents the main peak (200) of the XRD patterns which represents that the XRD peaks shifts towards greater angles demonstrating the decrease of the lattice parameters with the increase in Ca content [13]. However any type of structural phase transition has not been seen in the system. No splitting in the main peak (as shown in Fig. 4.1 (b)) suggests the possibility of being orthorhombic perovskite unit cell of all the studied samples.

For getting details information about structural change caused by Ca substitution in place of Sr, the Rietveld analysis was carried out using the 'X'Pert HighScore Plus' software which reveals that all the samples are in single phase within the measurement range and found to crystallize in the orthorhombic system with Pnma space group. The lattice parameters a, b and c as well as the cell volume are computed and summarized in Table 4.1. Fig. 4.2 shows Rietveld patterns for all the studied samples where the graphs show a good agreement between the observed and calculated values. The quality of the Rietveld refinement is estimated through the goodness of the fit indicator χ^2, weighted parameter R_{wp}, and the pattern R_p. The values of χ^2, R_{wp} and R_p have been inserted into Fig. 4.2. It is also observed that the lattice parameters a, b and c as well as the cell volume decreases with increase in Ca content (as shown in Fig. 4.3 (a)) due to the substitution of larger Sr^{2+} ion (r_A~1.32 Å) by smaller Ca^{2+} (r_A~1.18 Å). Mn-O-Mn bond angle was also found to decrease with increasing Ca content (as shown in Fig. 4.3 (b)).

Substitution of larger Sr^{2+} for smaller Ca^{2+} creates a void between MnO_6 octahedra which generate extra chemical pressure resulting reduction of Mn-O-Mn bond angles from the ideal 180° [69].

It is well known that the dependence of structural parameters of the manganite on the A-site substitution creates distortions and rotation of the MnO_6 octahedra due to the mismatch size of the A-site cation [75]. The tolerance factor which is a measure of the deviations from the ideal cubic perovskite structure, can be calculated from the ionic radii of the lattice sites in a perovskite structure and expressed by Goldschmidt [76] as

$$t = \frac{< r_A > + r_0}{\sqrt{2}(< r_{Mn} > + r_0)} \tag{4.1}$$

where $< r_A >$, $< r_{Mn} >$ and r_0 are the average ionic radius of the A-site, Mn and O ions respectively. The average A-site ionic radius for this series of samples have been calculated using $< r_A >= 0.55 < r_{Pr^{3+}} > + x < r_{Ca^{2+}} > + (0.45 - x) < r_{Sr^{2+}} >$. As t decreases from 1, the lattice structure transforms to the rhombohedral structure for 0.96<t<1 and then to the orthorhombic structure for t<0.96 [77]. For this series of samples the tolerance factor varies from 0.896 for x = 0.0 to 0.870 for x = 0.25 (Table 4.1). This result is attributed to the replacement of larger ion of Sr^{2+} by a smaller Ca^{2+} ion. The calculated values of tolerance factor also support for the distorted orthorhombic structure of the studied samples. These variations in structural parameters may affect the magnetic and magnetocaloric properties of the samples.

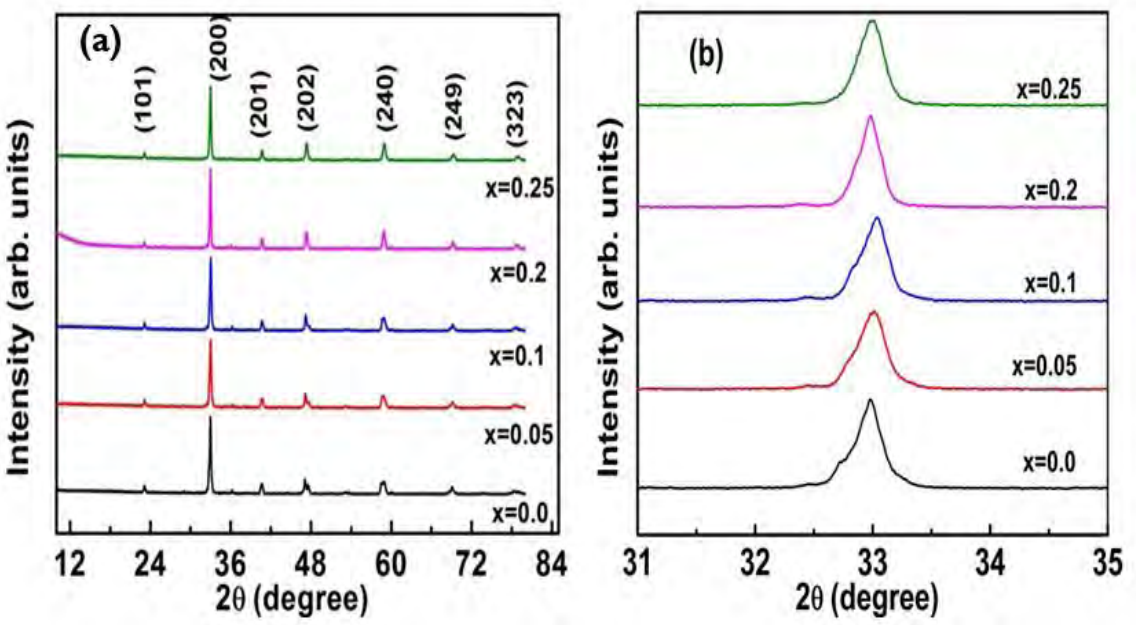

Fig. 4.1 (a) Room temperature XRD pattern, (b) main peak of XRD patterns of various $Pr_{0.55}Ca_xSr_{0.45-x}MnO_3$ compounds.

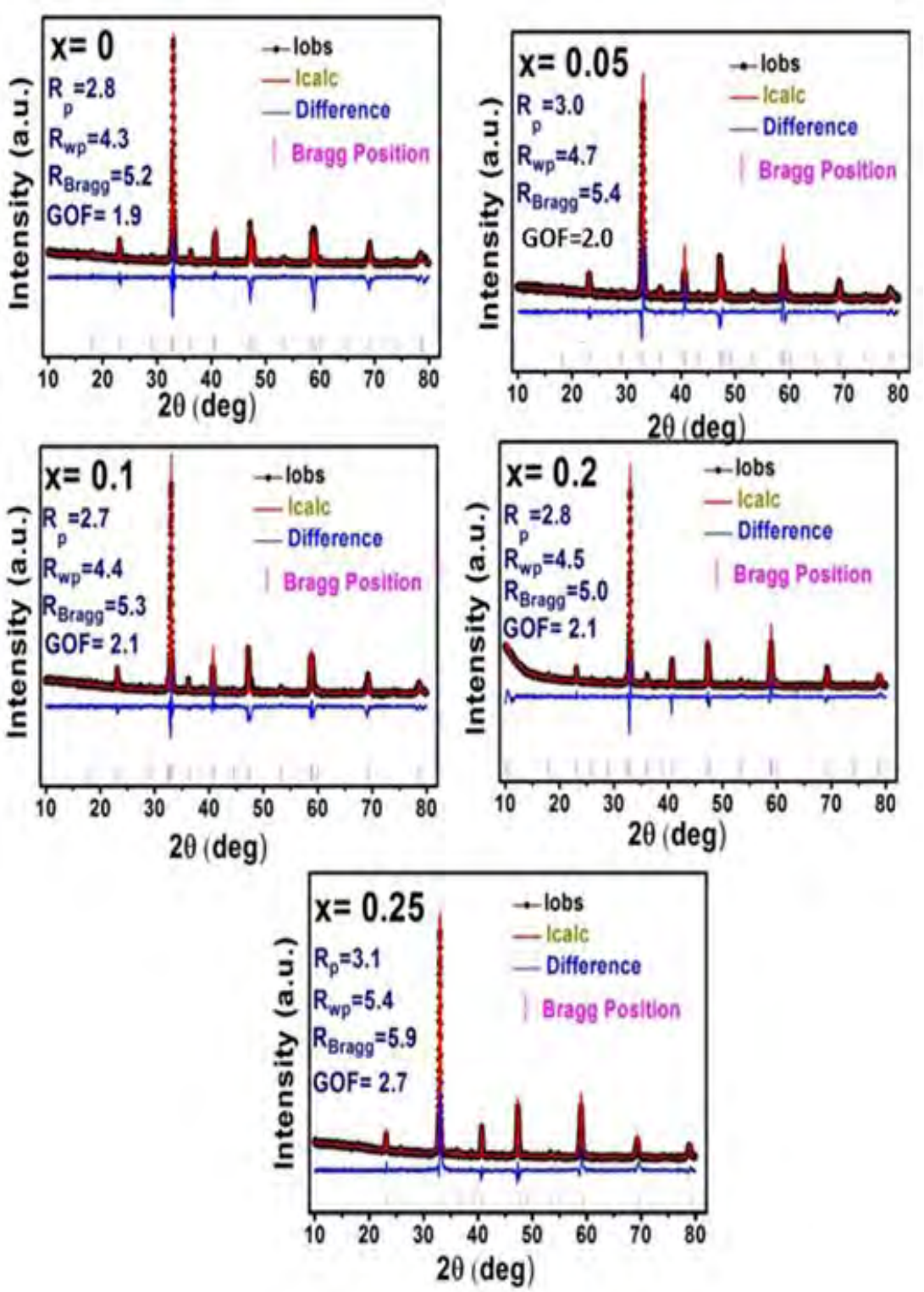

Fig. 4.2 Rietveld pattern for various $Pr_{0.55}Ca_xSr_{0.45-x}MnO_3$ compounds.

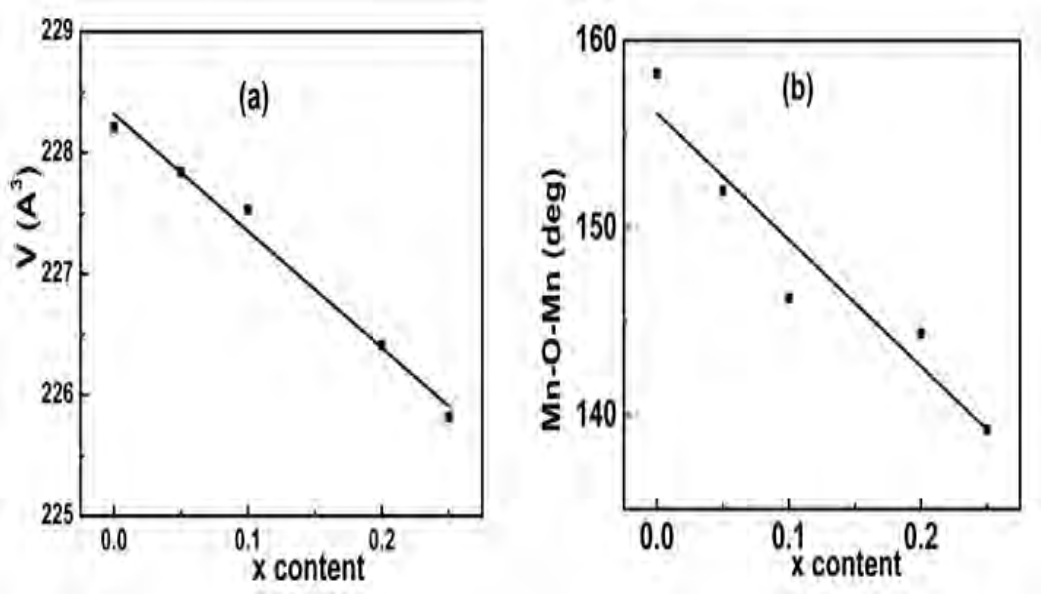

Fig. 4.3 (a) Cell volume vs x content, (b) Mn-O-Mn bond angle vs x content for $Pr_{0.55}Ca_xSr_{0.45-x}MnO_3$ compounds.

Table 4.1 Lattice parameter, cell volume (V), Mn-O-Mn bond angle, crystallite size (d) and grain size (D) of $Pr_{0.55}Ca_xSr_{0.45\ x}MnO_3$ polycrystal.

x	System	a (**Å**)	b (**Å**)	c (**Å**)	V (Å^3)	Mn-O-Mn (deg)	D (μm)	d (nm)
0.0	orthorhombic	5.4461	7.6511	5.4776	228.21	158.26	1.2	66
0.05	orthorhombic	5.4457	7.6542	5.4674	227.84	152.00	1.35	48
0.1	orthorhombic	5.4403	7.6550	5.4645	227.53	146.26	1.5	48
0.2	orthorhombic	5.4260	7.6509	5.4483	226.41	144.37	0.99	48
0.25	orthorhombic	5.4205	7.6591	5.4401	225.82	139.25	0.91	38

4.1.2 Microstructure observation

Fig. 4.4 shows the FESEM images of different $Pr_{0.55}Ca_xSr_{0.45-x}MnO_3$ samples. It is seen that the samples are porous and appear at different polygonal forms. Presence of the dispersed particles in form and size is also noticed. It may be produced due to the competition between the fracturing, cold welding, agglomeration and de-agglomeration of the powder particles during the ball milling. The average grain sizes have been calculated using 'ImageJ' software and tabulated in Table 4.1. Fig. 4.4 also shows a histogram for calculation of average grain sizes for a representative sample x=0.0. For all the samples, the average grain sizes are larger than the crystallite size, indicating a multi-domain structure. For x = 0.0, 0.05, 0.1 the grains are larger but for larger amount of Ca i.e. x = 0.2, 0.25, the size of the grains decreases. This observation reveals that for Ca content up to 0.1, the crystalline particles develop easily due to existence of local liquid phases [56] but substitution of Sr by Ca more than 0.1 does not favor grain growth in the studied samples. It is also observed that for x=0.2 and 0.25, the grain boundaries are obvious, and there are small number of necks among grains. But in case of x=0.0 to 0.1, the grain boundaries are not clear and there are large number of long necks among the grains. The neck is always distorted because of the different crystalline of grains. The distorted grain boundaries also affect the inside of grains [78]. Again due to larger distorted boundaries, the grain-boundary effect increases. Thus for our sample of series, the grain-boundary effect decreases from sample with x=0.0 to 0.25 which may influence magnetic and magnetocaloric properties of the studied samples.

4.1.3 Chemical composition analysis

Fig. 4.5 shows the EDX spectrum of various $Pr_{0.55}Ca_xSr_{0.45-x}MnO_3$ compounds. The spectrums contain only the peaks of Pr, Ca, Sr, Mn and O and no other impurity element rather than elemental composition of the investigated samples are found in the spectrums. Using the EDX data chemical composition of $Pr_{0.55}Ca_xSr_{0.45-x}MnO_3$ polycrystal normalized to 100 wt% was derived from average value of three spectra and it is found that the stoichiometrically calculated values agreed well with the experimental values. Table 4.2 represents elemental compositions of various $Pr_{0.55}Ca_xSr_{0.45-x}MnO_3$ compounds in weight %. It is observed from the table that there are excess amount of Mn and a lack of Pr content. Ca and Sr content values are exchanged in an approximately linear manner as expected composition. The anomaly

between calculated and experimental compositions may be arisen due to scattering effects as porosities influence on the X-ray peak intensities of the different elements in the sample [79].

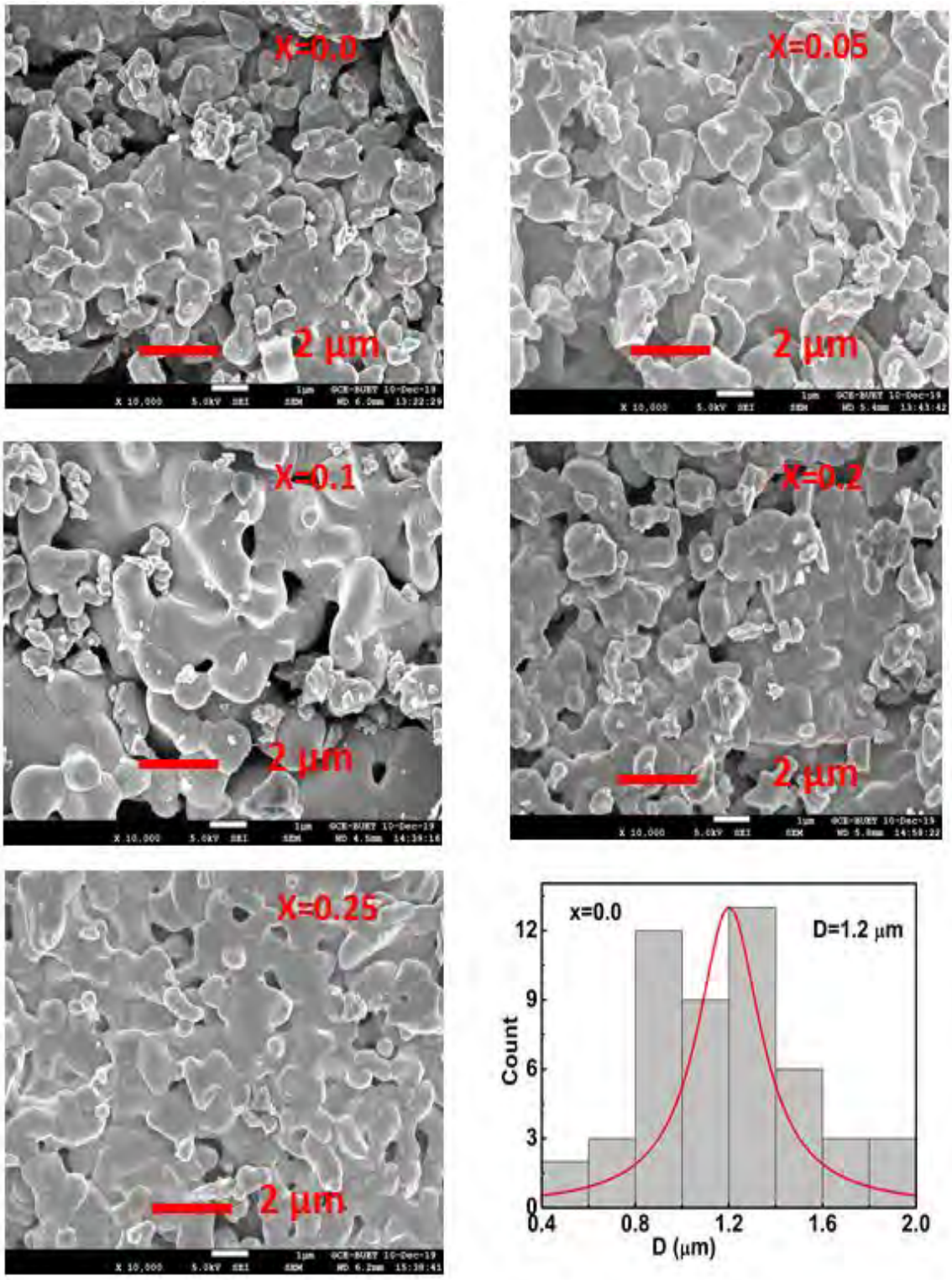

Fig. 4.4 FESEM images of the compound $Pr_{0.55}Ca_xSr_{0.45-x}MnO_3$ (x=0.00, 0.05, 0.1, 0.2 and 0.25) and histogram for x=0.0.

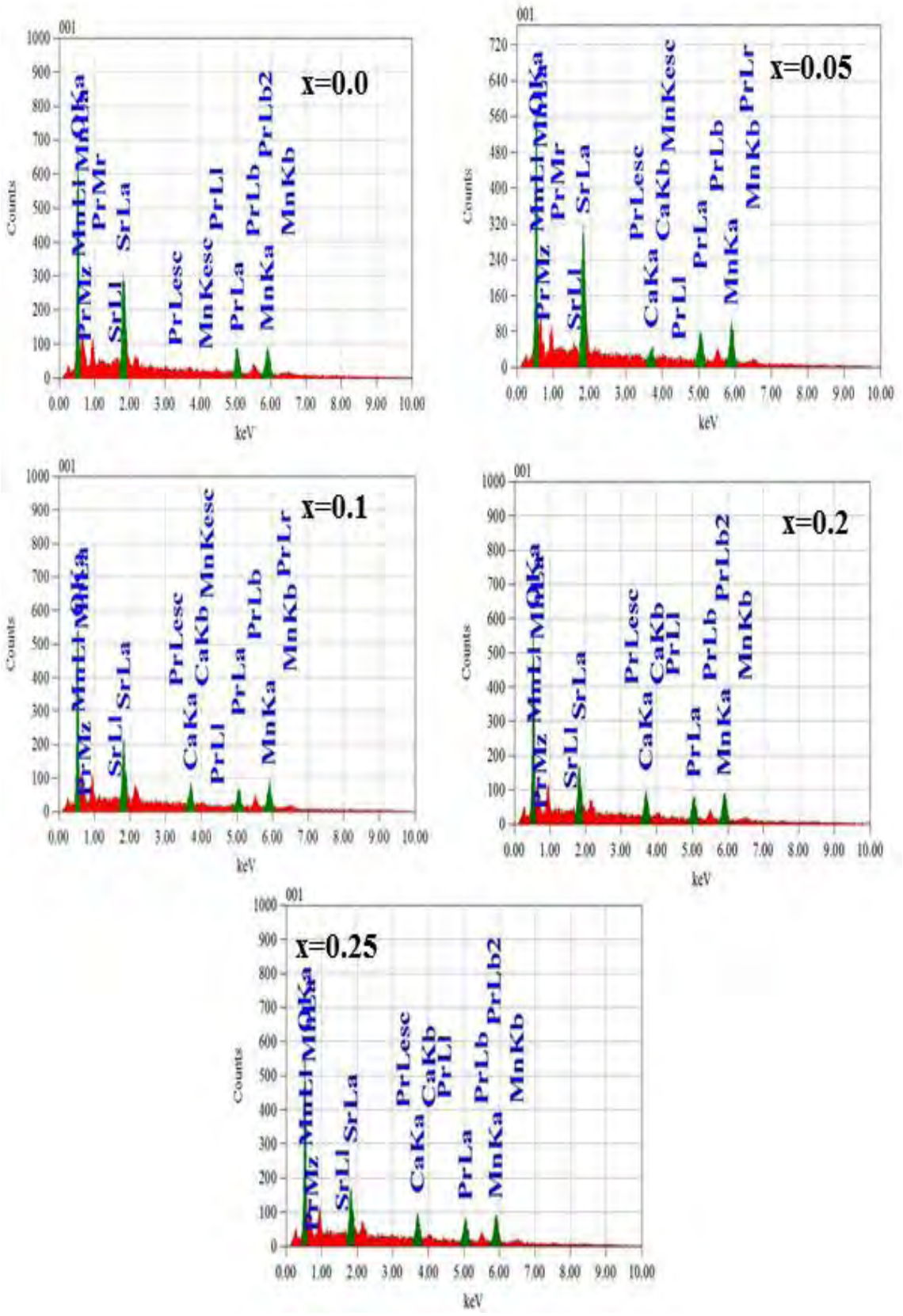

Fig. 4.5 EDX spectrum of various $Pr_{0.55}Ca_xSr_{0.45-x}MnO_3$ compounds.

Table 4.2 Elemental compositions of various $Pr_{0.55}Ca_xSr_{0.45-x}MnO_3$ compounds in weight %.

		Pr	Ca	Sr	Mn	O
x=0.0	Calculated Weight%	35.24	……..	17.93	24.98	21.83
	Weight % from EDX spectrum	34.25	……	16.82	26.76	22.17
x =0.05	Calculated Weight%	35.63	0.92	16.11	25.26	22.06
	Weight % from EDX spectrum	34.75	1.02	16.32	25.76	22.17
x =0.1	Calculated Weight%	36.05	1.87	13.02	25.68	22.38
	Weight % from EDX spectrum	35.72	2.05	12.76	26.73	21.76
x =0.2	Calculated Weight%	36.84	3.81	10.41	26.12	22.81
	Weight % from EDX spectrum	34.72	4.05	11.76	27.71	21.79
x =0.25	Calculated Weight%	37.21	4.76	8.46	26.54	23.03
	Weight % from EDX spectrum	36.09	5.67	8.67	27.36	22.21

4.1.4 Magnetic properties

4.1.4.1 Temperature dependent magnetic properties

Fig. 4.6 (a) shows the FC and ZFC magnetization curves taken in presence of a constant magnetic field of 0.01 T in temperature range 45–400 K for various $Pr_{0.55}Ca_xSr_{0.45-x}MnO_3$ compounds. In FC mode, magnetization for x=0.0 decreases gradually with increase in temperature following a sudden fall to zero value indicating FM to PM phase transition. After that the sample enters into PM state where the FM order of magnetic moments is destroyed by thermal energy. This sharp fall in magnetization indicates large magnetic entropy change around FM to PM transition temperature. All other Sr substituted samples undergoes FM to PM transition but they exhibit another AFM transition around 208 -180 K for x=0.05- 0.25. This type of transition is also seen in [63] and [64]. Except these, a considerable difference in FC and ZFC magnetization is observed at a lower temperature known as irreversibility temperature which may be occurred due to spin-glass like behavior originated from the interaction between FM

and AFM cluster [79]. This behavior is attributed to the competition between super exchange AFM and double exchange FM interactions at the grain boundaries and also the short-range ordering at grain boundary due to distorted crystal structure [80, 81].

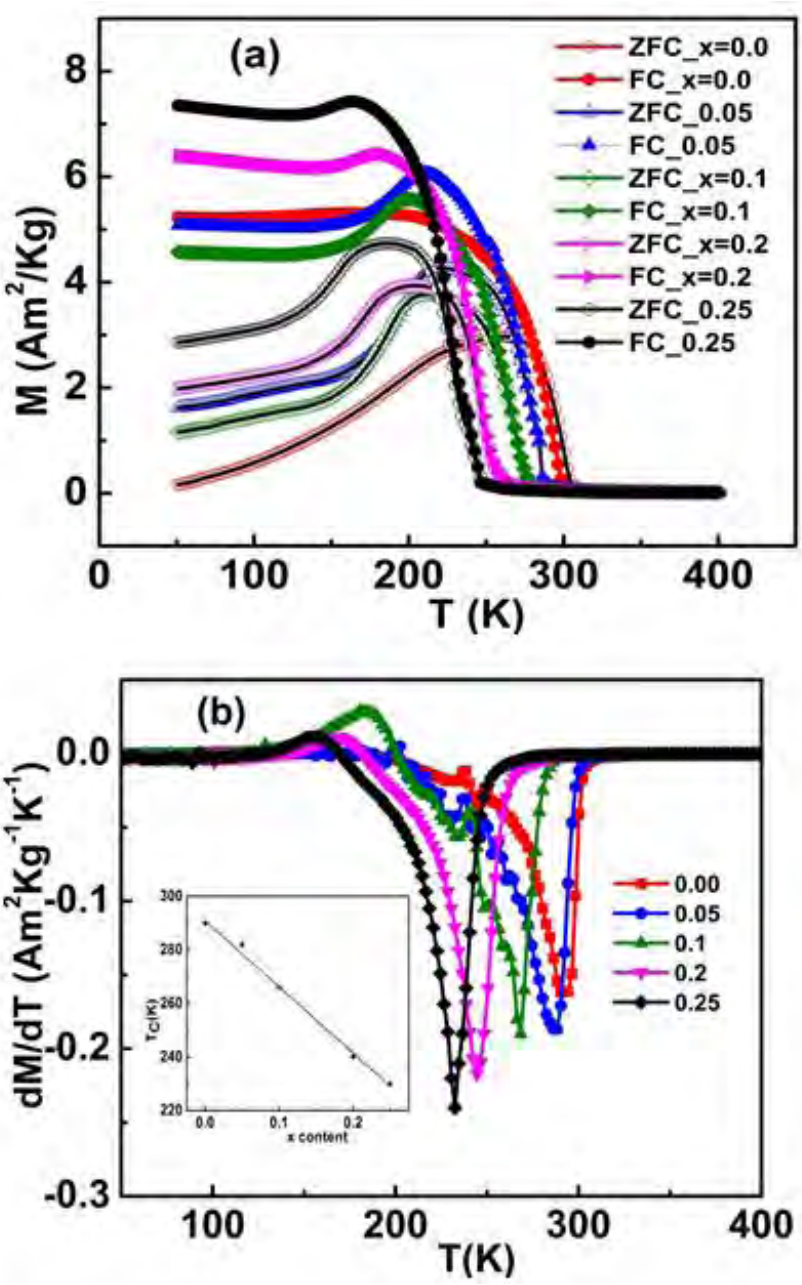

Fig. 4.6 (a) FC and ZFC magnetization curves, (b) dM/dT vs T curves, inset: T_C vs x content for various $Pr_{0.55}Ca_xSr_{0.45-x}MnO_3$ compounds at H=0.01 T.

The temperature at which the change in magnetization (dM/dT) is maximum, known as the Curie temperature and at that temperature magnetic entropy change also reaches maximum value. T_C is determined here from critical point of dM/dT versus temperature

curve (Fig. 4.6 (b)) where dM/dT was calculated from FC magnetization data. According to our experimental investigation the T_C value for the sample with x=0.00 is 290 K which has decreased to 230 K with the increase in Ca content from 0.00 to 0.25 as shown in inset of Fig. 4.6 (b). Substitution of larger Sr^{2+} by smaller Ca^{2+} in the samples causes a reduction in the A-site average atomic radius, as well as tolerance factor, resulting variation in Mn-O bond length and Mn-O-Mn bond angle which in turn decreases double exchange interaction. Consequently, T_C decreases as Ca content increases in $Pr_{0.55}Ca_xSr_{0.45-x}MnO_3$. This result agreed well with the reviewed previous publications on doped manganites where substitution of Ca^{2+} by Ba^{2+}, Sr^{2+} or Pb^{2+} increases T_C due to increase in average ionic radius [76, 82]. Comparing the ZFC and FC curves of the samples, it is also seen that magnetization at both modes increases as Ca content increases.

The inverse magnetic susceptibility ($1/\chi$=H/M) was determined from the FC magnetizations data taken in an applied magnetic field of 0.01 T. Fig. 4.7 shows $1/\chi$ vs T curves for sample $Pr_{0.55}Ca_xSr_{0.45-x}MnO_3$. At temperature above T_C, there is no difference between inverse susceptibility curve and its linear extrapolation to zero value for x=0.00, which indicates that the mean-field Curie–Weiss law $\frac{1}{\chi} = \frac{C}{(T-\theta)}$ is obeyed [83]. Where C is Curie constant, θ is the paramagnetic Curie temperature which is found from the extrapolation of linear part of $1/\chi$ vs T curve to zero inverse magnetic susceptibility as shown in Fig. 4.7. It is also found that the values of paramagnetic Curie temperature are very close to T_C values. These results clearly explain the magnetic homogeneity of investigated sample above T_C [84]. The effective magnetic moment for x=0.00, calculated from Curie constant 'C' is found $3.73\mu_B$. The theoretical value of effective paramagnetic moment was derived using the equation (1):

$$\mu_{eff}^{cal} = \sqrt{0.55[\mu_{eff}^{cal}(Pr^{3+})]^2 + 0.55[\mu_{eff}^{cal}(Mn^{3+})]^2 + 0.45[\mu_{eff}^{cal}(Mn^{4+})]^2} \qquad (4.2)$$

Where, $\mu_{eff}^{cal} = g\sqrt{S(S+1)}$, g=2 is the gyromagnetic ratio and S is the magnetic spin. μ_{eff}^{exp} is found to be 4.51 μ_B for the sample x=0.00. The difference between the μ_{eff}^{cal} and μ_{eff}^{exp} value indicates the presence of FM clusters in the PM phase. With increase in Ca content, the $1/\chi$ vs T curves deviate from Curie–Weiss law indicating existence of larger amount of FM cluster in the PM region.

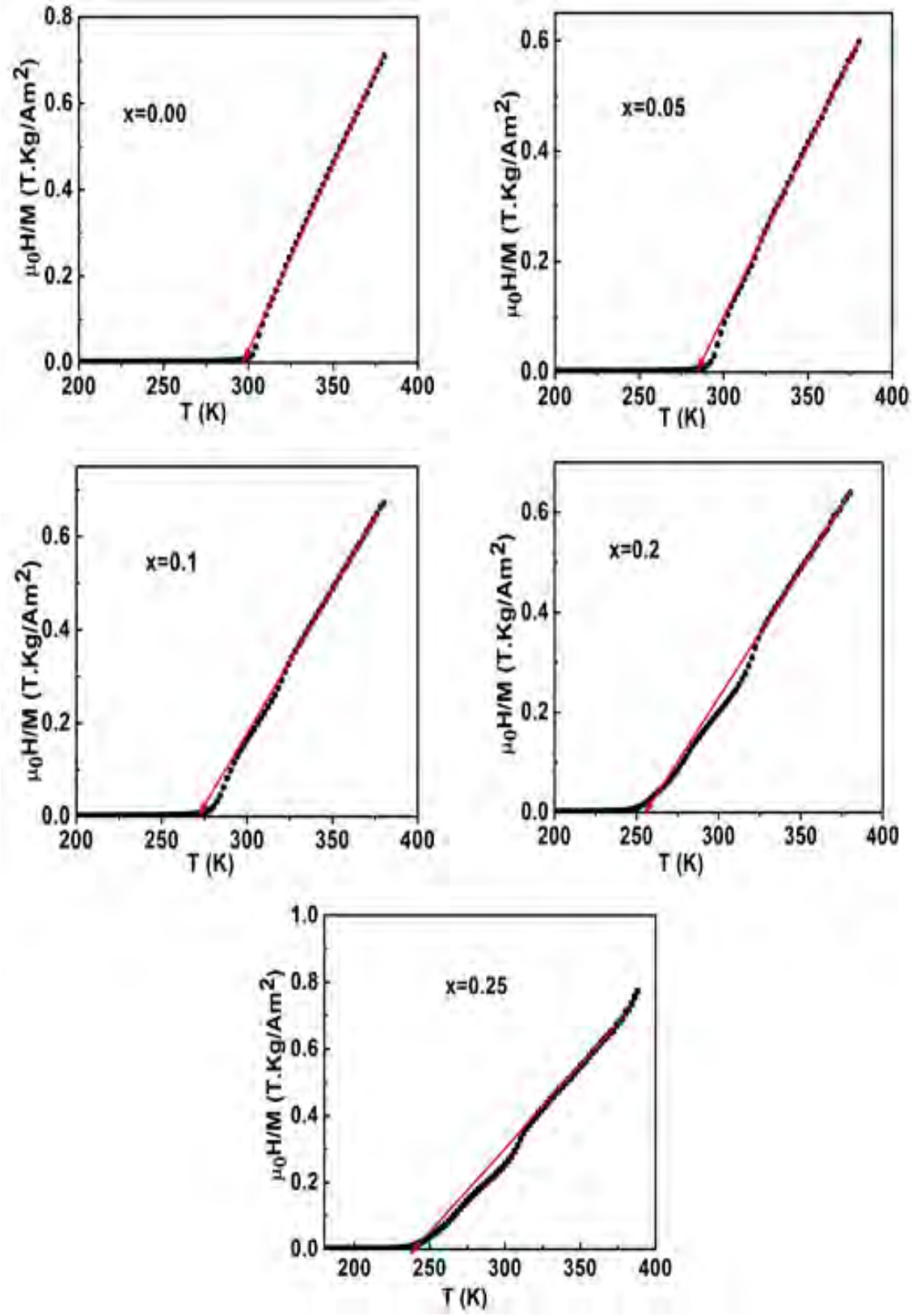

Fig. 4.7 $1/\chi$ vs T curves for various $Pr_{0.55}Ca_xSr_{0.45-x}MnO_3$ compounds.

4.1.4.2 Magnetic field dependent magnetic properties

Isothermal magnetizations as a function of applied magnetic field at different constant temperatures around FM-PM phase transition temperature were measured in order to investigate the magnetic field dependent magnetic properties and magnetocaloric effect of the studied samples.

Fig. 4.8 shows isothermal magnetization curves of different $Pr_{0.55}Ca_xSr_{0.45-x}MnO_3$ compounds which reveal the variation in magnetic behavior as the sample undergoes FM to PM phase with increase in temperature. At temperature below T_C, all the curves are nonlinear, show FM phase with sharp increase at low field and saturation at high field [84]. A rapid change in magnetization is seen around T_C and at temperatures above T_C, the curves are linear attributing to PM phase. It is also observed that enhancement in magnetic saturation occur with increase in Ca content from 0.00 to 0.25. It is well established that the magnetic properties of perovskite manganite are correlated to the Mn-O-Mn bond angle and Mn-O bond length. Decrease in Mn-O-Mn bond angle would reduce the magnetization and T_C because of the weaker double exchange interaction between the Mn^{3+}-O-Mn^{4+} ions. But with increase in Ca content in our sample, the spin interaction strengthens resulting increase in saturation magnetization. One possible reason for increased saturation magnetization may be due to the reduction of strain at the grain boundaries from x=0.0 to 0.25 as explained in FESEM images.

Based on Landau theory, the Gibb's free energy can be defined as a function of magnetization in the following form neglecting higher order parts [85]:

$$G(T, M) = G_0 + \frac{1}{2}AM^2 + \frac{1}{4}BM^4 - \mu_0 HM \qquad (4.3)$$

Where, A and B are Landau co-efficient and those are temperature dependent parameter. The parameter B is related to elastic and magneto-elastic terms of free energy. For equilibrium condition, $\partial G/\partial M = 0$,

Then the magnetic equation of state is found as

$$\frac{H}{M} = A + BM^2 \qquad (4.4)$$

Thus, according to equation (4.4), the M^2 versus $\mu_0 H/M$ plots should have linear behavior around phase transition temperature.

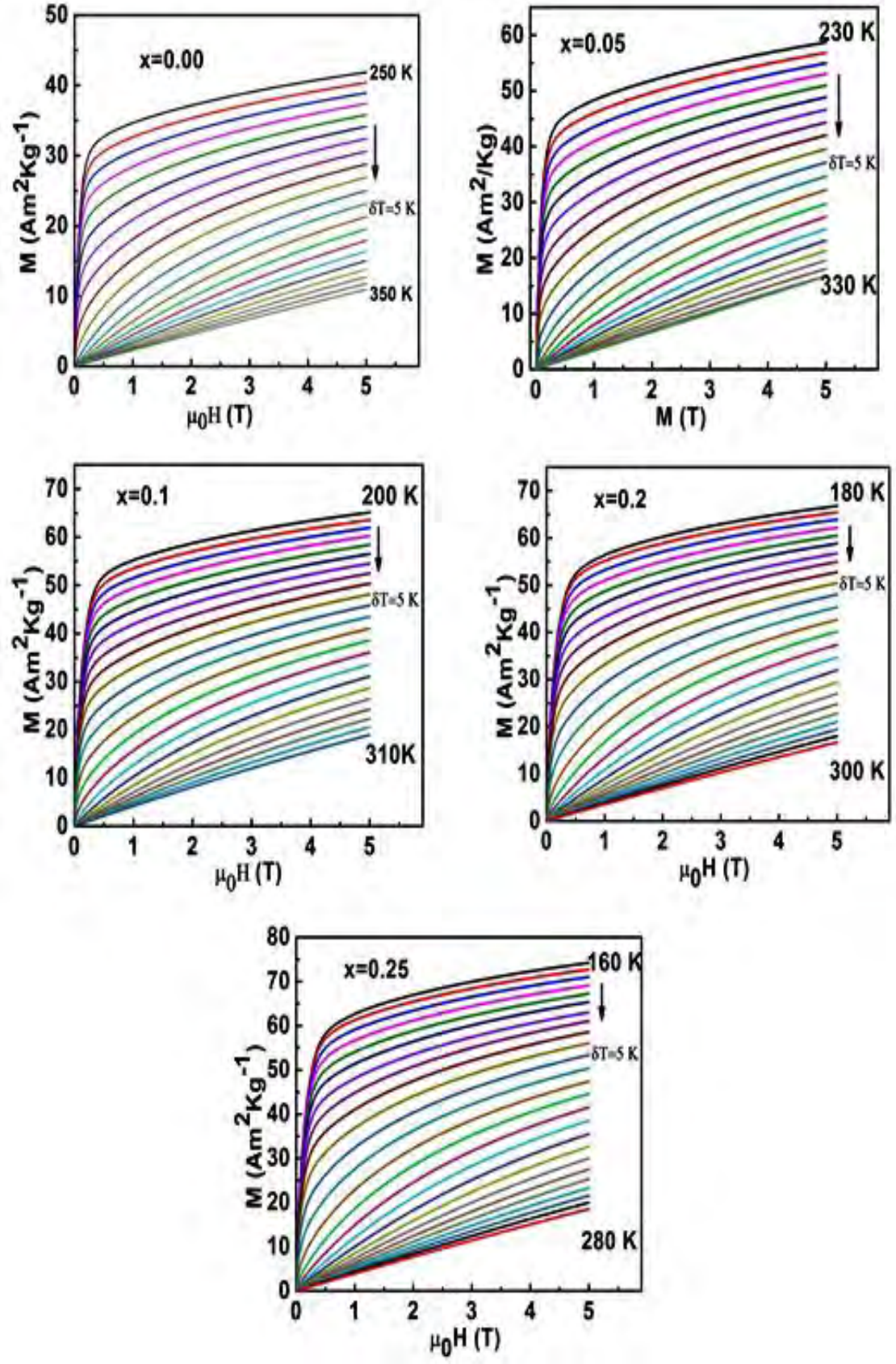

Fig. 4.8 Isothermal M-H curves for various $Pr_{0.55}Ca_xSr_{0.45-x}MnO_3$ compounds.

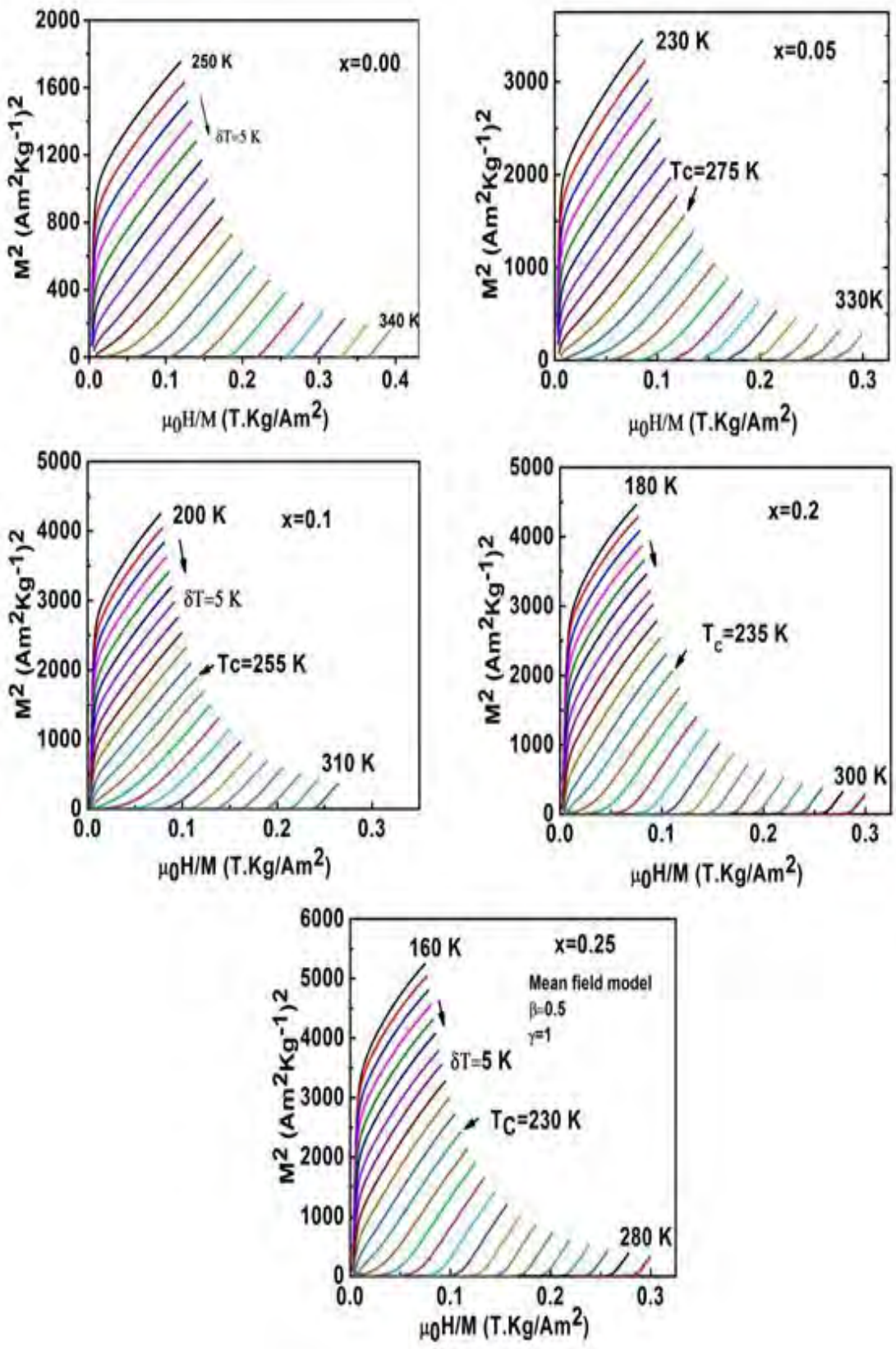

Fig. 4.9 Arrott plot around T_C for the samples $Pr_{0.55}Ca_xSr_{0.45-x}MnO_3$.

Fig. 4.9 shows M^2 vs μ_0H/M curves of $Pr_{0.55}Ca_xSr_{0.45-x}MnO_3$ compounds around T_C which is called Arrott plots. It is an alternative means used to determine the T_C as well as the type of FM-PM phase transition or critical behavior of spins around T_C in FM materials. According to Banerjee criterion [85], the order of magnetic phase transition can be obtained from the slope of M^2 vs μ_0H/M curve: "a negative sign of the slope of M^2 vs μ_0H/M curves indicates the first-order magnetic phase transition while positive sign indicates second-order magnetic phase transition". The Arrott plots of our samples have shown positive sign of the slope indicating second-order FM-PM phase transition. This property can be considered as a good characteristic of the sample as promising candidate for magnetic refrigerant as we know entropy is continuous for second order magnetic phase transition and discontinuous for first order magnetic phase transition [80]. Some other demerits of first-order phase transition are presence of hysteresis loop, changes in volume, and low refrigerator performance [85].

4.1.4.3 Critical behavior analysis

The critical point exponents near the FM to PM phase transition temperature were investigated to elucidate the critical behaviors that occur in the vicinity of FM to PM phase transition temperature and to relate it to the observed magnetocaloric behavior. The critical point exponent β is associated with the spontaneous magnetization, γ is related to the initial inverse susceptibility, and δ has relation with the field dependence critical isothermal magnetization at T_C [86]. The critical point exponents near the FM to PM phase transition temperature has been calculated through different methods such as modified Arrott plot method, Kouvel-Fisher method and critical isotherm analysis of $Pr_{0.55}Ca_xSr_{0.45-x}MnO_3$.

Generally, second-order FM-PM phase transition behavior is characterized by a set of critical exponents' β, γ and δ around T_C. Conventionally, critical exponents' β, γ and δ around T_C can be calculated from the modified Arrot plot using Arrott-Noakes [86] equations of state which is given by:

$$\left(\frac{H}{M}\right)^{1/\gamma} = A\frac{T - T_C}{T_C} + BM^{1/\beta} \tag{4.5}$$

Thus $M^{1/\beta}$ vs $\left(\frac{H}{M}\right)^{1/\gamma}$ plot is known as modified Arrot plot.

M^2 vs $\mu_0 H/M$ curves in Fig. 4.9 were constructed applying mean field theory model assuming the critical exponent value, β=0.5 and γ=1. To investigate the exact value of the critical exponents' β, γ and δ for the studied samples, the modified Arrott plots were also constructed using theoretical exponents for the 3-D Heisenberg model, 3-D Ising model and Tri-critical mean field model [86, 87]. The theoretical values of above mentioned four models have been listed in Table 4.3.

Fig. 4.10 represents modified Arrott plots of all the samples applying 3-D Heisenberg model, 3-D Ising model and Tri-critical mean field model. The correct exponents are those that linearize these curves around T_C at high field region, and T_C is defined as the temperature for which the critical isotherm passes through the origin. In Fig. 4.10, it seems that all the model yield nearly parallel straight lines. Now it is a question which model is applicable for the calculation of critical exponents.

To identify which model is applicable for our samples, the relative slope of the plots was calculated by RS=S(T)/S(T_C), where S(T) is the slopes of modified Arrott plots around T_C and S(T_C) is the slopes of modified Arrott plots at T_C [88]. The results have been plotted in Fig. 4.11 which reveals that RS for 3-D Heisenberg model, 3-D Ising model and Tri-critical mean field model deviate from ideal value 1 while RS for mean field model is the closest to 1 over the whole temperature rang indicating that mean field model is applicable to deduce the critical exponents. Ideally perfect parallel lines are identified by RS=1. Since present phase transition satisfy mean field model, true long range FM order may present in all the samples.

For determining the right value of β and γ, the mean field approximation based on Arrott-Noakes equations of state was used. The β, γ, δ and T_C follow the relation given below [89]:

$$M_S(T) = M_0(-\varepsilon)^{\beta}, \quad \varepsilon < 0 \tag{4.6}$$

$$\chi_0^{-1}(T) = \left(\frac{H_0}{M_0}\right)\varepsilon^{\gamma}, \quad \varepsilon > 0 \tag{4.7}$$

$$M = DH^{1/\delta}, \quad \varepsilon = 0 \tag{4.8}$$

Where, M_S is spontaneous magnetization, χ_0^{-1} is the initial inverse magnetic susceptibility, $\varepsilon=\frac{T-T_C}{T_C}$ is the reduced temperature which has been kept less than 0.3 during critical exponent calculation. M_0, $\frac{H_0}{M_0}$, and D are the critical amplitudes.

The spontaneous magnetization was determined from the linear extrapolation of the selected MAP curves from the high field region to the intercept with $M^{1/\beta}$ axes for $T<T_C$ while the initial magnetic susceptibility was determined similarly from the intercept with $(\frac{H}{M})^{1/\gamma}$ axes for $T>T_C$. The plot of M_S and χ_0^{-1} as a function of temperature has been shown in Fig. 4.12 from where β, and γ with T_C have been calculated using the best fit according to the equation (4.6) and (4.7) respectively and listed in Table 4.3. $\beta_{MAP}$is found 0.448, 0.441, 0.423, 0.398 and 0.388 while γ_{MAP} is found 1.05, 1.09, 1.15, 1.286 and 1.301 for x=0.00, 0.05, 0.1, 0.2 and 0.25, respectively.

The exponent δ can be determined from the Widom scaling relation [90]:

$$\delta = 1 + {}^{\gamma}/_{\beta} \tag{4.9}$$

Using the β, γ values found from modified Arrott plot in equation (4.9), δ_{MAP} is found 3.34, 3.47, 3.71, 4.3 and 4.5 for x=0.00, 0.05, 0.1, 0.2 and 0.25, respectively.

The critical exponent value, β, γ and δ derived from modified Arrott plot method are found to very close to mean field model for the samples with x=0.00, 0.05, 0.1 and that of 3-D Ising model for the samples with x=0.2, 0.25.

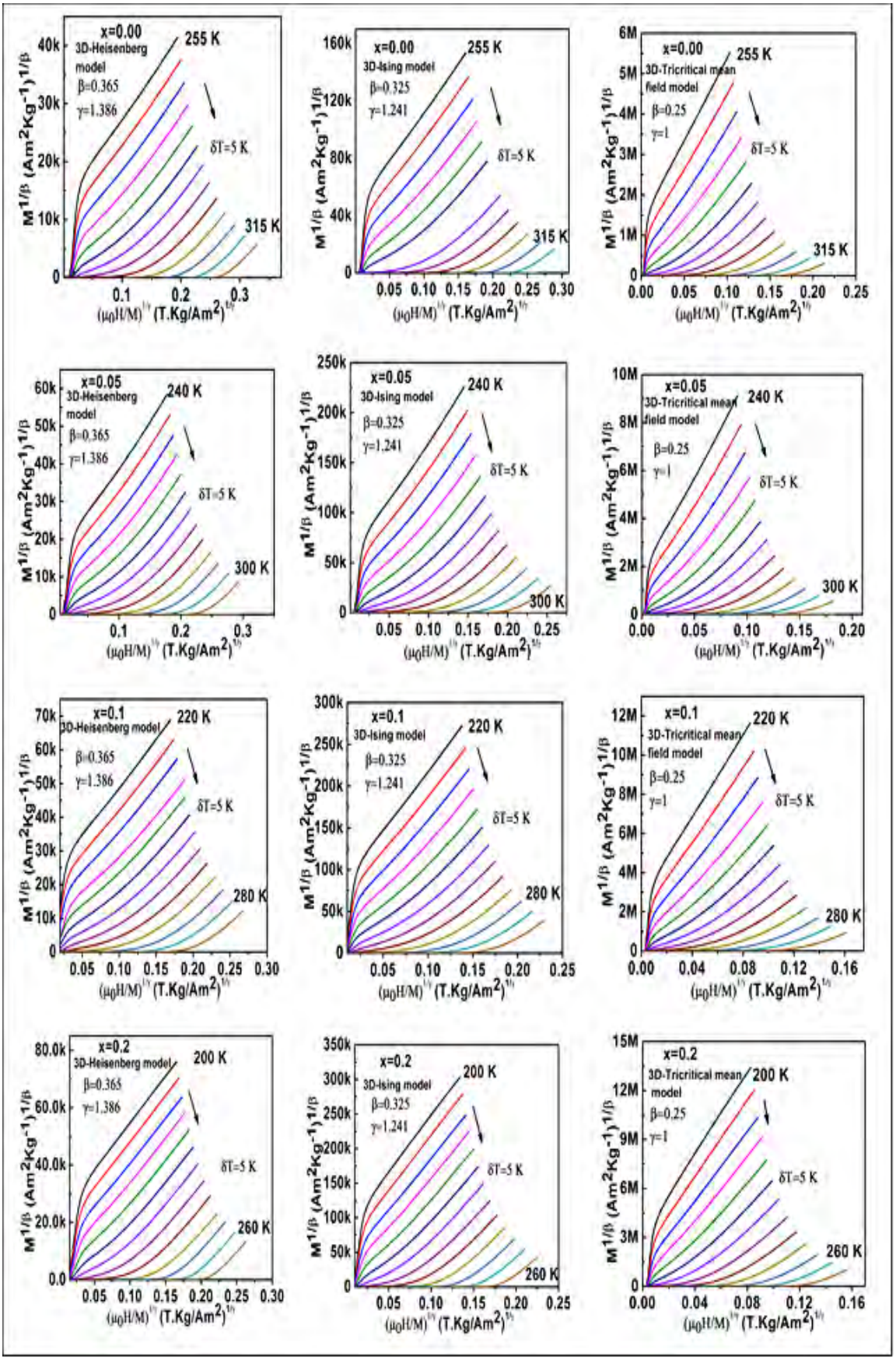

Fig. 4.10 Modified Arrott plot applying four theoretical models for various $Pr_{0.55}Ca_xSr_{0.45-x}MnO_3$ compounds.

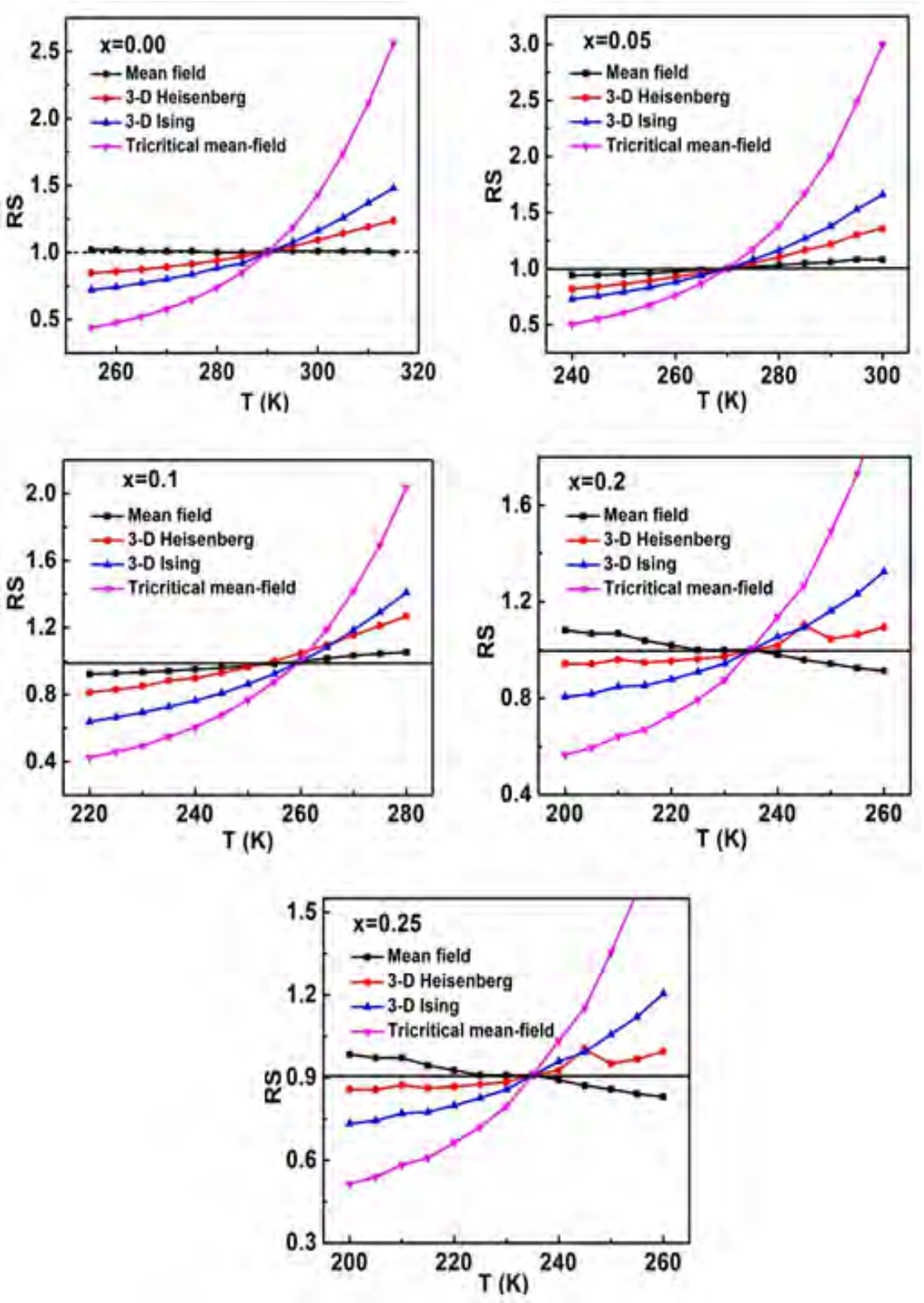

Fig. 4.11 RS vs T from various modified Arrott plots for $Pr_{0.55}Ca_xSr_{0.45-x}MnO_3$.

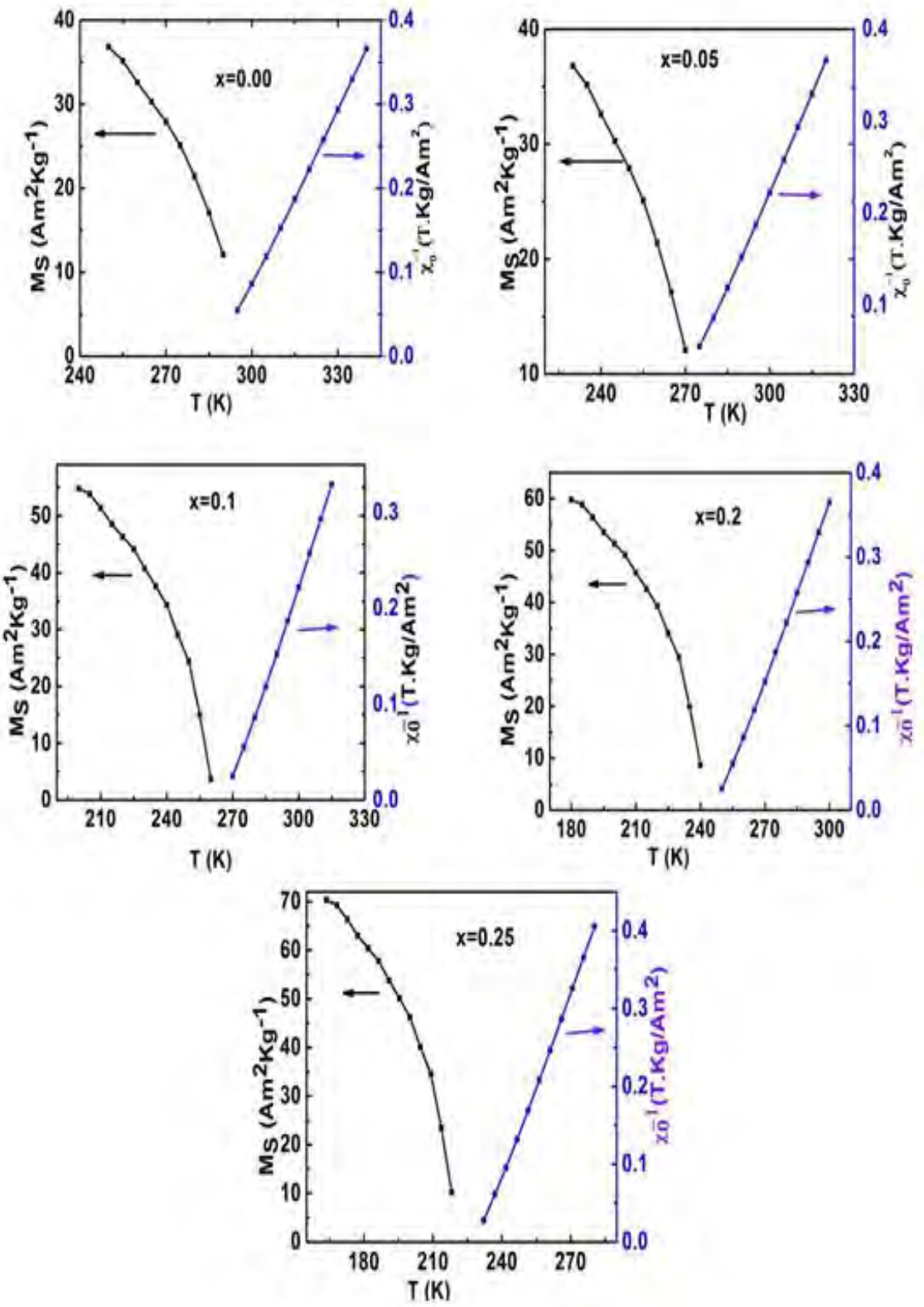

Fig. 4.12 M_S and χ_0^{-1} as a function of temperature for various $Pr_{0.55}Ca_xSr_{0.45-x}MnO_3$ compounds.

Table 4.3 Comparison of β, γ, δ and T_C of various $Pr_{0.55}Ca_xSr_{0.45-x}MnO_3$ compounds found from Modified Arrott plot (MAP) and Kouvel-Fisher (KF) method with those of theoretical models and some reported samples.

Composition	Method	T_C (K)	β	γ	δ	Reference
Mean field model	Theory	----	0.5	1	3	[86]
3-D Heisenberg model	Theory	-----	0.365	1.386	4.8	[86]
3-D Ising model	Theory	----	0.325	1.24	4.82	[86]
Tri-critical mean field model	Theory	----	0.25	1	5	[87]
$Pr_{0.55}Sr_{0.45}MnO_3$	MAP	289	0.448	1.05	3.09	This work
	KF	290	0.445	1.03	3.31	
$Pr_{0.55}Ca_{0.05}Sr_{0.4}MnO_3$	MAP	275	0.441	1.09	3.15	This work
	KF	274	0.44	1.05	3.38	
$Pr_{0.55}Ca_{0.1}Sr_{0.35}MnO_3$	MAP	265	0.423	1.15	3.23	This work
	KF	265	0.427	1.13	3.64	
$Pr_{0.55}Ca_{0.2}Sr_{0.25}MnO_3$	MAP	243	0.398	1.286	3.30	This work
	KF	243	0.40	1.24	4.1	
$Pr_{0.55}Ca_{0.2}Sr_{0.25}MnO_3$	MAP	233	0.388	1.301	3.35	This work
	KF	233	0.401	1.29	4.21	
$Pr_{0.5}Sr_{0.5}MnO_3$	MAP	261	0.443	1.339	4.022	[91]
$Pr_{0.55}Sr_{0.45}MnO_3$	MAP	292	0.449	1.113	….	[92]
$Pr_{0.6}Sr_{0.4}MnO_3$	MAP	301	0.365	1.309	4.586	[93]
$Pr_{0.55}K_{0.05}Sr_{0.4}MnO_3$	MF	301	0.44	1.04	3.34	[94]

Moreover, the critical point exponents' β, γ and δ were also computed using the Kouvel–Fisher method where they reformulated equation (4.6) and (4.7) as given bellow [95]:

$$M_S(T)\left[\frac{dM_S(T)}{dT}\right]^{-1} = \frac{T - T_C}{\beta} \tag{4.10}$$

$$\chi_0^{-1}(T)\left[\frac{d\chi_0^{-1}(T)}{dT}\right]^{-1} = \frac{T - T_C}{\gamma} \tag{4.11}$$

After plotting the $M_S(T)\left[\frac{dM_S(T)}{dT}\right]^{-1}$ vs T for below T_C and $\chi_0^{-1}(T)\left[\frac{d\chi_0^{-1}(T)}{dT}\right]^{-1}$ vs T for above T_C, two straight lines are found which are known as Kouvel-Fisher plot. Fig. 4.13 represents Kouvel-Fisher plots of M-H data for the studied samples. Straight lines represent the linear fits to the data, from which β, γ, T_{C1} and T_{C2} are computed. Finally the value of the T_C is found from the average of T_{C1} and T_{C2}. The result for the critical point exponent β is β_{KF}= 0.445, 0.44, 0.427, 0.40 and 0.401 respectively for x=0.00, 0.05, 0.1, 0.2 and 0.25. For temperatures higher than T_C, the value of the critical point exponent γ is γ_{KF} = 1.03, 1.05, 1.13, 1.24 and 1.29 with respectively for x=0.00, 0.05, 0.1, 0.2 and 0.25. The average values of T_C computed from T_{C1} and T_{C2} are 290, 274, 265, 243 and 233 K respectively for x=0.00, 0.05, 0.1, 0.2 and 0.25. The critical point exponent δ [90], derived from the Widom scaling equation (4.9) is found as δ_{KF} = 3.31, 3.38, 3.64, 4.1 and 4.21, respectively for x=0.00, 0.05, 0.1, 0.2 and 0.25.

Table 4.3 shows comparison of the critical point exponents calculated using the modified Arrott plot and Kouvel-Fisher methods for all of the studied samples. The well agreement between modified Arrott plot and Kouvel-Fisher methods confirms that the calculated critical exponents' values are reliable. Two separate methods modified Arrott plot and Kouvel-Fisher confirm the exact calculation of the critical point exponents of various $Pr_{0.55}Ca_xSr_{0.45-x}MnO_3$ compounds. The calculated critical exponents using the mean field model are not exactly equal to those of the mean field theory model. This result reveals complex magnetic behavior in the investigated samples. The derived β and γ values locate between those of the mean field and 3-D Heisenberg model. However with increase in Ca content the critical exponent values shifted toward those of 3-D Heisenberg model which belongs to magnetic system of short range ferromagnetic order. This means Ca doping does not favor long range FM order in

$Pr_{0.55}Ca_xSr_{0.45-x}MnO_3$ and A-site size disorder can break the long-range ferromagnetic ordering into short range magnetically ordered clusters.

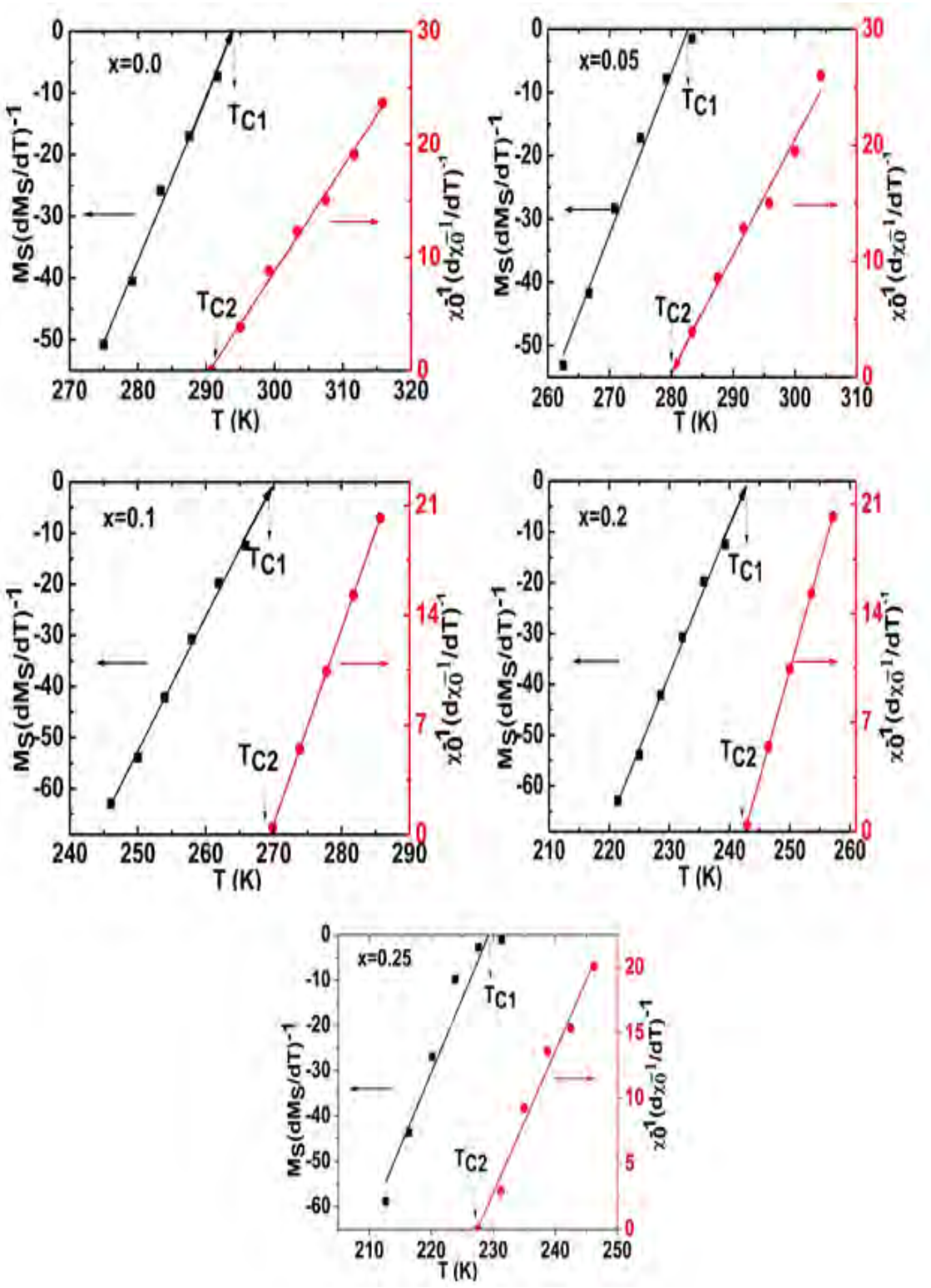

Fig. 4.13 $M_S(T)[\frac{dM_S(T)}{dT}]^{-1}$ vs T for below T_C and $\chi_0^{-1}(T)[\frac{d\chi_0^{-1}(T)}{dT}]^{-1}$ vs T for above T_C.

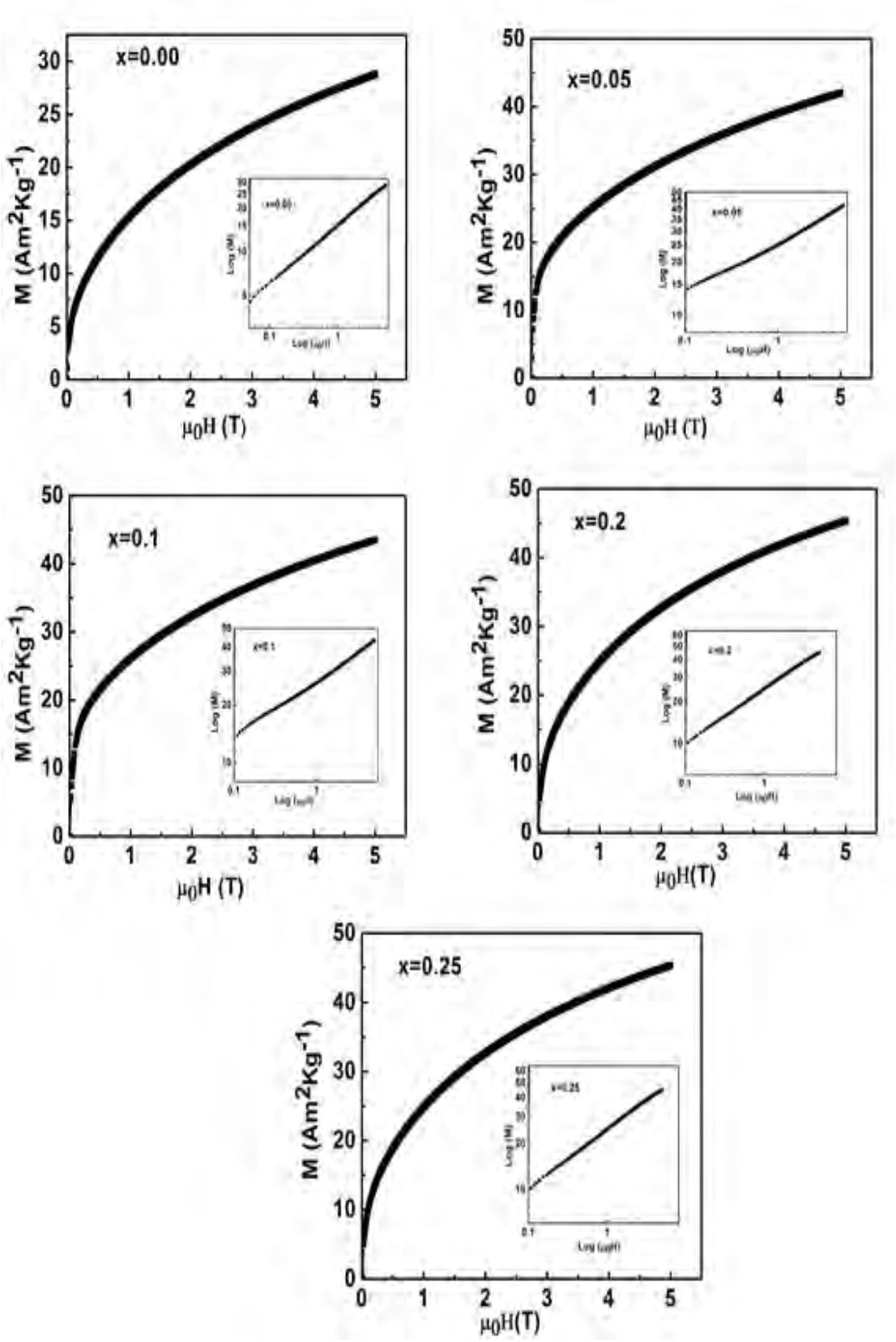

Fig. 4.14 M-H curve at T_C, inset: Corresponding logM vs logH plot of various $Pr_{0.55}Ca_xSr_{0.45-x}MnO_3$ compounds.

The exponent δ can also be calculated from the critical isotherm analysis [96] at T= T_C using equation (4.8). Fig. 4.14 represents M-H curves at T_C and inset shows the corresponding logM vs logH plot which shows linear behavior according to equation (4.8) with a slope of $(1/\delta)$ and therefore δ_{CIA} is found to be equal 3.09, 3.15, 3.23, 3.30 and 3.35 for x=0.00, 0.05, 0.1, 0.2 and 0.25, respectively. The value of exponent δ determined from the Widom scaling relation [90] are found very close to the value calculated from the critical isotherms. These results confirm that the calculated critical exponents and T_C values are self-consistent and reliable.

4.1.5 Magnetocaloric properties

Three important parameters are well known for identifying suitable magnetocaloric materials to be used as magnetic refrigerants. Those are ΔT_{ad}, ΔS_M, and RCP. ΔT_{ad} is not easy to measure experimentally, but ΔS_M can be determined using the Maxwell equation from isothermal M–H data. Another important parameter is RCP that depends on the value of $(-\Delta S_M)_{max}$ and its FWHM, which are controlled by the order of magnetic phase transition. Thus, an essential characteristic of a magnetic material as magnetic refrigerant is large magnetic entropy change.

The ΔS_M is maximized around the FM-PM transition temperature and its value depends on the applied field [90, 94]. The ΔS_M values of a magnetic material have been derived from the isothermal M-H data taken around T_C using the Maxwell's thermodynamic relation [97] as given below:

$$\Delta S_M = \int \left(\frac{\partial M}{\partial T}\right)_H \, dH \qquad (4.12)$$

Both temperature and magnetic field dependence of magnetic entropy change of the investigated samples have been calculated from the isothermal magnetization data using equation (4.12).

Fig. 4.15 represents the ΔS_M as a function of temperature and magnetic field. The values of ΔS_M were found to be negative and for convenience $-\Delta S_M$ vs T was plotted. The $-\Delta S_M$ of synthesized $Pr_{0.55}Ca_xSr_{0.45-x}MnO_3$ varies with temperature change and reaches its maximum value around their respective FM to PM transition temperature where the change of magnetization is maximum. The $(-\Delta S_M)_{max}$ of $Pr_{0.55}Ca_xSr_{0.45-}$

$_xMnO_3$ at different constant field are listed in Table 4.4. It is also observed that the $-\Delta S_M$ vs T curves are gradually broadened and $(-\Delta S_M)_{max}$ is increased with increase of applied field due to change in spin ordering process in the sample [36]. The $(-\Delta S_M)_{max}$ values are found as 2.83, 3.0, 3.1, 3.51, 4.05 $JKg^{-1}K^{-1}$ under a field change $\Delta H=5$ T and 1.87, 1.95, 1.97, 2.34 and 2.56 $JKg^{-1}K^{-1}$ for $\Delta H=2$ T for samples with x=0.00, 0.05, 0.1, 0.2, and 0.25, respectively. The variation in $(-\Delta S_M)_{max}$ can be correlated with increase of saturation magnetization as shown in Fig. 4.8 and sharper the FM-PM transition (Fig. 4.6 (a)) with increase in Ca content. As a results $(-\Delta S_M)_{max}$ is found to be increased with increase in Ca content in $Pr_{0.55}Ca_xSr_{0.45-x}MnO_3$ since entropy change is proportional to dM/dT [97]. Similar trend of entropy change are found in [42, 43].

Fig. 4.16 (a) shows $-\Delta S_M$ as a function of temperatures for different Ca value under a magnetic field change of 2 T for various $Pr_{0.55}Ca_xSr_{0.45-x}MnO_3$ compounds. This curve presents, as previously described, the T_C decreases but $-\Delta S_M$ increases with increase in Ca content. Working temperature for this series of samples is 180 to 320 K which is very expected for room temperature magnetic refrigerant material. This working temperature makes the materials as promising candidate for room temperature magnetic refrigeration. From this figure, the magnetocaloric properties of Ca doped $Pr_{0.55}Sr_{0.45}MnO_3$ manganite can be modulated by substituting Sr^{2+} with Ca^{2+} ions. Fig. 4.16 (b) represents $-\Delta S_M$ as a function of μ_0H for different Ca content at temperature T_C, which demonstrates that the rate of variation of maximum entropy change becomes slower with increase in applied field change for all the composition and agreed with the observation in other polycrystalline perovskite reported by [98, 99].

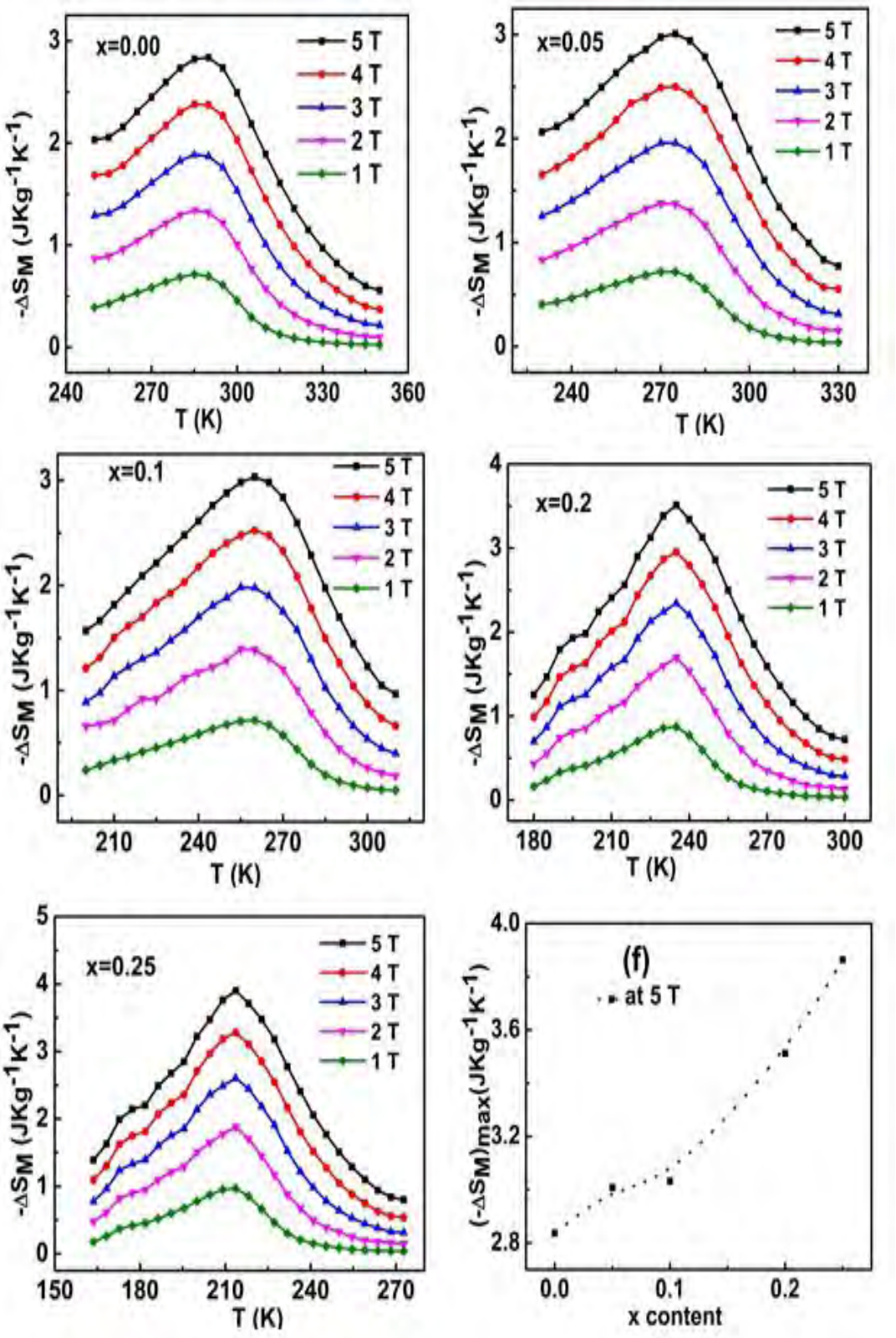

Fig. 4.15 (a) to (e) $-\Delta S_M$ vs T curves for different applied field, (f) $(-\Delta S_M)_{max}$ vs x content for $Pr_{0.55}Ca_xSr_{0.45-x}MnO_3$ compounds.

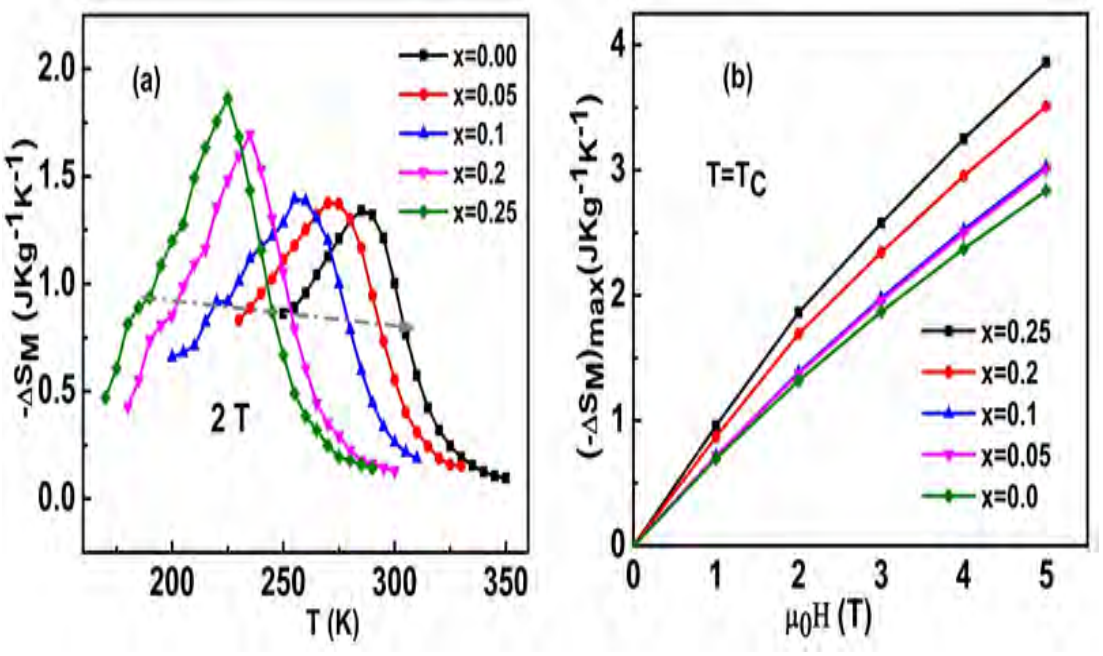

Fig. 4.16 (a) $-\Delta S_M$ vs T, (b) $(-\Delta S_M)_{max}$ vs $\mu_0 H$ at T_C for different x values for the sample $Pr_{0.55}Ca_xSr_{0.45-x}MnO_3$.

In order to investigate the origin of MCE, the experimental result of MCE was modulated with Landau theory of phase transition. Isothermal magnetic entropy can be calculated by differentiation of magnetic Gibbs free energy with respect to temperature [98]. Therefore, entropy change is found as

$$S_M(T,H) = -\frac{1}{2}\frac{\partial A}{\partial T}M^2 - \frac{1}{4}\frac{\partial B}{\partial T}M^4 \qquad (4.13)$$

Then, the theoretical magnetic entropy change becomes

$$\Delta S_M(T,H) = S_M(T,0) - S_M(T,H)$$
$$= -\frac{1}{2}\frac{\partial A}{\partial T}(M_0^2 - M^2) - \frac{1}{4}\frac{\partial B}{\partial T}(M_0^4 - M^4) \qquad (4.14)$$

Where, $S_M(T,0)$= magnetic entropy in zero field and M_0=magnetization in zero field and it can be estimated by extrapolating the magnetization to H=0. Comparison between theoretical and experimental results for the samples with x=0.0 has been shown in Fig. 4.17 where the open circle represents the theoretical magnetic entropy change calculated by using equation (4.14) and solid line represents the experimental magnetic entropy change calculated by using equation (4.12). The theoretical and experimental curves almost overlap with each other in FM region while those deviate from each other

at PM region. It is also observed that the temperature of $(-\Delta S_M)_{max}$ for theoretical curve is lower than that in the experimental curves. The experimental values of ΔS_M are calculated using the Maxwell's thermodynamic relation [66] where

$$\Delta S_M(T, H) = \Delta S_1(M) + \Delta S_2(E) + \Delta S_3(C) \quad (4.15)$$

Here, $\Delta S_1(M)$ is the net magnetic entropy change, $\Delta S_2(E)$ is the entropy change of electron and $\Delta S_3(C)$ is the entropy change of crystal lattice which remains constant for isothermal process. The experimental entropy change involves with first two parts where theoretical entropy change involves only first part. Thus, the entropy change of electron is the main reason for the deviation of two curves in the paramagnetic region.

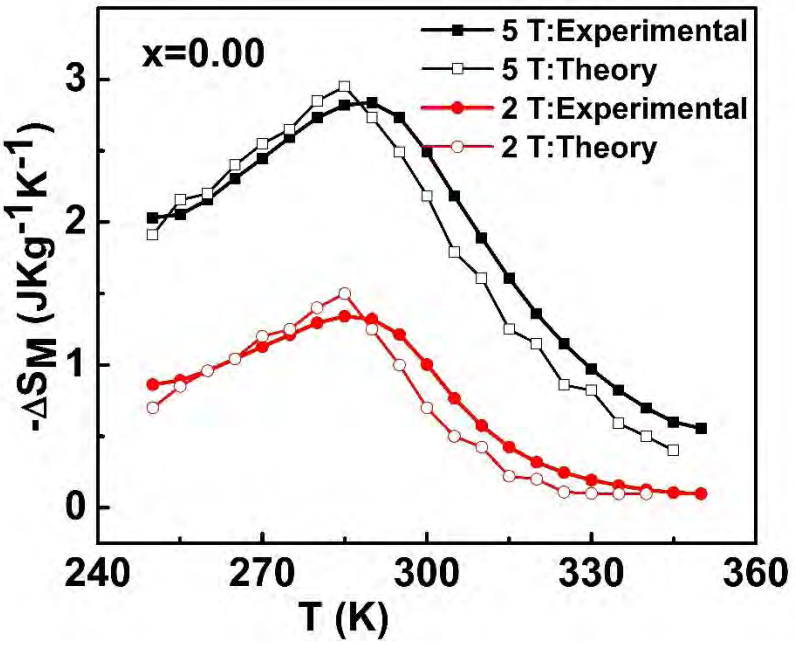

Fig. 4.17 $-\Delta S_M$ vs T for both theoretical and experimental values for the sample with x=0.00.

MCE of the studied samples was also calculated in terms of RCP which is defined as the amount of heat transferred between the cold and hot sinks in the refrigeration cycle and can be calculated using the following formula [100] and tabulated in Table 4.4:

$$RCP = (-\Delta S_M)_{max} . \delta T_{FWHM} \quad (4.16)$$

Here, δT_{FWHM} = full width at half maximum of the $-\Delta S_M$ vs T curve [41]. δT_{FWHM} is considered as the temperature limit within which the material may be used for refrigeration applications [101]. RCP is another important property of a magnetic

material to be used in magnetic refrigerator. It is seen that RCP value increases for our samples with the increase in Ca content. The RCP values are 196, 213, 217, 225 and 232 J/Kg for ΔH=5 T and 82, 88, 90, 99, 108 J/Kg for ΔH=2 T for the samples with x = 0.00, 0.05, 0.1, 0.20 and 0.25, respectively. Again both RCP and δT_{FWHM} increases uniformly with increase in applied field.

Table 4.4 T_C, $(-\Delta S_M)_{max}$ and RCP of $Pr_{0.55}Ca_xSr_{0.45-x}MnO_3$ polycrystal.

x content	T_C (K) from dM/dT	T_C (K) from Arrott plot	$(-\Delta S_M)_{max}$ $JKg^{-1}K^{-1}$ for ΔH= 2 T	$(-\Delta S_M)_{max}$ $JKg^{-1}K^{-1}$ for ΔH= 5 T	RCP (J/Kg) for ΔH= 2 T	RCP (J/Kg) for ΔH= 5 T
0.00	290	290	1.87	2.83	82	196
0.05	286	280	1.95	3.0	88	213
0.1	270	270	1.97	3.1	90	217
0.2	245	240	2.34	3.51	99	225
0.25	230	230	2.56	4.05	108	232

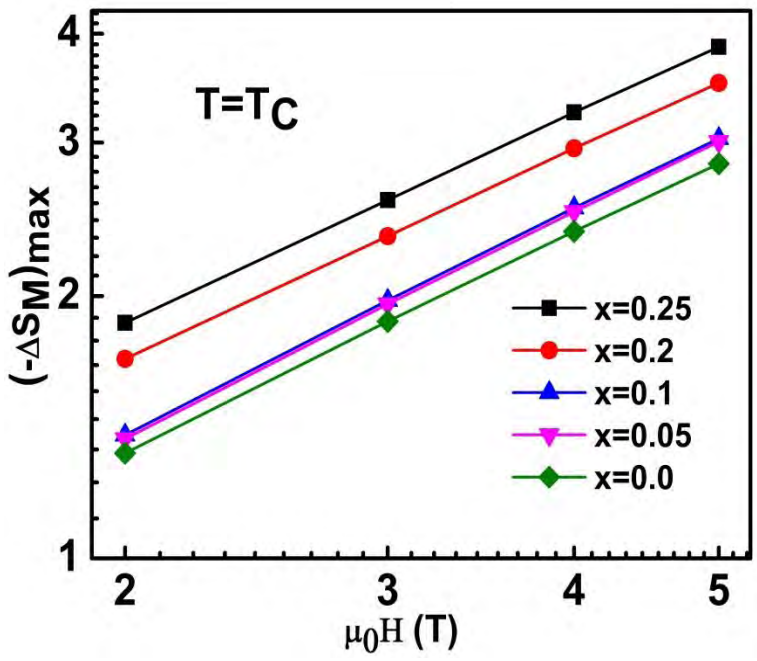

Fig. 4.18 Log-log plot of $(-\Delta S_M)_{max}$ vs $\mu_0 H$ for different x values of $Pr_{0.55}Ca_xSr_{0.45-x}MnO_3$ compounds.

Relation between the critical behavior and the magnetocaloric effect was also investigated in terms of scaling exponent 'n'. The dependence of $(-\Delta S_M)_{max}$ on applied magnetic field for the material with second order magnetic transition is expressed as a scaling law given bellow [102]:

$$(\Delta S_M)_{max} \propto \mu_0 H^n \quad (4.17)$$

Here, 'n' is the scaling exponent for magnetic field dependence of the maximum entropy change. For determining the exponent 'n' using Eq. (4.17), the $(-\Delta S_M)_{max}$ and $\mu_0 H$ values are re-plotted as $\log(-\Delta S_M)_{max}$ vs $\log(\mu_0 H)$. Fig. 4.18 represents log-log plot of $(-\Delta S_M)_{max}$ as a function of $\mu_0 H$ for different Ca content of various $Pr_{0.55}Ca_xSr_{0.45-x}MnO_3$ compounds. The slope of the linear fit of $\log(-\Delta S_M)_{max}$ vs $\log(\mu_0 H)$ gives the value of n=0.679, 0.702, 0.713, 0.611 and 0.612 for x=0.00, 0.05, 0.1, 0.2 and 0.25, respectively.

Table 4.5 Theoretical values of n for all four models.

Model	Method	n
Mean field model	Theory	0.67
3-D Heisenberg model	Theory	0.63
3-D Ising model	Theory	0.57
Tri-critical mean field model	Theory	0.4

The relation between n and the critical point exponent β and γ can be expressed as [103].

$$n = 1 + \frac{\beta - 1}{\beta + \gamma} \quad (4.18)$$

n_{MAP} and n_{KF} are found from above equation (4.18) using the critical point exponent β and γ calculated from the modified Arrott plot and Kouvel-Fisher methods. The n_{MAP} is found 0.681, 0.688, 0.665, 0.631 and 0.625 and n_{KF} is found 0.678, 0.679, 0.676, 0.641 and 0.632 for x = 0.00, 0.05, 0.1, 0.2 and 0.25, respectively. It was found that $n_{MAP} \approx n_{KF} \approx n$. Comparing theoretical and experimental values the derived scaling exponent n is found very close to that of the mean field model for x=0.0, 0.05 and 0.1 while it is

close to that of the 3D Heisenberg model for x=0.2 and 0.25. The derived n values also disclose that increasing amount of Ca doping does not favor long range FM order in $Pr_{0.55}Ca_xSr_{0.45-x}MnO_3$.

4.1.6 Summary

The investigated samples $Pr_{0.55}Ca_xSr_{0.45-x}MnO_3$ (x = 0.00, 0.05, 0.1, 0.2 and 0.25.) have been prepared by the conventional solid-state reaction technique. Their structural, morphological, chemical compositional, temperature and magnetic field dependent magnetic properties, critical behavior around transition temperature, magnetocaloric properties in terms of magnetic entropy change and relative cooling power have been investigated. Relation between the critical exponents near the FM to PM phase transition temperature and the observed magnetocaloric behavior has also been elucidated. Room temperature XRD analysis has confirmed the orthorhombic structure of all the samples with Pnma space group. The lattice parameters a, b and c as well as the cell volume and Mn-O-Mn bond angle decreases with increase in Ca content. The replacement of larger size Sr^{2+} ions by smaller Ca^{2+} ions changes the lattice parameters which affect magnetocaloric properties of the samples. The samples are porous and appear at different polygonal forms. Both the grain size and grain-boundary effect decreases with increase in Ca content. The chemical composition of $Pr_{0.55}Ca_xSr_{0.45-x}MnO_3$ normalized to 100 wt% was calculated from the EDX data and the calculated values were in well agreement with the experimental values. The small anomaly between calculated and expected compositions may have arisen from scattering effect due to some possible porosity in the sample. All the samples undergo PM to FM phase transition upon cooling. The divergence between FC and ZFC curve reveals the existence of AFM and FM clusters in the investigated samples. Curie temperature decreases from 290 to 230 K with increase in Ca content from 0.00 to 0.25, respectively. The Arrott plots confirm second-order nature of the FM to PM phase transitions for all the samples. The variation in magnetic behavior was also observed as the sample undergoes FM to PM phase with increase in temperature. The critical exponents of various $Pr_{0.55}Ca_xSr_{0.45-x}MnO_3$ compounds have been calculated using various methods such as modified Arrott plot, Kouvel–Fisher method and critical isotherm analysis. The well agreement among the methods confirms that the calculated

values of the critical exponents are reliable. The calculated critical exponents using the mean field model are not exactly equal to those of the mean field theory model. This result reveals complex magnetic behavior in the investigated samples. The derived critical exponent values locate between those of the mean field and 3-D Heisenberg model. The acceptance of the mean field model explains the existence of long range FM interactions in the studied samples. However with increase in Ca content the critical exponent values shifted toward those of 3-D Heisenberg model which belongs to magnetic system of short range FM order. This means increasing amount of Ca doping does not favor long range FM order in $Pr_{0.55}Ca_xSr_{0.45-x}MnO_3$. The $-\Delta S_M$ of synthesized samples varies with temperature change and reaches its maximum value around their respective FM to PM transition temperature where the change of magnetization is maximum. The $(-\Delta S_M)_{max}$ values are 2.83, 3.0, 3.1, 3.51 and 4.05 $JKg^{-1}K^{-1}$, for samples with x=0.00, 0.05, 0.1, 0.2 and 0.25, respectively under a field change ΔH=5 T and 1.87, 1.95, 1.97, 2.34 and 2.56 $JKg^{-1}K^{-1}$ for ΔH=2 T. The derived scaling exponent n is also found to be close to that of the mean field model for x=0.0, 0.05 and 0.1 while it is close to that of the 3D Heisenberg model for x=0.2 and 0.25. The RCP values are 196, 213, 217, 225 and 232 J/Kg for ΔH=5 T and 82, 88, 90, 99 and 108 J/Kg for ΔH=2 T for the samples with x = 0.00, 0.05, 0.1, 0.2 and 0.25, respectively. Working temperature for this series of samples is 180 to 320 K which cover the room temperature. Therefore the sample $Pr_{0.55}Ca_xSr_{0.45-x}MnO_3$ could be used as good solid state refrigerant for magnetic refrigeration from room temperature to below room temperature.

4.2 Characterization of $La_{0.55}Ca_xSr_{0.45-x}MnO_3$ (x=0.0, 0.05, 0.1, 0.2 and 0.25) Perovskite

4.2.1 X-ray diffraction analysis

Fig. 4.19 (a) represents room temperature XRD patterns of various $La_{0.55}Ca_xSr_{0.45-x}MnO_3$ compounds taken from 2θ=10 to 80°. All the patterns possess identical characteristic peaks and those are marked with miller indices. Fig. 4.19 (b) shows main peaks of XRD pattern of different $La_{0.55}Ca_xSr_{0.45-x}MnO_3$ compounds. The splitting of these main peaks indicates the possibility of being rhombohedral structure of the studied samples. The shift of the XRD peaks towards greater angles demonstrates the decrease of the lattice parameters in the prepared samples with the increase in Ca content.

Crystal structure analysis based on the Rietveld method using 'Full Prof' software reveals that all of the samples are observed to be crystallized in rhombohedral structure with R-3c space group. Fig. 4.20 shows Rietveld patterns of the studied samples where the graph shows well agreement between the observed and calculated values. The small values of the fit indicator χ^2, weighted parameter R_{wp}, and the pattern R_p indicate the good quality of the refinement (Table 4.6). It is found that all the samples are in single phase and no impurities were detected within the measurement range. The structural refinement was carried out in the hexagonal setting of the rhombohedral *R*-3*c* space group (number 167). Lattice parameters a and c as well as cell volume (tabulated in Table 4.6 and shown in Fig. 4.21 (a)) are found to be decreased with increasing Ca content because of replacement of larger size Sr^{2+} (r_A~1.32 Å) ion by smaller Ca^{2+} (r_A~1.18 Å) ion [104].

The crystallite size has been calculated from Debye- Scherer equation [105]. For getting the information about the deviation from the ideal cubic perovskite structure tolerance factor is measured from the ionic radii of the lattice sites using equation as defined by Goldschmidt [76] as given in equation (4.1). The average A-site ionic radius for this series of samples is determined from $< r_A >= 0.55 < r_{La^{3+}} > + x < r_{Ca^{2+}} > + (0.45 - x) < r_{Sr^{2+}} >$. The average A-site ionic radius, $< r_A >$, as well as tolerance factor decreases gradually from the sample with x=0.00 to sample x=0.25. As t decreases from 1, the lattice structure transforms to the rhombohedral structure for 0.96<t<1 and then to the orthorhombic structure for t<0.96 [77]. Thus the decrease in t

reduces the geometrical stability of $La_{0.55}Ca_xSr_{0.45-x}MnO_3$ with increase in Ca content. Thus Jahn-Teller distortion appears [106]. Mn-O-Mn bond angle was also found to decrease with increasing Ca content (as shown in Fig. 4.21 (b)). Substitution of larger Sr^{2+} for smaller Ca^{2+} creates a void between MnO_6 octahedra which generate extra chemical pressure resulting reduction of Mn-O-Mn bond angles from the ideal 180° [97]. These structural changes will affect the magnetic and magnetocaloric properties of the samples.

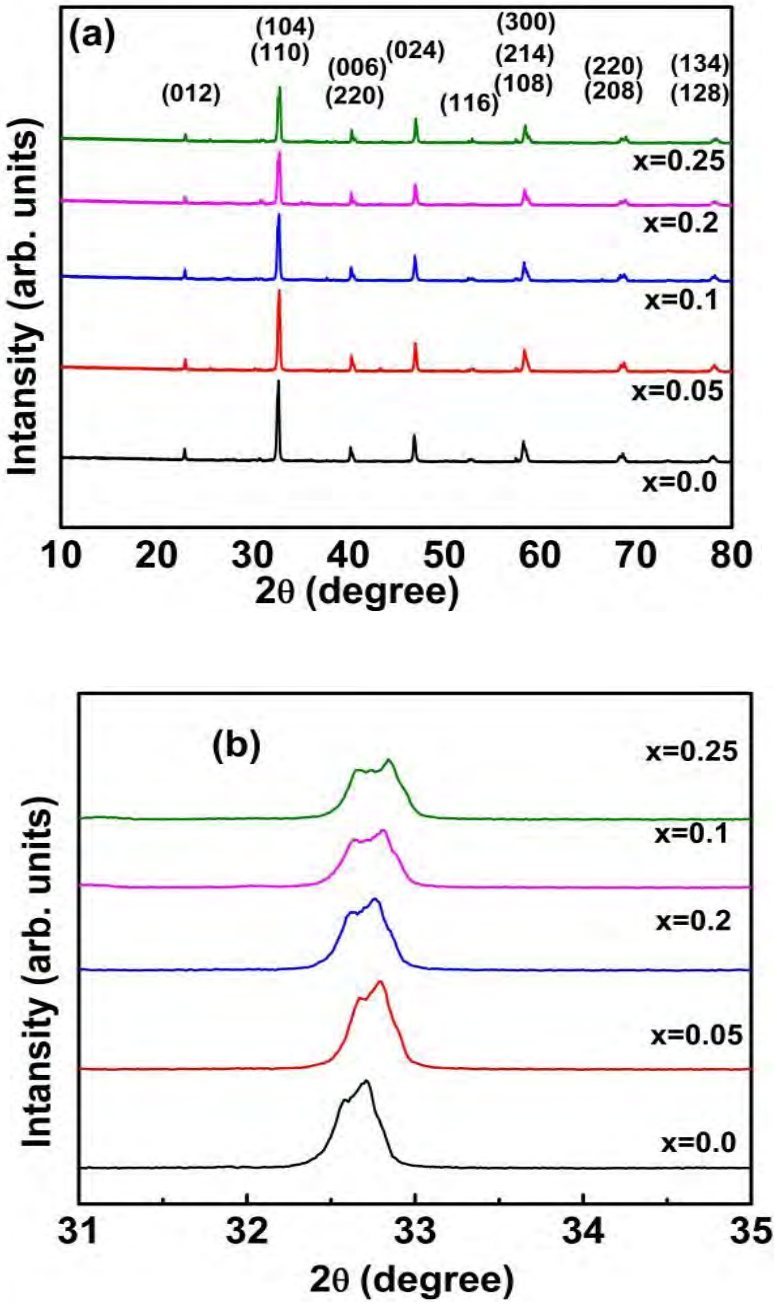

Fig. 4.19 (a) XRD patterns and (b) main peaks of XRD pattern of different $La_{0.55}Ca_xSr_{0.45-x}MnO_3$ compounds.

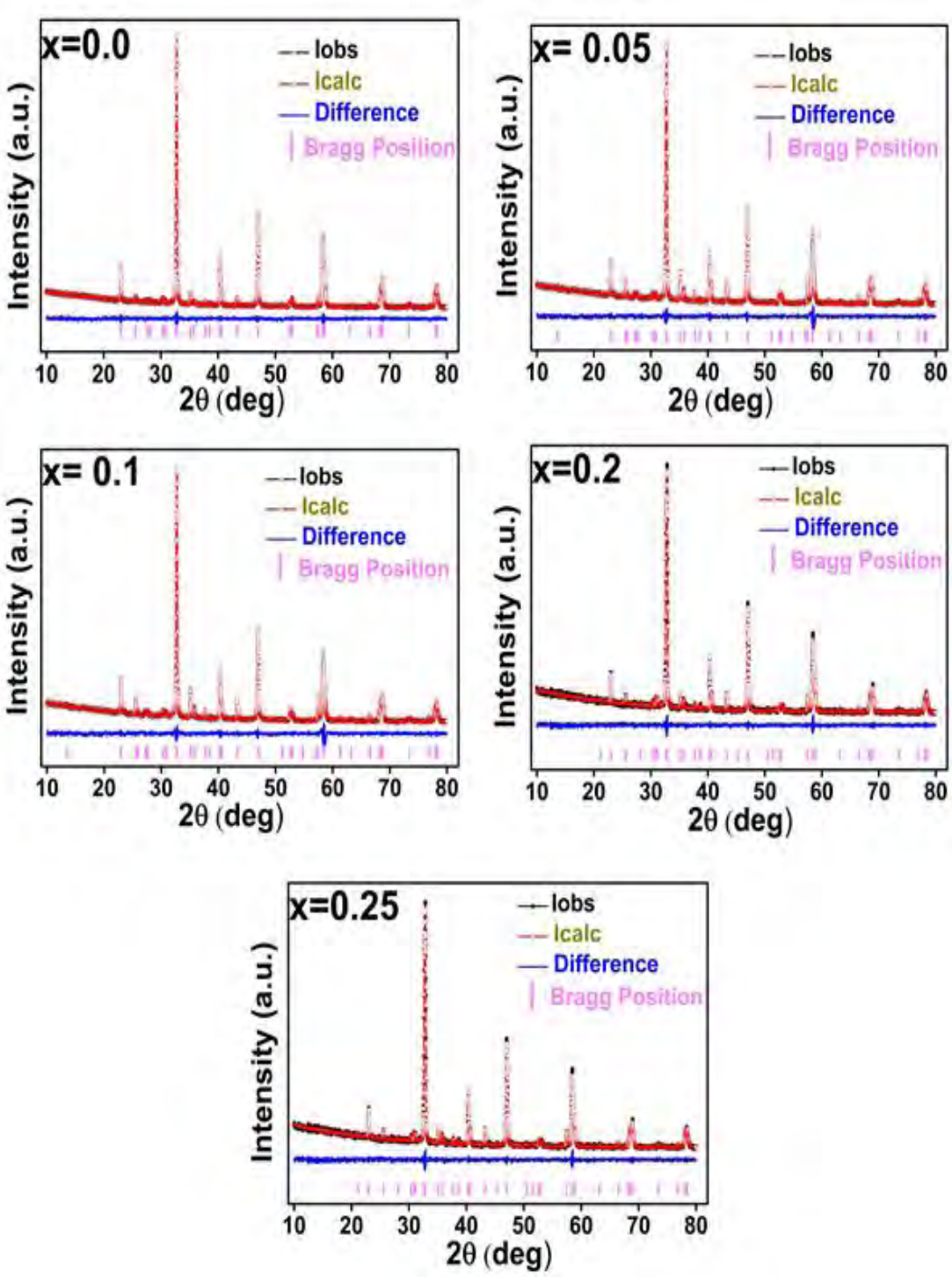

Fig. 4.20 Rietveld refinement of the XRD patterns for various $La_{0.55}Ca_xSr_{0.45-x}MnO_3$ compounds.

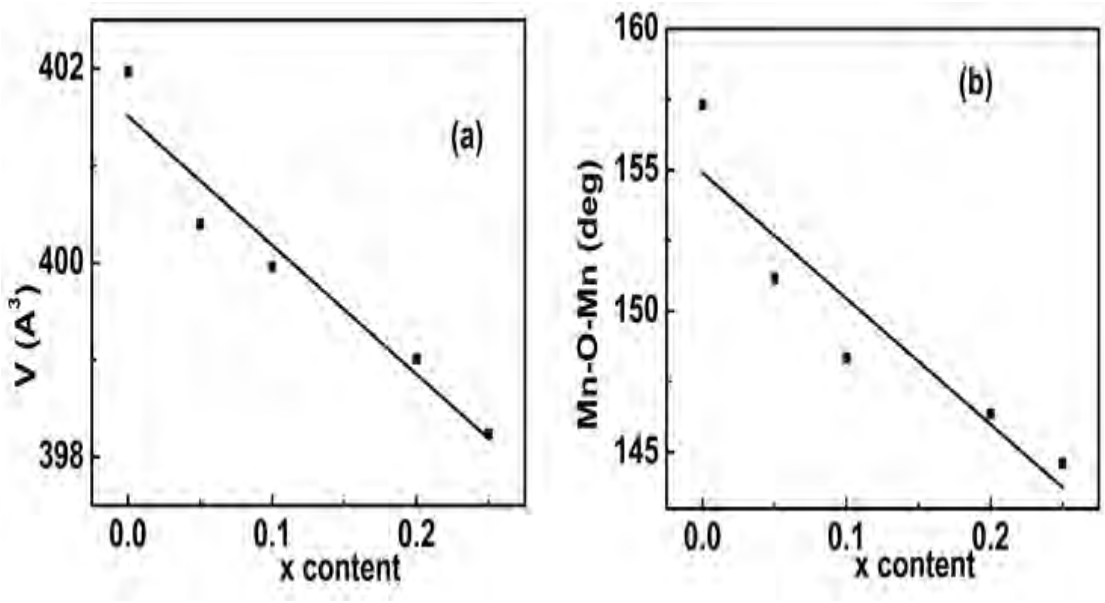

Fig. 4.21 (a) Cell volume vs x content, (b) Mn-O-Mn bond angle vs x content for $La_{0.55}Ca_xSr_{0.45-x}MnO_3$ compounds.

Table 4.6 Lattice parameters, cell volume (V), t, R_p, R_{wp}, χ^2, Mn-O-Mn bond angle and Grain size (D) of $La_{0.55}Ca_xSr_{0.45-x}MnO_3$ perovskite.

x content	System	a = b (Å)	c (Å)	V (Å^3)	t	R_p	R_{wp}	χ^2	Mn-O-Mn(deg)	D (μm)
0.00	rhombohedral	5.4855	13.3583	401.97	0.8924	3.0	5.2	2.7	157.31	0.51
0.05	rhombohedral	5.4784	13.3411	400.40	0.8860	2.9	5.1	2.6	151.15	0.43
0.1	rhombohedral	5.4780	13.3285	399.96	0.880	2.8	4.9	2.7	148.33	0.42
0.2	rhombohedral	5.4752	13.3102	399.01	0.871	2.9	5.1	2.7	146.56	0.45
0.25	rhombohedral	5.4724	13.2978	398.24	0.869	2.9	5	2.8	144.61	0.41

4.2.2 Microstructure observation

Fig. 4.22 shows the FESEM images which reveal that the microstructures are dependent on the composition of the compound $La_{0.55}Ca_xSr_{0.45-x}MnO_3$. The sample contains homogeneous distribution of small particles with clear grain boundary. It is also observed that the samples are porous and appear at different polygonal forms. Some particles are agglomerated. There are some large particles with sizes up to 1 μm. The average grain size was estimated by using 'ImageJ' software. After measuring the diameters of all the grains in FESEM image, the data are plotted as a histogram (as shown in Fig. 4.23) with Lauretz fitting to evaluate the average grain size (Table 4.6). The average grain size decreases slightly with increase in Ca content in $La_{0.55}Ca_xSr_{0.45-x}MnO_3$. It is observed that increasing amount of Sr substitution by Ca tends to hinder grain growth. This occurrence is attributed to the reduced diffusion rate due to the exchange of light Ca ions with heavy Sr ions since Sr is twice heavier than Ca [107]. Different surface morphologies are also observed for the samples depending on Ca content essentially due to large variation in the A-site average ionic radius. Thus Ca doping has great influence on microstructure of the compound $La_{0.55}Ca_xSr_{0.45-x}MnO_3$. Presence of the dispersed particles in form and size is also noticed. It may be produced due to the competition between the fracturing, cold welding, agglomeration and de-agglomeration of the powder particles during the ball milling.

4.2.3 Chemical composition analysis

The EDX spectrums of different $La_{0.55}Ca_xSr_{0.45-x}MnO_3$ compounds are presented in Fig. 4.24. No other elements except the elemental composition of the studied samples are seen in the spectrums. From the EDX data, the elemental composition of $La_{0.55}Ca_xSr_{0.45-x}MnO_3$ polycrystal normalized to 100 wt% was computed and the stoichiometrically calculated values were in well agreement with the experimental values. Table 4.7 shows the average amounts of La, Ca, Sr, Mn and O in the five samples, obtained from average values of three EDX spectra recorded at three different surface areas. The samples contain an excess amount of La and a lack of Mn. The Ca content is little bit high and Sr contents are also a little bit low compared to the expected values. However, it is clear that Ca and Sr content values are exchanged in an approximately linear manner, as expected composition. The anomaly between calculated and experimental compositions may be arisen due to an instrumental error since the EDX technique is not

very suitable for porous specimens [79]. According to FESEM images $La_{0.55}Ca_xSr_{0.45-x}MnO_3$ samples are quite porous. Due to scattering effects, porosities may influence on the X-ray peak intensities of the different elements in the sample, as well as on the relative distribution of elements obtained from the EDX spectra [108].

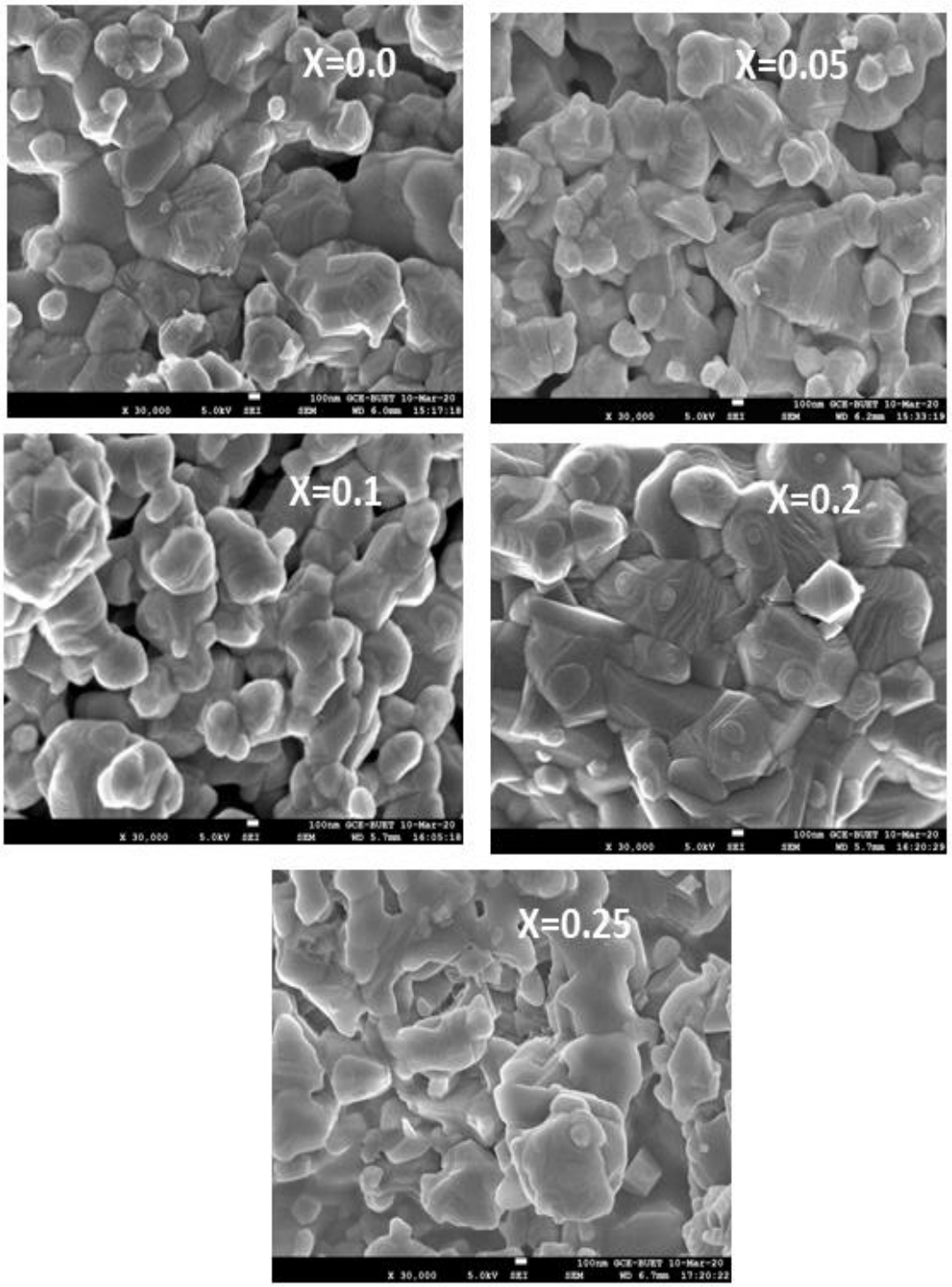

Fig. 4.22 FESEM images of the surface of different $La_{0.55}Ca_xSr_{0.45-x}MnO_3$ compounds.

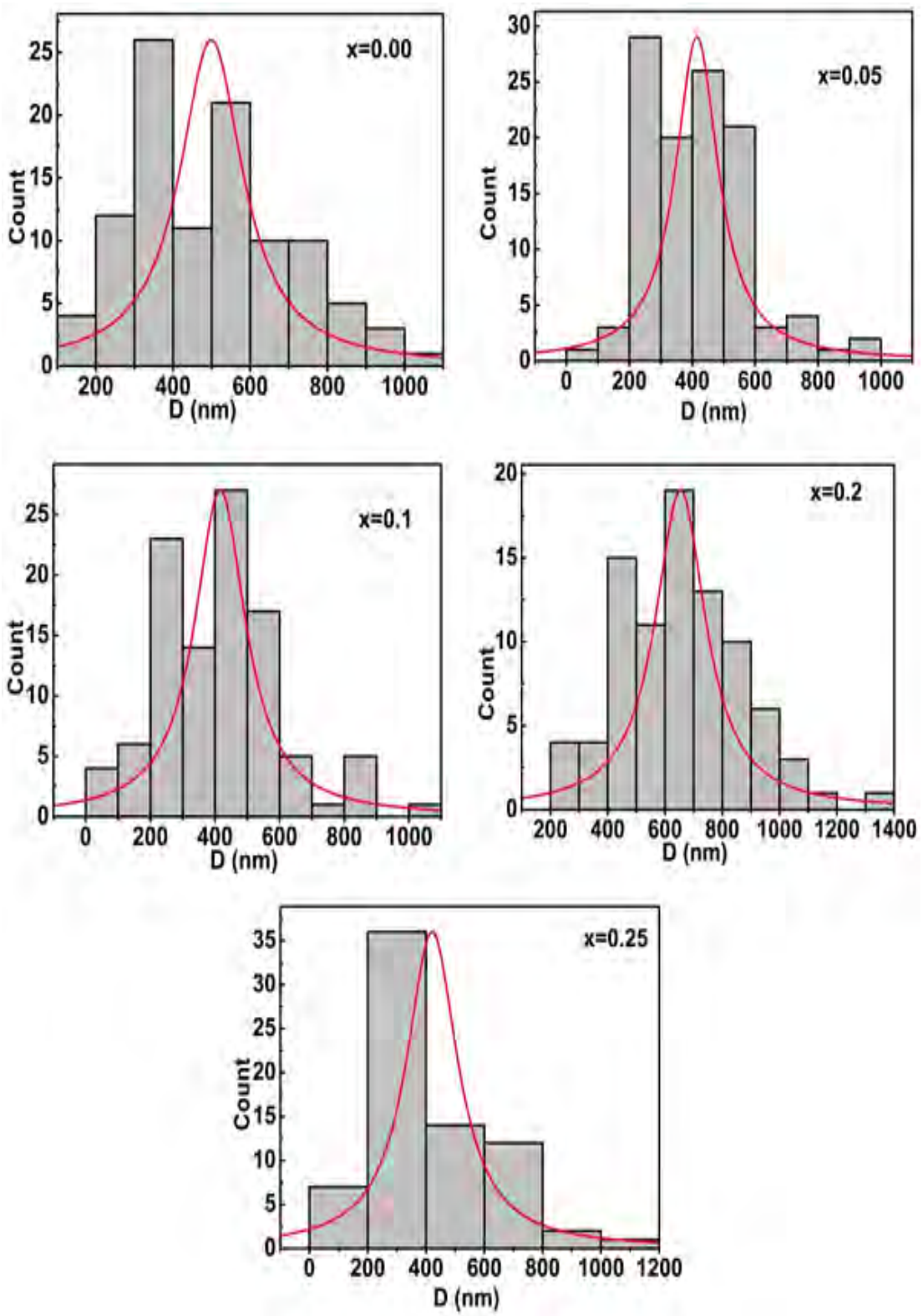

Fig. 4.23 Histogram for determination of grain size of $La_{0.55}Ca_xSr_{0.45-x}MnO_3$.

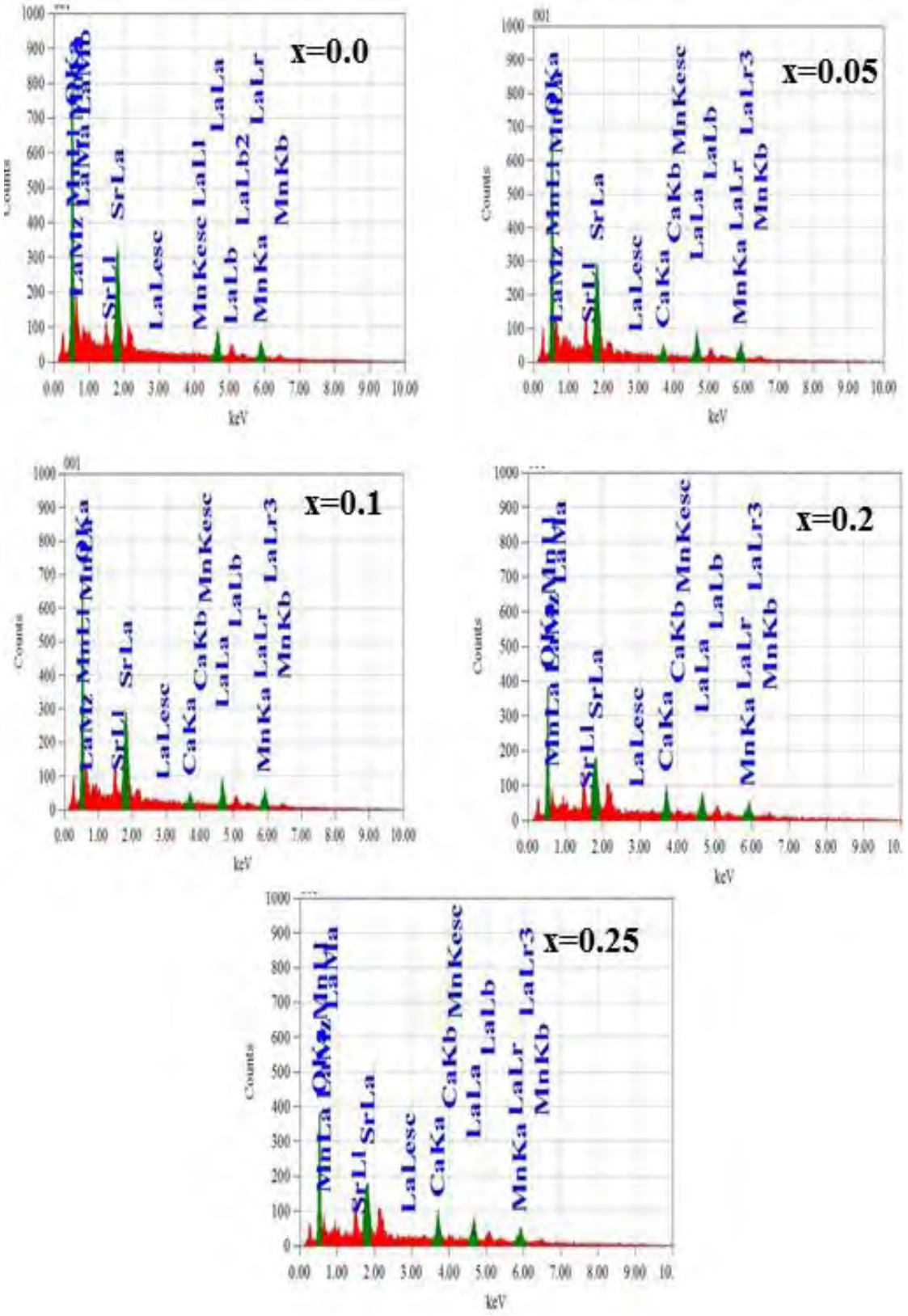

Fig. 4.24 EDX spectrum of different $La_{0.55}Ca_xSr_{0.45-x}MnO_3$ compounds.

Table 4.7 Elemental composition of different $La_{0.55}Ca_xSr_{0.45-x}MnO_3$ compounds in weight %.

		La	Ca	Sr	Mn	O
x=0.0	Calculated Weight%	34.92	……..	18.04	25.11	21.94
	Weight % from EDX spectrum	35.51	……	17.71	24.92	21.86
x=0.05	Calculated Weight%	35.31	0.93	16.19	25.39	22.18
	Weight % from EDX spectrum	34.69	1.07	16.32	25.67	22.43
x=0.1	Calculated Weight%	35.69	1.87	14.32	25.67	22.43
	Weight % from EDX spectrum	36.12	1.77	14.52	25.23	22.36
x=0.2	Calculated Weight%	36.51	3.83	10.47	26.25	22.94
	Weight % from EDX spectrum	36.7	3.87	10.32	25.69	23.42
x=0.25	Calculated Weight%	36.93	4.844	8.47	26.56	23.20
	Weight % from EDX spectrum	36.59	4.968	8.63	25.94	23.872

4.2.4 Magnetic properties

4.2.4.1 Temperature dependent magnetic properties

Fig. 4.25 (a) represents *dc* magnetization vs temperature curves taken at FC and ZFC process under application of a constant magnetic field of 0.01 T in temperature range 5–400 K for $La_{0.55}Ca_xSr_{0.45-x}MnO_3$ samples. With increase in temperature, magnetization in FC curve decreases gradually with a rapid fall to zero magnetization and enters into the paramagnetic phase (FM to PM phase transition) where the FM order of magnetic moments is destroyed by thermal energy. Sharp FM to PM phase transition of our compounds indicates high magnetic entropy change around T_C. It is also found that FC and ZFC magnetization curves deviates from each other at lower temperature known as irreversibility temperature which has been listed in Table 4.9. This divergence reveals the co-existence of AFM and FM clusters in the investigated samples [75]. This behavior is attributed to the competition between double exchange FM and super exchange AFM interactions at the grain boundaries and also the short-range ordering at grain boundary due to distorted crystal structure [75, 77]. Comparing the magnetizations in ZFC and FC modes of the samples, it is also observed that

magnetization at both modes decreases as Ca content increases due to decrease in double exchange interaction.

The T_C value is determined from the temperature at which the change in magnetization (dM/dT) is maximum. T_C has been calculated from dM/dT versus temperature curve as shown in Fig. 4.25 (b) where dM/dT was derived from FC magnetization curves. According to our experimental investigation T_C has decreased from 354 to 311 K with the increase in Ca content from 0.00 to 0.25 as shown in inset of Fig. 4.25 (b). This result indicates the influence of Ca doping in $La_{0.55}Ca_xSr_{0.45-x}MnO_3$. It is generally accepted that when the super exchange interaction dominates over the double exchange interaction, T_C is shifted towards the lower temperature. Substitution of Larger Sr^{2+} by smaller Ca^{2+} in this series of samples causes a reduction in the A-site average atomic radius, and tolerance factor which results a decrease in double exchange interaction. As a result T_C as well as maximum value of dM/dT decreases with increasing Ca content in $La_{0.55}Ca_xSr_{0.45-x}MnO_3$. This result agreed well with the reviewed previous publications on doped $La_{0.7}Ca_{0.3}MnO_3$ compounds, where substitution of Ca^{2+} by Ba^{2+}, Sr^{2+} or Pb^{2+} increases T_C due to increase in average ionic radius [56, 80, 101]. To determine the value of T_C we also used another method called Arrott plots. From Arrott plots T_C is found as 355, 340, 335, 320 and 310 K for the samples with x= 0.00, 0.05, 0.1, 0.2 and 0.25 (as shown in Fig. 4.28).

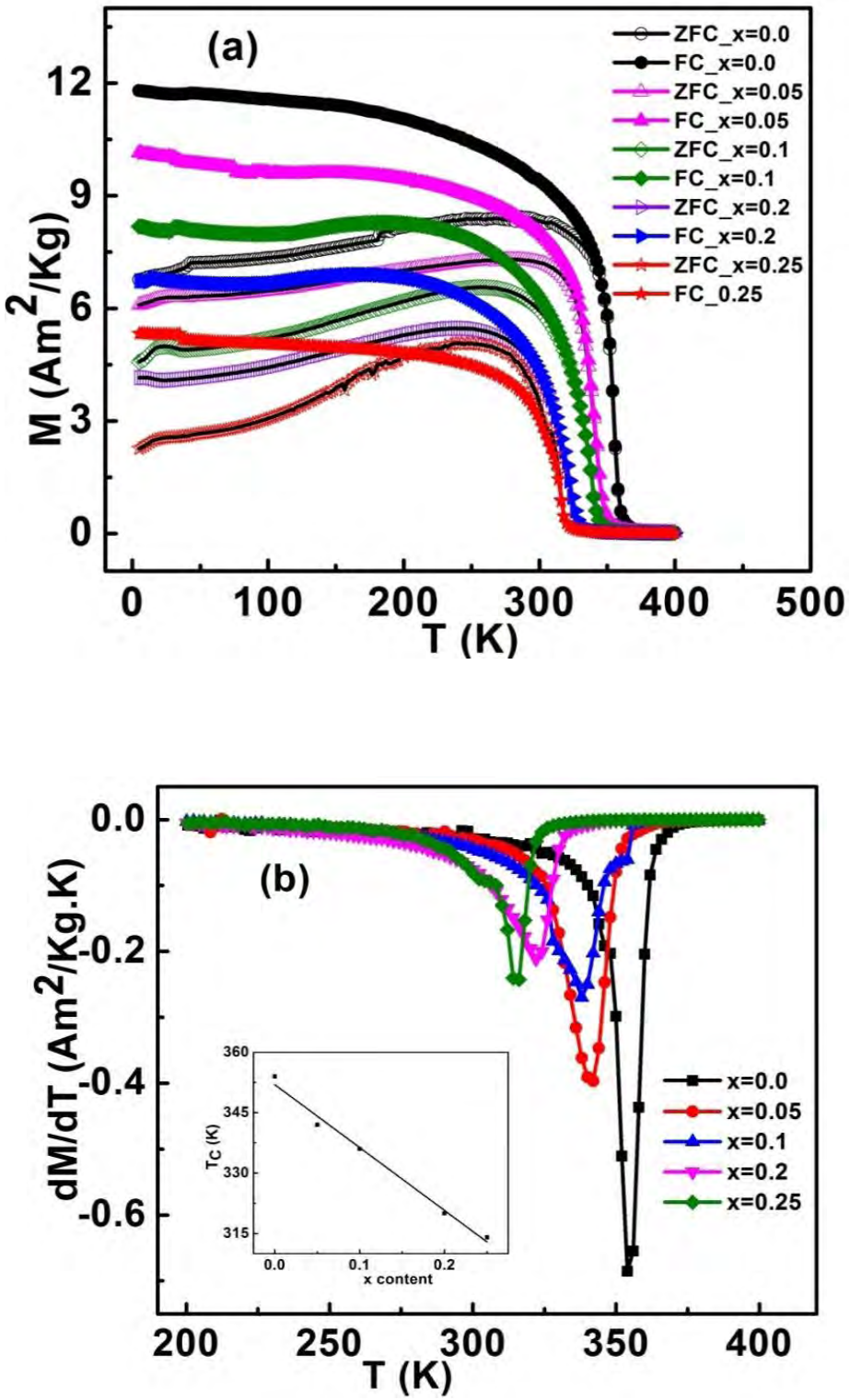

Fig. 4.25 (a) FC and ZFC magnetization curves at H=0.01 T, (b) dM/dT vs T curves, inset: T_C vs x content of various $La_{0.55}Ca_xSr_{0.45-x}MnO_3$ compounds.

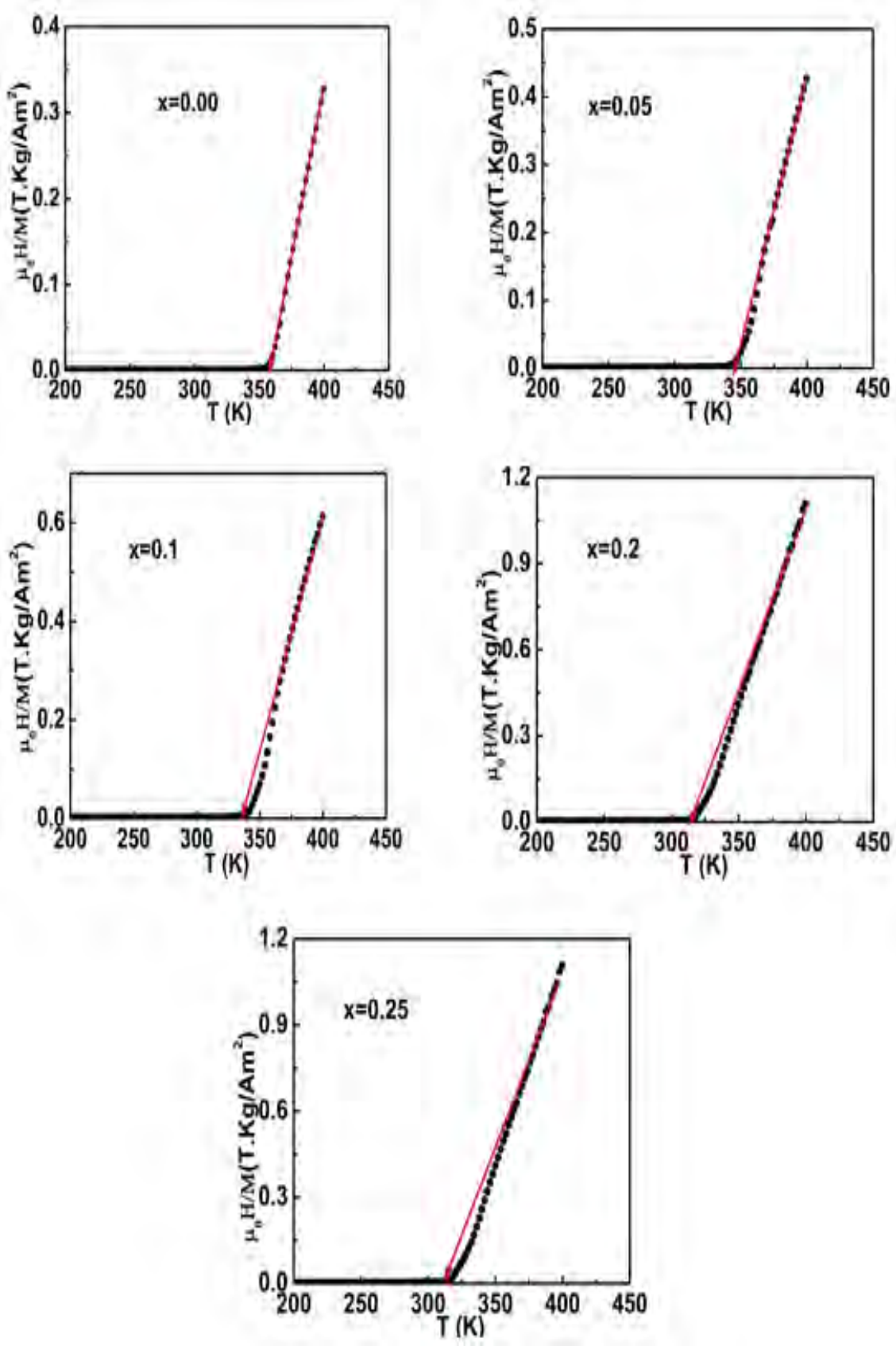

Fig. 4.26 1/χ vs T curves of different $La_{0.55}Ca_xSr_{0.45-x}MnO_3$ compounds at H=0.01 T.

The inverse magnetic susceptibility was determined from the FC magnetizations data taken in an applied magnetic field of 0.01 T. Fig. 4.26 shows 1/χ vs T curves for sample $La_{0.55}Ca_xSr_{0.45-x}MnO_3$. At temperature above T_C, the linear behavior of the susceptibility curve for the sample with x=0.00 indicates that the mean-field Curie–Weiss low is obeyed [83]. The paramagnetic Curie temperature is found from the extrapolation of linear part of 1/χ vs T curve to zero inverse magnetic susceptibility. It is also found that the values of paramagnetic Curie temperature are very close to T_C values. These results clearly explain the magnetic homogeneity of this sample above T_C [90]. But the difference between the μ_{eff}^{cal} and μ_{eff}^{exp} value indicates the existence of FM clusters in the PM phase. Where, the effective magnetic moment for x=0.00, calculated from Curie constant 'C' and the theoretical effective paramagnetic moment was calculated using the equation (4.2). For other samples, with increase in Ca content the 1/χ vs T curves deviate from linearity indicating presence of increasing amount of FM cluster in the PM region.

4.2.4.2 Magnetic field dependent magnetic properties

For investigating the magnetic field dependent magnetic properties and MCE of the samples, isothermal magnetizations were measured as a function of magnetic field ranging from 0-5 T at different constant temperatures in the vicinity of T_C with an interval of 5 K. To ensure isothermal process during the magnetization measurement, the sweep rate of the applied magnetic field was kept slow. Fig. 4.27 show isothermal magnetization curves of $La_{0.55}Ca_xSr_{0.45-x}MnO_3$ which reveal the change in magnetic behavior as the sample goes from PM to FM phase within the temperature range from 395 to 260 K. At temperature below T_C, all the curves show FM nature with sharp increase at low field and saturation at high field [104]. A rapid change in magnetization is seen around T_C. At temperatures above T_C, the curves show paramagnetic M-H behavior. It is also observed that saturation magnetization decreases with increase in Ca content from 0.00 to 0.25 due to decrease in double exchange interactions associated with decrease in Mn-O-Mn bond angle. Decrease in grain size with increase in Ca content may be also responsible for reduction of magnetic saturation with increase in Ca content.

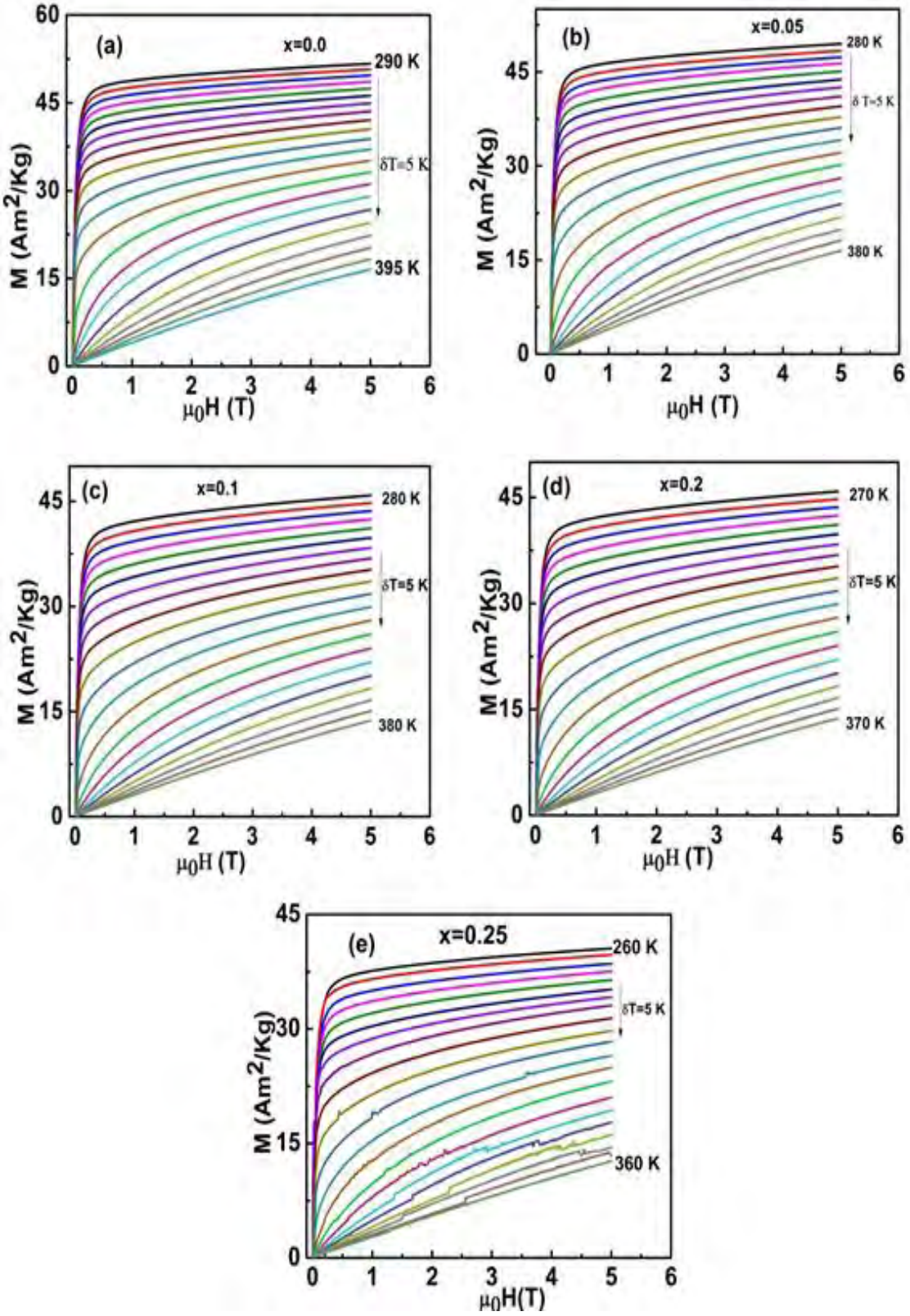

Fig. 4.27 Isothermal M-H curves of the samples $La_{0.55}Ca_xSr_{0.45-x}MnO_3$.

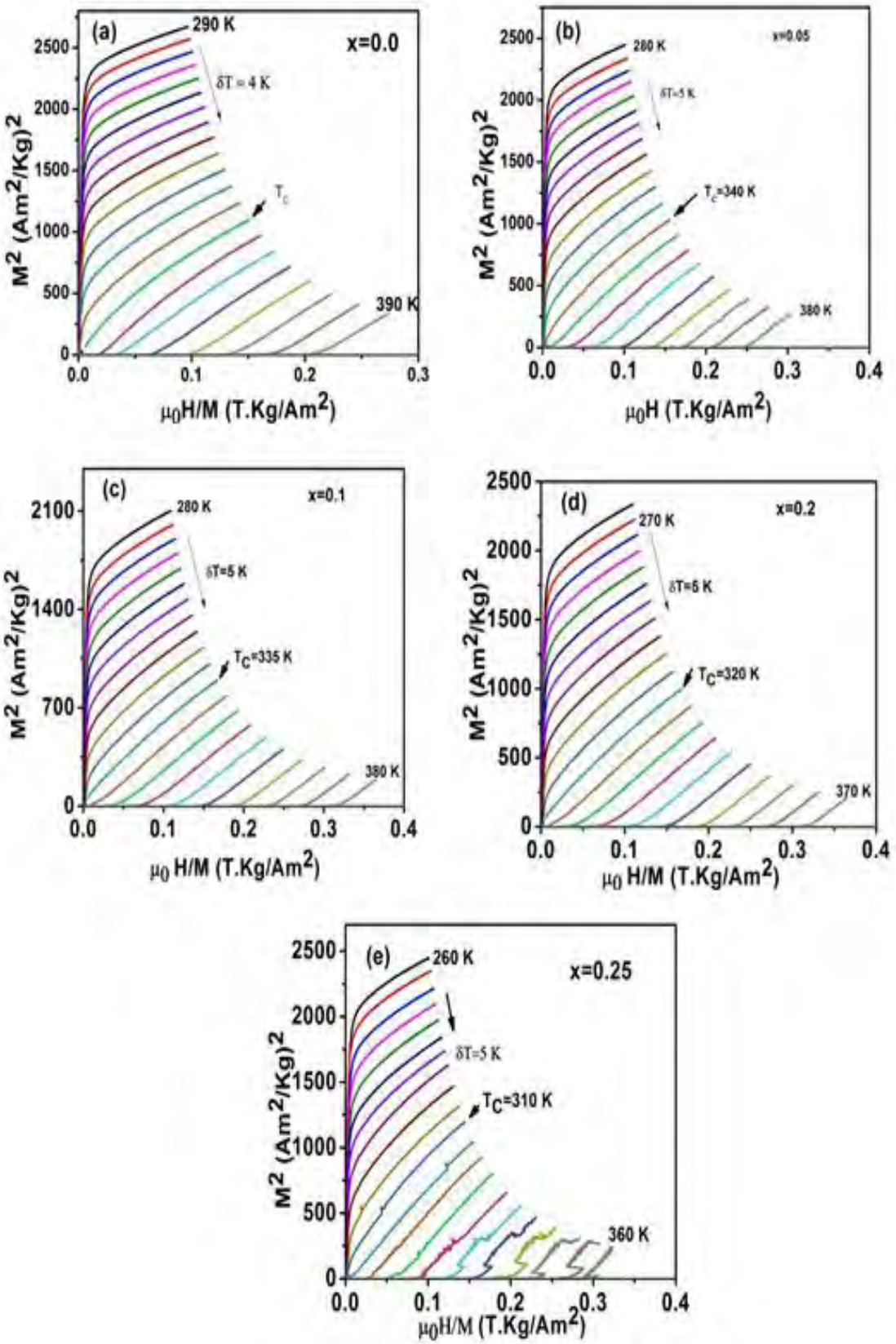

Fig. 4.28 Arrott plot at different temperatures around T_C of various $La_{0.55}Ca_xSr_{0.45-x}MnO_3$ compounds.

Fig. 4.28 shows the M-H data for all the samples after being converted as M^2 vs $\mu_0 H/M$ to identify the type of FM to PM phase transition and plotted as the so called Arrott plots. The Arrott plots of all the samples have shown positive sign of the slope indicating second-order FM to PM phase transitions according to Banerjee criterion [85]. This is regarded as a good characteristic of the sample as promising candidate for MCE. There are two transition modes in magnetic systems. One is first order magnetic phase transitions and other is second order magnetic phase transitions. In case of the first order phase transition, the entropy is not continuous while the second order phase transitions are known as continuous phase transitions [109]. Again there are some additional demerits of the first order phase transition materials are the presence of thermal and magnetic hysteresis, changes in volume and low refrigerator performance because of slow kinetic [110]. That is why for using a magnetic material as magnetic refrigerant, the first choice is to determine magnetic phase transition nature.

4.2.4.3 Critical behavior analysis

Here the critical exponents' β, γ and δ have also been calculated to find the origin of magnetic and magnetocaloric properties of the studied samples. The critical exponents' around T_C has been analyzed using different methods such as modified Arrot plots method, Kouvel–Fisher method and critical isotherm analysis of $La_{0.55}Ca_xSr_{0.45-x}MnO_3$. The three exponents β, γ, δ and T_C follow the power-law relations [86] given in equation (4.6), (4.7) and (4.8). Conventionally, critical exponents' β, γ and δ around T_C can be calculated from the modified Arrot plots using Arrott-Noakes [86] equations of state which is given by equation (4.5). In modified Arrot plots method, the isothermal magnetization data is reformulated into $M^{1/\beta}$ vs $(\frac{H}{M})^{1/\gamma}$ plot in the framework of mean field model, 3-D Heisenberg model, 3-D Ising model and Tri-critical mean field model. The correct exponents are those that linearize $M^{1/\beta}$ vs $(\frac{H}{M})^{1/\gamma}$ curves around T_C, and T_C is defined as the temperature for which the critical isotherm passes through the origin.

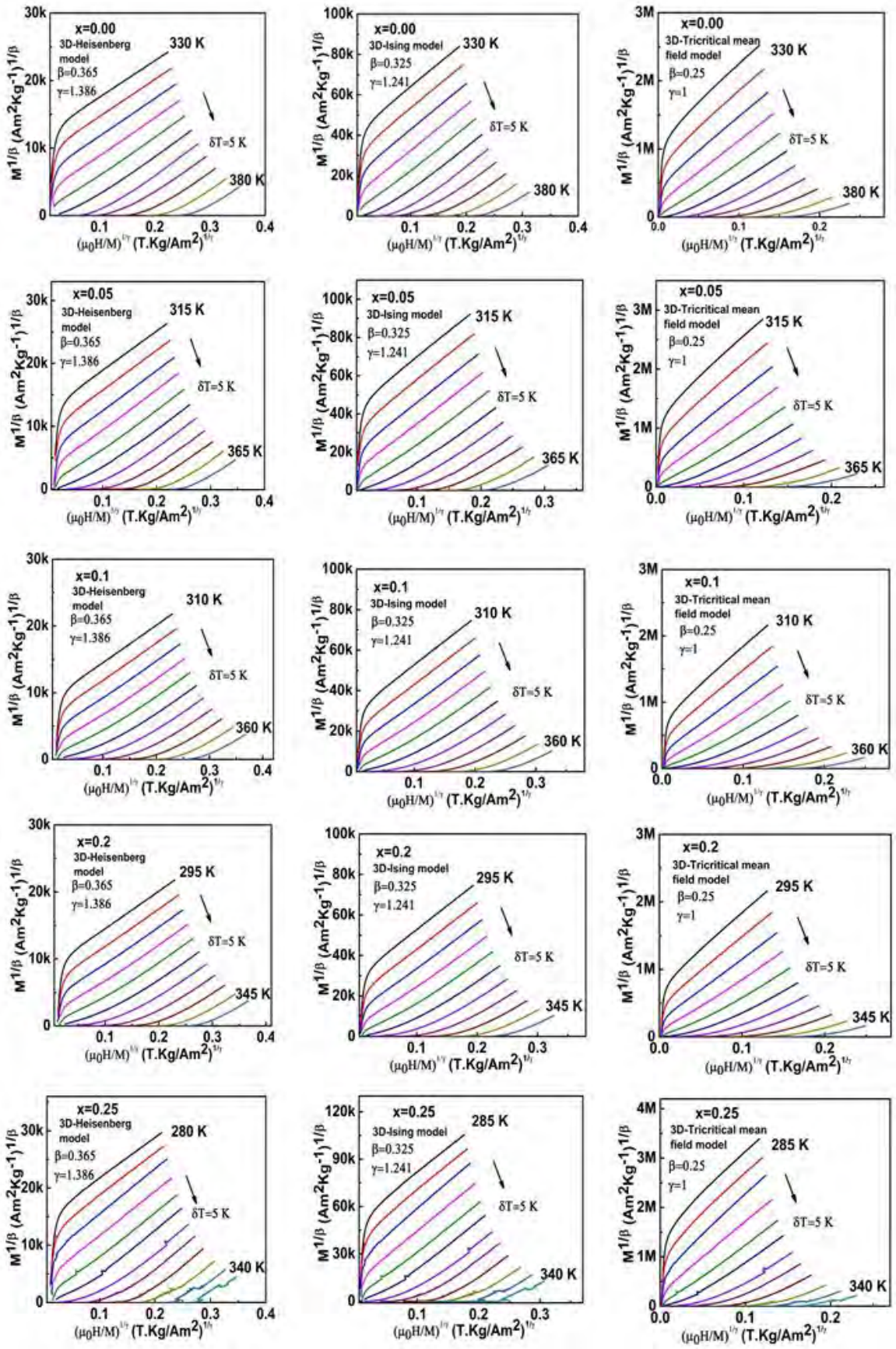

Fig. 4.29 Modified Arrot plots applying different theoretical models for various $La_{0.55}Ca_xSr_{0.45-x}MnO_3$ compounds.

For computing the critical exponents around the PM to FM phase transition temperature, modified Arrot plots using four theoretical models have been analyzed. M^2 vs $\mu_0 H/M$ curves in Fig. 4.28 were constructed applying mean field theory assuming the critical exponent value, β=0.5 and γ=1. The modified Arrot plots were also constructed using theoretical exponents for the 3-D Heisenberg model (β = 0.365, γ = 1.336), 3-D Ising model (β = 0.325, γ = 1.240) and Tri-critical mean field model (β = 0.25, γ = 1) [86, 87] which has been listed in Table 4.8.

Fig. 4.29 represents modified Arrot plots of all the samples applying 3-D Heisenberg model, 3-D Ising model and Tri-critical mean field model. To identify proper model which is applicable for our samples, the relative slope of the plots was calculated by RS=S(T)/S(T_C), where S(T) is the slopes of modified Arrot plots around T_C and and S(T_C) is the slopes of the same plot at T_C [88]. The results have been plotted in Fig. 4.30 which reveals that mean field model is applicable to deduce the critical point exponents for the sample with x=0.0, 0.05, 0.1 and 3D Heisenberg model is applicable for the sample with x=0.2, and 0.25.

Then the spontaneous magnetization was calculated from the linear extrapolation of the selected Arrott plot curves (mean field model for the sample with x=0.0, 0.05, 0.1 and 3D Heisenberg model for the sample with x=0.2, and 0.25) from the high field region to the intercept with $M^{1/\beta}$ axes for $T<T_C$ while the initial magnetic inverse susceptibility χ_0^{-1} was determined similarly from the intercept with $(\frac{H}{M})^{1/\gamma}$ axes for $T>T_C$. The plot of M_S and χ_0^{-1} as a function of temperature has been shown in Fig. 4.31 from where β, and γ with T_C have been computed by fitting M_S vs T curve with the relation $M_S \propto (-\varepsilon)^{\beta}$ as given in equation (4.6), and χ_0^{-1} vs T curve with the relation $\chi_0^{-1}(T) \propto \varepsilon^{\gamma}$ as given in equation (4.7). After that using these β and γ values, the above mentioned process has been repeated until the critical isotherm at $T = T_C$ passes through the origin. The final modified Arrot plots with stable β and γ represents good linearity of the isotherms achieved with β_{MAP} = 0.48, 0.467, 0.46, 0.409 and 0.41, γ_{MAP}= 1.03, 1.11, 1.10, 1.23 and 1.25 and T_{C-MAP}= 353, 341, 336, 320 and 309 K, respectively for x=0.00, 0.05, 0.1, 0.2 and 0.25. Using these β_{MAP} and γ_{MAP}, the exponent δ can be determined from the Widom scaling relation based on statistical theory [90] using equation (4.9) and δ_{MAP} is found 3.15, 3.37, 3.39, 4.01 and 4.05 for x=0.00, 0.05, 0.1, 0.2 and 0.25, respectively.

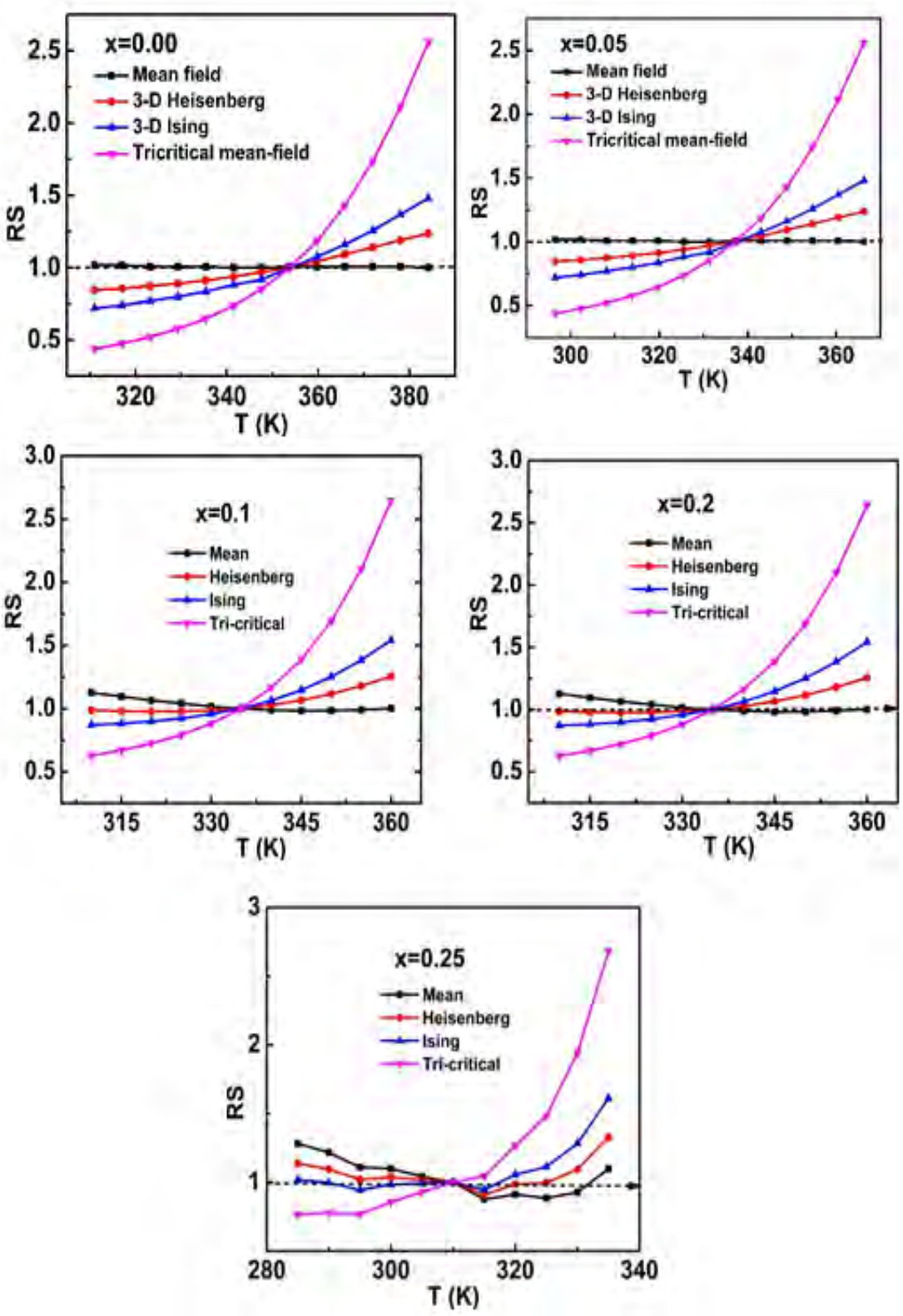

Fig. 4.30 RS vs T from various modified Arrot plots of $La_{0.55}Ca_xSr_{0.45-x}MnO_3$.

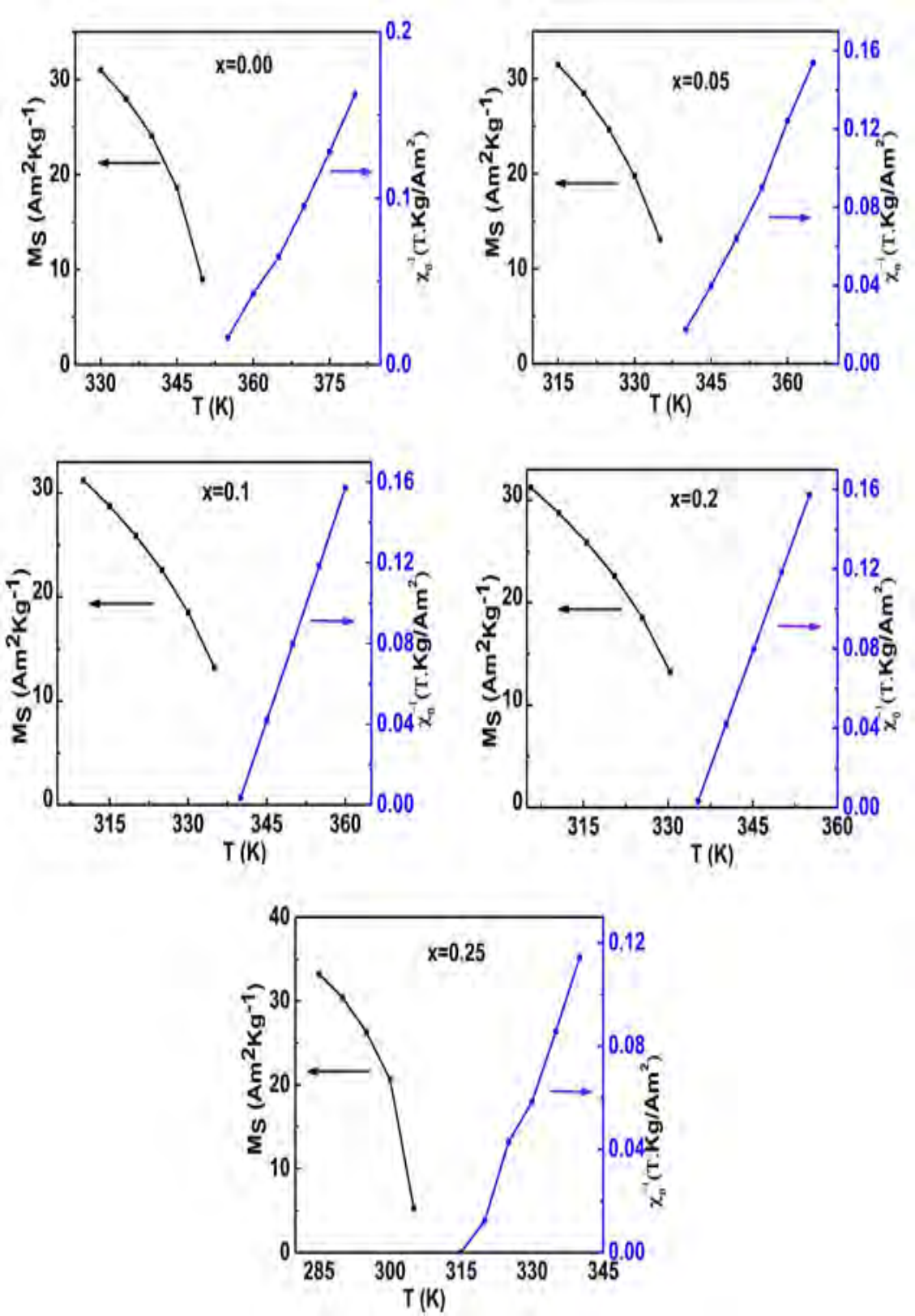

Fig. 4.31 $M_S(T)$ and χ_0^{-1} as a function of temperature for various $La_{0.55}Ca_xSr_{0.45-x}MnO_3$ compounds.

The critical point exponents' β, γ and δ have also been computed using the Kouvel–Fisher method [95] where they reformulated M-H data into equation (4.10) and equation (4.11). After plotting the $M_S(T)[\frac{dM_S(T)}{dT}]^{-1}$ vs T for below T_C and $\chi_0^{-1}(T)[\frac{d\chi_0^{-1}(T)}{dT}]^{-1}$ vs T for above T_C, two straight lines are found which are known as Kouvel–Fisher plot. Fig. 4.32 represents Kouvel–Fisher plots of M-H data for the studied samples. From the slope of these straight lines β, γ, T_{C1} and T_{C2} are computed. Finally the value of the T_C is found from the average of T_{C1} and T_{C2}. The result for the critical point exponent β is β_{KF}= 0.478, 0.47, 0.45, 0.41 and 0.408 with T_{C1} = 353, 340, 335, 320 and 308 K, respectively for x=0.00, 0.05, 0.1, 0.2 and 0.25. For temperatures higher than T_C, the value of the critical point exponent γ is γ_{KF} = 1.05, 1.20, 1.25, 1.24 and 1.23 with T_{C2}=350, 340, 335, 319 and 310 K respectively for x=0.00, 0.05, 0.1, 0.2 and 0.25. The mean values of T_C computed from T_{C1} and T_{C2} are 352, 340, 335, 320 and 309 K, respectively for x=0.00, 0.05, 0.1, 0.2 and 0.25. The critical point exponent δ, derived from the Widom scaling [90] equation (4.9) using these β_{MAP} and γ_{MAP} is found as δ_{KF} = 3.20, 3.55, 3.77, 4.02 and 4.01, respectively for x=0.00, 0.05, 0.1, 0.2 and 0.25. The well agreement between these two methods confirms that the calculated values of the critical exponents are reliable.

The exponent δ can also be determined from the critical isotherm analysis [96] at T= T_C using equation (4.8). Fig. 4.33 shows M vs H curves at T_C for all the studied samples and inset represents the corresponding logM vs logH plot which reveals linear behavior according to equation (4.8) with a slope of $(1/\delta)$ and therefore δ_{CIA} is found to be equal 3.44, 3.63, 3.68, 4.10 and 4.15 for x=0.00, 0.05, 0.1, 0.2 and 0.25, respectively which are almost equal to the value calculated from Widom relation based on the results of the modified Arrot plots and Kouvel–Fisher methods as summarized in Table 4.8. This result confirms that the computed critical exponents and T_C values are self-consistent and reliable. Comparing calculated and experimental values it is found that for the sample with x=0.0, 0.05, 0.1, the δ values are closest to mean field model while those are closest to 3D Heisenberg model for x=0.2 and 0.25.

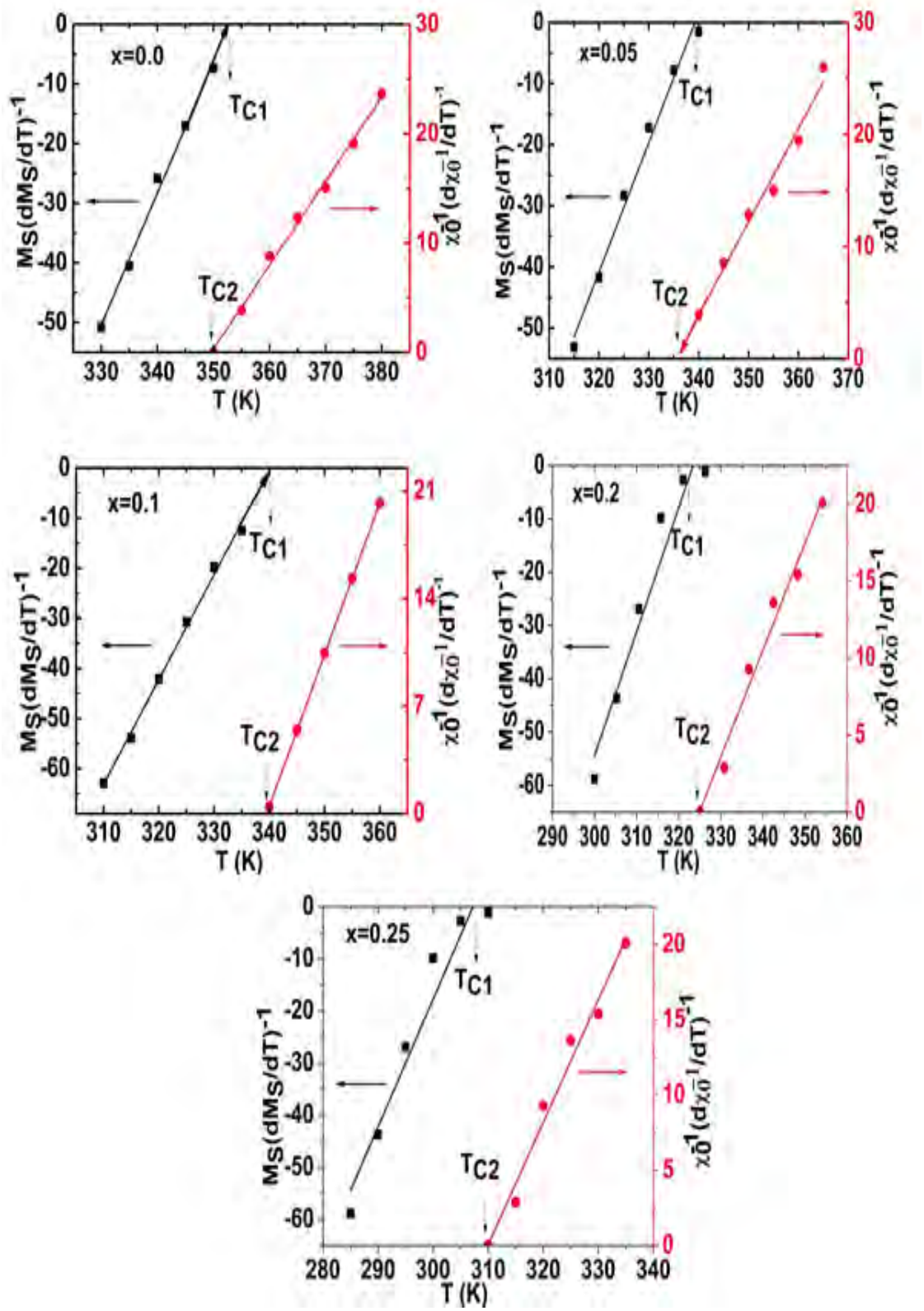

Fig. 4.32 $M_S(T)[\frac{dM_S(T)}{dT}]^{-1}$ vs T for below T_C and $\chi_0^{-1}(T)[\frac{d\chi_0^{-1}(T)}{dT}]^{-1}$ vs T for above T_C of various $La_{0.55}Ca_xSr_{0.45-x}MnO_3$ compounds..

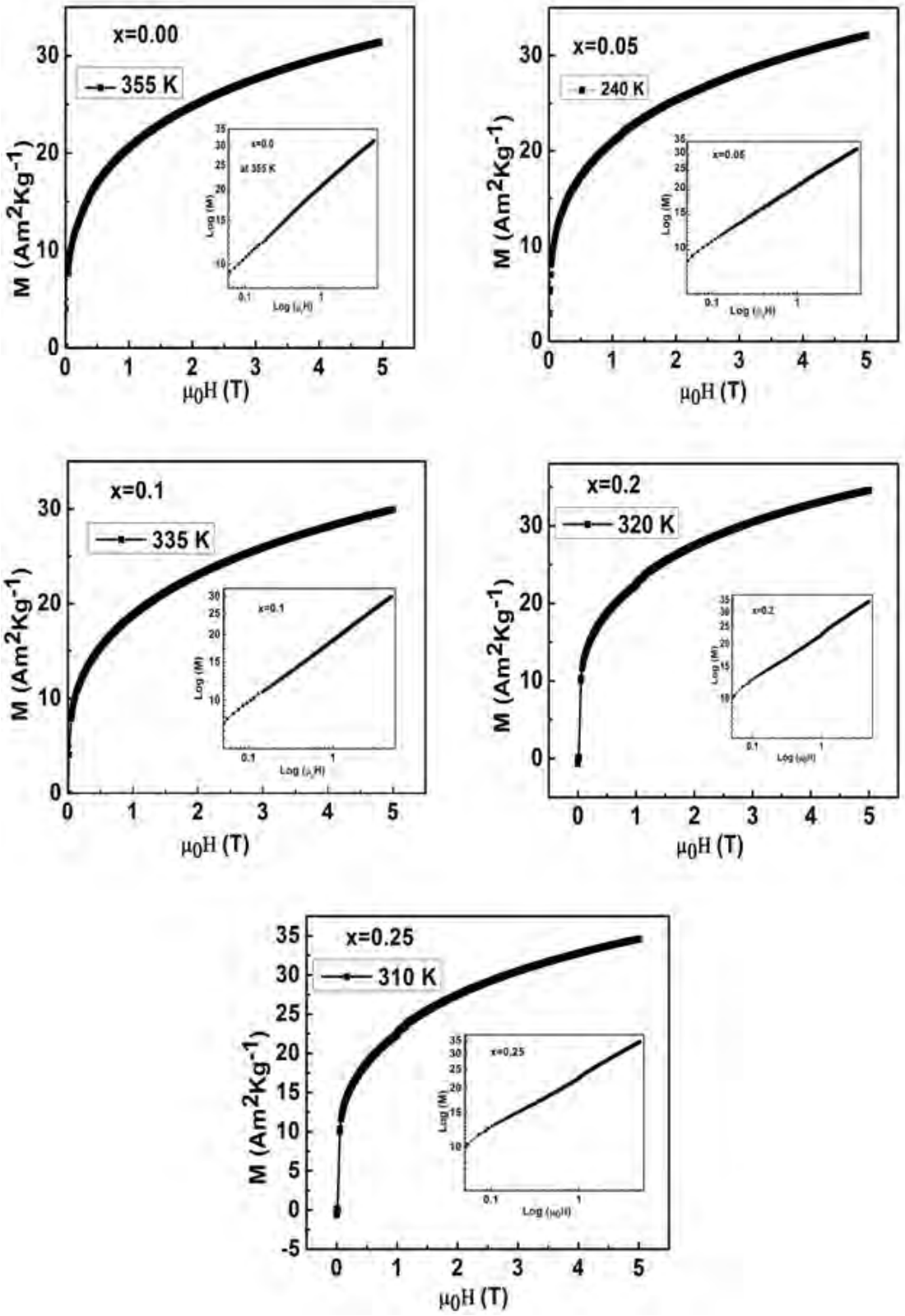

Fig. 4.33 M-H curve at T_C, Inset: corresponding logM vs logH plot of various $La_{0.55}Ca_xSr_{0.45-x}MnO_3$ compounds.

Table 4.8 Comparison of β, γ, δ and T_C of $La_{0.55}Ca_xSr_{0.45-x}MnO_3$ with those of theoretical models.

Composition or model	Method	T_C (K)	β	γ	δ	δ_{CIA}	n	Comment	Reference
Mean field model	Theory	----	0.5	1	3		0.67		[86]
3-D Heisenberg model	Theory	----	0.365	1.386	4.8		0.63		[86]
3-D Ising model	Theory	----	0.325	1.24	4.82		0.57		[86]
Tri-critical mean field model	Theory	----	0.25	1	5		0.4		[87]
$La_{0.55}Sr_{0.45}MnO_3$	MAP	353	0.48	1.03	3.15	3.44	0.687	MF	This work
	KF	352	0.48	1.05	3.20			MF	
$La_{0.55}Ca_{0.05}Sr_{0.4}MnO_3$	MAP	341	0.47	1.11	3.37	3.63	0.682	MF	This work
	KF	340	0.47	1.20	3.55			MF	
$La_{0.55}Ca_{0.1}Sr_{0.35}MnO_3$	MAP	336	0.46	1.10	3.39	3.68	0.655	MF	This work
	KF	335	0.45	1.25	3.77			MF	
$La_{0.55}Ca_{0.2}Sr_{0.25}MnO_3$	MAP	320	0.41	1.23	4.01	4.10	0.639	Heisenberg	This work
	KF	320	0.41	1.24	4.02			Heisenberg	
$La_{0.55}Ca_{0.2}Sr_{0.25}MnO_3$	MAP	309	0.41	1.25	4.05	4.15	0.629	Heisenberg	This work
	KF	309	0.40	1.23	4.01			Heisenberg	

Table 4.8 shows comparison of the critical point exponents calculated using the modified Arrot plots, Kouvel-Fisher methods and critical isotherm analysis for all of the studied samples. Well agreement between two separate methods modified Arrot plots

and Kouvel-Fisher confirm the exact determination of a set of critical point exponents of $La_{0.55}Ca_xSr_{0.45-x}MnO_3$. For x=0.0, 0.05 and 0.1, the β values are very close to that of the mean field model and β values for x=0.2 and 0.25 are close to 3D Heisenberg model. In summary, below T_C, samples with x=0.00, 0.05, 0.1 represent a long-range FM interaction which belongs to the mean-field model and x=0.2 and 0.25 represent FM short-range interactions which belongs to the 3D Heisenberg model. It is found that with increase in Ca content, critical exponents' value deviates from mean field model and shifted towards that of 3-D Heisenberg model meaning that substitution of Sr by Ca does not favor long range FM interaction in the studied samples. On the other hand, above T_C, only x=0.0 represents a long range FM interaction belonging to the mean-field model but FM short-range interactions belonging to the 3D Heisenberg model or 3D Ising model are observed for all other studied samples with x=0.05, 0.1, 0.2 and 0.25. This is a common feature of doped manganite systems [111, 112]. It is usually accepted that the PM to FM phase transition broadens due to the presence of FM clusters with a short-range interaction in the PM region near the phase transition temperature. As a result the temperature range i.e. FWHM of ΔS_M vs T curve increases [111-113] but the value of $(\Delta S_M)_{max}$ is lower than that value found in the absence of FM clusters. Thus by controlling the density and size of the magnetic clusters, magnetocaloric materials with high relative cooling power for useful magnetic refrigeration may be designed.

4.2.5 Magnetocaloric properties

Among three important parameters (discussed in section 4.1.5) for selecting magnetocaloric materials as solid state refrigerants, ΔS_M and RCP are easy to calculate using the Maxwell equation from isothermal M–H data. For this series of samples the ΔS_M value of a magnetic material due to change in applied field is found from the isothermal magnetization measurements using the Maxwell's thermodynamic relation [97] as given in equation (4.12).

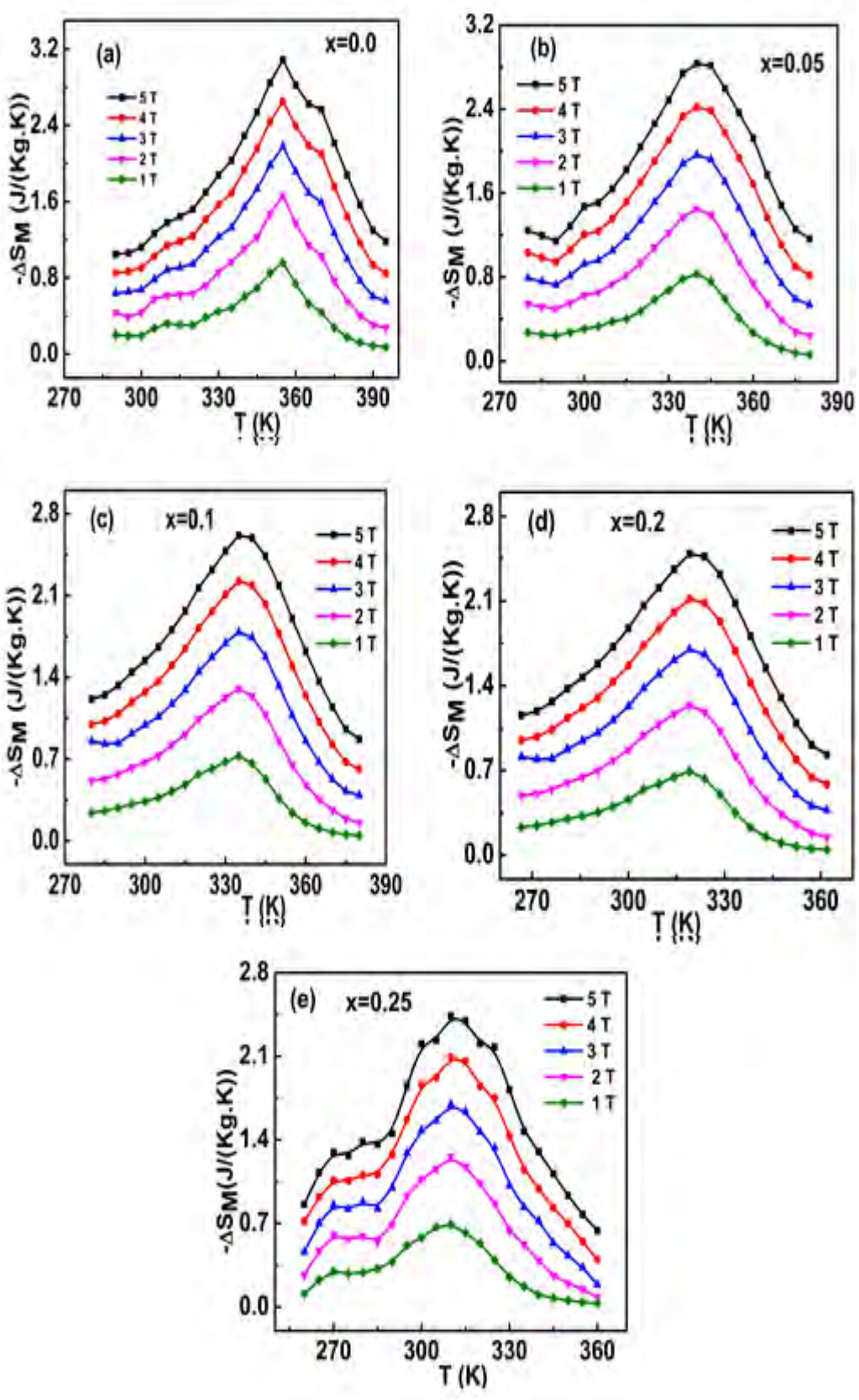

Fig. 4.34 $-\Delta S_M$ vs T curves at different applied field for various $La_{0.55}Ca_xSr_{0.45-x}MnO_3$ compounds.

The magnetic entropy change under different applied fields of different samples of this series has been calculated and plotted as a function of temperature shown in Fig. 4.34. The values of ΔS_M were found to be negative and for convenience $-\Delta S_M$ vs T was plotted. The highest values of magnetic entropy change of various $La_{0.55}Ca_xSr_{0.45-x}MnO_3$ compounds at different constant field are tabulated in Table 4.9. These values are observed around their respective T_C of the samples where the change of magnetization is maximum. The $-\Delta S_M$ vs T curves were gradually broadened and $(-\Delta S_M)_{max}$ increased with increase of applied field due to change in spin ordering process in the sample [57]. For samples with x=0.00, 0.05, 0.1, 0.2 and 0.25, the $(-\Delta S_M)_{max}$ values around their T_C are 3.088, 2.83, 2.71, 2.69, 2.55 $JKg^{-1}K^{-1}$ for ΔH=5 T and 1.66, 1.45, 1.35, 1.31, 1.25 $JKg^{-1}K^{-1}$ for ΔH=2 T, respectively.

Fig. 4.35 (a) shows $-\Delta S_M$ as a function of temperature for different Ca content under a magnetic field change of 2 T for different $La_{0.55}Ca_xSr_{0.45-x}MnO_3$ compounds to compare the MCE as a function of the level of Ca doping. These curves present, as previously described, both the T_C and $(-\Delta S_M)_{max}$ decreases as Ca content increases. From this figure, the MC properties of Ca doped $La_{0.55}Sr_{0.45}MnO_3$ manganite can be modulated by substituting Sr^{2+} with Ca^{2+} ions. Working temperature for this series of samples is 275 to 380 K which remains around room temperature. This working temperature makes the materials as promising candidate for room temperature magnetic refrigeration. The reduction in $(-\Delta S_M)_{max}$ value with increase in Ca content may have originated from the decrease in average ionic radius of A-site. This reduction causes structural change which affects double exchange mechanism that in turn reduces FM interaction [81, 100]. Fig. 4.35 (b) represents the change of maximum entropy change as a function of applied field change at temperature T_C for the sample $La_{0.55}Ca_xSr_{0.45-x}MnO_3$, which demonstrates that with increase in Ca doping magnetocaloric efect decreases due to structural change. It is also observed that greater entropy change occur for greater magnetic field change but the rate of variation of maximum entropy change becomes slower with increase in applied field change and agreed with the observation in other reported polycrystalline perovskite [85, 100].

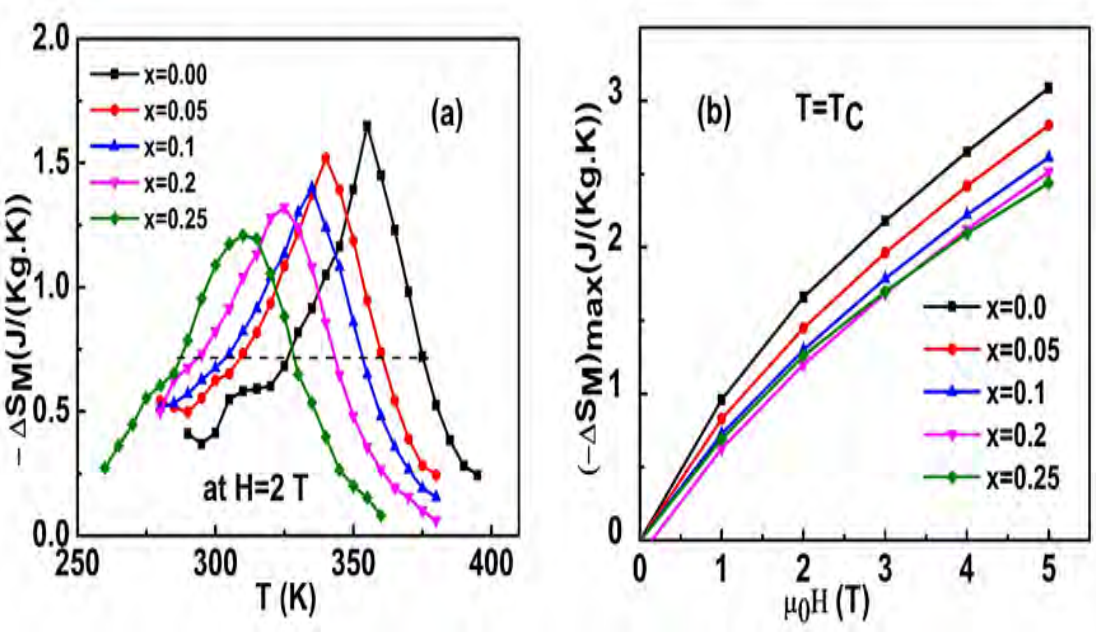

Fig. 4.35 (a) $-\Delta S_M$ vs T, (b) $(-\Delta S_M)_{max}$ vs $\mu_0 H$ for different x values of various $La_{0.55}Ca_xSr_{0.45-x}MnO_3$ compounds.

Applied magnetic field dependence of $(-\Delta S_M)_{max}$ for the material with second order magnetic phase transition is expressed as a scaling law [102] given in equation (4.17) where the scaling exponent is the measure of magnetic field dependence of the maximum entropy change. The $(-\Delta S_M)_{max}$ and $\mu_0 H$ values are re-plotted as $\log(-\Delta S_M)_{max}$ vs $\log(\mu_0 H)$ for determining the exponent n using equation (4.17). Fig. 4.36 represents log-log plot of maximum entropy change $(-\Delta S_M)_{max}$ as a function of $\mu_0 H$ for different Ca for the sample $La_{0.55}Ca_xSr_{0.45-x}MnO_3$. The slope of the linear fit of $\log(-\Delta S_M)_{max}$ vs $\log(\mu_0 H)$ gives the value of n=0.677, 0.732, 0.763, 0.61 and 0.62 for x=0.00, 0.05, 0.1, 0.2 and 0.25, respectively.

The relation between the scaling exponent and the critical point exponent β and γ can be expressed as given in equation (4.18) [103]. n_{MAP} and n_{KF} are found from above mentioned equation using the critical point exponent β and γ calculated from the modified Arrott plot and Kouvel-Fisher methods. The n_{MAP} is found 0.672, 0.662, 0.653, 0.639 and 0.644 while n_{KF} is found 0.658, 0.682, 0.676, 0.640 and 0.638 for x = 0.00, 0.05, 0.1, 0.2 and 0.25, respectively. Comparing the theoretical and experimental value, the derived scaling exponent n is found very close to that of the mean field model for x=0.0, 0.05 and 0.1 while it is close to that of the 3D Heisenberg model for x=0.2 and 0.25.

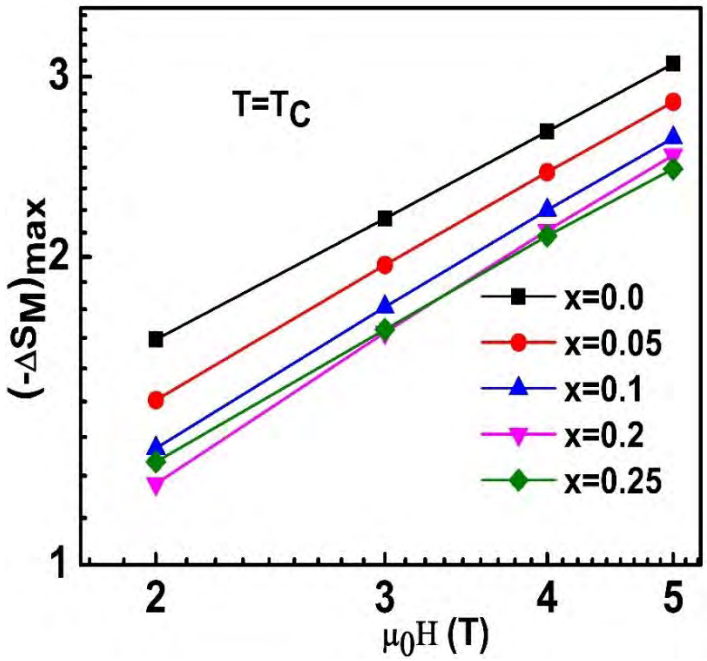

Fig. 4.36 Log-log plot of $(-\Delta S_M)_{max}$ as a function of $\mu_0 H$ for different Ca value for $La_{0.55}Ca_xSr_{0.45-x}MnO_3$ compounds.

Table 4.9 Curie temperature, irreversibility temperature (T_R), $(-\Delta S_M)_{max}$ and RCP of $La_{0.55}Ca_xSr_{0.45-x}MnO_3$ polycrystal.

x content	T_C (K) from dM/dT	T_C (K) from Arrott plot	T_R (K)	$(-\Delta S_M)_{max}$ $JKg^{-1}K^{-1}$ for ΔH= 2 T	$(-\Delta S_M)_{max}$ $JKg^{-1}K^{-1}$ for ΔH= 5 T	RCP (J/Kg) for ΔH= 2 T	RCP (J/Kg) for ΔH= 5 T
0.00	354	355	342	1.66	3.088	82	213
0.05	342	340	330	1.45	2.83	78	196
0.1	336	335	316	1.35	2.71	71	177
0.2	320	320	301	1.31	2.65	68	169
0.25	311	310	292	1.25	2.55	65	165

Another important property of a magnetic material to be used in magnetic refrigerator is relative cooling power which is the measure of the amount of heat transferred from the cold to hot sink in the refrigeration cycle [114]. The calculated RCP values using

equation (4.16) are listed in Table 4.9. It is seen that though $(-\Delta S_M)_{max}$ value decreases but δT_{FWHM} value increases for our samples with the increase in Ca content. The studied samples show large value of RCP. The RCP values are 213, 196, 177, 169, 165 J/Kg for ΔH=5 T and 82, 78, 71, 68, 65 J/Kg for ΔH=2 T for the samples with x = 0.00, 0.05, 0.1, 0.2 0.25, respectively. Again both RCP and δT_{FWHM} increases uniformly with increase in applied field.

Now we will discuss in details the origin of the decrease in T_C and maximum entropy change $(-\Delta S_M)_{max}$. Sr^{2+} substitution by Ca^{2+} in the sample $La_{0.55}Ca_xSr_{0.45-x}MnO_3$ does not change Mn^{4+}/Mn^{3+} ratio and therefore keeps the B-site average ionic radius constant but decreases slightly the A-site average atomic radius, and tolerance factor. Thus the decrease in T_C and $(-\Delta S_M)_{max}$ with increasing Ca content in our samples must have originated from the change in structural parameters accompanied with tolerance factor. The magnetic properties of perovskite manganite are known to be very sensitive to change in tolerance factor which describes the distortion of ideal perovskite structure due to tilting of MnO_6 octahedra [97]. Increasing substitution of larger Sr^{2+} by smaller Ca^{2+} in $La_{0.55}Ca_xSr_{0.45-x}MnO_3$ creates a void between MnO_6 octahedra resulting extra chemical pressure that in turns reduces Mn-O-Mn bond angles from the ideal 180° [98] as it is found in the XRD analysis (Table 4.6). The strength of ferromagnetic double exchange interaction, proposed by Zener, is calculated by the transfer integral, $t_{eff} = t\cos(\theta/2)$, where θ = angle between local spin [71]. Therefore, as tolerance factor decreases (Table 4.6) the double exchange interaction weakens resulting a shift in T_C to lower temperature with increase in Ca-doping content in $La_{0.55}Ca_xSr_{0.45-x}MnO_3$. The variation in $(-\Delta S_M)_{max}$ can also be correlated with tolerance factor. Structural distortion associated with decrease in tolerance factor reduces saturation magnetization (Fig. 4.25 (a) and Fig. 4.27) and slightly broaden the FM to PM transition (Fig. 4.25 (a)). As a results $(-\Delta S_M)_{max}$ is found to be reduced with increase in Ca-doping content in $La_{0.55}Ca_xSr_{0.45-x}MnO_3$ since entropy change is proportional to dM/dT [96]. The similar trend of decreasing T_C and $(-\Delta S_M)_{max}$ simultaneously with decrease in tolerance factor is also found in $La_{0.7-x}Pr_xSr_{0.3}MnO_3$ [101], $La_{0.7-x}Pr_xCa_{0.3}MnO_3$ [115].

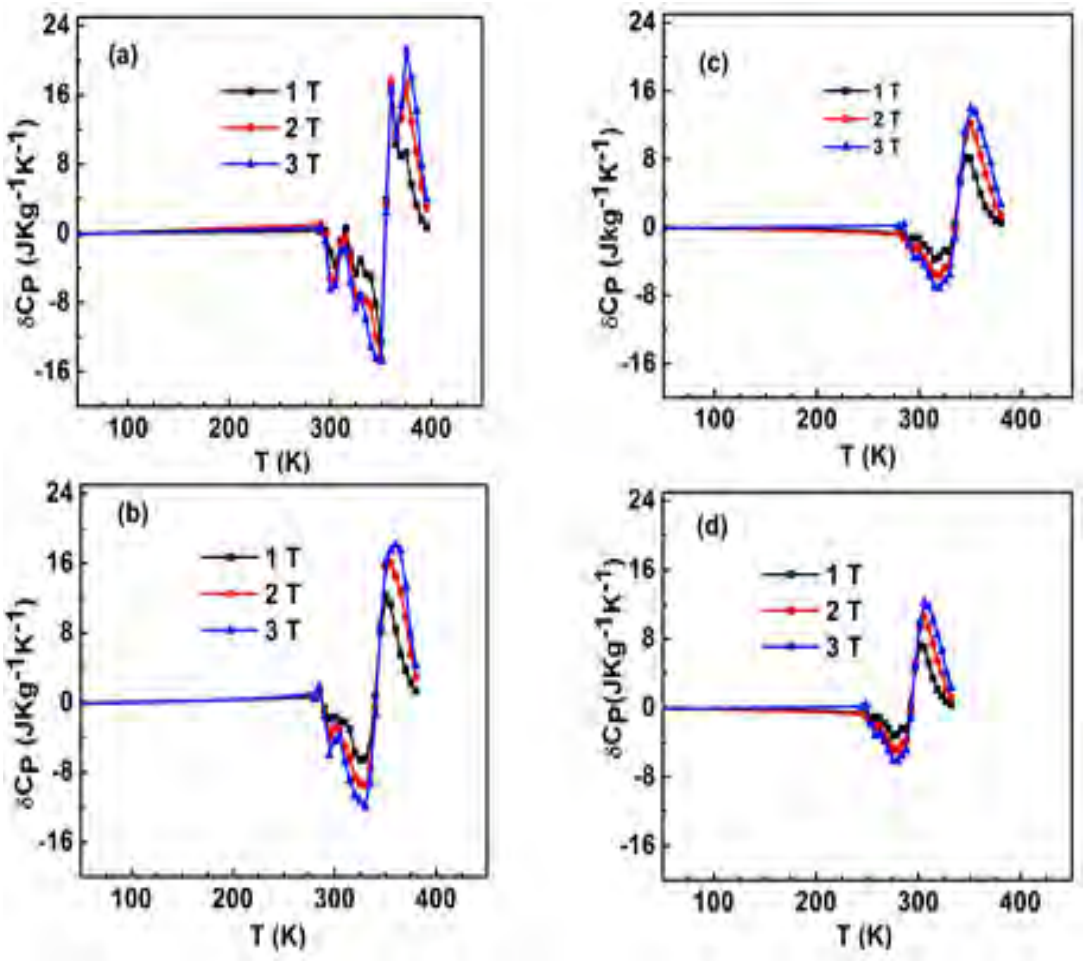

Fig. 4.37 Change in specific heat as a function of temperature for the sample $La_{0.55}Ca_xSr_{0.45-x}MnO_3$ with (a) x= 0.00, (b) x= 0.05, (c) x= 0.1 and (d) x= 0.25.

Another well-known relation between magnetic entropy change and specific heat of the materials is [81]:

$$\Delta S_M = \int_0^T \frac{C_P(T,H) - C_P(T,0)}{T} dT \qquad (4.19)$$

Thus, specific heat change for a change in magnetic field from 0 to H can be expressed by the equation [70]:

$$\Delta C_P(T,H) = C_P(T,H) - C_P(T,0) = T\left[\frac{\partial(\Delta S_M(T,H))}{\partial T}\right] \qquad (4.20)$$

Fig. 4.37 shows change in specific heat of different $La_{0.55}Ca_xSr_{0.45-x}MnO_3$ samples as a function of temperature at different constant field. These curves reveal that for all studied sample, a sharp change in specific heat occurs around their respective Curie

temperature in all constant fields indicating magnetic phase transition. Thus transition temperature T_C and maximum value of specific heat decreases as Ca content increases.

Table 4.10 Collected data for T_C, $(-\Delta S_M)_{max}$ and RCP at ΔH=2 T for the samples prepared by solid state (SS) reaction method.

	Preparation method	ΔH	T_C (K)	$(-\Delta S_M)_{max}$ $JKg^{-1}K^{-1}$	RCP (J/Kg)	References
Gd		2	299	4.2	-----	[7, 116]
$La_{0.6}Sr_{0.4}MnO_3$	SS	2	361	2.48	96.67	[58]
$La_{0.7}Sr_{0.3}Mn_{0.9}Fe_{0.1}O_3$	SS	2	260	1.7	83	[117]
$La_{0.67}Sr_{0.33}MnO_3$	SS	2	361	1.29	----	[118]
$La_{0.67}Sr_{0.33}MnO_3$	SS	2	377	2.02	------	[118]
$La_{0.67}Ba_{0.33}MnO_3$	SS	2	350	1.72	-------	[118]
$La_{0.6}Eu_{0.1}Sr0.3MnO_3$	SS	2	343	1.55	69	[119]
$La_{0.5}Eu_{0.2}Sr0.3MnO_3$	SS	2	281	0.93	67	[119]
$La_{0.4}Eu_{0.3}Sr_{0.3}MnO_3$	SS	2	272	1.17	49	[119]
$La_{0.57}Nd_{0.1}Sr_{0.23}MnO_3$	SS	2	339	2.4	70	[120]
$La_{0.57}Nd_{0.15}Sr_{0.18}MnO_3$	SS	2	315	2.25	80	[120]
$La_{0.7}Sr0.25Na_{0.05}MnO_3$	SS	2	363	2.4	-----	[120]
$La_{0.7}Sr_{0.3}MnO_3$	SS	2	369	1.27	29	[121]
$La_{0.7}Sr_{0.25}Mn_{0.95}Ti_{0.05}O_3$	SS	2	308	2.2	-------	[121]
$La_{0.6}Dy_{0.1}Sr_{0.3}MnO_3$	SS	2	307	3.5	-------	[122]
$La_{0.7}Sr_{0.3}Cr_{0.1}MnO_3$	SS	2	326	1.76	74	[123]

$La_{0.55}Sr_{0.45}MnO_3$	SS	2	354	1.66	82	This work
$La_{0.55}Ca_{0.05}Sr_{0.40}MnO_3$	SS	2	342	1.45	78	This work
$La_{0.55}Ca_{0.1}Sr_{0.35}MnO_3$	SS	2	336	1.35	71	This work
$La_{0.55}Ca_{0.2}Sr_{0.25}MnO_3$	SS	2	320	1.31	68	This work
$La_{0.55}Ca_{0.25}Sr0_{.2}MnO_3$	SS	2	311	1.25	65	This work

Table 4.10 represent collected data for T_C, $(-\Delta S_M)_{max}$ and RCP values for a field change ΔH=2 T for our investigated samples and previously reported samples. Data in Table 4.9 and 4.10 reveals that our samples have suitable values of T_C, moderate $(-\Delta S_M)_{max}$ values, and large relative cooling power. Gadolinium is considered as the best material in the magnetic refrigeration systems, $(-\Delta S_M)_{max}$ value of Gadolinium is 4.2 $JKg^{-1}K^{-1}$ at 299 K for a field change 2 T [116] where the result found from our work shows that $(-\Delta S_M)_{max}$ values are less than that of Gd. However, $(-\Delta S_M)_{max}$, and RCP values of our samples are more than many of those compounds shown in Table 4.10. Though $(-\Delta S_M)_{max}$ values of our investigated samples decreases, δT_{FWHM} values have shown an increases with increase in Ca content. As a result RCP values just decreases slightly with increase in Ca content while increase in Ca content tunes the T_C near room temperature. $(-\Delta S_M)_{max}$ = 1.50, 2.55 $JKg^{-1}K^{-1}$ and RCP =79, 165 J/Kg for ΔH=2, 5 T respectively have been estimated for the sample with x=0.25 having the T_C 311 K which is close to the room temperature. Thus it is proposed that the sample with x=0.25 i.e. $La_{0.55}Ca_{0.25}Sr_{0.2}MnO_3$ may be used as good refrigerant for near room temperature magnetic refrigerator. It is also found that although some materials show giant MCE they have low value of RCP or T_C value far above or bellow the room temperature. This series of samples possesses moderate value of $(-\Delta S_M)_{max}$ and large RCP where Ca substitution in place of Sr tunes the T_C toward room temperature. MCE with tunable T_C, high chemical stability, easier fabrication, and less expensive materials are also valuable factors that can make $La_{0.55}Ca_xSr_{0.45-x}MnO_3$ as a promising material for magnetic cooling technology like magnetic refrigerator at moderate field change (2 T).

4.2.6 Summary

$La_{0.55}Ca_xSr_{0.45-x}MnO_3$ has been synthesized by the solid state reaction method to investigate the effect of calcium doping on structural, magnetic and magnetocaloric properties of calcium-strontium doped lanthanum manganite. Relationship between the critical point exponents and the observed magnetocaloric behaviour has also been elucidated. Rhombohedral structures with R-3c space group of all the samples are confirmed by room temperature XRD technique. The replacement of larger size Sr^{2+} ions by smaller Ca^{2+} ions changes the lattice parameters as well as Mn-O-Mn bond angle which bring T_C to RT and affect magnetocaloric properties of the samples. No other elements rather than elemental composition of the investigated samples are seen in the EDX spectrums. The calculated values of chemical composition were in good agreement with the nominal values. Grain size gradually decreases with increase in Ca content in $La_{0.55}Ca_xSr_{0.45-x}MnO_3$. For Ca content up to 0.1, the crystalline particles develop easily and substitution of Sr by Ca more than 0.1 does not favour grain growth in the samples of $La_{0.55}Ca_xSr_{0.45-x}MnO_3$. Magnetic measurement as a function of temperature reveals a reduction of magnetic saturation with increase in Ca content and FM to PM phase transition with increase in temperature. The divergence between FC and ZFC curve reveals the existence of anti-ferromagnetic and ferromagnetic clusters in the investigated samples. Curie temperature decreases from 355 to 311 K for the samples with x=0.00 to 0.25. The Arrott plots of the samples reveal positive sign of the slope indicating second-order FM to PM phase transitions. The isothermal M-H data has been analysed in the framework of four theoretical model to calculated critical exponents. It is found that, below T_C, the samples with x=0.00, 0.05, 0.1 represent a long-range FM interaction belonging to the mean-field model and x=0.2 and 0.25 represent FM short-range interactions belonging to the 3D Heisenberg model. On the other hand, above T_C, only x=0.0 represents a long range FM interaction but FM short-range interactions are observed for all other studied samples with x=0.05, 0.1, 0.2 and 0.25. The magnetocaloric effect was determined in terms $-\Delta S_M$ of and RCP. The maximum $-\Delta S_M$ values are observed around their respective T_C of the samples where the change of magnetization is maximum. The $-\Delta S_M$ vs T curves were gradually broadened and $(-\Delta S_M)_{max}$ increased with increase of applied field due to change in spin ordering process in the sample. The highest value of $-\Delta S_M$ is found 3.088, 2.83, 2.71, 2.65 and 2.97 $JKg^{-1}K^{-1}$ for ΔH=5 T due to rapid change in magnetization around T_C for x=0.00, 0.05, 0.1, 0.2 and 0.25, respectively. The scaling exponent for magnetic field

dependence of $(-\Delta S_M)_{max}$ is found to be close to that of the mean field model for x=0.0, 0.05 and 0.1 while it is close to that of the 3D Heigenberg model for x=0.2 and 0.25. The values of relative cooling power were 213, 196, 177, 169 and 165 J/Kg for the samples with x = 0.00, 0.05, 0.1, 0.2 and 0.25, respectively. Though $(-\Delta S_M)_{max}$ values of our investigated samples decreases, δT_{FWHM} values have shown an increases with increase in Ca content. As a result RCP values just decreases slightly with increase in Ca content while increase in Ca content tunes the T_C to 311 K which is close to the room temperature. Therefore the sample $La_{0.55}Ca_xSr_{0.45-x}MnO_3$ could be used as good solid state refrigerant for magnetic refrigerator, working in the desired temperature range tuneable by Ca doping, because of the following reasons (i) tuneable T_C, (ii) large $(-\Delta S_M)_{max}$, and (iii) high value of RCP.

4.3 Characterization of $Sm_{0.55}Ca_xSr_{0.45-x}MnO_3$ (x= 0.00, 0.05, 0.1, 0.2 and 0.25) Perovskite

4.3.1 X-ray diffraction analysis

The room temperature XRD patterns of various $Sm_{0.55}Ca_xSr_{0.45-x}MnO_3$ compound as well as Miller indices are shown in Fig. 4.38 (a). All the patterns show identical characteristic peaks, and there are no anomalous peaks due to the precursors. The XRD patterns were recorded in the 2θ range of 10-80°. Fig. 4.38 (b) shows the main peaks of XRD patterns for $Sm_{0.55}Ca_xSr_{0.45-x}MnO_3$. No splitting in the main peak suggests the possibility of being orthorhombic perovskite unit cell of all the studied samples. The shift of the XRD peaks towards greater angles as seen in Fig. 4.38 (b) demonstrates the decrease of the lattice parameters in the prepared samples with the increase in Ca content.

Fig. 4.39 shows Rietveld patterns for all the studied samples where the graph shows a well agreement between the observed and calculated values. The Rietveld refinements were carried out using a 'X-Pert HighScore Plus' software. The quality of the refinement is estimated by keeping the goodness of the fit indicator χ^2, weighted parameter R_{wp}, and the pattern R_p to minimum. The value of χ^2, R_{wp}, and R_p have been inserted in Fig. 4.39. It is found that all the samples are in single phase and no impurity has been detected within the measurement range. All the samples of $Sm_{0.55}Ca_xSr_{0.45-x}MnO_3$ are found to crystallize in orthorhombic structure with Pnma space group. The lattice parameters a, b and c as well as the cell volume have been calculated and tabulated in Table 4.11. In this series of samples, the average ionic radius of the A site has systematically decreased from the sample with x = 0.00 to x = 0.25 due to substitution of larger Sr^{2+} (1.32 Å) by the smaller Ca^{2+} (1.14 Å) [57, 101]. Therefore, the volume of unit cell decreases with increase in Ca content (as shown in Fig. 4.40 (a)). However, no structural phase transition which is related to decreasing $\langle r_A \rangle$ has been found in this system. It is also found that Mn-O-Mn bond angle decreases with increase in Ca content as shown in Fig. 4.40 (a). Increasing substitution of larger Sr^{2+} by smaller Ca^{2+} in $Sm_{0.55}Ca_xSr_{0.45-x}MnO_3$ creates a void between MnO_6 octahedra resulting extra chemical pressure that in turns reduces Mn-O-Mn bond angles from the ideal 180° [69].

The crystallite size tabulated in Table 4.11 has been evaluated by the Debye-Scherer

equation [75], $d = \frac{K\lambda}{\beta\cos\theta}$, where, d = crystallite size in nm, K =Scherer constant which is equal to 0.9, λ = wavelength of the X-ray with a value of 0.15406 nm, β = FWHM in radians and θ = peak position in radians. The tolerance factor has been calculated from average ionic radius using Goldschmidt equation as previously stated [76, 111]. The average A-site ionic radius is given by $< r_A >= 0.55 < r_{Sm^{3+}} > + x < r_{Ca^{2+}} > + (0.45 - x) < r_{Sr^{2+}} >$. As previously stated with decreases in tolerance factor from 1, the lattice structure transforms to the rhombohedral for 0.96<t<1 and then to the orthorhombic structure for t<0.96 [77]. For this series of samples the tolerance factor varies from 0.870 for x = 0.0 to 0.845 for x = 0.25. This is associated to the replacement of larger Sr^{2+} ion by smaller Ca^{2+} ion. These values of tolerance factor confirm the distorted orthorhombic structure of the investigated samples.

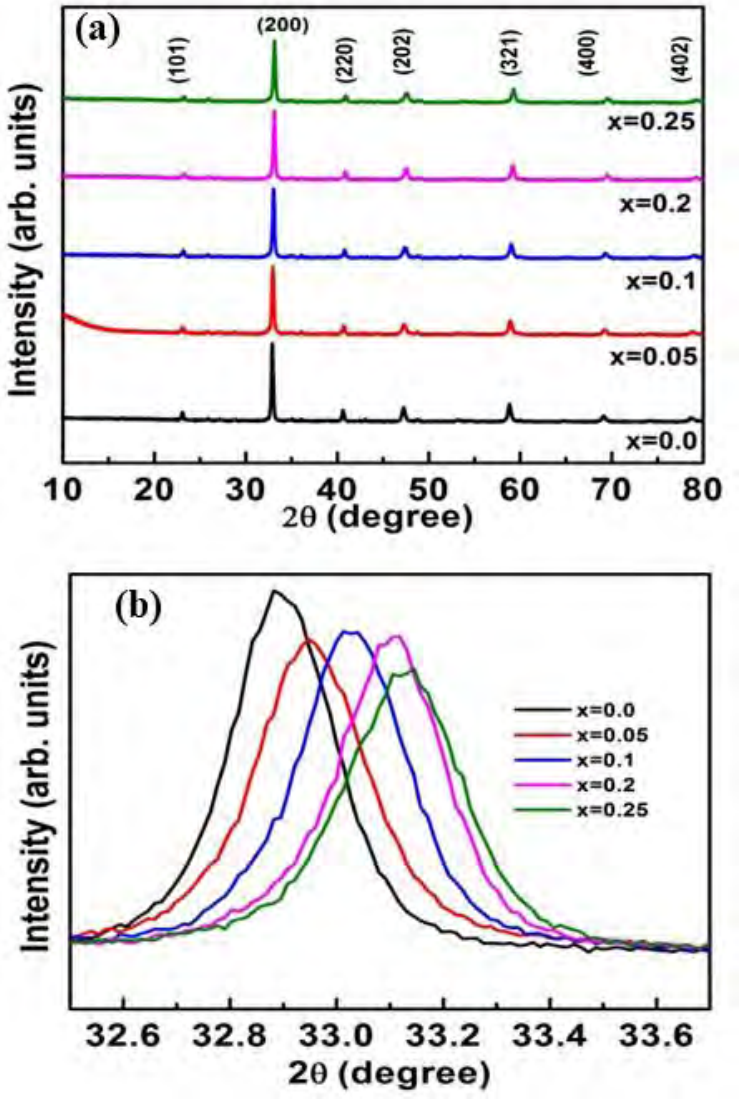

Fig. 4.38 (a) Room temperature XRD patterns, (b) Main peaks of XRD patterns for various $Sm_{0.55}Ca_xSr_{0.45-x}MnO_3$ compounds.

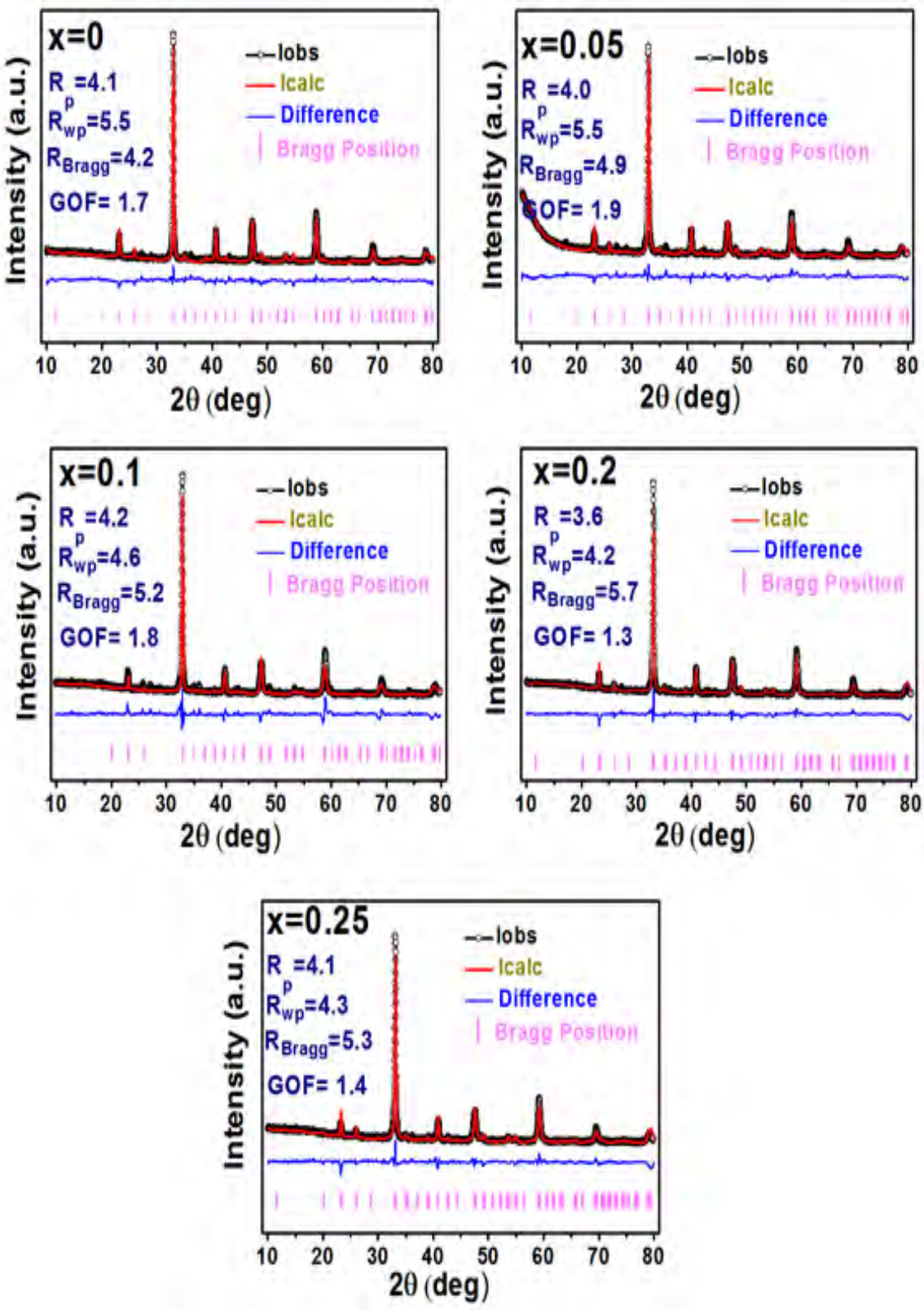

Fig. 4.39 Rietveld patterns for different $Sm_{0.55}Ca_xSr_{0.45-x}MnO_3$ compounds.

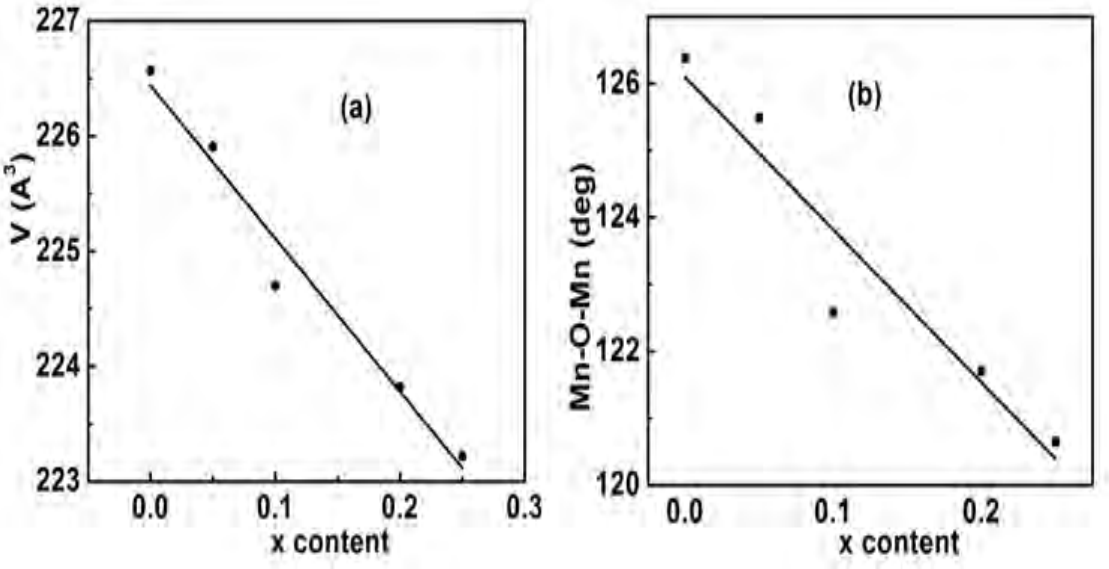

Fig. 4.40 (a) Cell volume, (b) Mn-O-Mn bond angle as a function of x content for various $Sm_{0.55}Ca_xSr_{0.45-x}MnO_3$ compounds.

Table 4.11 Lattice parameters, cell volume (V), Mn-O-Mn bond angle, crystallite size (d) and grain size (D) of various $Sm_{0.55}Ca_xSr_{0.45-x}MnO_3$ compounds.

x	System	a (Å)	b (Å)	c (Å)	V (Å³)	Mn-O-Mn (deg)	d (nm)	D (μm)
0.0	orthorhombic	5.4330	7.6613	5.4430	226.57	126.38	66	0.55
0.05	orthorhombic	5.4290	7.6495	5.4395	225.91	125.49	48	0.62
0.1	orthorhombic	5.4260	7.6354	5.4234	224.70	122.58	48	0.65
0.2	orthorhombic	5.4246	7.6273	5.4096	223.82	121.70	48	0.82
0.25	orthorhombic	5.4231	7.6162	5.4045	223.22	120.65	38	0.78

4.3.2 Microstructure observation

The grain size and surface morphology of the studied samples were examined by a FESEM. Fig. 4.41 shows the FESEM images of the samples $Sm_{0.55}Ca_xSr_{0.45-x}MnO_3$. It is observed that all the compounds contain both small and larger size particles that are homogeneously distributed throughout the sample. The compositional change causes

significant morphological variation. The samples are porous and appear at different polygonal forms. The average grain sizes have been calculated by using 'ImageJ' software and listed in Table 4.11. The size of a grain is defined as the mean diagonal of a polygon. After taking the diameters of all the grains in FESEM image, the data were plotted as a histogram with Lauretz fitting to evaluate the average grain size. The values of grain size for all the samples are larger in compared to that of the crystallite size, indicating a multi-domain structure. In the samples with small Ca content (x = 0.0, 0.05, 0.1), the grain sizes are small and for larger amount of Ca (x = 0.2, 0.25), the size of the grain sizes increases. There are several particles with sizes up to 1 μm. This observation reveals that in the sample with x = 0.2 and 0.25 the crystalline particles develop easily due to existence of local liquid phases [124]. In case of x=0.0 to 0.1, the grain boundaries are clear but for x=0.2 and 0.25, there are large number of long necks among the grains. The neck is always distorted and the distorted grain boundaries affect the inside of grains [78]. Thus for our sample of series, the grain-boundary effect increases with increase in Ca content. Presence of the dispersed particles in form and size is also noticed. It may be produced due to the ball milling effect.

4.3.3 Chemical composition analysis

The elemental composition of the studied samples was examined by means of EDX spectroscopy. Fig. 4.42 shows the EDX spectrum of the samples $Sm_{0.55}Ca_xSr_{0.45-x}MnO_3$ with x=0.0 to x=0.25. The spectrum contains only the characteristic peaks of Sm, Ca, Sr, Mn and O indicating absence of impurities in the studied sample. Using the EDX data chemical composition of $Sm_{0.55}Ca_xSr_{0.45-x}MnO_3$ polycrystal normalized to 100 wt% was calculated and found that the calculated value approximately agreed with the target composition. Table 4.12 shows the average amounts of Sm, Ca, Sr, Mn and O in the five samples, obtained from average values of three EDX spectra recorded at three different surface areas. The samples contain an excess amount of Sm and a lack of Mn. The Ca and Sr contents are also a little bit low compared to the expected values. However, it is clear that Ca and Sr content values are exchanged in an approximately linear manner, as stoichiometric composition. The anomaly between calculated and expected compositions may be arise due to an instrumental error since the EDX technique is not very suitable for porous specimens like $Sm_{0.55}Ca_xSr_{0.45-x}MnO_3$ samples [79]. According to FESEM images $Sm_{0.55}Ca_xSr_{0.45-x}MnO_3$ samples are quite porous.

The X-ray peak intensities of the EDX spectra of the different elements in the sample, as well as on the relative distribution of elements may be influenced due to porosities.

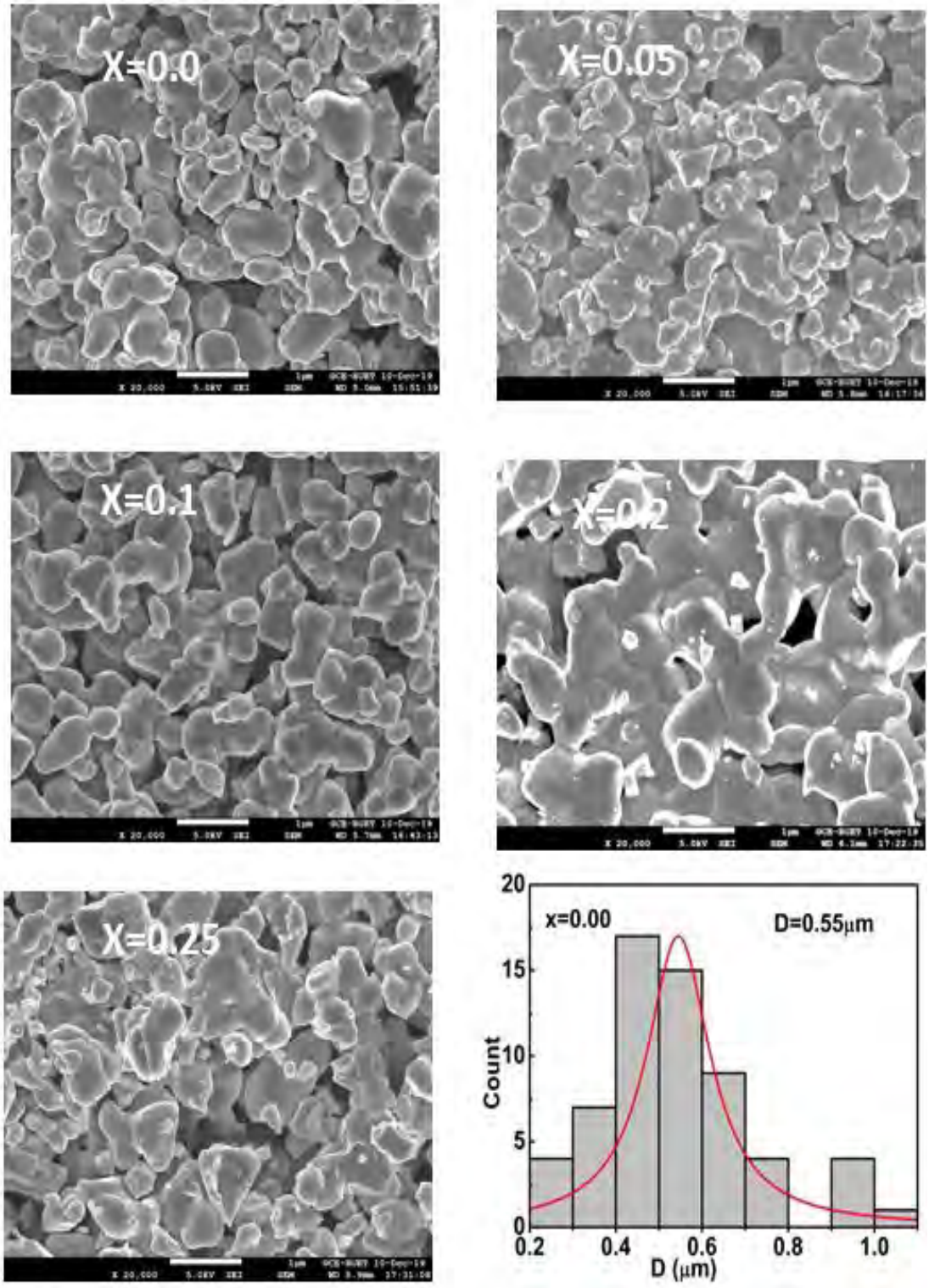

Fig. 4.41 FESEM images of various $Sm_{0.55}Ca_xSr_{0.45-x}MnO_3$ compounds (the images are scaled equally) and size distribution of the sample with x=0.0.

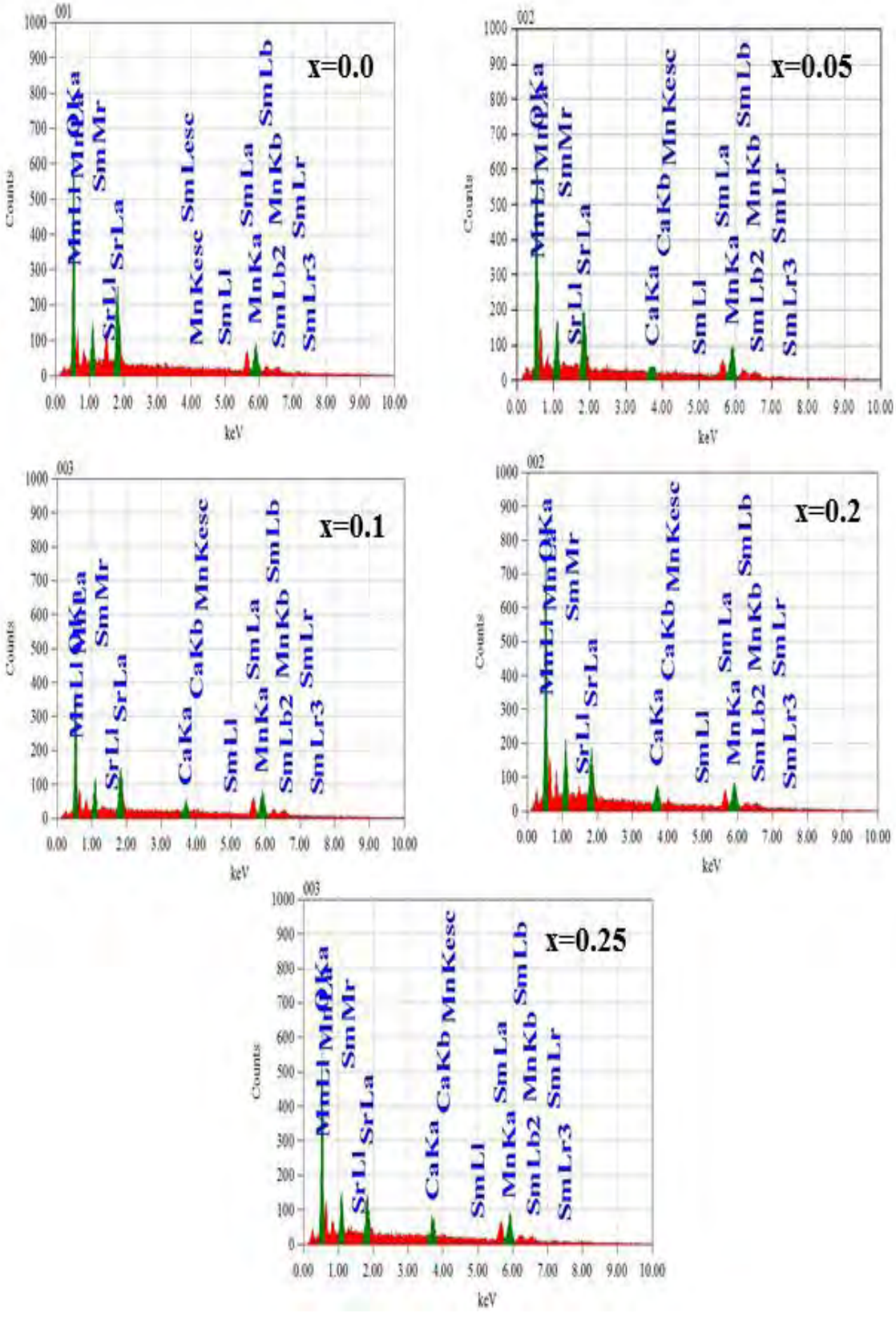

Fig. 4.42 EDX spectrum of various $Sm_{0.55}Ca_xSr_{0.45-x}MnO_3$ compounds.

Table 4.12 Elemental composition of various $Sm_{0.55}Ca_xSr_{0.45-x}MnO_3$ compounds in weight %.

		Sm	Ca	Sr	Mn	O
x=0.0	Calculated Weight%	36.74	……..	17.52	24.41	21.33
	Weight % from EDX spectrum	37.20	……..	16.94	23.93	21.93
x=0.05	Calculated Weight%	37.14	0.90	15.73	24.67	21.56
	Weight % from EDX spectrum	38.87	1.23	14.30	25.02	20.56
x=0.1	Calculated Weight%	37.53	1.82	13.92	24.95	21.78
	Weight % from EDX spectrum	38.03	2.19	13.41	25.42	20.95
x=0.2	Calculated Weight%	38.36	3.72	10.16	25.49	22.27
	Weight % from EDX spectrum	39.77	3.07	9.71	24.26	23.20
x=0.25	Calculated Weight%	38.79	4.70	8.22	25.78	22.51
	Weight % from EDX spectrum	39.94	4.23	8.97	25.46	21.44

4.3.4 Magnetic properties

4.3.4.1 Temperature dependent magnetic properties

For determining magnetic properties at low temperature, magnetizations were measured as a function of temperature in both ZFC and FC mode. Fig. 4.43 (a) shows ZFC and FC magnetizations for different $Sm_{0.55}Ca_xSr_{0.45-x}MnO_3$ compounds, measured at 0.01 T applied field from temperature 5 to 250 K. The divergence between the FC and ZFC magnetization curves at low field and low temperature (known as irreversibility temperature which has been listed in Table 4.13) reveals the coexistence of AFM and FM clusters in the studied samples. This behavior is attributed to the competition between super exchange AFM and double exchange FM interactions at the grain boundaries. Short-range ordering at grain boundary due to distorted crystal structure is also responsible for this behavior [80, 81]. Another feature of these curves is that with decrease in temperature all the samples exhibit a PM to FM magnetic phase transition at the Curie temperature, followed by a FM to AFM transition at Neel temperature. It is

also observed from Fig. 4.43 (a) that the peak magnetization decreases with increase in Ca content in $Sm_{0.55}Ca_xSr_{0.45-x}MnO_3$.

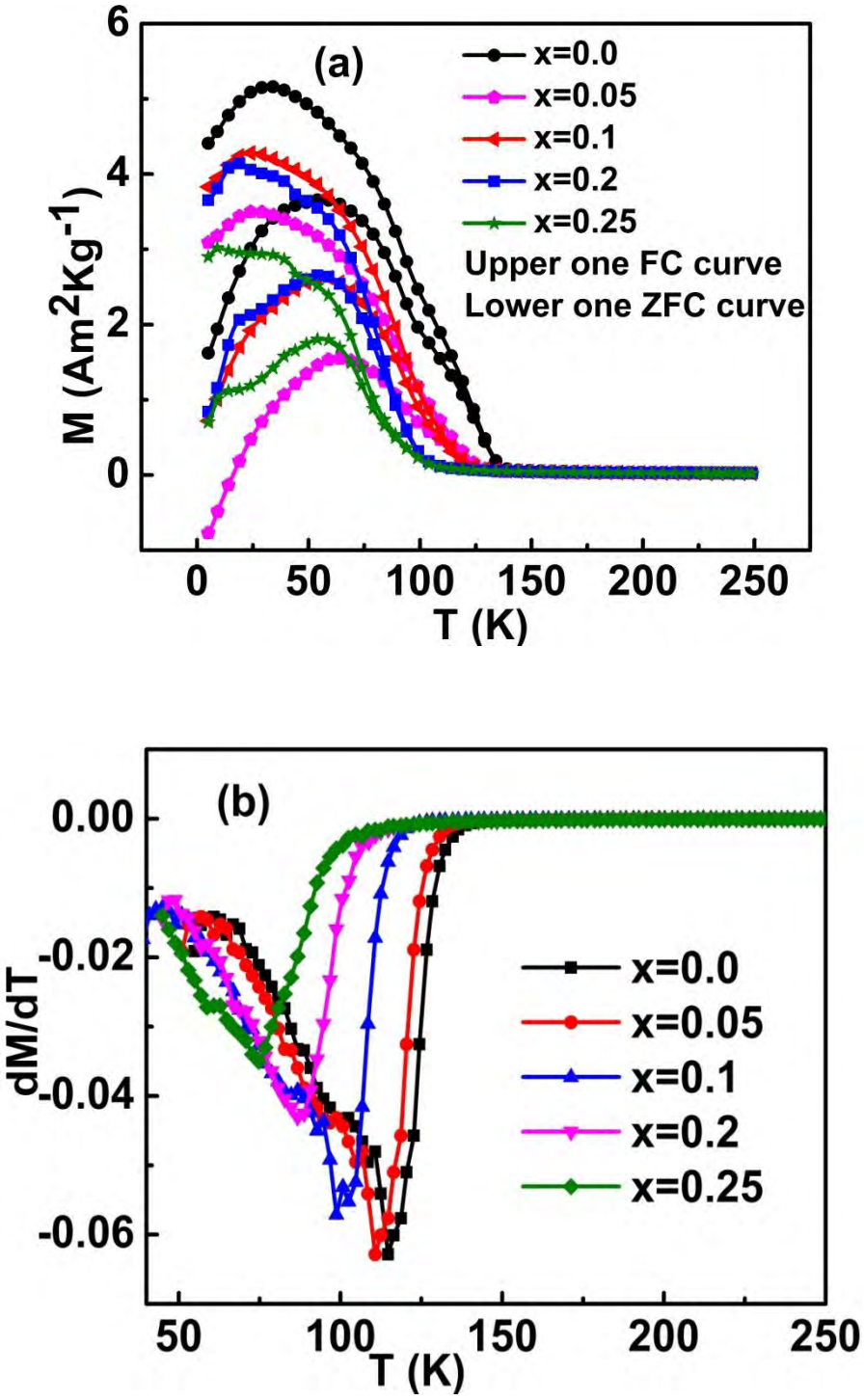

Fig. 4.43 (a) FC and ZFC magnetization curves, (b) dM/dT vs T curves, for various $Sm_{0.55}Ca_xSr_{0.45-x}MnO_3$ compounds measured at 0.01 T applied field.

The Curie temperature has been estimated as previously described from the minimum of the dM/dT vs T curves which has been presented in Fig. 4.43 (b). The T_C for the samples with x=0.00 is 116 K. The obtained value of T_C of this composition agrees very well with the phase diagram [62, 125]. Fig. 4.44 shows dM/dT and T_C as a function of Ca content. It is observed that T_C decreases with increasing Ca content from 116 K for x=0.0 to 75 K for x=0.25. Replacement of Sr^{2+} ion by Ca^{2+} ion does not change the Mn^{3+}/Mn^{4+} ratio in the studied samples, but slightly reduces the values of $< r_A >$ [19]. Therefore the decrease of T_C with increasing Ca content could be associated to the decrease of the double exchange FM interaction due to the decrease of $< r_A >$ [65]. The variation of T_C with change in $<r_A>$ is also observed in $Sm_{1-x}Sr_xMnO_3$ [65] and $Sm_{0.55-x}Pr_xSr_{0.45}MnO_3$ [125]. With increase in Ca content in A-site reduces the degree of quenched disorder resulting magnetic face transition broader.

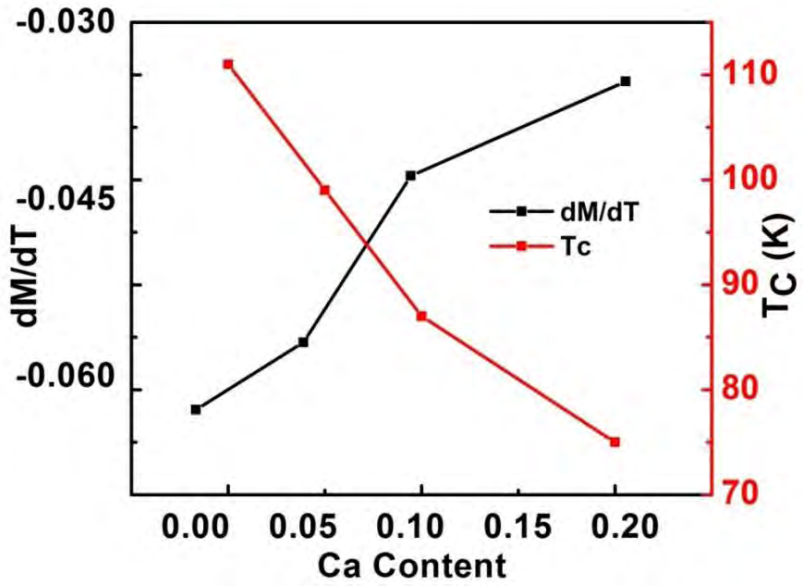

Fig. 4.44 dM/dT vs Ca content (left axis) and T_C vs Ca content (right axis) for various $Sm_{0.55}Ca_xSr_{0.45-x}MnO_3$ compounds.

Fig. 4.45 shows the inverse magnetic susceptibility as a function temperature for all the $Sm_{0.55}Ca_xSr_{0.45-x}MnO_3$ samples. $1/\chi$ was derived from the FC curve taken under a magnetic field of 0.01 T. The $1/\chi$ vs T curves for x=0.0 and 0.05 show a sudden change around T_C indicating first order PM to FM transition. While the curves for x = 0.1, 0.2 and 0.25 shows just a deviation from linearity meaning deviation from the Curie–Weiss

law above T_C. This behavior is attributed to the presence of FM clusters of Mn^{3+}, Mn^{4+} and/or Sm^{3+} ions together in the paramagnetic phase [68]. Since the deviation starts from far above T_C, this phenomenon may be associated to the disorder-induced phase separation [125]. The inverse susceptibility curve was fitted with Curie–Weiss law $1/\chi = \frac{C}{T-\theta}$, where C is the molar Curie constant, θ is the paramagnetic Curie temperature. It is observed from fitted curve that the PM phase does not completely obey the mean-field Curie–Weiss law. The effective PM moment has also calculated from this linear fit and found that this value is greater than the theoretical value. This difference confirms the magnetic inhomogeneity in the investigated samples just above T_C. It is also found that difference between T_C and θ as well as the theoretical and experimental values of the effective PM moment decreases as Ca content increases. These observations reveal that degree of magnetic frustration decreases with increase in Ca content.

Fig. 4.46 shows the magnetization as a function of temperature obtained from the field cooled warming mode within the temperature range 45-250 K at 2 T applied magnetic field. All the samples undergo a phase transition from PM to FM state upon cooling. In this case the T_C values are 133, 117, 99 and 81 K for x=0.0, 0.05, 0.1 and 0.2 respectively. This curve also possesses a clear AFM transition between 53 K and 65 K for x=0.0 to x=0.2. In this PM to FM transition, the Curie temperature has shifted to higher temperature (shown in Table 4.13) which is attributed to strengthening of the ferromagnetism and also the FM phase transition has become broader suggesting a possibility of field driven magnetic phase transition from first order to second order magnetic transition. These field induced behaviors are consistent well with the reported results of $Sm_{1-x}Sr_xMnO_3$ [65] and $Sm_{0.55}Sr_{0.45}MnO_3$ [66].

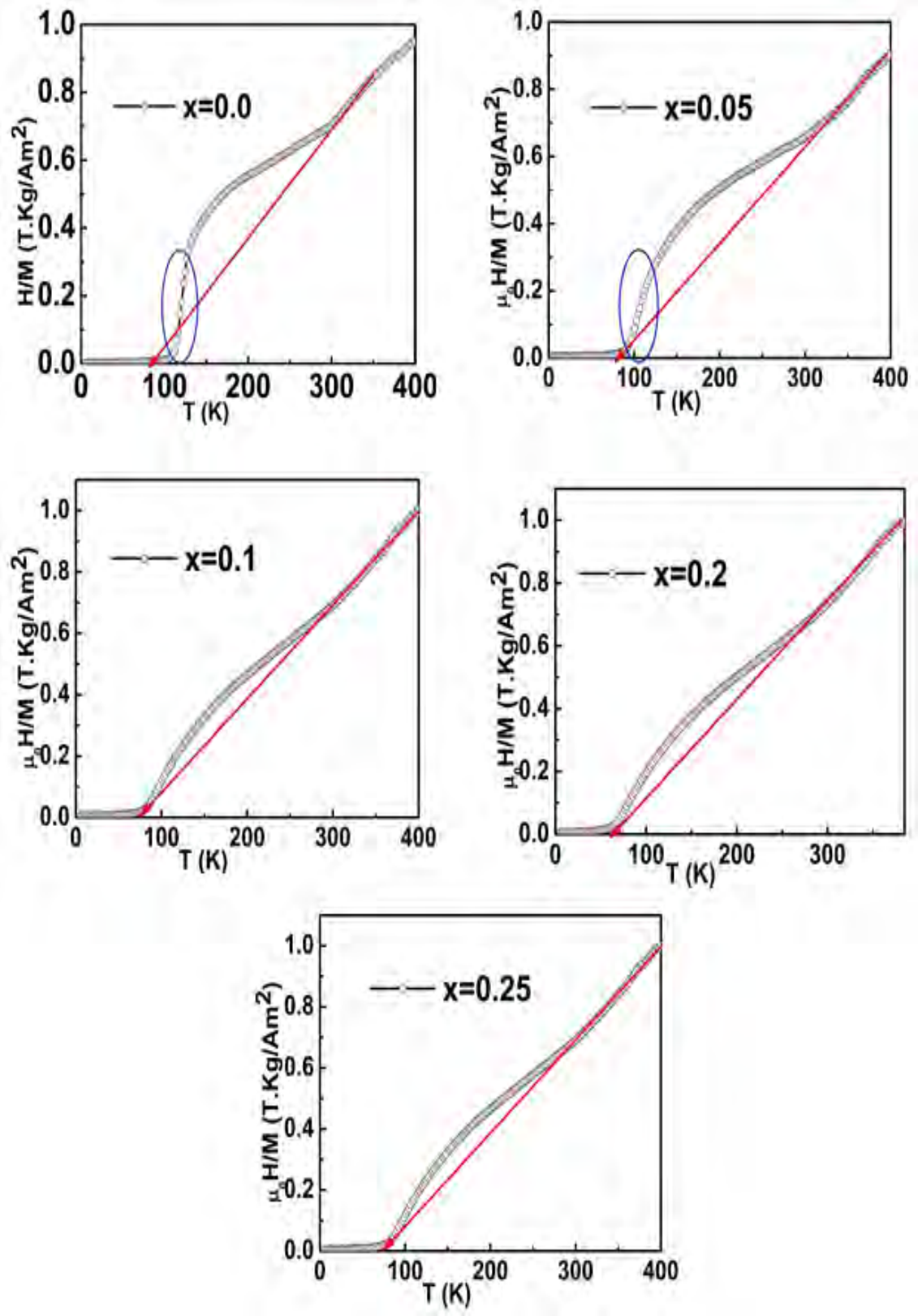

Fig. 4.45 1/χ vs T curves for various $Sm_{0.55}Ca_xSr_{0.45-x}MnO_3$ compounds at 0.01 T.

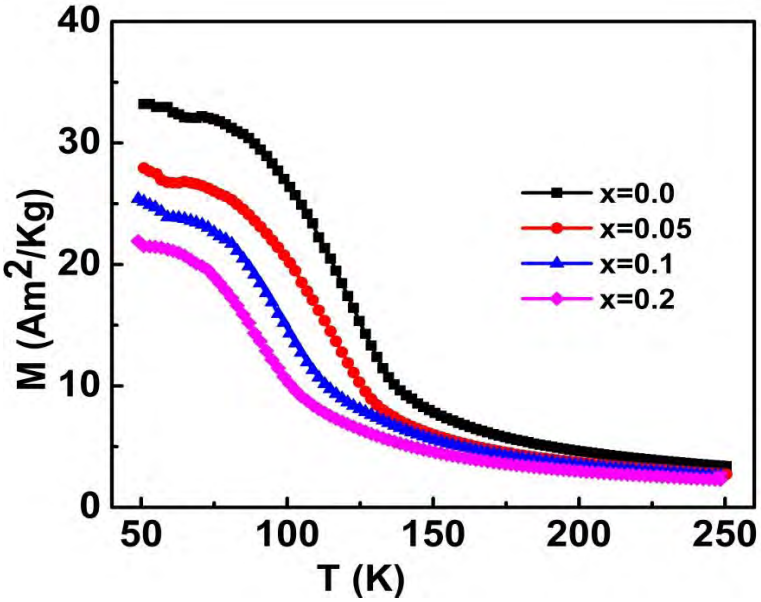

Fig. 4.46 The M - T plots within the temperature range 45-250 K at 2 T applied magnetic field for various $Sm_{0.55}Ca_xSr_{0.45-x}MnO_3$ compounds.

4.3.4.2 Magnetic field dependent magnetic properties

Fig. 4.47 shows the isothermal magnetization as a function of applied field of $Sm_{0.55}Ca_xSr_{0.45-x}MnO_3$ samples at temperature interval of 5 K around T_C. The value of saturation magnetization at 100 K were estimated to be 60, 50, 43, 41 and 38 Am^2/Kg for x = 0.0, 0.05, 0.1, 0.2 and 0.25 respectively. The decrease in magnetization at a certain temperature with the Ca doping corresponds to the competition between FM and AFM interactions in the investigated samples. The weakening of the FM state with the decreasing of Mn–O–Mn bond angle is responsible for decrease in magnetization. For x=0.00 and 0.05, the M-H curves are linear above 140 K (far above T_C) but they show two step behavior i. e. a rapid increase of magnetization is observed above a critical field in the PM phase, in the temperature range 115–140 K for x = 0.0 and at 10–130 K for x = 0.05 (just above T_C). This behavior in magnetization is associated to the inhomogeneous metastable state due to existence of quenched disorder [126] or coexistence of both FM and PM phases in the vicinity of T_C. It is notable that the meta-magnetic transition is not present in samples with x = 0.1, 0.2 and x = 0.25 where the M-H curves are almost equally spaced. This behavior may be happened due to reduction of quenched disorder caused by the partial substitution of Ca in the Sr site, since the

ionic radius of Ca is closer to Sm ion. Also the non-saturating tendency of these M-H curve suggests the mixed state of AFM and FM phases in the studied samples [68].

To find a deeper insight of the type of magnetic transition, the Arrott plots were constructed using M-H data and shown in Fig. 4.48 for $Sm_{0.55}Ca_xSr_{0.45-x}MnO_3$ (x=0.0, 0.05, 0.1, 0.2 and 0.25). According to Banerjee's criterion, "a negative sign of slope indicates the first order magnetic phase transition and a positive slope attributed to the second order magnetic phase transition. In $Sm_{0.55}Ca_xSr_{0.45-x}MnO_3$ compounds a mixture of first order and second order magnetic phase transition is observed. For the samples with x = 0.0 and x = 0.05, the S-shaped curve with a negative slope indicate the occurrence of a first order magnetic phase transition which is in agreement with the reported results [66, 126]. On the other hand, for the samples with x = 0.1, 0.2 and x = 0.25, the Arrott plots possess a positive slope meaning that these samples belong to the class of second order magnetic phase transition materials. So it is observed that Ca substitution in place of Sr suppress order magnetic phase transition but favors second order magnetic phase transition and leads to a transition from first order magnetic phase transition to second order magnetic phase transition for $x \geq 0.1$.

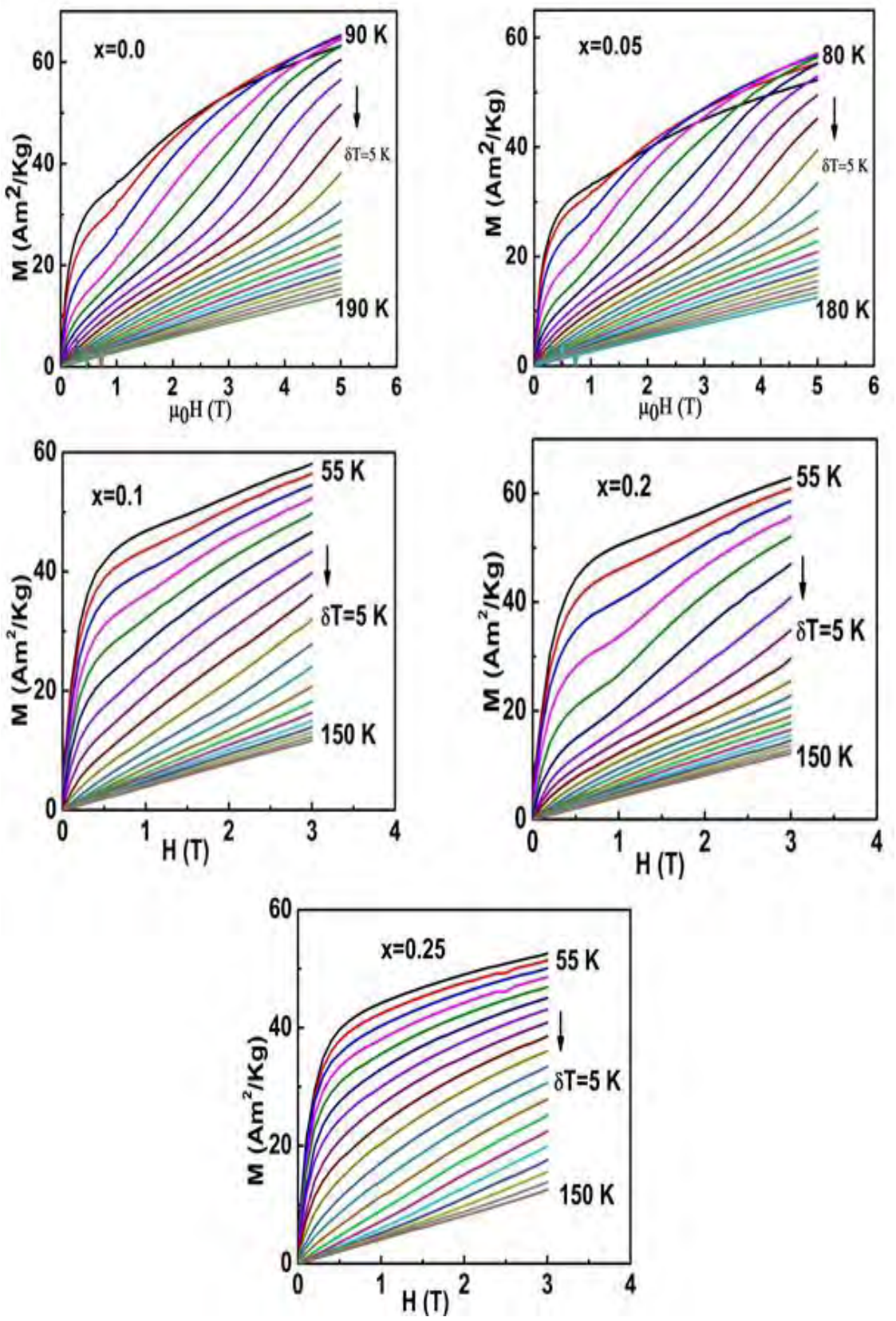

Fig. 4.47 Isothermal M-H curves of various $Sm_{0.55}Ca_xSr_{0.45-x}MnO_3$ compounds.

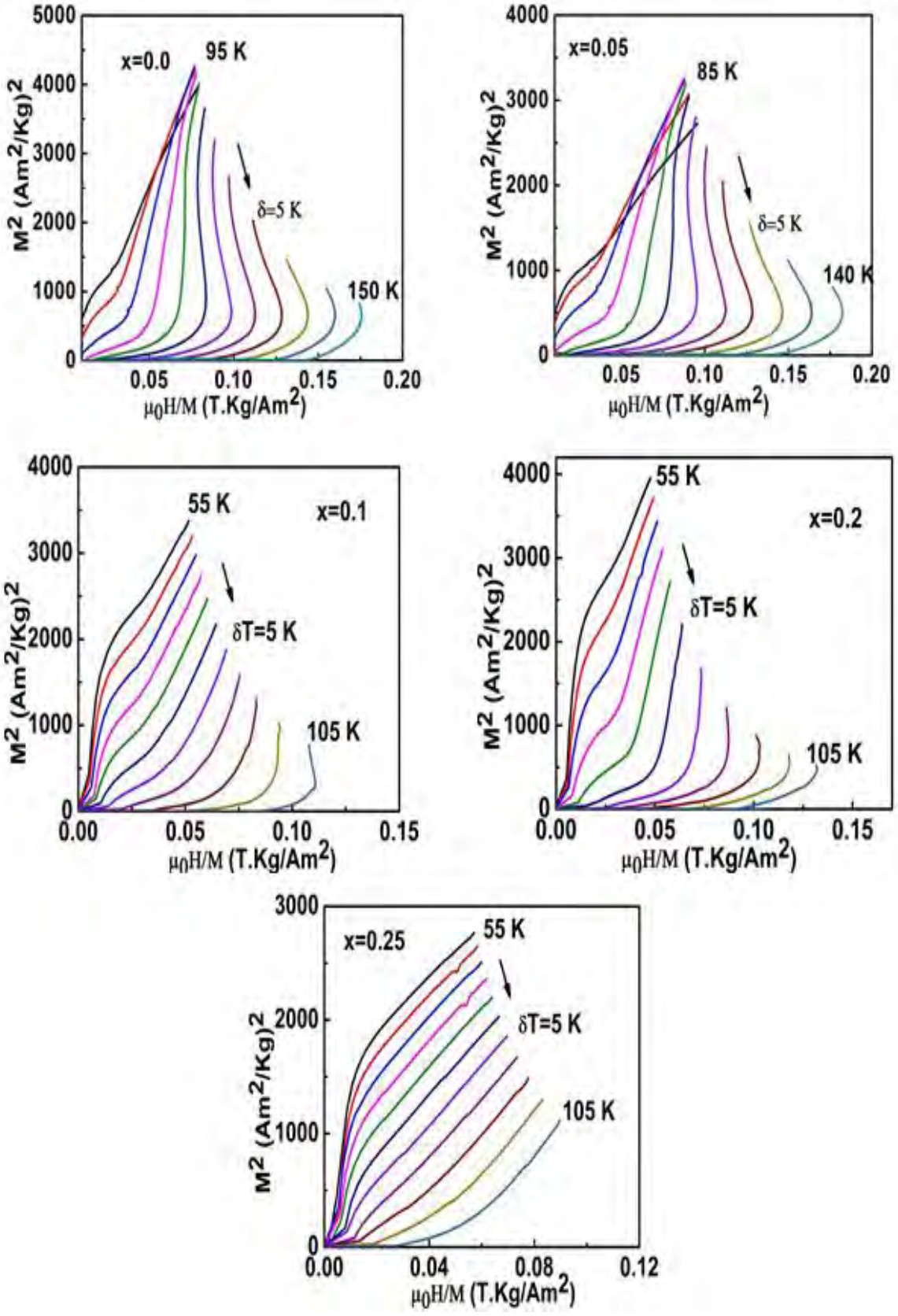

Fig. 4.48 Arrott plot at different temperatures of various $Sm_{0.55}Ca_xSr_{0.45-x}MnO_3$ compounds.

4.3.5 Magnetocaloric properties

The MCE is a magnetic property of some magnetic materials and its magnitude is maximum for ferromagnetic materials. The highest value of MCE is occurred when temperature of the magnetic material reaches around its phase transition temperature and the value of MCE is characterized in terms of adiabatic temperature change or by the magnetic entropy changes with change in applied magnetic field. In this section, ΔS_M of a magnetic material has been calculated using the Maxwell's thermodynamic relation from both magnetization data taken as a function of temperature at 2 T applied field and the isothermal magnetization data taken as function of applied magnetic field. For a magnetic field change ΔH, the equation (4.12) [97] can be re-written in the form as given below:

$$\Delta S_M = \left(\frac{\partial M}{\partial T}\right)_H \Delta H \qquad (4.21)$$

Here the magnetic entropy change of the studied samples has been computed from the M vs T measurement taken at H=2 T applied field using above mentioned equation (4.21) as presented in Fig. 4.49. The $-\Delta S_M$ values changes with change in temperature exhibits its largest value in the vicinity of FM to PM transition temperature due to larger value of change in magnetization. The maximum value of $-\Delta S_M$ is 1.2 $JKg^{-1}K^{-1}$ for x=0.00 which is found around FM to PM transition temperature for a magnetic field change of 2 T. For $Sm_{0.55}Ca_xSr_{0.45-x}MnO_3$, $(-\Delta S_M)_{max}$ decreases with increase in Ca content. From these $-\Delta S_M$ vs T curves, relative cooling power has been calculated using the equation (4.16) [87]. The RCP values are 93, 82, 72, 67 J/Kg under application of 2 T magnetic field for the samples with x = 0.00, 0.05, 0.1, and 0.2, respectively. Fig 4.50 shows $(-\Delta S_M)_{max}$ and RCP as a function of temperature for various $Sm_{0.55}Ca_xSr_{0.45-x}MnO_3$ compounds. It is observed that the RCP decreases with increase in Ca content due to decrease in $(-\Delta S_M)_{max}$.

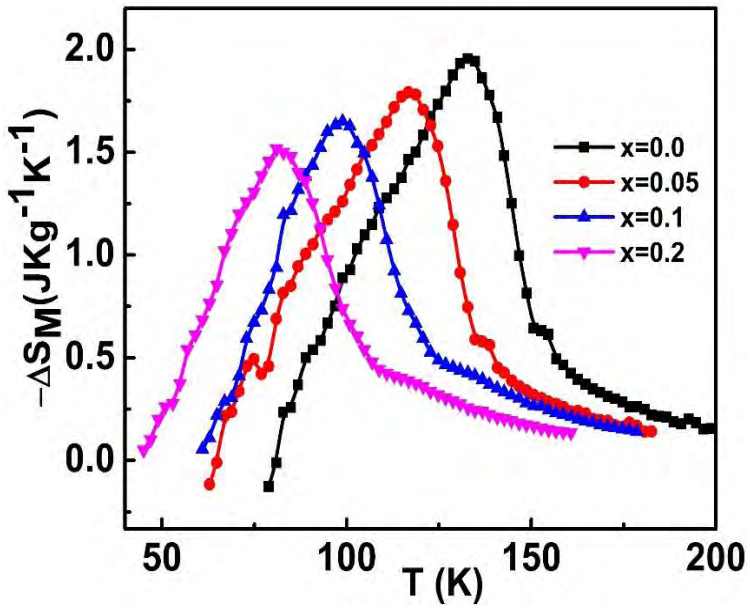

Fig. 4.49 -ΔS_M as a function of temperature for various $Sm_{0.55}Ca_xSr_{0.45-x}MnO_3$ compounds for ΔH=2 T.

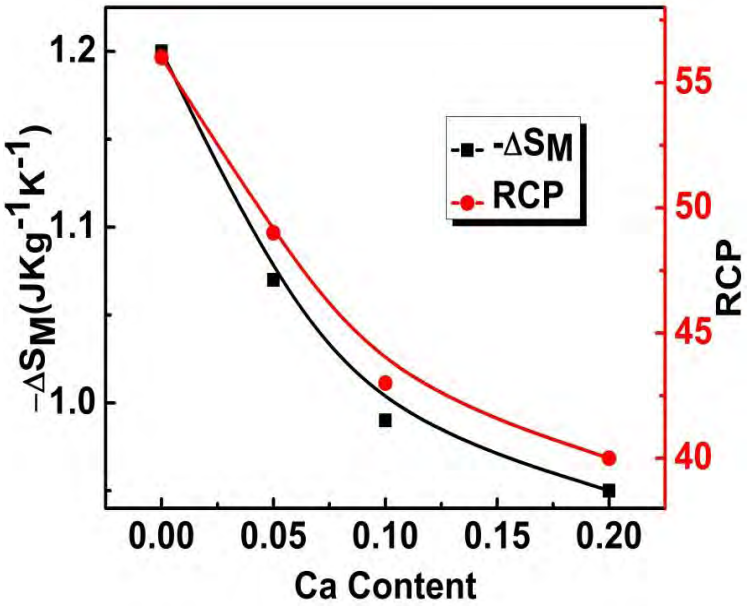

Fig. 4.50 $(-\Delta S_M)_{max}$ and RCP as a function of temperature for various $Sm_{0.55}Ca_xSr_{0.45-x}MnO_3$ compounds.

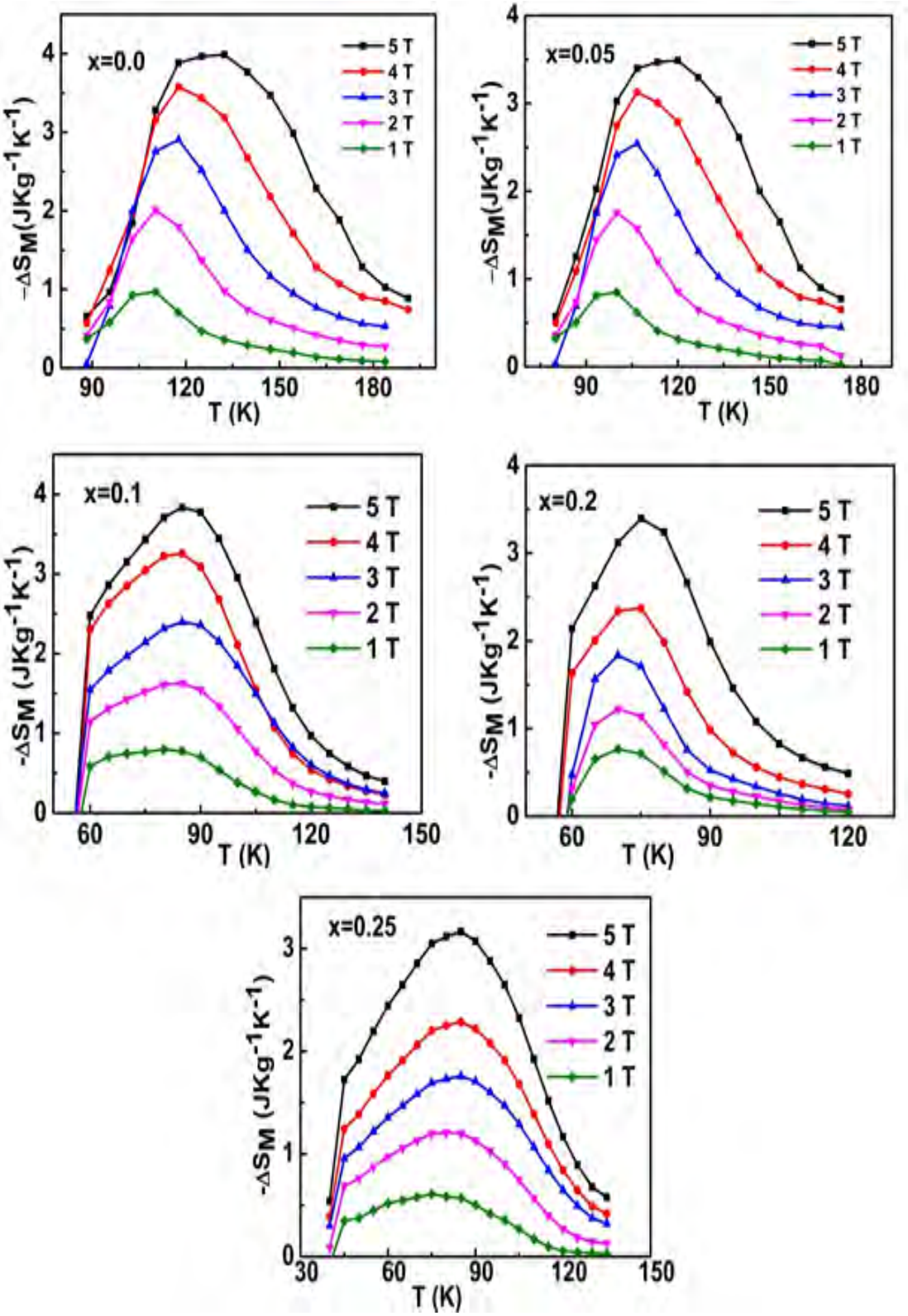

Fig. 4.51 $-\Delta S_M$ vs T at different magnetic field for various $Sm_{0.55}Ca_xSr_{0.45-x}MnO_3$ compounds.

Table 4.13 Curie temperature, irreversibility temperature (T_R), $(-\Delta S_M)_{max}$ and RCP of $Sm_{0.55}Ca_xSr_{0.45-x}MnO_3$ polycrystal.

x content	T_C (K) from FC curve under 100 Oe.	T_R (K)	$(-\Delta S_M)_{max}$ $JKg^{-1}K^{-1}$ for ΔH= 5 T	$(-\Delta S_M)_{max}$ $JKg^{-1}K^{-1}$ for ΔH= 2 T	RCP (J/Kg) for ΔH= 5 T	RCP (J/Kg) for ΔH= 2 T
0.00	116	107	4.02	2.2	222	121
0.05	108	104	3.7	1.8	216	90
0.1	99	92	3.8	1.6	209	72
0.2	87	76	3.51	1.4	187	56
0.25	75	58	3.3	1.3	198	64

The magnetic entropy change was also calculated from isothermal magnetization data using Maxwell's relation as given in equation (4.12). Fig. 4.51 represents $-\Delta S_M$ as a function of temperature for different $Sm_{0.55}Ca_xSr_{0.45-x}MnO_3$ compounds under applied magnetic field change from 1 to 5 T. The $-\Delta S_M$ of the series of sample $Sm_{0.55}Ca_xSr_{0.45-x}MnO_3$varies with temperature and exhibits a maximum, $(-\Delta S_M)_{max}$, in the temperature region vicinity to the two step behavior of the M-H curve and origin of this peak is associated to the coexistence of FM and PM phases near T_C. It is also observed that the $-\Delta S_M$ vs T curves have been gradually broadened and $(-\Delta S_M)_{max}$ is increased with increase of applied field due to change in spin ordering process in the sample [36]. The $(-\Delta S_M)_{max}$ of $Pr_{0.55}Ca_xSr_{0.45-x}MnO_3$ at different constant field are listed in Table 4.13. It is also noticed that largest entropy change $(-\Delta S_M)_{max}$ =4.02 $JKg^{-1}K^{-1}$is occurred for x=0.00, then $(-\Delta S_M)_{max}$ decreases with increase in Ca content. The $(-\Delta S_M)_{max}$ values are 4.02, 3.7, 3.8, 3.51 and 3.3 $JKg^{-1}K^{-1}$, under a field change ΔH=5 T and 2.2, 1.8, 1.6, 1.4 and 1.3 $JKg^{-1}K^{-1}$ for ΔH=2 T for samples with x=0.00, 0.05, 0.1, 0.2, and 0.25, respectively. This result can be associated with the strength of ferromagnetic double exchange interaction, proposed by Zener. He proposed that the transfer integral can be calculated by $t_{eff} = t\cos(\theta/2)$, θ = angle between local spin [71, 90]. Therefore, as tolerance factor decreases, the double exchange FM interaction weakens resulting a

shift in T_C to lower temperature with increase in Ca-doping content in $Sm_{0.55}Ca_xSr_{0.45-x}MnO_3$. The variation in $(-\Delta S_M)_{max}$ can also be explained in terms of tolerance factor. Structural distortion associated with decrease in 't' reduces saturation magnetization (Fig. 4.47) and slightly broaden the FM to PM transition (Fig. 4.43 (a)). As a results $(-\Delta S_M)_{max}$ is found to be reduced with increase in Ca content in $Sm_{0.55}Ca_xSr_{0.45-x}MnO_3$ since entropy change is proportional to dM/dT [90]. Also there may have some other reasons. (1) Decreases in dM/dT due to first order to second order magnetic phase transition [127]. (2) Comparing with $Sm_{0.55}Sr_{0.45}MnO_3$, it is easily understood that the substitution of Sr^{2+} by Ca^{2+} ion decreases the distortion of MnO_6 octahedra, because the ionic radius of Ca is closer to Sm ion resulting a decrease of Mn–O–Mn bond angle and a narrow e_g-electron bandwidth that resist the Mn^{3+} and Mn^{4+} spins to be aligned parallel to the applied field.

It is also observed that temperature of $(-\Delta S_M)_{max}$ shifted toward higher temperature due to higher applied magnetic field. For example, the peak position shifts from 110 to 13 K for H= 1 T to 5 T for the sample with x=0.00. This result suggests a possibility of field induced magnetic phase transition from first order to second order magnetic transition.

The relative cooling power has also been calculated using the equation (4.16) [87] and tabulated in Table 4.13. RCP values for this series of samples are seen to decreases with the increase in Ca content as $(-\Delta S_M)_{max}$ decreases. The RCP values are 222, 216, 209, 187 and 198 J/Kg for ΔH=5 T and 121, 90, 72, 56 and 64 J/Kg for ΔH=2 T for the samples with x = 0.00, 0.05, 0.1, 0.2 and 0.25, respectively.

Table 4.14 represent collected data for T_C, $(-\Delta S_M)_{max}$ and RCP values for a field change ΔH=2 T for the investigated samples and previously reported samples. Data in Table 4.14 reveals that the result found from this research work shows that $(-\Delta S_M)_{max}$ values are less than that of Gd but these samples have tunable T_C toward cryogenic temperature, higher $(-\Delta S_M)_{max}$ values, and larger relative cooling power compared to similar composition prepared by solid state reaction method. These properties make the compounds as a potential material for application in low temperature magnetic refrigeration.

Table 4.14 Collected data for Curie temperature, $(-\Delta S_M)_{max}$ and RCP for ΔH=2 T for the samples prepared by solid state (SS) reaction.

	Method	ΔH	T_C (K)	$(-\Delta S_M)_{max}$ $JKg^{-1}K^{-1}$	RCP (J/Kg)	References
Gd		2	299	4.2	160	[7, 116]
$Sm_{0.56}Sr_{0.44}MnO_3$	SS	2		1.95	120	[128]
$Sm_{0.6}Sr_{0.4}MnO_3$	SS	2	118	2.1	108	[129]
$Sm_{0.55}Sr_{0.45}MnO_3$	Pyrophoric reaction	2	121	2.5	150	[66]
$Sm_{0.55}Sr_{0.45}MnO_3$	SS	2	116	2.2	121	This work
$Sm_{0.55}Ca_{0.05}Sr_{0.40}MnO_3$	SS	2	108	1.8	90	This work
$Sm_{0.55}Ca_{0.1}Sr_{0.35}MnO_3$	SS	2	99	1.6	72	This work
$Sm_{0.55}Ca_{0.2}Sr_{0.25}MnO_3$	SS	2	87	1.4	56	This work
$Sm_{0.55}Ca_{0.25}Sr0.2MnO_3$	SS	2	75	1.3	64	This work

4.3.6 Summary

The studied samples $Sm_{0.55}Ca_xSr_{0.45-x}MnO_3$ have been synthesized by the conventional solid-state reaction method. Their structural, morphological, chemical compositional, temperature and magnetic field dependent magnetic properties, critical behavior around transition temperature, magnetocaloric properties in terms of magnetic entropy change and relative cooling power have been investigated. Room temperature XRD analysis has revealed the orthorhombic structure of all samples with space group Pnma. The structural parameters, Curie temperature, magnetic properties and magnetocaloric effect as a function of Ca content has been investigated. Substitution of larger Sr^{2+} by smaller Ca^{2+} decreases the lattice parameter, tolerance factor and Mn-O-Mn bond angle. Grain size gradually increases while grain boundary effect increases with increase in Ca content in $Sm_{0.55}Ca_xSr_{0.45-x}MnO_3$. No other elements rather than elemental composition

of the studied samples are seen in the EDX spectrums. The calculated values of chemical composition using the EDX data were in good agreement with the nominal one. Coexistence of FM and AFM state in the studied samples are confirmed from the bifurcation between FC and ZFC curves at low field and low temperature. All samples exhibit a paramagnetic to ferromagnetic transition upon cooling, followed by a ferromagnetic to ant-ferromagnetic transition. The FM to PM transition temperature decreases from 116 to 75 K with increasing Ca-doping content from x=0.0 to x=0.25 while the peak magnetization decreases with increasing Ca content in $Sm_{0.55}Ca_xSr_{0.45-x}MnO_3$. The samples with x=0.0 and 0.05 possess first order FM to PM phase transition at low magnetic field. However, the samples exhibit a second order magnetic phase transition for x≥0.1. The inverse magnetic susceptibility as a function temperature reveals that degree of magnetic frustration decreases with increase in Ca content. The FM to PM transitions has been confirmed as first order or second order in nature from dc magnetization measurements and Arrott plots. Under application of higher magnetic field, the Curie temperature has shifted to higher temperature which is attributed to strengthening of the ferromagnetism. Also the FM phase transition has become broader suggesting a possibility of field induced magnetic phase transition from first order to second order magnetic transition. The magnetic entropy change of the studied samples has been calculated from the isothermal M-H data using the Maxwell's thermodynamic relation. The $-\Delta S_M$ of the samples varies with temperature and reaches at the maximum value around its Curie temperature and $(-\Delta S_M)_{max}$ values have been decreased with increasing Ca content. It is also found that the temperature of $(-\Delta S_M)_{max}$ shifted to higher temperature due to higher applied magnetic field. The highest value of $(-\Delta S_M)_{max}$ is 4.02, 3.7, 3.8, 3.51 and 3.3 $JKg^{-1}K^{-1}$ which are observed in the vicinity of magnetic phase transition temperature, for a magnetic field change $\Delta H = 5$ T for x=0.0, 0.05, 0.1, 0.2 and 0.25, respectively. The RCP values are 222, 216, 209, 187 and 198 J/Kg for ΔH=5 T. Thus for (1) the large value of $(-\Delta S_M)_{max}$, and RCP at moderate magnetic field and (2) easily tunable T_C, this compound may be very promising materials for low temperature refrigeration.

CHAPTER 5
CONCLUSIONS

5.1 Summary

The significant findings of this research work are as follows:

- All three series of samples $La_{0.55}Ca_xSr_{0.45-x}MnO_3$, $Pr_{0.55}Ca_xSr_{0.45-x}MnO_3$ and $Sm_{0.55}Ca_xSr_{0.45-x}MnO_3$ have been prepared successfully.
- Rietveld refinement of XRD pattern discloses rhombohedral structure for all the samples of $La_{0.55}Ca_xSr_{0.45-x}MnO_3$ and orthorhombic structure for all the samples of $Pr_{0.55}Ca_xSr_{0.45-x}MnO_3$ and $Sm_{0.55}Ca_xSr_{0.45-x}MnO_3$.
- With increasing Ca content, lattice parameters as well as cell volume and Mn-O-Mn bond angles are found to decrease for all three series of samples
- The change in Ca/Sr ratio does not change Mn^{3+}/Mn^{4+} ratio but changes A-site average ionic radius that causes significant structural changes and in turns controls ferromagnetism in these materials via the double exchange mechanism.
- All the samples are porous and appear at different polygonal forms.
- For Ca content up to 0.1, the grains develop easily and substitution of Sr by Ca more than 0.1 does not favor grain growth in the samples of $La_{0.55}Ca_xSr_{0.45-x}MnO_3$ and $Pr_{0.55}Ca_xSr_{0.45-x}MnO_3$ series. On the other hand, grain size gradually increases with increase in Ca content in $Sm_{0.55}Ca_xSr_{0.45-x}MnO_3$.
- No other elements rather than elemental composition of the investigated samples are seen in the EDX spectrums. The calculated values of chemical composition using the EDX data were in well agreement with the nominal one. The small anomaly between calculated and expected compositions may have arisen due to some possible porosity in the sample.
- For $La_{0.55}Ca_xSr_{0.45-x}MnO_3$ and $Pr_{0.55}Ca_xSr_{0.45-x}MnO_3$, all the samples undergo PM to FM phase transition upon cooling. But for $Sm_{0.55}Ca_xSr_{0.45-x}MnO_3$, with decrease in temperature all the samples exhibit a PM to FM transition, followed by a FM to AFM transition.
- Second-order PM to FM phase transition for all the samples of $La_{0.55}Ca_xSr_{0.45-x}MnO_3$ and $Pr_{0.55}Ca_xSr_{0.45-x}MnO_3$ is confirmed from Arrott plots. But $Sm_{0.55}Ca_xSr_{0.45-x}MnO_3$ underwent first-order PM to FM phase transition for x=0.00 and 0.05 and second-order PM to FM phase transition for x=0.1, 0.2 and 0.25.
- Curie temperature decreases with increase in Ca content for all three series.

- Saturation magnetization increases for $Pr_{0.55}Ca_xSr_{0.45-x}MnO_3$ while decreases with increase in Ca content in $La_{0.55}Ca_xSr_{0.45-x}MnO_3$, and $Sm_{0.55}Ca_xSr_{0.45-x}MnO_3$.
- Bifurcation between ZFC and FC dc magnetizations curves at low field and low temperature reveals coexistence of FM and AFM state in the samples of all three series.
- For temperature above T_C, $La_{0.55}Ca_xSr_{0.45-x}MnO_3$ and $Pr_{0.55}Ca_xSr_{0.45-x}MnO_3$ with x=0.00 obey the Curie–Weiss law. But with increase in Ca content gradual deviation from the Curie–Weiss law is observed meaning the presence of random distribution of FM clusters of Mn^{3+}-O-Mn^{4+} double exchange pairs within the PM phase. On the other hand, $Sm_{0.55}Ca_xSr_{0.45-x}MnO_3$ sample does not obey mean-field Curie–Weiss law for x=0.0 and 0.05 but obeys the Curie–Weiss law above a certain temperature for x=0.1, 0.2 and 0.25.
- Critical point behaviour in the vicinity of T_C has also been elucited for second order magnetic transition materials $Pr_{0.55}Ca_xSr_{0.45-x}MnO_3$ and $La_{0.55}Ca_xSr_{0.45-x}MnO_3$. The well agreement among the various methods confirms that the calculated values of the critical exponents are reliable.
- The calculated critical exponent values disclose the existence of long range FM interaction which belongs to the mean-field model in the studied samples of $Pr_{0.55}Ca_xSr_{0.45-x}MnO_3$ and $La_{0.55}Ca_xSr_{0.45-x}MnO_3$ with x=0.00, 0.05, 0.1 while samples with x=0.2 and 0.25 represent FM short-range interactions which belongs to the 3D Heisenberg model.
- The magnetic entropy change of all series of samples varies with temperature and reaches at the maximum value around its T_C.
- The $-\Delta S_M$ vs T curves were gradually broadened and $(-\Delta S_M)_{max}$ increased with increase of applied field due to change in spin ordering process in all the samples.
- For $La_{0.55}Ca_xSr_{0.45-x}MnO_3$ and $Pr_{0.55}Ca_xSr_{0.45-x}MnO_3$ the temperature of $(-\Delta S_M)_{max}$ remains unchanged while for $Sm_{0.55}Ca_xSr_{0.45-x}MnO_3$ the temperature of $(-\Delta S_M)_{max}$ shifted to higher temperature due to higher applied magnetic field.
- $(-\Delta S_M)_{max}$ increases with increase in Ca content for $Pr_{0.55}Ca_xSr_{0.45-x}MnO_3$ while decreases in $La_{0.55}Ca_xSr_{0.45-x}MnO_3$, and $Sm_{0.55}Ca_xSr_{0.45-x}MnO_3$.
- The scaling exponent for magnetic field dependence of $(-\Delta S_M)_{max}$ is found very close to that of the mean field model for x=0.0, 0.05 and 0.1 while it is close to that

of the 3D Heigenberg model for x=0.2 and 0.25 for both series of $La_{0.55}Ca_xSr_{0.45-x}MnO_3$ and $Pr_{0.55}Ca_xSr_{0.45-x}MnO_3$.

- Working temperature ranges for $Pr_{0.55}Ca_xSr_{0.45-x}MnO_3$, $La_{0.55}Ca_xSr_{0.45-x}MnO_3$ and $Sm_{0.55}Ca_xSr_{0.45-x}MnO_3$ are 180-320 K, 275-380 K and 60-160 K, respectively.
- The RCP increases with increase in Ca content for $Pr_{0.55}Ca_xSr_{0.45-x}MnO_3$ while decreases in $La_{0.55}Ca_xSr_{0.45-x}MnO_3$, and $Sm_{0.55}Ca_xSr_{0.45-x}MnO_3$.
- Both RCP and δT_{FWHM} increases uniformly with increase in applied field for all three series of samples.
- All three series of samples $Pr_{0.55}Ca_xSr_{0.45-x}MnO_3$, $La_{0.55}Ca_xSr_{0.45-x}MnO_3$ and $Sm_{0.55}Ca_xSr_{0.45-x}MnO_3$ possess moderate value of entropy change, large relative cooling power, wide working temperature range and tunable T_C. These properties along with T_C near room temperature make $Pr_{0.55}Ca_xSr_{0.45-x}MnO_3$ and $La_{0.55}Ca_xSr_{0.45-x}MnO_3$ as promising candidate for around room temperature application while tunable T_C at low temperature make $Sm_{0.55}Ca_xSr_{0.45-x}MnO_3$ as strong candidate for low temperature magnetic refrigeration application.

Table 5.1 Comparison among different parameters of three series of samples.

x content	$Pr_{0.55}Ca_xSr_{0.45-x}MnO_3$			$La_{0.55}Ca_xSr_{0.45-x}MnO_3$			$Sm_{0.55}Ca_xSr_{0.45-x}MnO_3$		
	T_C	$(-\Delta S_M)_{max}$ ($JKg^{-1}K^{-1}$) for ΔH= 5 T	RCP (J/Kg) for ΔH= 5 T	T_C	$(-\Delta S_M)_{max}$ ($JKg^{-1}K^{-1}$) for ΔH= 5 T	RCP (J/Kg) for ΔH= 5 T	T_C	$(-\Delta S_M)_{max}$ ($JKg^{-1}K^{-1}$) for ΔH= 5 T	RCP (J/Kg) for ΔH= 5 T
0.00	290	2.83	196	354	3.088	213	116	4.02	222
0.05	286	3.0	213	342	2.83	196	108	3.7	216
0.1	270	3.1	217	336	2.71	177	99	3.8	209
0.2	245	3.51	225	320	2.65	169	87	3.51	187
0.25	230	4.08	232	311	2.55	165	75	3.3	198

5.2 Suggestions for future work

- In order to know the cation distribution in A- and B-sites, neutron diffraction analysis can be performed.
- All the investigated samples of this research work are polycrystalline perovskites. A large value of entropy change can be found in single crystalline samples.
- Also for testing the performance of these fascinating materials in real devices, future work may be carried out.

Novelty of the Present Research

The moderate value of $(-\Delta S_M)_{max}$, large RCP, tunable T_C and wide working temperature range at moderate magnetic field, make $Pr_{0.55}Sr_{0.45}MnO_3$ and $La_{0.55}Ca_{0.25}Sr_{0.2}MnO_3$ very promising materials for room temperature magnetic refrigeration and $Sm_{0.55}Ca_xSr_{0.45-x}MnO_3$ for low temperature refrigeration.

References

[1] Anwar, M. S., Kumar, S., Ahmed, F., Kim, G. W., and Koo, B. H., "Microwave assisted hydrothermal synthesis and magnetocaloric properties of $La_{0.67}Sr_{0.33}MnO_3$ manganite," *J. Nanosci. Nanotechnol*., vol. 12, pp. 5523, 2012.

[2] Aliev, A. M., Batdalov, A. B., and Khanov, L. N., "Magnetic and lattice contributions to the magnetocaloric effect in $Sm_{1-x}Sr_xMnO_3$ Manganites," *Appl. Phys. Lett.,* vol. 112, pp.142407, 2018.

[3] Guo, Z. B., Du, Y. W., Zhu, J. S., Huang, H., Ding, W. P., and Feng, D., "Large Magnetic Entropy Change in Perovskite-Type Manganese Oxides," *Phys. Rev. Lett*., vol. 78, pp. 1142, 1997.

[4] Demin, R. V., and Koroleva, L. I., "Anomalous magnetic susceptibility and inhomogeneous magnetic state in lanthanum strontium manganites," *Phys. Solid State*, vol. 46, pp. 1081, 2004.

[5] Ehsani, M. H., Kameli, P., Ghazi, M. E., Razavi, F. S., and Taheri, M., "Tunable magnetic and magnetocaloric properties of $La_{0.6}Sr_{0.4}MnO_3$ Nanoparticles," *J. Appl. Phys.*, vol. 114, pp. 223907, 2013.

[6] Gschneidner, J. K. A., Pecharsky, V. K., and Tsokol, A. O., "Recent developments in magnetocaloric materials," *Rep. Prog. Phys*., vol. 68, pp. 1479, 2005.

[7] Dankov, S. Y., Tishin, A. M., Pecharsky, V. K., and Gschneidner, J. K. A., "Magnetic phase transitions and the magnetothermal properties of gadolinium," *Phys. Rev. B*, vol. 57, pp. 3478, 1998.

[8] Pecharsky, V. K., and Gschneidner, J. K. A., "Giant magnetocaloric effect in $Gd_5(Si_2Ge_2)$," *J. Phys. Rev. Lett*., vol. 78, pp. 4494, 1997.

[9] Chernenko, V. A., Barandiarán, J. M., Fernández, J. R., Rojas, D. P., Gutiérrez, J., Lázpita, P., and Orue, I., "Magnetic and magnetocaloric properties of martensitic $Ni_2Mn_{1.4}Sn_{0.6}$ Heusler alloy," *J. Magn. Magn. Mater*., vol. 324, pp. 3519, 2012.

[10] Hueso, L. E., Sande, P., Miguens, D. R., Rivas, J., Rivadulla, F., and Lopez-Quintela, M. A., "Magneto caloric effect in $MnFeP_{1-x}As_x$ based compounds," J. *Appl. Phys.*, vol. 91, pp. 9943, 2002.

[11] Zemni, S., Gasmi, A., Boudard, M., and Oumezzine, M., "Effect of nominal strontium deficiency on the structure and the magnetic properties of $La_{0.6}Sr_{0.4-\delta}MnO_3$ manganese perovskites," *Mater. Sci. Eng. B*, vol. 144, pp. 117–122, 2007.

[12] Sun, J. Z., Gallagher, W. J., Duncombe, P. R., Krusin-Elbaum, L., Altman, R. A., Gupta, A., Lu, Y., Gong, G. Q., and Xio, G., "Observation of large low-field magnetoresistance in tri-layer perpendicular transport devices made using doped manganate perovskites," *Appl. Phys. Lett*., vol. 69, pp. 3266–3268, 1996.

[13] Broussard, P. R., Qadri, S. B., Browning, V. M., and Cestone, V. C., "Characterization of transport and magnetic properties in thin film $La_{0.67}(Ca_xSr_{1-x})_{0.33}MnO_3$ mixtures," *J. Appl. Phys.,* vol. 85, pp. 6563–6566, 1999.

[14] Bridges, F., Booth, C. H., Kwei, G. H., Neumeir, J. J., and Swatzky, G. A., "Temperature dependent changes of the Mn 3d and 4p bands near T_C in colossal magnetoresistance systems: XANES study of $La_{1-x}Ca_xMnO_3$," *Phys., Rev. B*, vol. 61, pp 237, 2000.

[15] Phan, M. H., and Yu, S. C., "Review of the magnetocaloric effect in manganite materials," *J. Magn. Magn. Mater*., vol. 308, pp. 325, 2007.

[16] Chau, N., Nhat, H. N., Luong, N. H., L. Minh, D., Tho N. D., Chau, N. N., "Structure, magnetic, magnetocaloric and magnetoresistance properties of $La_{1x}Pb_xMnO_3$ perovskite," *Phys. Rev. B Condens. Matter.*, vol. 327, pp. 270–278, 2003.

[17] Nisha, P., Santhosh, P. N., Suresh, K. G., Pavithran, C., and Varma, M. R., "Near room temperature magneto caloric effect in V doped $La_{0.67}Ca_{0.33}MnO_3$ ceramics," *J. Alloys Compd.*, vol. 47, pp. 566, 2009.

[18] Tomioka, Y., and Tokura, Y., "Global phase diagram of perovskite manganites in the plane of quenched disorder versus one-electron bandwidth," *Phys. Rev. B*, vol. 70, pp. 014432, 2004.

[19] Tokur, Y., and Tomioka, Y., "Colossal magnetoresistive manganites," *J. Magn. Magn. Mater.*, vol. 200, pp. 1–23, 1999.

[20] Rostamnejadi, A., Venkatesan, M., Kameli, P., Salamati, H., Coey, J. M. D., "Magnetocaloric effect in $La_{0.67}Sr_{0.33}MnO_3$ manganite above room temperature", *J. Magn. Magn. Mater*., vol. 323, pp. 2214–2218, 2011.

[21] Szymczak, R., Czepelak, M., Kolano, R., Kolano-Burian, A., Krzymanska, B., & Szymczak, H., "Magnetocaloric effect in $La_{1-x}Ca_xMnO_3$ for x = 0.3, 0.35, and 0.4," *J. Mater. Sci*., vol. 43, pp. 1734–1739, 2008.

[22] Hou, D. L., Bai, Y., Xu, J., Tang, G. D., Nie, X. F., "Magnetic entropy change in $La_{0.67-x}Ca_{0.33}MnO_3$," *J. Alloys Compd.,* vol. 384, pp. 62, 2004.

[23] Sarkar, P., Mandal, P., and Choudhury, P., "Large magnetocaloric effect in $Sm_{0.52}Sr_{0.48}MnO_3$ in low magnetic field," *Appl. Phys. Lett*., vol. 92, pp. 182506, 2008.

[24] Bhatt, R. C., Singh, S. K., Srivastava, P. C., Agarwal, S. K., and Awana, A. P. S., "Impact of sintering temperature on room temperature magneto-resistive and magneto-caloric properties of $Pr_{2/3}Sr_{1/3}MnO_3$," *J. Alloys Compd.*, vol. 580, pp. 377, 2013.

[25] Bahl, C. R. H., Velzáquez, D., Nielsen, K. K., Engelbrecht, K., Andersen, K. B., Bulatova, R., and Pryds, N., "High performance magnetocaloric perovskites for magnetic refrigeration," *Appl. Phys. Lett.*, vol. 100, pp. 121905, 2012.

[26] Mleiki, A., Othmani, S., Cheikhrouhou-Kouba, W., Cheikhrouhou, A., and Hlil, E. K. "Normal and inverse magnetocaloric effect and short range ferromagnetic interaction in $(SmPr)_{0.5}Sr_{0.5}MnO_3$ phase separated manganite," *J. Alloys Compd.*, vol. 688, pp. 1214-1224, 2016.

[27] Torrance, J. B., Lacorre, P., Nazzal, A. I., Ansaldo, E. J., and Niedermayer, C., "Systematic study of insulator-metal transitions in perovskites $RNiO_3$ (R=Pr, Nd, Sm, Eu) due to closing of charge-transfer gap," *Phys. Rev. B*, vol. 45, pp. 8209, 1992.

[28] Aliev, A. M., Batdalov, A. B. and Khanov, L. N., "Magnetic and lattice contributions to the magnetocaloric effect in $Sm_{1-x}Sr_xMnO_3$ Manganites," *Appl. Phys. Lett*., vol. 112, pp. 142407, 2018.

[29] Mleiki, A., Othmani, S., Cheikhrouhou-Koubaa, W., Kouba, M., Cheikhrouhou, A., and Hlil, E. K. "Critical behavior near the ferromagnetice to paramagnetic phase transition in $Sm_{0.55-x}Pr_xSr_{0.45}MnO_3$ compounds ($0.3 \leq x \leq 0.4$)," *J. Alloys Compd.*, vol. 648, pp. 1043-1050, 2015.

[30] Das, K., Banu, N., Das, I., and Dev, B. N., "Magnetocaloric effect of polycrystalline $Sm_{0.5}Ca_{0.5}MnO_3$ compound: Investigation of low temperature magnetic state," *Solid State Commu.,* vol. 274, pp. 36-40, 2018.

[31] Saw, A. K., Channagoudra, G., Hunagund, S., Hadimani, R. L., and Dayal, V., "Study of transport, magnetic and magnetocaloric properties in Sr^{2+} substituted praseodymium manganite," *Mater. Res. Express*, vol. 7, pp. 016105, 2020.

[32] Pramanik, A. K., and Banerjee, A., "Phase separation and the effect of quenched disorder in $Pr_{0.5}Sr_{0.5}MnO_3$," *J. Phys. Condens. Matter.*, vol. 20, pp. 275207, 2008.

[33] Wu, T., and Mitchell, M., "Magnetization steps in manganite films: Time delay of the metamagnetic transition," *Phys. Rev. B*, vol. 69, pp. 100405, 2004.

[34] Kumar, V. S., and Mahendiran, R., "Effect of impurity doping at the Mn-site on magnetocaloric effect in $Pr_{0.6}Ca_{0.4}Mn_{0.96}B_{0.04}O_3$," *J. Appl. Phys*., vol. 109, pp. 023903, 2011.

[35] Mahandiran, R., Maignan, A., Hebert, S., Martin, C., Hervieu, M., Raveau, B., Mitchell, J. F., and Schiffer, P., "Ultrasharp magnetization steps in perovskite manganites," *Phys. Rev. Lett*., vol. 89, pp. 286602, 2002.

[36] Pecharsky, V. K., and Gschneidner, K. A., "Magnetocaloric effect in $Gd_{56}Ni_{15}Al_{27}Zr_2$ alloy and its field independence feature," *Appl. Phys. Lett.,* vol. 70, pp. 3299, 1997.

[37] Li, L., and Yan, M., "Recent progresses in exploring the rare earth based intermetallic compounds for cryogenic magnetic refrigeration," *J. Alloys Compd.,* vol. 823, pp. 153810, 2020.

[38] Zhang, Y., "Review of the structural, magnetic and magnetocaloric properties in ternary rare earth RE_2T_2X type intermetallic compounds," *J. Alloys Compd.*, vol. 787, pp. 1173-1186, 2019.

[39] Kamarad, F., Albertini, M., Arnold Z., Fabbrici, S., and Kastil, J., "Extraordinary magnetic and structural properties of the off-stoichiometric and the Co-doped Ni_2MnGa Heusler alloys under high pressure," *Acta Mater.*, vol. 77, pp. 60-67, 2014.

[40] Wu, B., Zhang, Y., Guo, D., Wang, J., and Ren, Z., "Structure, magnetic properties and cryogenic magneto-caloric effect in RE_2FeAlO_6 (RE = Gd, Dy, Ho) oxides," *Ceram. Int.*, vol. 47, pp. 6290-6297, 2021.

[41] Wada, H., and Tanabe, Y., "Giant magnetocaloric effect of $MnAs_{1-x}Sb_x$," *Appl. Phys. Lett.,* vol. 79, pp. 3302, 2001.

[42] Tegus, Q., Bruck, E., Buschow, K. H., and de Boer, F. R., "Transition-metal-based magnetic refrigerants for room-temperature applications," *Nature*, vol. 415, pp. 150–152, 2002.

[43] Morelli, D. T., Mance, A. M., Mantese, J. V., and Micheli, A. L., "Structure, magnetic, magneto caloric and magneto resistance properties of $Pr_{1-x}Pb_xMnO_3$ perovskite," *J. Appl. Phys*., vol. 79, pp. 373, 1996.

[44] Guo, Z. B., Zhang, J. R., Huang, H., Ding, W. P., and Du, Y. W., "Magneto-caloric effect in LaCaMnO and LaYCaMnO bulk materials," *Appl. Phys. Lett*., vol. 70, pp. 904, 1996.

[45] Zhang, X. X., Tejada, J., Xin, Y., Sun, G. F., Wong, K. W., and Bohigas, X., "Large magnetic entropy change in LaCaMnO perovskite," *Appl. Phys. Lett*., vol. 69, pp. 3596, 1996.

[46] Sun, Y., Xu, X., and Zhang, Y. H., "Direct observation of charge and orbital ordering in $La_{0.5}Sr_{0.5}MnO_3$," *J. Magn. Magn. Mater*., vol. 219, pp. 183, 2000.

[47] Mira, J., Rivas, J., Hueso, L. E., Rivadulla, F., and Lopez Quintela, M. A., "Magnetocaloric effects in $La_{0.7}Ca_{0.3}MnO_3$ single crystal," *J. Appl. Phys*., vol. 91, pp. 8903, 2002.

[48] Lin, G. C., Wei, Q., and Zhang, J. X., "Direct measurement of the magnetocaloric effect in $La_{0.67}Ca_{0.33}MnO_3$," *J. Magn. Magn. Mater.,* vol. 300, pp.

392, 2006.

[49] Szymczak, R., Czepelak, M., Kolano, R., Kolano-Burian, A., Krzymanska, B., and Szymczak, H., "Magnetocaloric effect in $La_{1-x}Ca_xMnO_3$ for x = 0.3, 0.35, and 0.4," *J. Mater. Sci.*, vol. 43, pp.1734–1739, 2008.

[50] Phan, M. H., Yu, S. C., and Hur, H., "Magnetocaloric effect in $La_{0.8-x}Ca_{0.2}Sr_xMnO_3$ (x=0.05, 0.08, 0.1)," *J. Magn. Magn. Mater*., vol. 262, pp. 407, 2003.

[51] Phan, M. H., Yu, S. C., Moon, Y. M., and Hur, N. H., "Dependence of the magneto caloric effect on oxygen stoichiometry in polycrystalline $La_{2/3}Ba_{1/3}MnO_{3-\delta}$," *J. Magn. Magn. Mater.*, vol. 503, pp. 272–276, 2004.

[52] Szewczyk, A., Gutowska, M., Dabrowski, B., Plackowski, T., Danilova, N. P., and Gaidukov, Y. P., "Indirect measurement of the magnetocaloric effect using a novel differential scanning calorimeter with magnetic field," *Phys. Rev. B*, vol. 71, pp. 224432, 2005.

[53] Bally, M. A. A., and Khan, F. A., "Structural, dielectric and magnetic properties of $La_{0.55}Sr_{0.45}MnO_3$ polycrystalline perovskite," *J. Magn. Magn. Mater*., vol. 509, pp. 166897, 2020.

[54] Phan, M. H., Tian, S. B., Hoang, D. Q., Yu S. C., Nguyen, C., and Ulyanov, A. N., "Large magnetic entropy change above 300 K in Colossal magneto resistance materials," *J. Magn. Magn. Mater*., vol. 309, pp. 258–259, 2003.

[55] Xu, Y., Memmert, U., and Hartmann, U., "Direct and specific heat study of magnetocaloric effect in $La_{0.845}Sr_{0.155}MnO_3$," *J. Magn. Magn. Mater*., vol. 698, pp. 242, 2002.

[56] Hanh, D. T., Islam, M. S., Khan, F. A., Minh, D. L., and Chau, N., "Large magnetocaloric effect around room temperature in $La_{0.7}Ca_{0.3-x}Pb_xMnO_3$ perovskites," *J. Magn. Magn. Mater.*, vol. 310, pp. 2826, 2007.

[57]. Islam, M. S., Hanh, D. T., Khan, F. A., Hakim, M. A., Minh, D. L., Hoang, N. N., Hai, N. H., and Chau, N., "Giant magnetocaloric effect around room temperature at moderate low field variation in $La_{0.7}(Ca_{1-x}Sr_x)_{0.3}MnO_3$ perovskites," *Phys. B: Condens. Matter.*, vol. 404, pp. 2495–2498, 2009.

[58]. Raoufi, T., Ehsani, M. H., and Khoshnoud, D. S., "Magnetocaloric properties of $La_{0.6}Sr_{0.4}MnO_3$ prepared by solid state reaction method," *J. Alloys Compd.*, vol. 689, pp. 865-873, 2016.

[59] Nasri, M., Triki, M., Dhahri, E., and Hlil, E. K., "Critical behavior in Sr-doped manganites $La_{0.6}Ca_{0.4-x}Sr_xMnO_3$," *J. Alloys Compd.*, vol. 546, pp. 84–91, 2013.

[60] Wang, K. F., Luo, W. Z., Dong, S., Li, D., Zhang, Z. D., Ren, Z. F., and Liu, J. M., "The A-site disorder effects and enhanced magnetoresistance in $La_{0.55}Sr_{0.45}MnO_3$," *Thin Solid Films*, vol. 518, pp. 38, 2010.

[61] Pekała, M., Drozd, V., Fagnard, J. F., and Vanderbemden, P., "Magnetocaloric effect in nano and polycrystalline manganites $La_{0.5}Ca_{0.5}MnO_3$," *J. Alloys Compd.*, vol. 507, pp. 350–355, 2010.

[62] Martin, C., Maignan, A., Hervieu, M., and Raveau, B., "Magnetic phase diagrams of $L_{1-x}A_xMnO_3$ manganites (L=Pr, Sm; A=Ca, Sr)," *Phys. Rev. B*, vol. 60, pp. 17, 1999.

[63] Fan, J., Pi, L., Zhang, L., Tong, W., Ling, L., Hong, B. Shi, Y., Zhang, W., Lu, D., and Zhang, Y., "Magnetic and magnetocaloric properties of perovskite manganite $Pr_{0.55}Sr_{0.45}MnO_3$," *Phys. B: Condens. Matter.*, vol. 406, pp. 2289, 2011.

[64] Saw, A. K., Hunagund, S., Hadimani, R. L., and Dayal, V., "Magnetic phase transition, magnetocaloric and magnetotransport properties in $Pr_{0.55}Sr_{0.45}MnO_3$ perovskite manganite," *Mater. Today: Proc.,* vol. 46, pp. 6218–6222, 2020.

[65] Nagaraj, B. S., Rao, N., Poornesh, A., Tarachand, P., and Okram, G. S., "Investigation on structural, electrical, magnetic and thermoelectric properties of low bandwith $Sm_{1-x}Sr_xMnO_3$ ($0.2 \leq x \leq 0.5$) manganites," *Phys. B: Condens. Matter.*, vol. 523, pp. 67–77, 2017

[66] Giri, S. K., Dasgupta, P., Poddar A., Nigam, A. K., and Nath, T. K., "Field induced ferromagnetic phase transition and large magnetocaloric effect in $Sm_{0.55}Sr_{0.45}MnO_3$ phase separated manganites," *J. Alloys Compd.*, vol. 582, pp. 609–616, 2014.

[67] Andrade, V. M., Pedro, S. S., Vivas, R. J. C., Rocco, D. L., Reis M. S, Campos, A. P. C., Coelho, A. A., Escote, M., Zenatti, A., and Rossi, A. L., "Magnetocaloric functional properties of $Sm_{0.6}Sr_{0.4}MnO_3$ manganite due to advanced nanostructured morphology," *Mater. Chem. Phy.*, vol. 172, pp. 20-25, 2016.

[68] Banik, S., Das, K., Paramanik, T., Lalla, N. P., Satpati, B., Pradhan, K., and Das, I., "Huge magnetoresistance and ultrasharp metamagnetic transition in polycrystalline $Sm_{0.5}Ca_{0.25}Sr_{0.25}MnO_3$" *NPG Asia Mater.,* vol. 10, pp. 923–930 2018.

[69] Anwar, M. S., Ahmed, F., Lee, S. R., Danish, R., and Koo, B. H., "Study of A-Site Disorder Dependent Structural, Magnetic, and Magnetocaloric Properties in $La_{0.7-x}Sm_xCa_{0.3}MnO_3$ Manganites," *Jpn. J. Appl. Phys.*, vol. 52, pp. 1012, 2013.

[70] Tishin, A. M., and Spichkin, Y. I., "The magneto-caloric effect and its application," *Institute of Physics Publishing,* Bristol, 2003.

[71] Zener, C., "Interaction between the d-Shells in the Transition Metals III: Calculation of the Weiss Factors in Fe, Co, and Ni," *Phys. Rev.*, vol. 83, pp.

299, 1951.

[72] Suk-Joong, Kang L., "Sintering densification, grain growth, and microstructure," Elsevier Butterworth-Heinemann Linacre house, Jordan Hill, *Oxford OX 8DP 30 Corporate Drive,* Burlington, MA0803, 2005.

[73] Globus, A., Pascard, H., and Cagan, V., "Distance between magnetic ions and fundamental properties in ferrites," *J. Phys. Colloq.,* Cl supplement no.4, Tome 38, April 1977, pp. C1-164.

[74] Castricum, H. L., "Mehanically induced chemical and structural changes in materials," *Ph. D thesis*, University of Amsterdam, 2001.

[75] Bally, M. A. A., Islam, M. A., Hoque, S. M., Rashid, R., Islam, M. F. and Khan, F. A, "Magnetocaloric properties and analysis of the critical point exponents of $Pr_{0.55}Ca_xSr_{0.45-x}MnO_3$ (x = 0.00, 0.05, 0.1 and 0.2) at PM-FM phase transition," *Results Phys.,* vol. 28, pp. 104546, 2021.

[76] Goldschmidt, V. M., Skrifter Norske Viedenskaps-Akad, Oslo, I., *Mathemat. Naturwiss.* Klasse No. 8, 1926.

[77] Rodriguez-Martinez, L. M., and Attfield, J. P., "Cation disorder and size effects in magnetoresistive manganese oxide perovskites," *Phys. Rev. B*, vol. 54, pp. R15622, 1996.

[78] Yonglai, F. "Grain-boundary effects on the electrical resistivity and the ferromagnetic transition temperature of $La_{0.8}Ca_{0.2}MnO_3$," *Appl. Phys. Lett.,* vol. 77, pp. 118, 2000.

[79] Bilde-Sørensen, J. B., *Microscopy Today,* pp. 10, 1998.

[80] Bally, M. A. A., Khan, F. A., and Islam, M. A., "Study of A-site disorder dependent structural properties and magnetic ordering in the polycrystalline perovskite $Sm_{0.5}Ca_{0.5-x}Sr_xMnO_3$," *J. Phys. Commun*., vol. 3, pp. 105012, 2019.

[81] Bally, M. A. A., Ahsan, M. Z., Islam, M. A., Alam, M. K., and Khan, F. A., "Magnetic, magnetocaloric and dielectric properties of polycrystalline perovskite $La_{0.7}Ca_{0.2}Pb_{0.1}CoO_3$," *AIP Adv.*, vol. 10, pp. 015033, 2020.

[82] Thanh, T. D., Nguyen, L. H., Manh, D. H., Chien, N. V., Phong, P. T., Khiem, N. V., Hong, L. V., and Phuc, N. X., "Structural, magnetic and magneto-transport behavior of LaSrCaMnO compounds," *Phys. B: Condens. Matter.*, vol. 407, pp. 145, 2012.

[83] Bourouina, M., Krichene, A. N., Khitouni, M., and Boujelben, W., "Structural, magnetic and magnetocaloric properties of nanostructured $Pr_{0.5}Sr_{0.5}MnO_3$ manganite synthesized by mechanical alloying," *Ceram. Int.*, vol. 43, pp. 8139-8145, 2017.

[84] Thaljaoui, R., Pękała, M., Fagnard, J. F., Vanderbemden, P., “Critical analysis of the paramagnetic to ferromagnetic phase transition in $Pr_{0.55}K_{0.05}Sr_{0.4}MnO_3$,” *Phys. B: Condens. Matter.*, vol. 482, pp. 8–13, 2016.

[85] Banerjee, B. K., "On a generalized approach to first and second order magnetic transitions," *J. Phys. Lett*., vol. 12, pp. 16, 1964.

[86] Stanley, H. E., “Introduction to Phase Transitions and Critical Phenomena,” *Oxford University Press,* London, 1971.

[87] Fisher, M. E., “The theory of equilibrium critical phenomena,” *Rep. Prog. Phys*., vol. 31, pp. 418, 1968.

[88] Varvescu, A., and Deac, I. G., "Critical magnetic behavior and large magnetocaloric effect in $Pr_{0.67}Ba_{0.33}MnO_3$ perovskite manganite," *Phys. B: Condens. Matter.,* vol. 470, pp. 96-101, 2015.

[89] Kim, D., Revaz, B., Zink, B. L., Rhyne, J. J., and Mitchell, J. F., “Tricritical Point and the Doping Dependence of the Order of the Ferromagnetic Phase Transition of $La_{1-x}Ca_xMnO_3$,” *Phys. Rev. Lett*., vol. 89, pp. 227202, 2002.

[90] Widom, B., “Equation of State in the Neighborhood of the Critical Point,” *J. Chem. Phys*., vol. 43, pp. 3898, 1965.

[91] Pramanik, A. K., and Banerjee, A., “Critical behavior at paramagnetic to ferromagnetic phase transition in $Pr_{0.5}Sr_{0.5}MnO_3$: A bulk magnetization study,” *Phys. Rev. B*, vol. 79, pp. 214426, 2009.

[92] Fan, J., Pi, L., Zhang, L., Tong, W., Ling, L., Hong, B., Shi, Y., Zhang, W., Lu, D., and Zhang, Y., “Investigation of critical behavior in $Pr_{0.55}Sr_{0.45}MnO_3$ by using the field dependence of magnetic entropy change,” *Appl. Phys. Lett*., vol. 98, pp. 072508, 2011.

[93] Rößler, S., Harikrishnan, S., Nair, M., Roessler, U. K., Kumar, C. M. N., Elizabeth, S., and Wirth, S., “Ferromagnetic transition and specific heat of $Pr_{0.6}Sr_{0.4}MnO_3$,” *Phys. Rev. B*, vol. 84, pp. 184422, 2011.

[94] Anwar, M. S., Kumar, S., Ahmed, F., Arshi, N., Kim, G. W., and Koo, B. H., “Above room temperature magnetic transition and magnetocaloric effect in $La_{0.66}Sr_{0.34}MnO_3$,” *J. Korean Phys. Soc.*, vol. 60, pp. 1587, 2012.

[95] Kouvel, J. S. and Fisher, M. E., “Detailed Magnetic Behavior of Nickel Near its Curie Point,” *Phys. Rev*., vol. 136, pp. A1626, 1964.

[96] Thanh, T. D., Linh, D. C., Uyen Tuyen, N. T., Phan, T. L., and Yu, S. C., "Magnetic and magnetocaloric properties in Ba-doped $La_{0.7}Ca_{0.3}MnO_3$ nanoparticles," *J. Alloys Compd.*, vol. 649, pp. 981-987, 2015.

[97] Narlikar, A. V., "Frontiers in Magnetic Materials," *Springer-Verlag,* Berlin Heidelberg, 2005.

[98] Zubov, E. E., Puzniak, R., Pashchenko, V. P., Mikhailov, V. I., Esenchuk, A., Mironova, S. F., Piechota, S., Dyakonov, V. P., Varyukhin, V. N. and Szymczak, H., *Phys. Solid State,* vol. 51, pp. 2090, 2009.

[99] Bejar, M., Dhahri, E., Hlil, E. K., and Heniti, S., "Influence of A-site cation size-disorder on structural, magnetic and magnetocaloric properties of $La_{0.7}Ca_{0.3-x}K_xMnO_3$ compounds," *J. Alloys Compd.*, vol. 440, pp. 36–42, 2007.

[100] Wood, M. E., and Potter, W. H., "General analysis of magnetic refrigeration and its optimization using a new concept: maximization of refrigerant capacity," *Cryogenics,* vol. 25, pp. 667, 1985.

[101] Zhang, Y., Lampen, P. J., Phan, T. L., Yu, S. C., Srikanth, H., and Phan, M. H., "Tunable magnetocaloric effect near room temperature in $La_{0.7-x}Pr_xSr_{0.3}MnO_3$ ($0.02 \leq x \leq 0.30$) manganites," *J. Appl. Phys.*, vol. 111, pp. 063918, 2012.

[102] Campostrini, M., Hasenbusch, M., Pelissetto, A., Rossi, P., and Vicari, E., "Critical exponents and equation of state of the three-dimensional Heisenberg universality class," *Phys. Rev. B*, vol. 65, pp. 144520, 2002.

[103] Franco, V., Conde, A., Romero-Enrique, J. M., and Blazquez, J. S, "A universal curve for the magnetocaloric effect: an analysis based on scaling relations," *J. Phys.: Condens. Matter*., vol. 20, pp. 285207, 2008.

[104] Cherif, K., Zemni, S., Dhahri, J., Dhahri, J., Oumezzine, M., Ghedira, M., Vincent, H., "Magnetocaloric effect in the doped perovskite manganese oxide $La_{0.7-x}Nd_xSr_{0.3}MnO_3$," *J. Alloys Compd.*, vol. 396, pp. 29–33, 2005.

[105] Sarkar, T., Raychaudhuri, A. K., Bera, S. M., and Yusuf, A. K., "Effect of size reduction on the ferromagnetism of the manganite $La_{1-x}Ca_xMnO_3$ (x=0.33)," *New J. Phys*., vol. 12, pp. 123026, 2010.

[106] Duc, N. T. M., Hung, C. M., Huong, N. T., and Phan, M. H, 'Magnetic Interactions and Magnetocaloric Effect in $(La_{0.5}Pr_{0.5})_{0.6}$ $Ba_{0.4}MnO_3$: Effect of A-Site Codoping," *J. Electron. Mater.,* vol. 49, pp. 11, 2020.

[107] Mori, M., Sammens, N. M., and Tompsett, G. A., "Fabrication processing condition for dense sintered $La_{0.6}AE_{0.4}MnO_3$ perovskites synthesized by the co-precipitation method (AE = Ca and Sr)," *J. Power Sources*, vol. 86, pp. 395–400, 2000.

[108] Yan, K., Fan, R., Shi, Z., Chen, M., Qian, L., Wei, Y.,Sun, K., and Li, J., "Negative permittivity behavior and magnetic performance of perovskite $La_{1-x}Sr_xMnO_3$ at high-frequency," *J. Mater. Chem. C,* vol. 2(6), pp. 1028-1033,

2014.

[109] Phan, M. H., Franco, V., Bingham, N. S., Srikanth, H., Hur, N. H., and Yu, S. C., “Tricritical point and critical exponents of $La_{0.7}Ca_{0.3-x}Sr_xMnO_3$ (x = 0, 0.05, 0.1, 0.2, 0.25) single crystals,” *J. Alloys Compd*., vol. 508, pp. 238, 2010.

[110] Go´mez, J. R., Garcia, R. F., Catoira, A. D., and Go´mez, M. R., "Magnetocaloric effect: A review of the thermodynamic cycles in magnetic refrigeration," *Renew. Sust. Energy Rev*., vol. 17, pp. 74–82, 2013.

[111] Caballero-Flores, R., Bingham, N. S., Phan, M. H., Franco, V., Conde, A., Phan, T. L., Yu, S. C., and Srikanth, H., “Magnetocalotic effect and critical behavior in $Pr_{0.5}Sr_{0.5}MnO_3$: an analysis of the validity of the Maxwell relation and the nature of the phase transition,” *J. Phys. Condens. Matter*, vol. 26, pp. 286001, 2014.

[112] Ho, T. A., Phan, M. H., Lam, V. D., Phan, T. L., and Yu, S. C., “Influence of Pb Doping on the Magnetocaloric Effect and Critical Behavior of $(La_{0.9}Dy_{0.1})_{0.8}Pb_{0.2}MnO_3$,” *J. Electron. Mater*., vol. 45, pp. 2508, 2016.

[113] Biswas, A., Chandra, S., Samanta, T., Ghosh, B., Phan, M. H., Raychaudhuri, A. K., Das, I., and Srikanth, H., “Universality in the entropy change for the inverse magnetocaloric effect,” *Phys. Rev. B*, vol. 87, pp. 134420, 2013.

[114] Debnath, J. C., Zeng, R., Strydom, A. M., and Wang, J. Q., "Ideal Ericsson cycle magnetocaloric effect in $(La_{0.9}Gd_{0.1})_{0.67}Sr_{0.33}MnO_3$ single crystalline nanoparticles," *J. Alloys Compd*., vol. 555, pp. 33-38, 2013.

[115] Rebello, A., Naik, V. B., and Mahendiran, R., “Large reversible magnetocaloric effect in $La_{0.7-x}Pr_xCa_{0.3}MnO_3$,” *J. Appl. Phys*., vol. 110, pp. 013906, 2011.

[116] Franco, V., Conde, A., Romero-Enrique, J. M., Spichkin, Y. I., Zverev, V. I., and Tishin A. M., "Field dependence of the adiabatic temperature change in second order phase transition materials: Application to Gd," *J. Appl. Phys.,* vol. 106, pp. 103911, 2009.

[117] Barik, S. K., Krishamoorthi, C., and Mahediran, R., "Effect of Fe substitution on magnetocaloric effect in $La_{0.7}Sr_{0.3}Mn_{1-x}Fe_xO_3$ ($0.05 \leq x \leq 0.20$) ", *J. Magn. Magn. Mater*., vol. 323, pp. 1015, 2011.

[118] Xu, Y., Meier, M., Das, P., Koblischka, M. R., and Hartmann, U., "Perovskite manganites: potential materials for magnetic cooling at or near room temperature," *J. Crys. Eng*., vol. 5, pp. 383-389, 2002.

[120] Kossi, S., Ghodhbane, E. L., Mnefgui, S., Dhahri, J., and Hlil, E. K., "The impact of disorder on magnetocaloric properties in Ti-doped manganites of

$La_{0.7}Sr_{0.25}Na_{0.05}Mn_{(1-x)}Ti_xO_3$ ($0 \leq x \leq 0.2$)," *J. Magn. Magn. Mater*., vol. 395, pp. 134-142, 2015.

[121] Nam, D. N. H., Dai, N. V., Hong, L. V., Phuc, N. X., Yu, S. C., Tachibana, M., and Takayama-Muromachi, E., "Room temperature magnetocaloric effect in $La_{0.7}Sr_{0.3}Mn_{1-x}M'_xO_3$ (M′=Al, Ti)," *J. Appl. Phys*., vol. 103, pp. 043905, 2008.

[122] Xu, L., Chen, L., Fan, J., Bärner, K., Zhang, L., and Zhu, Y., "Room-temperature large magnetocaloric effect and critical behavior in $La_{0.6}Dy_{0.1}Sr_{0.3}MnO_3$," *J. Ceram. Inter*., vol. 42, pp. 8234-8239, 2016.

[123] Arayedh, B., Kallel, S., Kallel, N., and Pena, O., "Influence of non-magnetic and magnetic ions on the Magneto-Caloric properties of $La_{0.7}Sr_{0.3}Mn_{0.9}M_{0.1}O_3$ doped in the Mn sites by M= Cr, Sn, Ti," *J. Magn. Magn. Mater*., vol. 361, pp. 68-73, 2014.

[124] Chau, N., Nhat, H. N., Luong, N. H., Minh, D. L., Tho, N. D., and Chau, N. N., "Structure, magnetic, magnetocaloric and magnetoresistance properties of $La_{1-x}Pb_xMnO_3$ perovskite," *Phys. B: Condens. Matter.*, vol. 327, pp. 270–278, 2003.

[125] Mleiki, A., Othmani, S., Cheikhrouhou-Koubaa, W., and kouba, M., and Cheikhrouhou, A., "Effect of praseodymium doping on the structural, magnetic and magnetocaloric properties of $Sm_{0.55-x}Pr_xSr_{0.45}MnO_3$ ($0.1 \leqslant x \leqslant 0.4$) manganites," *J. Alloys Compd.*, vol. 645, pp. 559-565, 2015.

[126] Aparnadevi, M., and Mahendiran, R., "Electrical detection of spin reorientation transition in ferromagnetic $La_{0.4}Sm_{0.3}Sr_{0.3}MnO_3$," *J. Appl. Phys*., vol. 113, pp. 17D719, 2013.

[127] Koroleva1, L. I., Zashichirinskii, D. M., and Morozov, A. S., "Influence of magnetic heterogeneous state on magnetocaloric effect in $Sm_{0.55}Sr_{0.45}MnO_3$," *J. Phys.: Conf. Ser*., vol. 303, pp. 012062, 2011.

[128] Bingham, N. S., Lampen, P. J., Phan, L., Phan, M. H., Yu, S. C. and Srikanth, H., "Magnetocaloric effect and refrigerant capacity in $Sm_{1-x}Sr_xMnO_3$ (x=0.42, 0.44, 0.46) manganites," *J. Appl. Phys.*, vol. 111, pp. 07D705, 2012.

[129] Rebello, A., Mahendiran, R., "Composition dependence of magnetocaloric effect in $Sm_{1-x}Sr_xMnO_3$ (x = 0.3–0.5)," *Appl. Phys. Lett.*, vol. 93, pp. 232501, 2008.

Appendices

List of peer-reviewed journal articles

From thesis

1. **Bally, M. A. A.**, Khan, F. A, "Structural, dielectric and magnetic properties of $La_{0.55}Sr_{0.45}MnO_3$ polycrystalline perovskite," *J. Magn. Magn. Mater.,* vol. 509, pp. 166897, 2020.

2. **Bally M. A. A.**, Islam, M. A., Hoque, S. M., Rashid, R., Islam, M. F., Khan, F. A, "Magnetocaloric properties and analysis of the critical point exponents of $Pr_{0.55}Ca_xSr_{0.45-x}MnO_3$ (x = 0.00, 0.05, 0.1 and 0.2) at PM-FM phase transition," *Results Phys.*, vol. 28, pp. 104546, 2021.

3. **Bally, M. A. A.**, Ahsan, M. Z., Islam, M. A., Khan, F. A., "Magnetic properties of $La_{0.55}Ca_xSr_{0.45-x}MnO_3$ perovskite manganite," *Results Phys.*, vol. 21, pp. 103800, 2021.

4. **Bally, M. A. A.**, Khan, F. A. and Islam, M. A., "Study of A-Site Disorder Dependent Structural Properties and Magnetic ordering in the polycrystalline perovskite $Sm_{0.5}Ca_{0.5-x}Sr_xMnO_3$," *J. Phys. Commun*., vol. 3, pp. 105012, 2019.

Related to thesis

5. **Bally, M. A. A.**, Ahsan, M. Z., Islam, M. A., Alam, M. K. and Khan, F. A., "Magnetic, magnetocaloric and dielectric properties of polycrystalline perovskite $La_{0.7}Ca_{0.2}Pb_{0.1}CoO_3$," *AIP Adv.*, vol. 10, pp. 015033, 2020.

6. Ahsan, M. Z., Islam, M. A., **Bally, M. A. A.**, and Khan, F. A., "Spectroscopic analysis for electric and magnetic properties of manganese doped cobalt nanoferrite," *Results Phys.*, vol. 17, pp. 103172, 2020.

7. Islam, M. A., Khan, F. A., Ahsan, M. Z. and **Bally, M. A. A.**, "Influence of manganese substitution on magnetoresistance and magnetic properties of $(Fe_{1-x}Mn_x)_{75}P_{15}C_{10}$ alloy ribbons", *J. Non-Cryst. Solids*, vol. 521, pp. 119473, 2019.

8. Islam, M. A., Ahsan, M. Z., Satter, S., S., **Bally, M. A. A.**, and Khan, F. A., "Structural and magnetic properties of ball-milled powders of $(Fe_{1-x}Mn_x)_{75}P_{15}C_{10}$ met-glass," *AIP Adv.*, vol. 11, pp. 025036, 2021.

Articles under review

1. **Bally, M. A. A.**, Islam, M. A., Ahasan M. Z. and Khan, F. A., "Effect of calcium doping on structural, magnetic and magneto-caloric properties of $La_{0.55}Ca_xSr_{0.45-x}MnO_3$ manganites," *J. Magn. Magn. Mater*., manuscript number: MAGMA-D-20-01026R1.

List of conference presentations

1. **Bally, M. A. A.**, Khan, F. A., Svedlindh, P., Ivanov, S. A., Nordblad, P., Mathieu, R., Sarkar, T., Andersson, M. S., "Structural and magnetic properties of $Sm_{0.5}Ca_{0.5-x}Sr_x$ MnO_3," *Seminar organized by International Science Program (ISP)*, Uppsala University, Sweden, 13th November, 2017.

2. **Bally, M. A. A.,** Khan, F. A, Svedlindh, P., Ivanov, S. A., Nordblad, P., Andersson, M. S., "Structural and magnetic properties of $Sm_{0.5}Ca_{0.5-x}Sr_x$ MnO_3," *International Conference on Nanotechnology and Condensed Matter Physics*, January 11-12, 2018, Bangladesh University of Engineering and Technology, Dhaka, Bangladesh.

3. **Bally, M. A. A.**, Khan, F. A., Svedlindh, P., Ivanov, S. A., Nordblad, P., and Andersson, M. S., "Magnetic ordering in $Sm_{0.5}$ $Ca_{0.2}Sr_{0.3}MnO_3$ peroveskite," *International Conference on Physics-2018*, 08-10 March, 2018, Dhaka University, Dhaka, Bangladesh.

4. **Bally, M. A. A.**, Khan, F. A., Svedlindh, P., Ivanov, S. A., Nordblad, P., Mathieu, R., Sarkar, T. and Andersson, M. S., "Study of A-Site Disorder Dependent Structural Properties and Magnetic ordering in the polycrystalline perovskite $Sm_{0.5}Ca_{0.5-x}Sr_xMnO_3$," *2019 Joint MMM-Intermag Conference*, January 14-18, 2019, Washington, DC.

5. **Bally, M. A. A.** and Khan F. A., "Investigation of structural, electrical and magnetic properties of $La_{0.55}Sr_{0.45}MnO_3$ perovskite," *JEMS 2019*, 26th to 31st August, 2019.

6. **Bally, M. A. A.** and Khan, F. A, "Effect of A-site doping on structural, magnetic and magnetocaloric properties in the polycrystalline perovskite $Sm_{0.55}Ca_xSr_{0.45-x}MnO_3$," *International Conference on Physics-2020*, 05-07 March, 2020, Dhaka, Bangladesh.

7. **Bally, M. A. A.** and Khan F. A., "Effect of calcium doping on structural, magnetic and magneto-caloric properties of $La_{0.55}Ca_xSr_{0.45-x}MnO_3$ manganites," *JEMS 2020*, 8th to 12th December, 2020.

Results in Physics 28 (2021) 104546

Contents lists available at ScienceDirect

Results in Physics

journal homepage: www.elsevier.com/locate/rinp

Magnetocaloric properties and analysis of the critical point exponents of $Pr_{0.55}Ca_xSr_{0.45-x}MnO_3$ (x = 0.00, 0.05, 0.1 and 0.2) at PM-FM phase transition

M.A.A. Bally [a,b,*], M.A. Islam [a], S.M. Hoque [c], R. Rashid [c], Md Fakhrul Islam [a], F.A. Khan [a]

[a] Bangladesh University of Engineering and Technology (BUET), Dhaka 1000, Bangladesh
[b] Directorate of Secondary and Higher Education, Dhaka 1000, Bangladesh
[c] Atomic Energy Commission, Dhaka, Bangladesh

ARTICLE INFO

Keywords:
Solid-state reaction
Orthorhombic
Arrott plot
Entropy change
Relative cooling power
Critical behaviour

ABSTRACT

The polycrystalline manganite $Pr_{0.55}Ca_xSr_{0.45-x}MnO_3$ (x = 0.00, 0.05, 0.1, and 0.2) has been prepared by the solid state reaction technique to investigate its crystal structure, magnetic, and magnetocaloric properties. Critical behaviour around PM-FM phase transition has also been analyzed through various methods including modified Arrott plots (MAP), and critical isotherm analysis of $Pr_{0.55}Ca_xSr_{0.45-x}MnO_3$ (x = 0.00, 0.05, 0.1, and 0.2). XRD analysis reveals that all the samples are found to be crystallized in the orthorhombic system with Pnma space group and lattice parameters a, b and c as well as the cell volume are found to decrease with increasing Ca (x) content. Microstructure is observed with the field emission scanning electron microscopy (FESEM) photograph and elemental compositions are determined by energy dispersive X-ray diffractometer (EDX). Temperature and field dependent magnetization measurement disclose that all the samples undergo second-order FM to PM phase transition but the Curie temperature (T_C) value decreases from 290 K to 245 K with the increase in Ca (x) content from 0.00 to 0.20. The magnetocaloric effect (MCE) in terms of maximum entropy change, $(-\Delta S_m)_{max}$ and relative cooling power (RCP) was calculated from isothermal magnetization measurements around T_C, using Maxwell's thermodynamic relations. Both $(-\Delta S_m)_{max}$ and RCP increases with increasing Ca content suggests the suitability of this compound as a potential solid state refrigerent. Contribution of itinerant electron in the entropy change is found from modulating MCE with Landau theory of phase transition.

Introduction

The rare earth metal Gd and its alloys [1], intermetallic compounds [2–4] and double perovskite [5] are considered as the most suitable magnetic refrigerant because they possesses high value of magnetic entropy change but those have some limitations such as expensive price or limitations in using in air atmosphere or not easy to prepare. Over the past few years manganite materials have been considered as more promising materials since its T_C value and saturation magnetization greatly depends on their composition to make them applicable for different temperature range. In addition, manganite as magnetoaloric compounds exhibit moderate value of magnetic entropy change, large relative cooling power, simple preparation technique, tunable transition temperature, and high chemical stability and low manufacturing cost. The hole-doped manganites with the general formula $Ln_{1-x}M_xMnO_3$ (Ln = rare earth ion, M = divalent alkaline-earth metal ion) [6–10] have attracted considerable attention in the scientific community due to their complex phase diagrams and their important properties such as colossal magnetoresistance (CMR) and magneto caloric effect (MCE) [10]. Generally, these behaviors have been interpreted with the help of the AFM super-exchange and FM double exchange interactions, polaronic effects and phase separation [11]. In recent days, determination of critical point exponent at the phase transition are considering as important way for theoretical and experimental description of magnetic materials. The critical behavior in DE model is generally clarified by long range mean field theory [12]. However some reports suggest that critical behavior can also be interpreted by short range 3-D Heisenberg model [12], and 3-D Ising model [13].

The perovskite $Pr_{1-x}Sr_xMnO_3$ is an important member in manganite family with intermediate one electron band width [14] showing

* Corresponding author at: Directorate of Secondary and Higher Education, Dhaka 1000, Bangladesh.
E-mail address: ballyphybd@gmail.com (M.A.A. Bally).

https://doi.org/10.1016/j.rinp.2021.104546
Received 26 April 2021; Received in revised form 24 June 2021; Accepted 10 July 2021
Available online 14 July 2021

Journal of Magnetism and Magnetic Materials 509 (2020) 166897

Contents lists available at ScienceDirect

Journal of Magnetism and Magnetic Materials

journal homepage: www.elsevier.com/locate/jmmm

Research articles

Structural, dielectric and magnetic properties of $La_{0.55}Sr_{0.45}MnO_3$ polycrystalline perovskite

M.A.A. Bally[a,b,*], F.A. Khan[a]

[a] Bangladesh University of Engineering and Technology (BUET), Dhaka 1000, Bangladesh
[b] Directorate of Secondary and Higher Education, Dhaka 1000, Bangladesh

ARTICLE INFO

Keywords:
Perovskite
Rhombohedral structure
Curie temperature
Permeability
Complex permittivity
Ferromagnetism

ABSTRACT

Polycrystalline perovskite $La_{0.55}Sr_{0.45}MnO_3$ has been prepared by the conventional solid-state reaction route using planetary ball milling technique. The structural properties have been investigated using XRD and SEM data. Rhombohedral structure with space group R-3c of the sample is confirmed by room temperature XRD investigation. Microstructure and chemical composition were determined by Scanning Electron Microscopy (SEM), which includes an energy dispersive X-ray diffractometer (EDX). The study of the dielectric properties of the sample reveals that $La_{0.55}Sr_{0.45}MnO_3$ possesses a high dielectric constant at room temperature and at low frequencies. The real part of the dielectric constant ε' is also observed to be strongly dependent on the temperature and the best properties are found in the sample at room temperature for which $\varepsilon' \approx 10^4$ up to $f = 4x10^6$ Hz. The dispersion of dielectric constants at low frequency is explained in the light of Maxwell–Wagner model. A pronounced increase in Capacitance C is observed from 273 K to 298 K and likely to be caused by the redistribution of ions due to the thermal agitation. The resistivity decreases with increasing temperature indicating that the sample has a semiconductor-like behavior. The constant value of μ' over a wide range of frequency indicates the compositional stability and the range of the suitability of the perovskite. A significant decrease of ac permeability has occurred around 298 K indicating a magnetic phase transition from ferromagnetic to paramagnetic state. Low temperature magnetization measurement reveals paramagnetic to ferromagnetic (FM) transition upon cooling at $T_C = 244$ K. But the FM state coexists with the residual canted AFM (anti-ferromagnetic) state rather than a pure FM state. Presence of external field H favors the FM phase which expands at the expense of the AFM phase. Thus M – H measurement reveals high saturation magnetization.

1. Introduction

In recent decades there has been an increasing interest in materials known as magnetoelectric multiferroics [1]. The electrical control on the ferromagnetism in these materials has a great impact on magnetic data storage, spintronics, miniaturized filters, diplexers and dielectric resonator antennas (DRA) and high-frequency magnetic devices [2–5]. Manganites belongs to manganese oxide with peroveskite structure (ABO_3-type) and hole doped manganites with general formula $Ln_{1-x}M_xMnO_3$ (Ln = rare earth cation, M = divalent alkaline-earth cation) has attracted considerable attention in the study of these compounds for their remarkable magneto transport phenomena in basic physics as well as for their significant technological applications. By A-site doping in the parent compound $LaMnO_3$ with divalent alkaline-earth cation (M^{2+}) causes a conversion of Mn^{3+} to Mn^{4+} proportional to doping amount resulting a mixed valence state of Mn ions which plays a vital role in double exchange (DE) interaction [6]. This is responsible for the metallic character and ferromagnetic properties in these doped manganites. Again in these doped manganites the change of the average A-site ionic radius ($\langle r_A \rangle$) changes the e_g electron bandwidth (W) that in turn results in carrier localization through the Jahn–Teller (JT) distortion of the MnO_6 octahedra. As a consequence, in the vicinity of the half doping, the coexistence of magneto-electric phase appears as a natural tendency. Thus it is well-known that the origin of magneto-electric properties in these perovskite materials is structural as it arises due to displacement of the centre of the positive charges in the lattice with respect to that of the negative charges along a specific polarization direction [7,8]. Besides, these properties are tunable by adjusting substitution level of dopants, sintering temperature and their particle size. Many efforts have already been made to substitute A-site or B-site by metal ions for tuning the structural, magnetic and electrical properties in a controlled manner [9–11].

* Corresponding author.
E-mail address: ballyphybd@gmail.com (M.A.A. Bally).

https://doi.org/10.1016/j.jmmm.2020.166897
Received 16 October 2019; Received in revised form 19 February 2020; Accepted 14 April 2020
Available online 15 April 2020

Results in Physics 21 (2021) 103800

Contents lists available at ScienceDirect

Results in Physics

journal homepage: www.elsevier.com/locate/rinp

Magnetic properties of $La_{0.55}Ca_xSr_{0.45-x}MnO_3$ perovskite manganite

M.A.A. Bally [a,b,*], M.Z. Ahsan [a], M.A. Islam [a], F.A. Khan [a]

[a] Bangladesh University of Engineering and Technology (BUET), Dhaka 1000, Bangladesh
[b] Directorate of Secondary and Higher Education, Dhaka 1000, Bangladesh

ARTICLE INFO

Keywords:
Solid-state reaction
Rhombohedral structure
Curie temperature
Permeability
Ferromagnetism
Magnetic modulus
Magnetic relaxation

ABSTRACT

Conventional solid-state reaction technique was used to prepare the studied samples $La_{0.55}Ca_xSr_{0.45-x}MnO_3$ (x = 0.0, 0.1, 0.2). Their structural and magnetic properties have been investigated to find the effect of calcium doping on the D.C. and A.C. magnetic properties of the compounds. Room temperature XRD investigations confirm rhombohedral structure with space group R-3c for all the samples. Lattice parameter is found to decrease with increase in Ca(x) content. Microstructure was examined from the images taken by Scanning Electron Microscopy (SEM) and chemical compositions were determined by an energy dispersive X-ray diffractometer (EDX). The zero-field cooled (ZFC) and field cooled (FC) DC magnetization measurements reveal paramagnetic (PM) to ferromagnetic (FM) transition in them upon cooling through their Curie temperature (T_C). But the FM state coexists with the residual canted anti-ferromagnetic state rather than a pure FM state in the samples. The T_C values are dependent on Ca(x) content of the samples. Moreover, XRD analysis and EDX data reveals the presence of Mn deficiency in the studied samples. Presence of minor secondary Mn_3O_4 phase creates this deficiency resulting a significant decrease in T_C and strongly influences the magnetic properties. The values of A.C. permeability (μ') also depend on Ca(x) content as well as grain size that can be explained by Globus equation. However, μ' values of the samples remain almost constant over a wide range of frequency which indicates the compositional stability of the perovskites. The magnetic modulus demonstrates the dynamics of their A.C. permeability by screening out the stray/any other effects in them. The Nyquist plots of magnetic modulus of the samples show the type of their magnetic relaxation.

Introduction

Manganites are special type of manganese oxide with perovskite structure (ABO_3-type) and mixed valent manganites with general formula $R_{1-x}A_xMnO_3$ (R = rare earth cation, A = divalent alkaline-earth cation) have attracted much attention in the study of these compounds due to interesting phenomena in basic physics such as colossal magnetoresistance (CMR), magnetocaloric effect (MCE) as well as for their considerable technological applications in spintronics, sensors and catalysis [1–3]. Substitution of divalent alkaline-earth cation (M^{2+}) in the A-site of the parent compound $LaMnO_3$ causes a conversion of Mn^{3+} to Mn^{4+} ions which are proportional to doping amount. As a result, unequal proportion of Mn ions are created in these manganite which takes a vital role in double exchange (DE) interaction [4] and is regarded as the source of the metallic and ferromagnetic properties in these doped manganite. Besides, change in average ionic radius of A-site ($\langle r_A \rangle$) may create carrier localization through the Jahn–Teller (JT) distortion of the MnO_6 octahedra in these doped manganite. As a consequence, it is well-known that the origin of magnetic properties in these perovskite materials depends on structural parameters [5,6]. Moreover, small change in composition or presence of small amount of impurity in these types of compounds causes a large change in magnetic properties. $La_{0.55}Sr_{0.45}MnO_3$ is regarded as ferromagnetic double exchange (DE) systems having the T_C value around 355 K [4]. Over the years, a series of investigations have been performed on tuning the structural, magnetic and magnetocaloric properties by substituting divalent alkaline-earth ions in place of A or B sites in a controlled manner [7–9]. However, very seldom analyses were reported so on D.C. and A.C. magnetic properties of this kind of perovskite compound. The D.C. magnetic property includes the magnetization, Curie temperature, coercivity and remanent ratio of the material and their response under the influence of the D.C. magnetic field and temperatures as well. Conversely, the A.C. magnetic property demonstrates the response of permeability in the material under the application of A.C. magnetic field. The magnetic modulus analysis is another important tool to understand and explain the dynamical mechanism of permeability and magnetization in the

* Corresponding author.

https://doi.org/10.1016/j.rinp.2020.103800
Received 15 October 2020; Received in revised form 13 December 2020; Accepted 29 December 2020
Available online 4 January 2021

AIP Advances ARTICLE scitation.org/journal/adv

Magnetic, magnetocaloric, and dielectric properties of polycrystalline perovskite $La_{0.7}Ca_{0.2}Pb_{0.1}CoO_3$

Cite as: AIP Advances 10, 015033 (2020); doi: 10.1063/1.5134732
Submitted: 4 November 2019 • Accepted: 18 December 2019 •
Published Online: 16 January 2020

M. A. A. Bally,[a] M. Z. Ahsan, M. A. Islam, M. K. Alam, and F. A. Khan

AFFILIATIONS

Bangladesh University of Engineering and Technology (BUET), Dhaka 1000, Bangladesh

[a]Author to whom correspondence should be addressed: ballyphybd@yahoo.com

ABSTRACT

The polycrystalline perovskite $La_{0.7}Ca_{0.2}Pb_{0.1}CoO_3$ has been prepared by the conventional solid-state reaction technique, and then the structural, magnetic, magnetocaloric, and dielectric properties of the sample have been investigated. The monoclinic structure with space group I2/a of the sample is confirmed by X-ray diffraction investigation at room temperature. The microstructure was examined by scanning electron microscopy (SEM), and chemical composition was determined using an energy dispersive X-ray diffractometer attached to the SEM. Magnetic measurement reveals that the sample undergoes ferromagnetic to paramagnetic transition with increasing temperature and behaves as a soft magnetic material. Field cooled and zero-field cooled *dc* magnetization curves at low field and low temperature show divergence, indicating the coexistence of antiferromagnetic and ferro-magnetic clusters in the sample. Magnetic inhomogeneity of the sample has also been clearly confirmed by the divergence between the Curie temperature, T_c, and the paramagnetic Curie temperature, θ. The sample also shows a magnetocaloric effect at a very low field (H = 0.01 T). The high negative value of the real part of complex permittivity, ε′, reveals metallic behavior of the sample at low frequency around room temperature. However, the frequency dependent ac conductivity (σ) exhibits three distinct bands, namely, the metallic, insulating, and anomalous band, around room temperature. Temperature dependent ε′ reveals that the sample undergoes insulator to metallic transition above −20 °C.

I. INTRODUCTION

Samples with a perovskite structure have the common formula ABO_3, where A and B are cations, and O is the anion. Cobaltites have a perovskite structure with a rare earth element in the A-site and Co in the B-site. In recent years, there has been increased research interest on the electromagnetism of cobaltite materials because of their improved properties like colossal magnetoresistance, charge ordering, phase separation, and presence of various spin states of Co^{3+} and Co^{4+} ions depending on the A-site substitution and temperature.[1,2] Substitution of a 3^+ rare earth element by a 2^+ ion changes the oxidation state of cobalt ions from Co^{3+} to Co^{4+} for which cobaltite compounds exhibit multifunctional properties.[3–6] Besides the doping level, properties of cobaltites can be tuned by the average ionic radius of the A-cation site. Many works have been carried out on $LaCoO_3$ regarding its spin state, magnetic behavior, and phase transition.[7–13] $LaCoO_3$ is a nonmagnetic insulator which is transformed to a paramagnetic insulating state and then transforms from an insulating state to a metallic state with variation of Ca content and temperature.[1,2] Influence of A-site doping with alkaline-earth elements, for example, Sr, Ba, Ca, or combinations of these elements, changes the electromagnetic properties in $LaCoO_3$. Roy and Das showed that the particle size controls the electro-magnetic properties of $La_{0.5}A_{0.5}CoO_3$ (A = Sr, Ca, and Ba) nanoparticles.[13] Structural and magnetic properties of $La_{0.7}Pb_{0.3}Mn_{1-x}Co_xO_3$ ($0 \le x \le 1$) perovskites have been investigated by Young *et al.*[14,15] Debnath *et al.* studied the magnetic and magnetocaloric property of $La_{0.7}Ca_{0.3}CoO_3$.[16] Recently, dielectric properties of perovskites has attracted much attention in the field of many electric and electronic devices, like capacitors, thermistors, piezoelectric transducers, and a variety of electro-magnetic devices.[17] In perovskites, the origin of dielectric properties is structural because they arise due to

IOP Publishing J. Phys. Commun. 3 (2019) 105012 https://doi.org/10.1088/2399-6528/ab3336

Journal of Physics Communications

PAPER

OPEN ACCESS

RECEIVED
4 February 2019

REVISED
5 June 2019

ACCEPTED FOR PUBLICATION
17 July 2019

PUBLISHED
29 October 2019

Study of A-site disorder dependent structural properties and magnetic ordering in polycrystalline perovskite $Sm_{0.5}Ca_{0.5-x}Sr_xMnO_3$

M A A Bally, F A Khan and M A Islam

Department of Physics, Bangladesh University of Engineering and Technology (BUET), Dhaka-1000, Bangladesh

E-mail: ballyphybd@yahoo.com

Keywords: Perovskite, spin-glass, polycrystalline, charge/orbital ordering, Curie temperature.

Abstract

This paper reports the studies on the effect of A-site substitution by strontium on the structural properties and magnetic ordering in polycrystalline perovskite $Sm_{0.5}Ca_{0.5-x}Sr_xMnO_3$ (x = 0.1, 0.2 and 0.3). The investigated samples are prepared by conventional solid-state reaction technique. XRD analysis at room temperature has confirmed orthorhombic structure of the sample with space group Pnma. The dependence of structural parameter, Curie temperature and coercivity on Sr doping content has been thoroughly investigated. It is observed that substitution of Sr^{2+} for Ca^{2+} increases lattice parameter, tolerance factor and the Curie temperature. However, the coercivity (H_c) decreases with increasing Sr content while the charge ordering process is weakened with increasing Sr content. Field cooled (FC) and zero-field cooled (ZFC) *dc* magnetizations measurements at low field and low temperature indicate that there is a spin-glass (SG) like state occurred. Temperature dependent ac susceptibility at different frequency indicates a spin-glass-like transition of the sample.

Introduction:

The alkaline doped rare-earth manganites, $RE_{1-x}AE_xMnO_3$ (RE = rare earth and AE = alkaline-earth element) have been studied extensively as they show interesting properties like metal insulator transition, colossal magnetoresistance (CMR) and magnetocaloric effect [1–3]. These compounds also show a higher electrical resistivity, which is favorable for reducing eddy current heating [4]. In these manganites, a decrease in the average ionic radii of the RE^{3+} and AE^{2+}cations, generally leads to an increase in tilting of MnO_6 octahedral or the Mn–O–Mn bond angle [5]. As a result ferromagnetic (FM) state is relatively destabilized in a distorted perovskite manganite. In such a case, a FM state is frequently replaced by an anti-ferromagnetic (AFM) insulator with Charge/orbital ordering (CO/OO) [6]. $Sm_{0.5}Sr_{0.5}MnO_3$ shows ferromagnetic metallic behavior and $Sm_{0.5}Ca_{0.5}MnO_3$ behaves like an antiferromagnetic charge/orbital ordered insulator. Our goal is to investigate the competing features between FM and CO/OO with Sr content in $Sm_{0.5}Ca_{0.5-x}Sr_xMnO_3$.

Experimental:

Polycrystalline samples of $Sm_{0.5}Ca_{0.5-x}Sr_xMnO_3$ (x = 0.1, 0.2 and 0.3) were prepared by conventional solid-state reaction technique. High purity oxides and carbonates ($MnCO_3$, Sm_2O_3, $SrCO_3$, and $CaCO_3$) were weighed in stoichiometric proportion and mixed thoroughly by hand in an agate mortar and pestle. The mixed sample was then ball milled in a planetary ball mill for 6 h and then calcined at 800 °C. The calcined samples were sintered at 850 °C, 900 °C, 950 °C, 980 °C, 1020 °C and 1050 °C temperature each for 12 h with intermediate grounding and pelletizing. Structural characterizations were done by X-ray diffraction (XRD) technique (Geol. Diffractometer) and structural parameters were extracted using a commertial software. Microstructure and